Nanostructured Catalysts for Conversion of CO2 into Hydrocarbons

Williamson, David

Award date:
2020

Awarding institution:
University of Bath

Nanostructured Catalysts for Conversion of CO_2 into Hydrocarbons

A thesis submitted for the degree of Doctor of Philosophy

PhD student – David L. Williamson, Department of Chemical Engineering

Primary supervisor – Professor Davide Mattia, Department of Chemical Engineering

Joint supervisor – Dr Matthew Jones, Department of Chemistry

June 2019

University of Bath
Claverton Down
Bath, BA2 7AY
United Kingdom

For my family.

Contents

List of figures

List of tables

List of equations

Nomenclature

Notation	Definition
°C	Degrees Celcius
5-HMF	5-hydroxymethylfurfu
ACN	Acetonitrile
Ar	Argon
ASF	Anderson-Schulz-Flory
at. %	Atom percentage
BDD	Boron-doped diamond
BET	Brunauer-Emmett-Teller surface area analysis
ca.	Circa
CAES	Compressed air energy storage
CCS	Carbon capture and storage
CCU	Carbon capture and utilisation
cCVD	Catalytic CVD
CNT	Carbon nanotube
CO	Carbon monoxide
CO2	Carbon dioxide
CSTR	Continuous stirred tank reactor
CVD	Chemical vapour deposition
DC-PECVD	Direct current PECVD
DFAFC	Direct formic acid fuel cell
DFF	2,5-diformylfuran
DI	Dry impregnation
DPECVD	Diffusion PECVD
DRIFTS	Diffuse reflectance FT-IR spectroscopy
EDS	Energy-dispersive X-ray spectroscopy
EGR	Enhanced gas recovery
EOR	Enhanced oil recovery
EU	European Union
eV	Electron volts
FA	Formic acid
FCCVD	Floating catalyst CVD
FcH	Ferrocene
FDCA	2,5-furandicarboxylic acid
Fe	Iron
FESEM	Field emission SEM
FFCA	2-formyl-5-furancrboxylic acid
FID	Flame ionization detector
FT	Fischer-Tropsch
FT-IR	Fourier-transform infrared spectroscopy
GHG	Greenhouse gas
GNF	Graphitic nanofibre
GTL	Gas-to-liquid
GWP	Global warming potential
H2	Molecular hydrogen
hr	Hours

HSE	Health and Safety Executive
HTFT	High-Temperature Fischer-Tropsch
HTS	High-Temperature Shift
ID	Intensity of the D band
IG	Intensity of the G band
IMFP	Inelastic mean free path
IPCC	Intergovernmental Panel on Climate Change
IR	Infrared
IWI	Incipient wetness impregnation
K	Kelvin
LA	Levulinic acid
LCA	Life cycle assessment
LJ	Lennard-Jones
LTFT	Low-Temperature Fischer-Tropsch
LTS	Low-Temperature Shift
MFC	Mass flow controller
mg	Milligrams
min	Minutes
mL	Millilitres
mmol	Millimoles
mol	Moles
MS	Mass spectrometry
MTBE	Methyl tert-butyl ether
MTS	Medium-Temperature Shift
MTY	Million tonnes per year
MWCNT	Multi-walled CNT
MWPECVD	Microwave PECVD
NCNT	*In situ*-doped nitrogen-doped CNT
N-CNT	Post-doped nitrogen-dope CNT
NIOSH	National Institute for Occupational Safety and Health
nm	Nanometres
OA	Oxalic acid
OEL	Occupational exposure limit
ORR	Oxygen reduction reaction
P2G	Power-to-gas
PBR	Packed bed reactor
PECVD	Plasma-enhanced CVD
PES	Photoelectron spectroscopy
PHS	Pumped hydro storage
PV	Photovoltaic
PVI	Pore volume impregnation
pXRD	Powder XRD
Q^2	Q-squared
R^2	R-squared
RBM	Radial breathing mode
RF-PECVD	Radio frequency PECVD
r_{obs}	Observed rate of reaction
RP-HPLC	Reversed phase high-performance liquid chromatography

RWGS	Reverse water gas shift reaction
SA	Succinic acid
sccm	Standard cubic centimetre
SEM	Scanning electron microscopy
SMR	Steam methane reforming
SNG	Synthetic natural gas
SR15	Special Report 15
SSITKA	Steady-state isotopic transient kinetic analysis
SWCNT	Single-walled CNT
syncrude	Synthetic crude oil
T_{act}	Activation temperature
TCD	Thermal conductivity detector
TEM	Transmission electron microscopy
TGA	Thermogravimetric analysis
TG-MS	Thermogravimetric mass spectrometry
TOF	Turnover frequency
TON	Turnover number
TPD	Temperature programmed desorption
TPR	Temperature programmed reduction
TRL	Technology readiness level
UV	Ultraviolet
VLS	Vapour-liquid solid model
VSS	Vapour-solid-solid model
w/w	Weight-per-weight based percentage solution
WGS	Water gas shift reaction
WHSV	Weight hour space velocity
WI	Wet impregnation
wt. %	Weight percentage
XPS	X-ray photoelectron spectroscopy
XRD	X-ray diffraction spectroscopy
α	FT chain growth probability
µm	Microns
µmol	Micromoles

Affiliated conferences, awards, placements and publications

- Conference: *ChemEngDayUK16* – March 31-April 1, 2016 – Bath, UK – event support, seminar attendance, and poster judging.
- Conference: *7th European Chemical Society Chemistry Congress (EuCheMS2018)* – August 26-30, 2018 – Liverpool, UK – seminar attendance and poster presentation.
- Award: *RSC Energy & Environmental Science Prize* – poster prize for CO_2 methanation research presented at EuCheMS2018.
- Placement: *Ørsted A/S (formerly DONG Energy)* – September 1-November 30, 2017 – Copenhagen, Denmark – 3 months industrial placement with a world leader in renewable energy, researching and presenting CO_2 utilisation techniques for applications in waste-to-energy and biogas production projects.
- Publication: M. Ventura, D. Williamson, F. Lobefaro, M. D. Jones, D. Mattia, F. Nocito, M. Aresta and A. Dibenedetto, *ChemSusChem*, 2018, **11**, 1073-1081.
- Publication: D. L. Williamson, M. D. Jones and D. Mattia, *Energ. Technol.*, 2019, **7**, 294-306.
- Publication: D. L. Williamson, C. Herdes, L. Torrente-Murciano, M. D. Jones and D. Mattia, *ACS Sustain Chem Eng*, 2019, **7**, 7395-7402.

ChemPubSoc Europe

DOI: 10.1002/cssc.201702347

CHEMSUSCHEM Full Papers

Sustainable Synthesis of Oxalic and Succinic Acid through Aerobic Oxidation of C6 Polyols Under Mild Conditions

Maria Ventura,[a] David Williamson,[c] Francesco Lobefaro,[d] Matthew D. Jones,[e] Davide Mattia,*[c] Francesco Nocito,[b] Michele Aresta,[d] and Angela Dibenedetto*[a, b]

The sustainable chemical industry encompasses a shift from the use of fossil carbon to renewable carbon. The synthesis of chemicals from nonedible biomass (cellulosic or oil) represents one of the key steps for "greening" the chemical industry. In this paper, we report the aerobic oxidative cleavage of C6 polyols (5-HMF, glucose, fructose and sucrose) to oxalic acid (OA) and succinic acid (SA) in water under mild conditions using M@CNT and M@NCNT (M = Fe, V; CNT = carbon nanotubes; NCNT = N-doped CNT), which, under suitable conditions, were recoverable and reusable without any loss of efficiency. The influence of the temperature, O_2 pressure (P_{O_2}), reaction time and stirring rate are discussed and the best reaction conditions are determined for an almost complete conversion of the starting material and a good OA yield of 48%. SA and formic acid were the only co-products. The former could be further converted into OA by oxidation in the presence of formic acid, resulting in an overall OA yield of >62%. This process was clean and did not produce organic waste nor gas emissions.

Introduction

The petrochemical industry has contributed to the worldwide economic development for the past 150 years, but now, there are serious environmental problems that are associated with it. The need to establish environmentally friendly chemical processes is imperative and requires the development of novel and cost-effective methods for the prevention of pollution.[1] In recent decades, the substitution of nonrenewable fossil resources such as crude oil, coal, and natural gas with renewable carbon sources such as biomass, including lignocellulose and vegetal oils, as a sustainable feedstock has been extensively investigated for the manufacture of biofuels, commodity chemicals,[2a] high-added-value products and new biobased materials such as bioplastics.[3] Recently, even CO_2 has been taken into serious consideration as a building block for chemicals or as a source of carbon for fuels.[2b] Among renewable feedstock, lignocellulosic biomass has attracted considerable attention owing to its potential as a source of a wide range of platform chemicals such as C6-polyols,[4] 5-hydroxymethylfurfural (5-HMF),[5] levulinic acid (LA)[6] or formic acid (FA).[7] Among such chemicals, 5-HMF, synthesized by dehydration of fructose or directly from glucose,[8] is considered as one of the most important intermediates. Its furan structure bearing an aldehyde and a hydroxyl moiety can be transformed into numerous high-value chemicals capable of replacing their analogs synthesized from fossil fuels (Scheme 1).

The oxidative cleavage of glucose (or fructose), has been considered as a candidate for the biomass-based production of monocarboxylic and dicarboxylic acids, a technology that has not yet reached a "sustainable" level today. Recently, efforts have been made to convert C6 into lactic acid,[9] succinic acid or oxalic acid.

Oxalic acid (OA) and its derivatives have widespread applications in industrial sectors such as textiles, tanning, oil refining, catalyst preparation, pharmaceuticals, dyes, explosives, straw bleaching, printing, marble polishing, and metal and cloth cleaning.[10] It is also a very important chemical in petroleum refinery, rare-earth and ink manufacturing, rust and corrosion prevention, and dental adhesive processing.[11]

Currently, the methods for producing OA are classified into six groups according to the starting raw material: (i) fusion of sawdust with caustic soda, (ii) oxidation of olefins and glycols, (iii) radiation processing of carbonate solutions and molasses, (iv) fermentation of carbohydrates, (v) oxidation of carbohydrates with nitric and sulfuric acid, and (vi) decomposition of formates. The last three are the most used technologies. Fermentation routes to OA have been studied with renewed interest in the last decade, yielding mainly citric acid or OA from su-

[a] Dr. M. Ventura, Prof. A. Dibenedetto
CIRCC, Via Celso Ulpiani, 27, 70126 Bari (Italy)
E-mail: angela.dibenedetto@uniba.it

[b] Dr. F. Nocito, Prof. A. Dibenedetto
Department of Chemistry, University of Bari
Campus Universitario, 70126 Bari (Italy)

[c] Dr. D. Williamson, Prof. D. Mattia
Centre for Advanced Separations Engineering and
Department of Chemical Engineering
University of Bath, Claverton Down, Bath BA27AY (UK)
E-mail: D.Mattia@bath.ac.uk

[d] F. Lobefaro, Prof. M. Aresta
IC²R, Viale Einaudi 25, 70125 Bari (Italy)

[e] M. D. Jones
Department of Chemistry
University of Bath, Bath BA27AY (UK)

The ORCID identification number(s) for the author(s) of this article can be found under https://doi.org/10.1002/cssc.201702347.

Energy Technology DOI: 10.1002/ente.201800923 FULL PAPER

Highly Selective, Iron-Driven CO_2 Methanation

David L. Williamson,[a] Matthew D. Jones,*[b] and Davide Mattia*[a]

CO_2 methanation has gained traction for its potential in renewable energy storage, though the high cost of renewable hydrogen production and costly metals used in methanation catalyst synthesis remain a significant barrier to implementation. Herein we present a Ru–Fe@NCNT catalyst, consisting of ruthenium and iron nanoparticles on nitrogen-doped carbon nanotubes, as a highly selective, hydrogen efficient, iron-driven alternative to typical nickel and ruthenium catalysts used for CO and CO_2 methanation. Ru–Fe@NCNT offer competitive CO_2 conversion and methane selectivity, and a reduction of up to 80% in ruthenium loading versus similar literature and commercial catalysts. It is proposed that this desirable CO_2 methanation performance, using an atypical optimal feed gas composition where $P_{H2}/P_{CO2}=3$, is the result of effective cooperation between the iron-catalysed reverse water gas shift and methane-selective Fischer-Tropsch, and ruthenium-catalysed CO methanation reactions.

Introduction

CO and CO_2 methanation have long been used in industry, typically to produce synthetic natural gas or to avoid catalyst poisoning in ammonia production.[1] In recent years these processes have garnered additional interest as a means of storing excess wind and solar energy as methane in existing natural gas grids due to their large potential storage capacity, by coupling waste CO_2 with renewable hydrogen as reagents. While this application is potentially valuable, the high cost of renewable hydrogen production and scarcity of high purity CO_2 streams have prohibited large scale implementation of such technologies.[2] However, advances in the efficiency of water electrolysis processes are anticipated to reach a point of commercial viability in the coming years, supporting the need for concurrent research on active, selective and cost-effective CO_2 methanation catalysts to make the overall process of CO_2 methanation for energy storage as effective as possible.[2b,d]

Ruthenium, nickel and iron have been identified as the most active species for CO methanation, with nickel being the preferred choice in industry owing to its favourable balance between activity, selectivity and cost. Ruthenium and iron are recognized as having higher activity than nickel but are less suitable for industry due to the high cost of ruthenium and the tendency towards side reactions observed in iron-based catalysts despite it being the least expensive of these metals.[3] Comparing the performance of these metals in CO_2 methanation is a more complex undertaking. While the species that are the most active in CO methanation are also the most active in CO_2 methanation, their activities suffer notably when using CO_2 as the feedstock rather than CO due to its enhanced thermodynamic stability. Furthermore, it has been noted that the activity and selectivity of iron-based catalysts suffer in particular when applied in direct CO_2 methanation.[3c,4] This has been previously attributed to "over-binding" of CO_2 on Fe causing a thermodynamic sink on the reaction coordinate.[5] However, it must be noted that the mechanism of CO_2 methanation remains poorly understood, with current discussion in literature centring around the possible associative versus dissociative pathways to direct CO_2 methanation.[6] While iron appears to suffer in activity towards direct CO_2 methanation relative to other active CO methanation catalysts, it remains a highly active water-gas shift catalyst, allowing for the reduction of CO_2 to CO, and a preferred Fischer-Tropsch (FT) catalyst, allowing for the production of varied hydrocarbons and alcohols from CO. Thus, an alternate pathway to methane production from CO_2 over iron-based catalysts exists, which relies on effective coupling its high activity in these two reactions rather than proceeding through a direct CO_2 methanation pathway.

Common industrial methanation catalysts operate via the Sabatier reaction (Equation 1), which is assumed to proceed through one of the proposed direct CO_2 methanation mechanisms, and are thus operated using a feed gas where at $P_{H2}/P_{CO2}=4$.[7]

$$CO_2 + 4H_2 \rightleftharpoons CH_4 + 2H_2O \quad (1)$$

Parallel to CO_2 methanation, significant research has also been invested in coupling Reverse Water-Gas Shift (RWGS) and FT chemistry to produce longer chain hydrocarbons beyond CH_4. In combined RWGS/FT chemistry, CO_2 is initially reduced to CO via RWGS (Equation 2), and the resulting CO is then consumed in FT to produce a distribution of hydrocarbon species (Equation 3):[8]

[a] D. L. Williamson, Dr. D. Mattia
Department of Chemical Engineering
University of Bath
Claverton Down, Bath BA2 7AY (UK)
E-mail: d.mattia@bath.ac.uk
[b] Dr. M. D. Jones
Department of Chemistry
University of Bath
Claverton Down, Bath BA2 7AY (UK)
E-mail: m.jones2@bath.ac.uk

Supporting information for this article is available on the WWW under https://doi.org/10.1002/ente.201800923

ACS Sustainable Chemistry & Engineering

Research Article

Cite This: ACS Sustainable Chem. Eng. 2019, 7, 7395−7402

pubs.acs.org/journal/ascecg

N-Doped Fe@CNT for Combined RWGS/FT CO_2 Hydrogenation

David L. Williamson,[†] Carmelo Herdes,[†] Laura Torrente-Murciano,[‡] Matthew D. Jones,*[,§] and Davide Mattia*[,†]

[†]Department of Chemical Engineering, University of Bath, Claverton Down, Bath BA2 7AY, United Kingdom

[‡]Department of Chemical Engineering and Biotechnology University of Cambridge, West Cambridge Site, Philippa Fawcett Drive, Cambridge CB3 0AS, United Kingdom

[§]Department of Chemistry, University of Bath, Claverton Down, Bath BA2 7AY, United Kingdom

Supporting Information

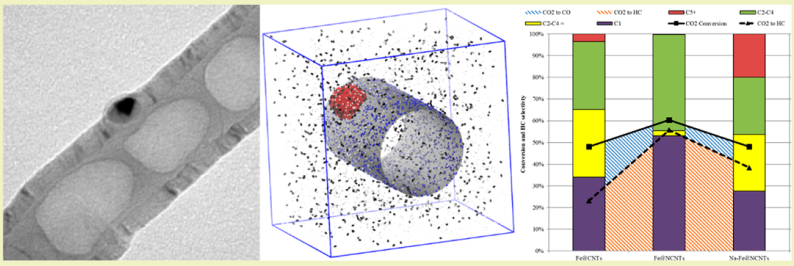

ABSTRACT: The conversion of CO_2 into chemical fuels represents an attractive route for greenhouse gas emission reductions and renewable energy storage. Iron nanoparticles supported on graphitic carbon materials (e.g., carbon nanotubes (CNTs)) have proven themselves to be effective catalysts for this process. This is due to their stability and ability to support simultaneous reverse water-gas shift (RWGS) and Fischer−Tropsch (FT) catalysis. Typically, these catalytic iron particles are postdoped onto an existing carbon support via wet impregnation. Nitrogen doping of the catalyst support enhances particle−support interactions by providing electron-rich anchoring sites for nanoparticles during wet impregnation. This is typically credited for improving CO_2 conversion and product selectivity in subsequent catalysis. However, the mechanism for RWGS/FT catalysis remains underexplored. Current research places significant emphasis on the importance of enhanced particle−support interactions due to N doping, which may mask further mechanistic effects arising from the presence or absence of nitrogen during CO_2 hydrogenation. Here we report a clear relationship between the presence of nitrogen in the CNT support of an RWGS/FT iron catalyst and significant shifts in the activity and product distribution of the reaction. Particle−support interactions are maximized (and discrepancies between N-doped and pristine support materials are minimized) by incorporating iron and nitrogen directly into the support during synthesis. Reactivity is thus rationalized in terms of the influence of C−N dipoles in the support upon the adsorption properties of CO_2 and CO on the surface rather than improved particle−support interactions. These results show that the direct hydrogenation of CO_2 to hydrocarbons is a potentially viable route to reduce carbon emissions from human activities.

KEYWORDS: *CO_2, Catalysis, Nitrogen, Doping, Iron, Carbon nanotube, Hydrocarbon, Water gas shift, Fischer−Tropsch, Storage, Adsorption, Simulation*

INTRODUCTION

The water-gas shift (WGS) (reaction 1) and Fischer−Tropsch (FT) (reaction 2) processes have long been used in industry for hydrogen and hydrocarbon formation.[1−8]

$$CO + H_2O \rightleftarrows CO_2 + H_2 \quad (1)$$

$$(2n + 1)H_2 + nCO \rightarrow C_nH_{2n+2} + nH_2O \quad (2)$$

However, to mitigate CO_2 emissions and cope with the intermittent supply patterns of renewable energy sources, research has been increasingly focused on converting CO_2 into hydrocarbon fuels. This could allow for energy storage directly from CO_2 and excess renewable energy.[9−14] Coupling the reverse water-gas shift (RWGS) and FT reactions together into a single process is considered to be especially desirable.[15] Simultaneous consumption of CO produced by RWGS via subsequent FT catalysis shifts the equilibrium of the RWGS

Received: February 1, 2019
Revised: March 7, 2019
Published: March 11, 2019

DOI: 10.1021/acssuschemeng.9b00672
ACS Sustainable Chem. Eng. 2019, 7, 7395−7402

Abstract

Increasing greenhouse gas emissions since the onset of industrialisation now pose a significant threat to modern society and the habitability our planet for future generations. It has been determined that we must achieve zero net emissions by 2050 with a 45% decrease in emissions by 2030 (relative to 2010 levels) in order to limit warming to 1.5 °C by the end of the century. A wide variety of solutions are being explored to limit the impact of modern emissions and transition to a more sustainable energy infrastructure. One such example is the capture, storage and conversion of CO_2 into valuable products and fuels for emissions mitigation and energy storage.

Iron nanoparticles supported on carbon nanotubes known as Fe@CNT have proven themselves to be active for the catalytic hydrogenation of CO_2 into hydrocarbons. This is due to their ability to catalyse both the reverse water-gas shift and Fischer-Tropsch processes, resulting in a coupled process that generates chemical fuels directly from a feed gas of hydrogen and CO_2. Furthermore, the integration of the iron particles into the carbon nanotube support structure during synthesis results in a nanotube-particle bridged structure that enhances catalyst activity due to improved hydrogen spillover. However, the distribution of the resulting products is notoriously difficult to control, often requiring the addition of promoter metals to enhance catalyst activity and selectivity towards desirable products.

These promoters are typically doped onto the surface of the catalyst using a wet impregnation technique, and are said to enhance reactivity by increasing the catalyst's Lewis basicity. Herein, however, an alternative method of increasing the basicity of the catalyst is explored by doping nitrogen heteroatoms directly carbon nanotube support structure during synthesis resulting in a novel catalyst referred to as Fe@NCNT. This thesis explores the synthesis, characterisation and reactivity of Fe@NCNT to determine the potential for nitrogen doping to enhance the activity of carbon-supported iron nanoparticles in CO_2 hydrogenation. The influence of reaction conditions and the addition of synergistic promoter metals are also explored.

Nitrogen doping in Fe@NCNT serves to enhance the basicity of the catalyst, resulting in notably increased CO_2 conversion and decreased CO selectivity relative to nitrogen-free Fe@CNT. However, methane production also increases as a consequence of nitrogen doping, and a trade-off is observed between CO_2 conversion and high α values in the FT product distribution. This unexpected observation is largely attributed to the influence of

local C—N dipoles in the catalyst surface upon the adsorption properties of the dipole-containing CO_2 and CO reactant molecules and the significantly less polar hydrocarbon products. This behaviour is subsequently exploited further to develop a primarily iron-based, FT-driven methanation catalyst using a significantly lower ruthenium loading than similar catalysts in literature.

Chapter 1 – Introduction

1.1. Climate change and the risks of excessive carbon emissions

Carbon dioxide (CO_2) is a colourless gas generated as a by-product of a wide variety of chemical processes both in nature and in industry. These processes include – but are not limited to – the respiratory functions of all aerobic organisms, the decay and fermentation processes of organic materials and sugars, and the hydrocarbon combustion processes that have driven modern society since the onset of the industrial revolution. Critically, it must be noted that the asymmetric stretch and bend vibrational modes of CO_2 are infrared (IR) active. This means that it is capable of absorbing and re-emitting energy in the IR spectrum. This is significant in the context of our modern energy infrastructure, as increasing concentrations of atmospheric CO_2 on a large scale therefore has the potential to affect the energy balance of sunlight absorbed by the earth as ultraviolet (UV) radiation versus the amount that is subsequently reflected back into space as blackbody radiation in the IR spectrum. As the global concentration of atmospheric CO_2 increases, the amount of blackbody radiation that would normally be reflected by the earth back into space decreases. This IR radiation instead becomes increasingly trapped in the earth's atmosphere, reflecting between the planet itself and its atmospheric CO_2 molecules, mimicking the effect of a greenhouse and leading to an overall increase in global temperatures. The energy balance of solar energy that is absorbed by the earth's atmosphere rather than reflected back into space is referred to as radiative forcing, as seen in Figure 1.1. This concept exists at the heart of modern climate science.

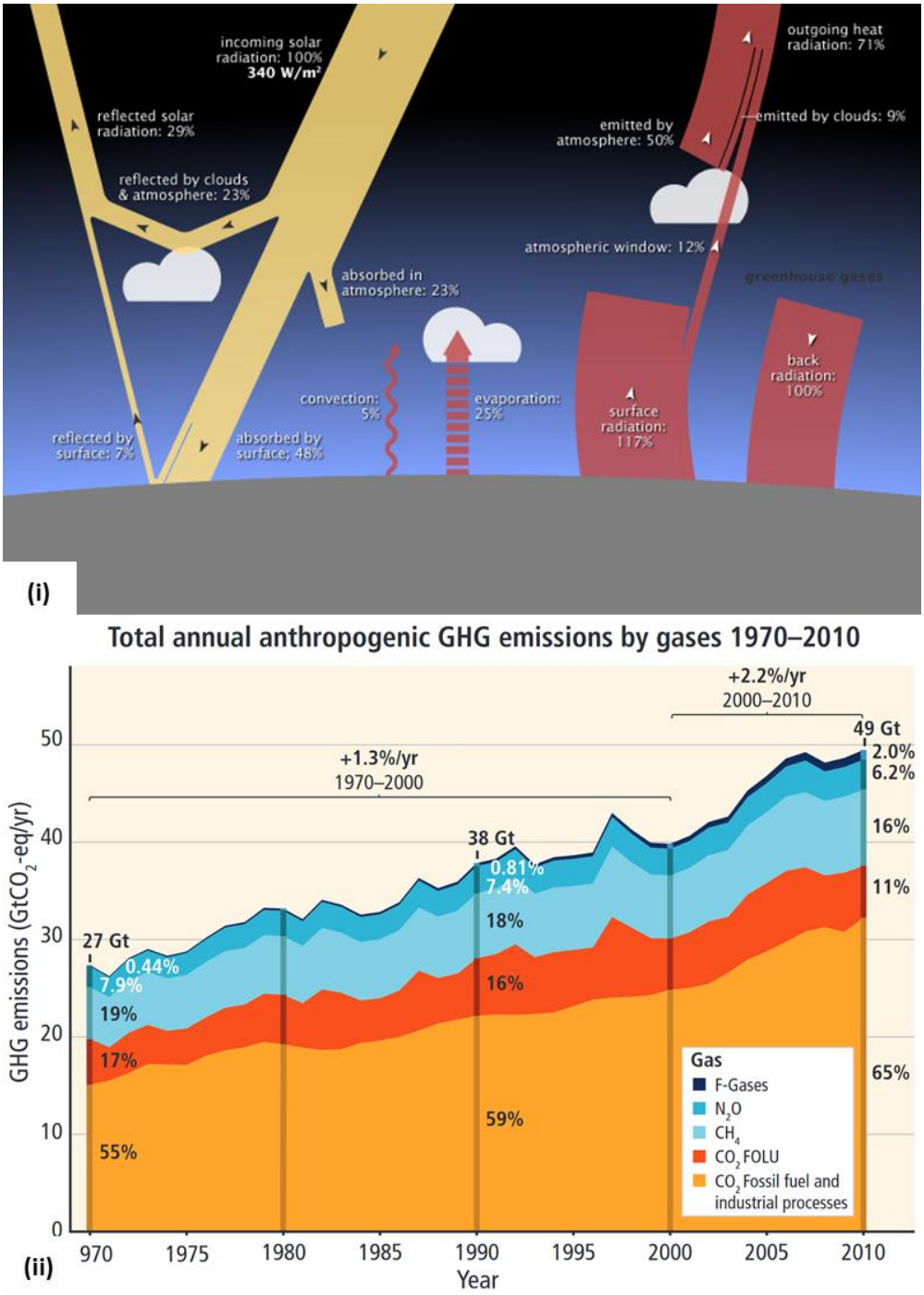

Figure 1.1. (i) The global energy balance, illustrating the effect of greenhouse gases (IR-active molecules such as CO_2) on global energy temperatures via adsorption and re-emission of blackbody radiation from the earth. Reproduced from reference 1. (ii) Global greenhouse gas (GHG) emissions by gas. Reproduced from reference 2.

The greenhouse effect was first theorized by Joseph Fourier in 1824,[3] and was first investigated experimentally by Eunice Newton Foote in 1856 before being quantified in greater detail by John Tyndall in 1859 and Svante Arrhenius in 1896.[4-6] The most recent Special Report (SR15) published by the Intergovernmental Panel on Climate Change (IPCC) has concluded that human activity is responsible for a rise in global temperatures of

approximately 1.0 °C (likely range: 0.8-1.2 °C) since pre-industrial levels, with warming expected to reach 1.5 °C between 2030 and 2052 at the current rate of carbon emissions, as seen in Figure 1.2.[7]

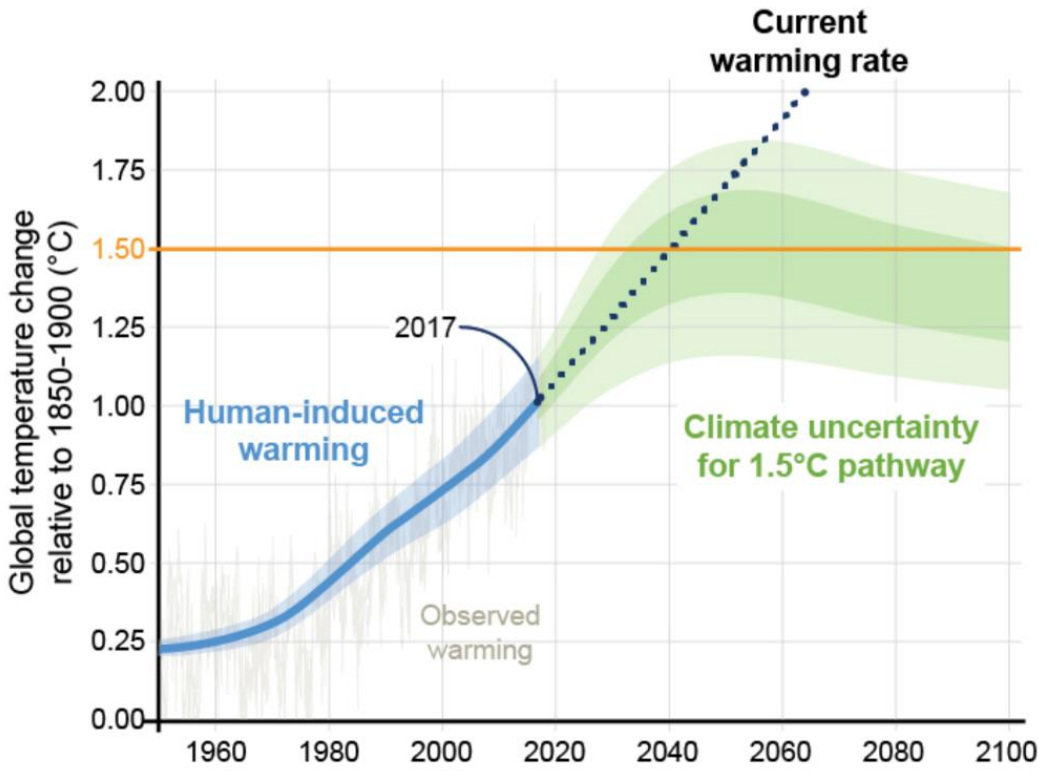

Figure 1.2. Observed and expected trends in human induced warming since 1950. Reproduced from reference 7.

The unprecedented impact of humanity upon global climate and temperatures has prompted climatologists to acknowledge that the earth has entered a new geological epoch known as the Anthropocene. This is said to have begun ca. 1945 and is characterized by exceptionally large quantities of atmospheric CO_2 and increases in the rate of CO_2 emissions when compared with historical data.[7, 8] Atmospheric CO_2 has been increasing by 20 ppm per decade since 2000, which is up to 10 times faster than any sustained rise in CO_2 in the past 800,000 years, as seen in Figure 1.3.[9] Since 1970 the global average temperature has been increasing at a rate of 1.7 °C per century, compared to a long-term decline over the past 7,000 years at a baseline rate of 0.01°C per century,[10] and the last geological epoch with similar atmospheric CO_2 concentration was the Pliocene, 3.3 to 3.0 Ma.[11] It is these remarkable increases in the rate of CO_2 emissions and overall concentration that establish the high level of confidence in the link between human activity and changes in the global climate, as modern trends have not been previously observed in the historical global warming and cooling processes driven by nature.

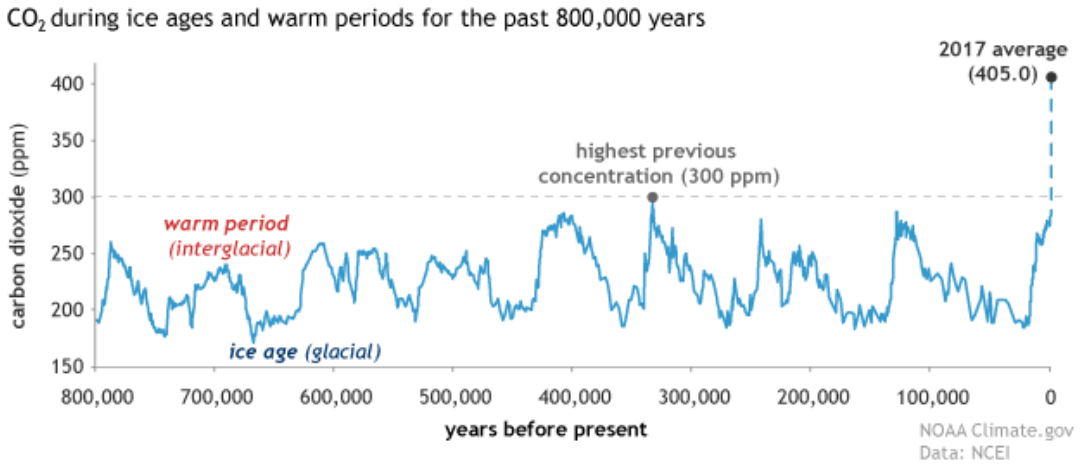

Figure 1.3. High-resolution CO_2 concentration record 650,000–800,000 years before present. Reproduced from references 9, 12.

The consequences of these increases have been outlined in great detail by the IPCC and supporting researchers, with climate models predicting significant differences in regional climate characteristics between present-day and global warming of 1.5 °C. Additional consequences are also predicted for increased warming between 1.5 and 2.0 °C, as seen in Figure 1.4. These differences include an increase in the mean temperature of most land and ocean regions (predicted with high confidence), hot extremes in most inhabited regions (high confidence), heavy precipitation in several regions (medium confidence), and the probability of drought and precipitation deficits in some regions (medium confidence).[7] It is very likely that the rate of global mean sea level rise during the 21st century will exceed the rate observed during 1971-2019 for all scenarios due to increases in ocean warming and losses of glacial ice. Global mean sea level rise is projected to be ca. 0.1 m lower with global warming of 1.5 °C compared to 2.0 °C (medium confidence), with a best-case scenario predicting sea level rise to remain below 1 m above pre-industrial levels by the year 2100 if emissions peak, decline and remain below 500 ppm (scenario RCP 2.6). A worst-case scenario predicts sea level rise greater than 3 m above pre-industrial levels if emissions are allowed to increase to 1500 ppm (scenario RCP8.5).[11, 13] Ocean acidification is expected to increase, and ecosystems and biodiversity are expected to suffer as species are unable to adapt to these changes quickly enough to endure them. Further human costs are also expected, as draught and increasingly inhospitable climates around the world contribute to food and water scarcity, thereby magnifying these vectors for geopolitical unrest.

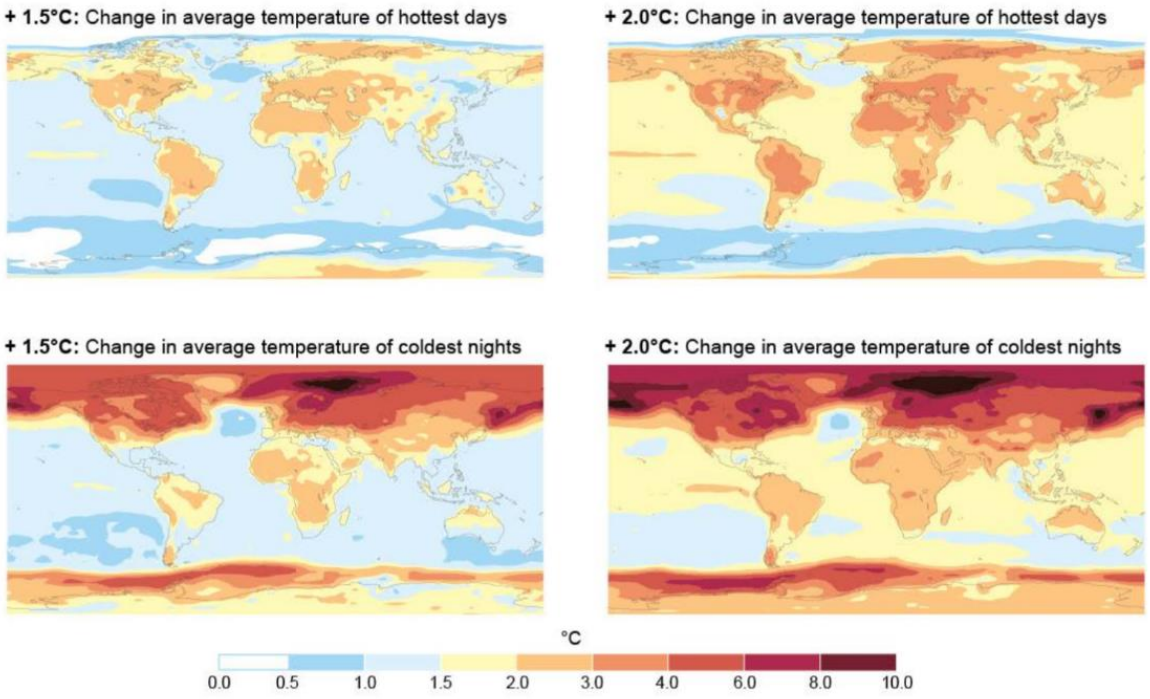

Figure 1.4. Regional temperature change around the world under scenarios of 1.5 °C and 2.0 °C warming. Reproduced from reference 7.

It is therefore clear that anthropogenic climate change poses a significant risk to modern society and represents a challenge of unprecedented scope and scale. This challenge can only be overcome through international cooperation, rigorous scientific study, and significant financial investment in reworking the modern global energy infrastructure to favour clean energy technologies and disincentivize the emission of further greenhouse pollutants. While a large-scale, multifaceted approach is required to address this challenge, this work discusses fundamental research into one of the many proposed solutions to reducing the impact of greenhouse gas emissions. Specifically, efforts to convert CO_2 from polluting waste streams into useful chemical fuels for energy storage – a process commonly referred to as CO_2 utilization, CO_2 conversion, or CO_2 valorisation. The fundamentals of CO_2 capture, storage, and conversion by similar catalytic materials have been outlined below and serve as a starting point for further discussion of the novel catalytic processes reported in this thesis.

1.2. CO_2 capture and potential applications

Capturing CO_2 from waste gas streams and either storing or utilizing it rather than emitting it into the atmosphere has been proposed as a potential route to decarbonizing our energy infrastructure and reducing the impact of significant industrial emitters.[14] The premise of these solutions is attractive, as they can be retrofitted into existing energy and industrial infrastructure with relative ease, offering an immediate means of reducing CO_2 emissions with some potential for additional value generation. This is achieved by fitting the outlet of a large-scale emissions source, such as a coal power plant or cement factory, with a CO_2 processing unit that can strip a waste gas stream of its CO_2 and prepare it for subsequent storage or utilization, which may also occur on-site. A breakdown of the different sectors and categories of global CO_2 emissions is outlined in Figure 1.5.

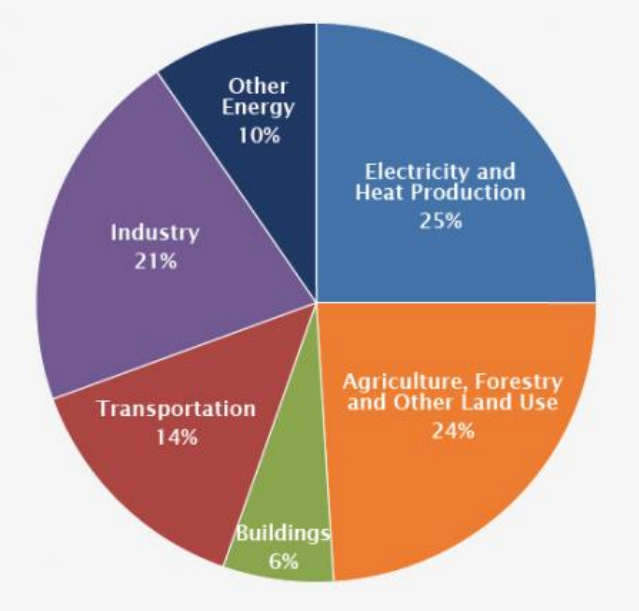

Figure 1.5. Global GHG emissions by sector. Reproduced from reference 2.

In order for CO_2 to be stored or utilized in such a manner it must first be separated from industrial waste streams through dedicated CO_2 capture technology. This initial separation step is critical in establishing the viability of any subsequent storage or utilization step, as high purity CO_2 is required for chemical utilization where CO_2 might be used to generate further value, and a high cost for the initial separation significantly hampers the attractiveness of any further storage or utilization process. CO_2 capture, storage and utilization schemes are generally targeted at large-scale emission sources rather than small sources such as homes and private vehicles, as large-scale emitters provide high concentrations of CO_2 that can be used to improve the efficiency of the separation process,

while CO_2 from smaller sources is more diffuse and therefore harder to capture and lacks the benefits of economies scale. Notable examples of carbon capture, storage, and utilisation have been presented with respect to their technology readiness level (TRL) in Figure 1.6

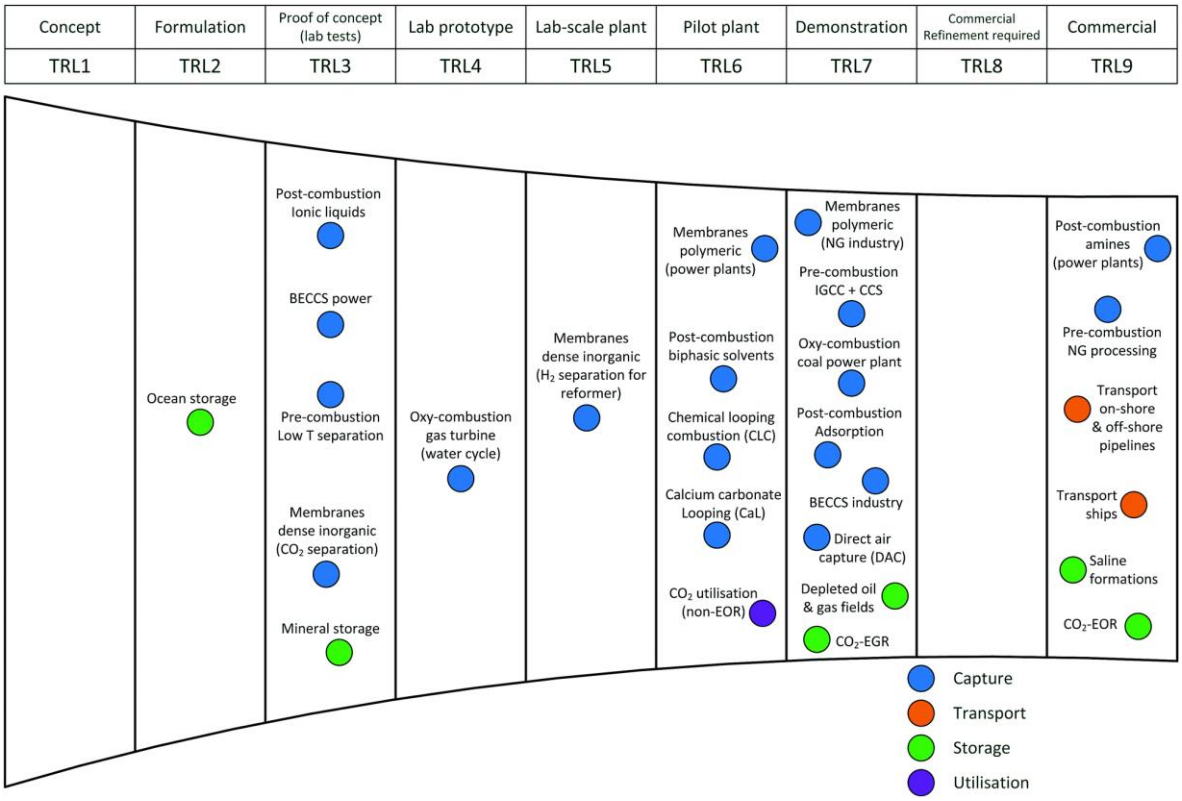

Figure 1.6. Current development progress of carbon capture, storage and utilisation technologies in terms of technology readiness level. BECCS = bioenergy with CCS, IGCC = integrated gasification combined cycle, EGR = enhanced gas recovery, EOR = enhanced oil recovery, NG = natural gas. Note: CO_2 utilisation (non-EOR) reflects a wide range of technologies, most of which have been demonstrated conceptually at the lab scale. The list of technologies is not intended to be exhaustive. Reproduced from reference 14.

A variety of carbon capture technologies have been investigated to-date, including amine absorption, pressure swing adsorption, chemical looping combustion, membrane separation, hydrate-based separation, and cryogenic distillation as premier examples.[15] The most mature and commonly employed technology in industry remains amine absorption scrubbing, which relies on a liquid sorbent (typically amines such as monoethanolamine or diethanolamine) to separate CO_2 from the flue gas stream and can then be regenerated through heating or depressurization.[15, 16] This technology is reported to provide greater than 90% CO_2 removal, though remains a relatively poor solution due to its high cost, energy requirement, susceptibility to amine degradation, and dependence upon high concentrations of CO_2 to drive the process. The sorbent solution typically consists of ca. 30% amine and 70% water, contributing significantly to the weight, cost, and energy required to recover the amine; thus also increasing the environmental footprint of the separation process.[15] Several notable

examples of commercial membrane separation technologies have been noted in recent years, though the overall removal efficiency of membranes remains low relative to amine technologies.[17] Due to these limitation, improving the energy and cost efficiency of CO_2 separation technologies remains a significant area of research and investment in academia and industry.

Several potential applications exist for captured CO_2. It may be used directly for dry cleaning and sterilization, greenhouse enrichment, food refrigeration, beverage carbonation, concrete curing, dry ice production, or as a supercritical solvent or working fluid. However, these applications provide little value for the captured CO_2 relative to the cost of separation. Additionally, while these applications do "recycle" waste CO_2, in most cases they do not prevent its eventual re-release into the atmosphere after it has been used. Thus, applications that store or convert CO_2 into value-added commodity chemicals and fuels are preferable.

1.3. **Carbon capture and storage (CCS)**

CCS refers to the process of capturing waste CO_2 and sealing it away in self-contained reservoirs rather than releasing it into the atmosphere. The most prominent routes to CCS currently include storage in deep saline sedimentary formations and CO_2 enhanced oil recovery (EOR), as seen in Figure 1.6. The estimated storage capacities and times for notable CCS technologies have been highlighted in Figure 1.7.

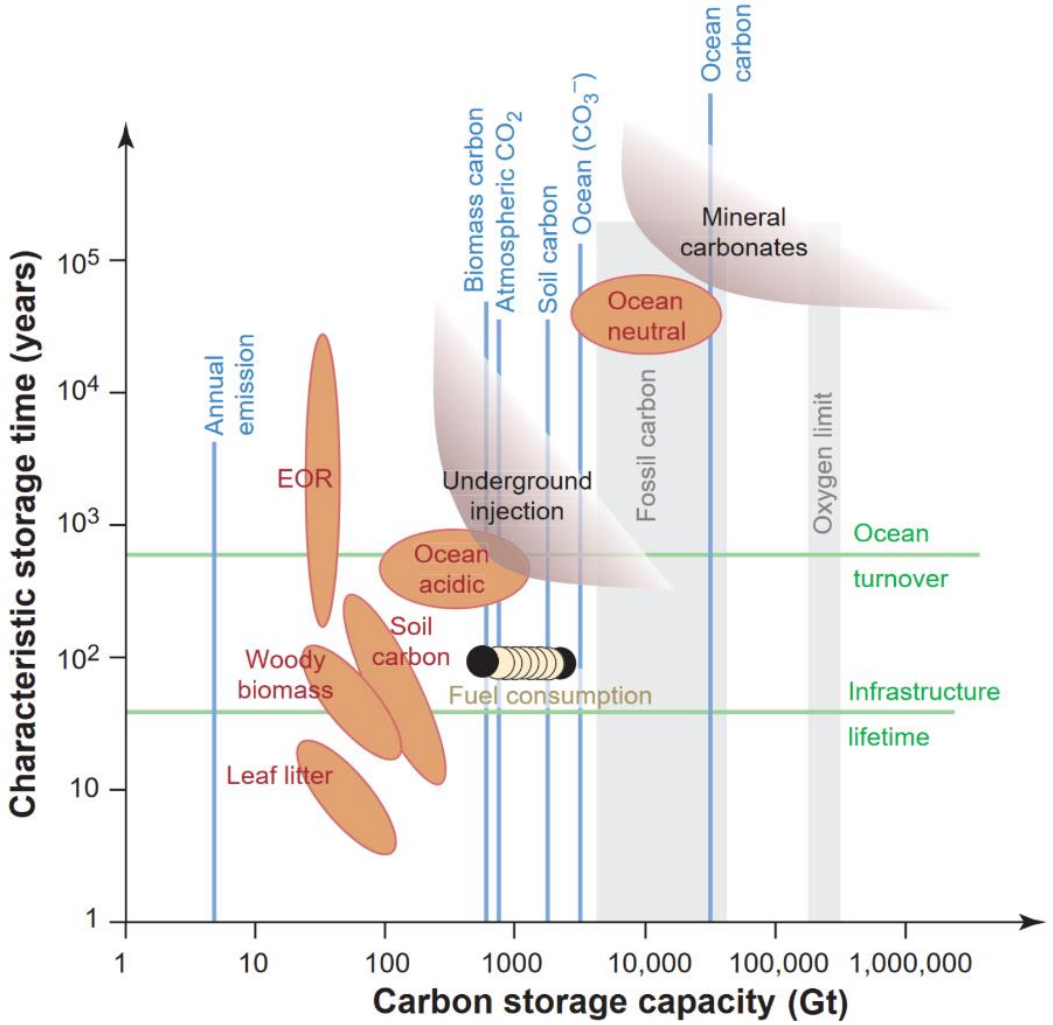

Figure 1.7. Estimated storage capacities and times for various sequestration methods. Reproduced from reference 18.

Deep saline formations are deeply buried sedimentary reservoirs filled with saline water, typically located deeper than 800 m below the surface; the depth at which CO_2 in its hydrostatic equilibrium reaches its critical pressure. Water in these reservoirs is typically unsuitable for human consumption and agricultural applications, and is said to be hydraulically separated from shallower aquifers that are used for these purposes.[19, 20] Deep saline formations represent a significant storage capacity for CO_2, and this technique has

seen notable commercial implementation since Statoil first employed it beneath the North Sea in 1996 to avoid paying a $50 per ton carbon tax while stripping natural gas of its CO_2 to meet specifications for sale in Europe.[19] EOR involves injecting CO_2 into depleted oil wells to harvest more oil from these reserves while reducing their carbon footprint. EOR has been used commercially for several decades and is considered to be a mature technology, though efforts continue to be made to improve its commercial attractiveness by both increasing oil yields and capacity for for-profit CO_2 storage.[14, 21] Other technologies that have been proposed for CO_2 storage include enhanced gas recovery (EGR), CO_2 mineralization and ocean storage, though these technologies remain relatively undeveloped at this time.[14]

The value of CCS is derived from the fact that it is the only technology that can simultaneously address carbon reduction objectives across all main carbon emitting sectors of the economy (including power generation, industry, transport and heating), without compromising their cost-effective provision of service.[14] While other technologies are currently being developed to derive additional value from CO_2, CCS remains the only technology that is currently mature enough to significantly mitigate CO_2 emissions from suitable sources such as CCS-enabled power stations, making room in carbon budgets for the continued operation of sectors that remain more difficult to decarbonize, such as transport.[14] However, it must be noted that CCS solutions that only provide carbon storage capacity, such as deep saline storage, do not generate value from the stored CO_2, relying on non-market-derived sources of income such as tax incentives and government-funded rewards for carbon recycling. Furthermore, the CCS solutions that do generate value from CO_2, such as EOR, derive this value by using CO_2 waste to harvest more CO_2-producing fuels from the earth, calling the ultimate sustainability of these processes into question. CCS remains an important technology in current efforts to mitigate carbon emissions, while research to convert CO_2 into valuable products remains valuable in the pursuit of more effective mitigation. However, the ultimate solution to the challenge of achieving a sustainable, low-carbon society remains the replacement of fossil fuel energy technologies with non-carbon-emitting alternatives.

1.4. **Carbon capture and utilisation (CCU)**

CCU offers more cost-efficient options for CO_2 mitigation relative to CSS by using CO_2 for further value generation, such as in the production of value-added fuels and commodity chemicals. CO_2 is already utilized in industry today, primarily in the synthesis of urea (150 MTY),[22] methanol (4.4 MTY),[23, 24] salicylic acid (0.17 MTY),[24] organic carbonates (0.1 MTY),[25] bisphenol-A polycarbonate (0.6 MTY),[26] and polypropylene carbonate (0.07 MTY).[27] The total amount of CO_2 utilized in these processes is estimated to be ca. 116 MTY, 94% of which goes towards the production of urea, which produces more CO_2 than it consumes.[26] Numerous other products can be chemically produced from CO_2, as seen in Figure 1.8.

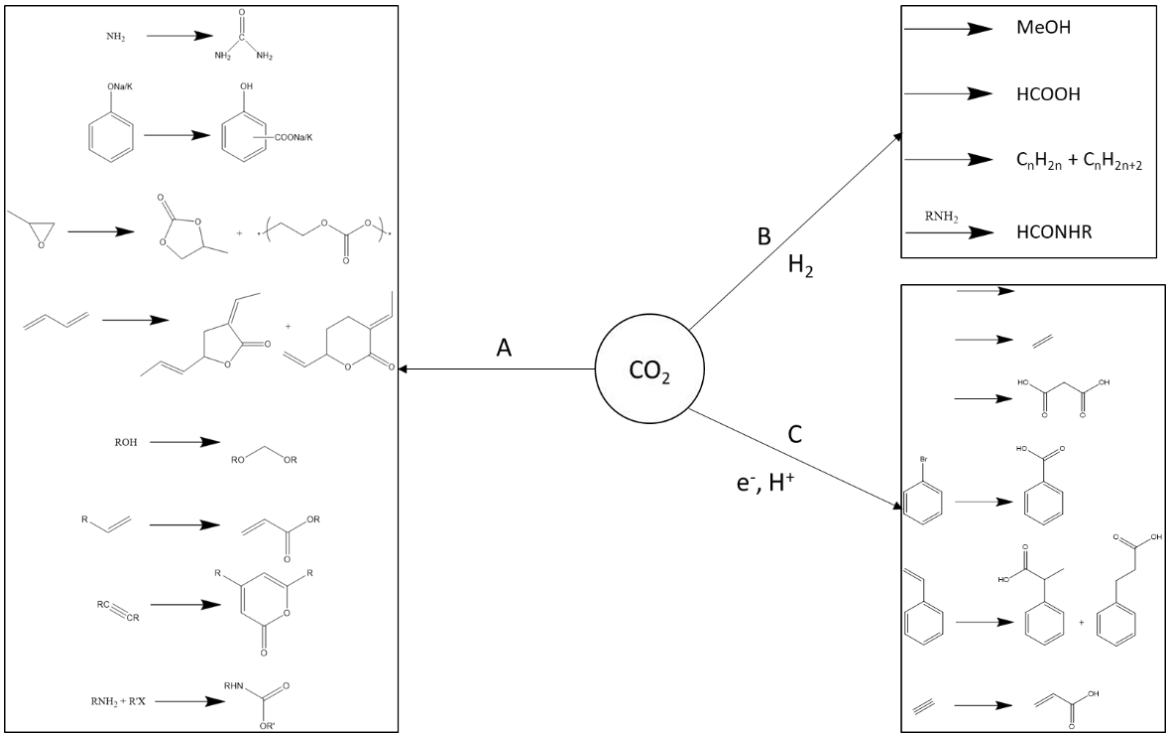

Figure 1.8. Possible products from chemical version of CO_2 via (A) reaction with other chemicals, (B) hydrogenation and (C) electrochemically. Adapted from reference 28.

However, these require further research before they can be considered suitable for industrial implementation.[14, 26] Furthermore, CO_2 can be reused in a number of non-chemical applications such as dry cleaning and sterilization, food refrigeration, beverage carbonation, concrete curing, dry ice production, or as a supercritical solvent or working fluid. Some forms of CCS can also technically be considered as forms of CCU, such as greenhouse enrichment and EOR, as they generate additional value from the captured CO_2. However, this thesis primarily concerns the catalytic conversion of CO_2 into other products, and

therefore such non-chemical forms of CCU will not be discussed further. A summary of noteworthy examples of chemical CCU techniques, their requirements and large-scale viability has been outlined in the sections below.

1.4.1. Major products of CO_2 hydrogenation

Over one hundred desirable bulk and fine chemicals with potential syntheses using CO_2 as a feedstock have been identified.[26] These processes involve the reaction of CO_2 with a wide variety of chemical species. However, as this thesis concerns the production of hydrocarbon fuels using a feedstock of just CO_2 and hydrogen, the possible products of CO_2 hydrogenation are of particular interest and have been highlighted here. In general, direct CO_2 hydrogenation is known to produce primarily C_1 species with very little likelihood of forming C–C bonds when reacting just CO_2 and hydrogen. However, subsequent hydrogenation reactions between the products of CO_2 hydrogenation do allow for the production of $C_{n>1}$ species as a result of CO_2 hydrogenation. As these subsequent reactions are the primary mechanism by which $C_{n>1}$ hydrocarbons can be produced from CO_2 hydrogenation, they have also been highlighted here.

$$CO_2 + 4H_2 \leftrightharpoons CH_4 + 2H_2O$$

Equation 1.1. The reversible hydrogenation of CO_2 into methane. ΔH_r^o = -251.1 kJ mol^{-1}; ΔS_r^o = -410.5 J K^{-1} mol^{-1}; ΔG_r^o = -128.8 kJ mol^{-1}.

Methane plays a significant role worldwide as a fuel for the production of energy and district heating. It is the primary component of natural gas (ca. 70-90% by volume) and is considered to be naturally abundant with a relatively low commercial value. While natural gas is the primary source of methane production with ca. 37 trillion cubic metres produced in 2017,[29] it is also produced during anaerobic digestion and is therefore the principle component of biogas (ca. 50-75% by volume).[30] Methane is itself a potent greenhouse gas with a global warming potential (GWP) of 28.[11, 31] However, it produces less CO_2 per unit of heat generated when combusted than any other hydrocarbon fuel, with a high heat per mass unit of 55.7 kJ g^{-1}. Aside from heat and electricity generation as a component in natural gas and biogas, methane is also used industrially as a chemical feedstock for CO and H_2 production through steam methane reforming (SMR), and can additionally be used to produce methyl halides.

The process of producing methane directly from CO_2 is known as the Sabatier process.[32] It is one of the earliest known catalytic processes and has therefore been significantly studied,

though it remains uncommon in industry in the context of CO_2 methanation due to the low value of methane and comparatively cost-effective production method of harvesting methane as natural gas. It is estimated that CO_2-based methane production increases costs by anywhere from 2.4-30 times the cost of conventional production.[14] However, CO methanation can also occur via Sabatier chemistry and this process has been commercialized by multiple ventures across Asia, Europe and North America.[33] The reaction is known to be catalysed by a variety of group 8-10 metals, with ruthenium, nickel, cobalt, iron and molybdenum being the most notable species in terms of their activity.[33] The process is typically operated at elevated temperatures and pressures of ca. 300-500 °C and 10-30 bar, with commercial ruthenium and nickel catalysts being noted to achieve high conversion and methane selectivity of 90% or more.[34-38] Iron remains relatively ignored as a selective methanation catalyst due to its tendency towards side reactions, despite its high activity and low cost. However, developments in iron-based methanation catalysts could allow for this process to become more cost-effective in the future by reducing the cost of catalyst manufacturing.

$$CO_2 + 3H_2 \leftrightharpoons CH_3OH + H_2O$$

Equation 1.2. The reversible hydrogenation of CO_2 into methanol. ΔH_r^o = -129.3 kJ mol^{-1}; ΔS_r^o = -408.7 J K^{-1} mol^{-1}; ΔG_r^o = -7.4 kJ mol^{-1}.

Methanol has been a key industrial chemical worldwide since its initial commercial catalytic production by BASF in 1923, with production totalling ca. 62 MTY in 2014.[39] It is an intermediate in the production of numerous other chemicals such as formaldehyde and methyl-tert-butyl ether (MTBE), and is also used as a solvent, fuel, antifreeze, and denaturant for ethanol. The modern standard for industrial methanol production involves the catalytic reaction of syngas over a $Cu/ZnO/Al_2O_3$ catalyst at conditions of ca. 40-100 bar and 200-300 °C, favouring low temperatures and high pressures.[39] Because the syngas used during methanol synthesis is itself derived from SMR, methanol production remains tied to the extraction of fossil fuels and natural gas. However, in recent years efforts have increase to implement CO_2-based methanol production using the same catalysts employed during the syngas synthesis. Typically these processes involve mixing CO_2 into existing syngas streams, though several small commercial and pilot-scale plants exist for the direct production of methanol from CO_2, such as the George Olah Renewable Methanol plant in Iceland, which produces 4,000 MTY.[14, 26] However, a significant financial challenge exists for pure CO_2-based processes compared to their syngas-based competitors, as the

equilibrium yield methanol is significantly lower for CO_2 than CO (ca. 40% versus 80% at 200 °C).[40] At this time it is estimated that CO_2-based methanol production processes increase the selling price by a factor of 1.8.[14]

$$CO_2 + H_2 \leftrightharpoons HCOOH$$

Equation 1.3. The reversible hydrogenation of CO_2 into formic acid. ΔH_r^o = -31.1 kJ mol^{-1}; ΔS_r^o = -212.6 J K^{-1} mol^{-1}; ΔG_r^o = 32.3 kJ mol^{-1}.

Formic acid is an industrial chemical with an annual demand of ca. 700,000 MTY.[41] It sees significant use in the agricultural and textiles industries, as a chemical reagent, and as a component of mobile phase in reversed-phase high-performance liquid chromatography (RP-HPLC). In recent years, formic acid has been proposed as a potential vector for hydrogen storage, with research increasing into the potential for direct formic acid fuel cells (DFAFC).[42-44] However, these systems remain in the early stages of development and suffer from catalyst deactivation and a significant trade-off between performance and longevity.[45] Conventional production of formic acid relies on hydrolysis of methyl formate (which is itself derived from methanol and CO in the presence of a strong base). This requires a large excess of water; hence, the process is sometimes achieved indirectly by first treating the methyl formate with ammonia to produce formamide, which can then be hydrolysed with sulfuric acid (though this requires subsequent disposal of the ammonium sulfate by-product). These processes have been successfully commercialized but require numerous steps and produce a significant amount of waste.

In this context, CO_2-based formic acid production is an appealing alternative as it has the potential to reduce CO_2 emissions while being atom efficient and requiring fewer steps.[14] Several homogeneous catalysts have been investigated for this process and exhibit attractive activity, though they are largely hampered by difficult recycling of the expensive metal species employed (Rh, Ru, Ir), the requirement of a base (typically NEt_3) to shift the unfavourable equilibrium of the CO_2 hydrogenation, and non-trivial separation of formic acid from the resulting salts.[27, 46, 47] Iron-based catalysts have been explored but exhibit relatively low turnover numbers (TON).[48] A Schiff-base-mediated gold nanocatalyst for the reduction of CO_2 to formate has also been recently reported.[49] This is said to avoid thermodynamic sinks present in previously reported processes, though the consequences of this work remain to be seen. Several heterogeneous catalysts have also been explored, including a Raney nickel catalyst and a heterogeneous ruthenium hydroxide catalyst.[50, 51] As

the reaction is thermodynamically unfavourable at STP, successful processes are typically reported at high pressures of ca. 5-50 bar and temperatures of 20-120 °C.[27, 51, 52]

$$CO_2 + 2H_2 \leftrightharpoons HCOH + H_2O \quad (1.4)$$

Equation 1.4. The reversible hydrogenation of CO_2 into formaldehyde. ΔH_r^o = -7.2 kJ mol^{-1}; ΔS_r^o = -186.3 J K^{-1} mol^{-1}; ΔG_r^o = 48.3 kJ mol^{-1}.

Formaldehyde is an industrial chemical that is used in the manufacturing of thousands of consumer and industrial products, primarily polymers, with a global production capacity of ca. 13 MTY in 2016.[53, 54] Industrially, formaldehyde is produced via the catalytic oxidation of methanol. Because the syngas used during methanol synthesis is itself derived from SMR, formaldehyde production remains tied to the extraction of fossil fuels and natural gas.[55] While several studies have reported the formation of formaldehyde and formates as adsorbed intermediates during methanol synthesis, there is little evidence of these species desorbing as products.[38, 56]

The direct hydrogenation of CO_2 into formaldehyde is thermodynamically unfavourable, difficult to control, and must avoid the typical decomposition of formaldehyde into CO_2 and H_2 above 150 °C.[53, 55] It is also relatively underdeveloped compared to CO_2 reduction into products such as methanol and formic acid.[55] Despite the small number of publications focusing on CO_2-to-formaldehyde transformations, successful processes have been reported using stoichiometric, enzymatic, photo-, electro-, and thermocatalytic chemistry.[55] The most notable thermocatalytic process reported to-date used a methanol production catalyst (Pt/Cu) at 150 °C, 6 bar and a H_2/CO_2 ratio of 20:1.[56] A promising electrocatalytic process has also been reported more recently, using boron-doped diamond (BDD) electrodes with p-type surfaces and a platinum counter electrode to produce formaldehyde from seawater.[57] A patent has also been recently filed for the direct conversion of syngas into formaldehyde in aqueous media, which could result in the indirect consumption of CO_2 for formaldehyde production.[58] While CO_2-to-formaldehyde processes are relatively unexplored at this time, they remain attractive for their potential to circumvent the cost and complexity of modern multi-step formaldehyde synthesis.

$$CO_2 + H_2 \leftrightharpoons CO + H_2O$$

Equation 1.5. The reversible hydrogenation of CO_2 into CO. ΔH_r^o = -2.4 kJ mol^{-1}; ΔS_r^o = -76.9 J K^{-1} mol^{-1}; ΔG_r^o = 20.6 kJ mol^{-1}.

Carbon monoxide is a key intermediate in the production of a wide variety of chemicals from methanol to formaldehyde to synthetic natural gas (SNG). Modern CO production is typically achieved via SMR (largely as a consequence of hydrogen production, which is significantly required for ammonia synthesis)[59] or gasification of coal and biomass (typically intended for subsequent SNG production).[60] The reversible oxidation of CO and water into CO_2 and H_2 has long been used in industry to control the ratio of CO and H_2 in syngas intended for hydrogen production or subsequent chemical processing (such as methanol production or Fischer-Tropsch synthesis).[61-63] This reaction is known as the water gas shift (WGS) reaction, and it has been extensively studied as a result of its industrial applicability. The reverse water gas shift (RWGS) reaction thus allows for the production of CO from CO_2 and hydrogen. This is appealing, as CO is a versatile intermediate molecule with established applications compared to relatively novel CO_2-based processes. A wide variety of metals have been applied in WGS catalysis. The most common active species in industrial WGS catalysts have been reported as promoted iron oxides and promoted copper oxides depending on the temperature range of the reaction.[64, 65] While the RWGS reaction is less common and has been the subject of significantly less investigation, interest in RWGS reactivity has increased in recent years as attempts to valorise CO_2 have increased. When comparing the activity of different metals in RWGS catalysis, Pt-based catalysts have been reported to show high activity and selectivity but are unattractive due to their cost.[66] Iron- and nickel-based catalysts with high particle dispersion show promising activity and selectivity at a much lower cost.[66] The RWGS reaction is thermodynamically unfavourable on its own but becomes favourable when coupled with subsequent Fischer-Tropsch (FT) to consume the CO, thereby shifting the reaction towards products.[66-69]

$$nCO_2 + (2n+2)H_2 \rightarrow C_nH_{2n+2} + (n+1)H_2O$$

Equation 1.6. The "direct" hydrogenation of CO_2 into hydrocarbons. ΔH_r^o = various kJ mol^{-1}; ΔS_r^o = various J K^{-1} mol^{-1}; ΔG_r^o = various kJ mol^{-1}.

$C_{n>1}$ linear hydrocarbons play a vital role in the global energy infrastructure as well as chemical processing. Natural gas (C_{1-4}), gasoline (C_{4-12}) and kerosene (C_{11-13}) are all composed of these hydrocarbons, and short-chain olefins ($C_{2=4}$) play a critical role as reagents for further chemical processing, particularly in polymer manufacturing. $C_{n>1}$ hydrocarbons are not strictly products of direct CO_2 hydrogenation. However, initial conversion of CO_2 into CO via RWGS, followed by subsequent FT synthesis to produce hydrocarbons from CO allows for a combined process that allows for the production of

hydrocarbons from a feedstock containing only H_2 and CO_2.[68-78] Current research into these processes typically proceeds over supported iron- or cobalt-based catalysts, often promoted by potassium, manganese or other alkali metals at conditions of 250-400 °C, 1-30 bar and a H_2:CO_2 feed ratio of 3:1. The ratio of hydrogen and CO_2 in the feedstock is critical, as a ratio closer to 3:1 starves the reaction of hydrogen, encouraging the formation of longer hydrocarbons while a ratio closer to 4:1 tends to favour methane production.[67]

In pure FT synthesis, the potential for iron to catalyse WGS as a side reaction is conventionally viewed as a detriment that must be suppressed in order to achieve high selectivity towards hydrocarbons. In combined RWGS/FT processes, high RWGS activity is required in addition to high FT activity in order to facilitate the combination of these two reactions. Thus, while conventional FT catalysts designed to suppress WGS activity are less amenable to combined RWGS/FT chemistry, new iron-based catalysts are attractive due to iron's activity towards both reactions. Any process based on FT-chemistry will produce a distribution of hydrocarbons as products, and the selectivity of these products is difficult to control. Factors governing the activity and selectivity of these catalysts include particle size, catalyst reducibility and basicity, ability to support the active phase of both reactions, and strength of interactions between the catalyst and its support.[70, 72, 78-81] Despite these challenges, this process remains attractive as a potential route for renewable energy storage as either methane or liquid fuels. This has the potential to significantly increase the CO_2 emissions mitigation relative to the production of bulk and fine chemicals alone, depending on the source of CO_2 and hydrogen used during conversion.[14, 26]

1.4.2. Sources of CO_2

CO_2 is produced by a wide variety of emission sources representing a broad range of gas compositions and physical configurations of the emitter.[82] Large, stationary point-source emitters such as coal fired power plants or cement factories are far more amenable to on-site CO_2 capture and utilisation than small and mobile emitters such as consumer vehicles due to the cost and scale of technology required.[14] Furthermore, different sources emit gas streams with differing concentrations of CO_2, often accompanied by additional impurities and catalyst poisons such as H_2S that must be removed prior to any attempts at chemical utilisation.[83] Representative CO_2 concentrations present in noteworthy industrial emissions sources are outlined in Table 1.1.

Table 1.1. CO_2 concentration by source for prominent stationary CO_2 emitters. Reproduced from reference 82.

CO_2 source	CO_2 concentration
Atmospheric	400 ppm
Natural gas combined cycle power plant	3–4%
Refineries and steam cracker	3–13%
Coal power plant	12–15%
Integrated pulp and paper mills	7–20%
Market pulp mills	7–20%
Iron and steel manufacturing	17–35%
Cement manufacturing	14–33%
Integrated gasification combined cycle power plant	1/40%[b]
Ammonia production	≈100%
Ethylene oxide production	≈100%
Gas processing	≈100%
Hydrogen production	≈100%

Emitters that produce large volumes of high purity CO_2 are preferable, as these benefit from easier CO_2 separation and processing, as well as economies of scale. The potential for a centralised CO_2 distribution and processing network has been theorised, though this has been discussed primarily in the context of CCS rather than CCU. Furthermore, the required infrastructure remains underdeveloped in the USA and relatively non-existent in Europe.[14, 84]

1.4.3. Sources of hydrogen

There are numerous desirable products that can be obtained through CO_2 hydrogenation. However, none can be produced sustainably (without relying on fossil fuels) unless the hydrogen used in their synthesis is obtained from renewable sources. At this time the majority of global hydrogen production relies on SMR. Methane (typically from natural gas) is reacted with steam, typically at ca. 3-25 bar and 700-1000 °C in the presence of a nickel catalyst to produce carbon monoxide and hydrogen, as seen in Equation 1.7. The ratio of these products can then be tuned using the WGS reaction to produce further hydrogen from carbon monoxide and water, as seen in Equation 1.8.[85, 86]

$$CH_4 + H_2O \rightarrow CO + 3H_2$$

Equation 1.7. SMR produces hydrogen and CO by reacting methane (natural gas) with water.

$$CO + H_2O \leftrightharpoons CO_2 + H_2$$

Equation 1.8. The water gas shift reaction produces hydrogen and CO_2 by reacting CO with water.

Thus, if standard production methods are used to generate the hydrogen for CO_2 hydrogenation, net CO_2 emissions will be positive and the overall process will remain tied to fossil fuels. To produce truly carbon-neutral and carbon-negative products through CO_2 hydrogenation, and to break the process's dependence upon fossil fuels, entirely new routes to hydrogen production must be implemented.[86-89] At this time, the most notable route to renewable hydrogen production being discussed in literature is water splitting via either electrolysis or photochemical routes (using renewable electricity).[86, 90, 91] Gasification of biomass is also being explored.[92, 93] Further improvements in process efficiency and decreases in the cost of renewable energy are required before these processes can be implemented on a large scale, though it is anticipated that a cost-effective water electrolysis efficiency of 80% is achievable in the near future through electrolysis R&D and increased market penetration of renewable energy sources.

1.4.4. Feasibility of large-scale CCU

While the CO_2 mitigation potential of a process is often discussed in the context of the amount of CO_2 consumed, the amount of CO_2 emitted must also be taken into account. Viable chemical CCU processes should produce either (i) carbon-neutral products, or (ii) carbon-negative products. Carbon-neutral products may eventually re-emit their CO_2 at the end of their lifecycle, but do not require any new CO_2 to be emitted to drive their production (e.g. CO_2 to renewable fuels via Fischer-Tropsch catalysis). This leaves the overall atmospheric CO_2 concentration unchanged by their utilisation, mitigating the emissions that would have normally occurred via conventional alternatives. In carbon-negative products, CO_2 is permanently fixed by the process into a product that will not decompose over a meaningful timescale (e.g. CO_2 to carbonates for the production of building materials). This reduces the overall atmospheric CO_2 concentration via their utilisation. Unviable CCU technologies can easily produce more CO_2 than they consume unless renewable energy and renewable reagents such as hydrogen from electrolysis rather than fossil fuels are used.[14] The final fate of the utilized CO_2 must also be considered, as the amount of CO_2 used in a process is not necessarily the same as the amount removed or stored by that process. For example, while CO_2 is consumed in the production of urea, the CO_2 contained within urea will be re-emitted into the atmosphere after ca. 1 week upon being applied as fertilizer due to hydrolysis, and the carbon contained in urea only constitutes ca. 14% of its overall GHG footprint in conventional production.[94]

While the premise of CCU for the production of commodity chemicals seems initially appealing, several significant complications exist. These combine to make chemical CCU only a marginal component of the solution to achieving acceptable levels of atmospheric CO_2. Total CO_2 emissions were estimated to be ca. 32.3 Gt annually in 2014,[26] while energy-related emissions are estimated to have risen by 1.7% to a historic high of 33.1 Gt in 2018.[95] They are anticipated to increase to 43 Gt by 2030.[96] However, the global market for carbon-negative bulk and fine chemicals that can be manufactured from CO_2 is estimated to be no more than 1-3 Gt per year.[28, 96] Concurrently, the IEA has estimated that CO_2 emissions must total no more than 22.1 Gt per year by 2035 if we are to limit end-of-century warming to less than 2.0 °C.[97] Within Europe, the bulk and fine commodity chemicals processes that have been determined to be reasonably replaceable with CO_2-based processes are estimated to be capable of utilising ca. 0.43% and 0.029% of annual EU greenhouse gas emissions for the bulk and fine chemicals, respectively. This is if all market demand for these chemicals were saturated with CO_2-based products.[26] The CO_2 avoidance potentials of notable bulk chemicals within the EU are highlighted in Figure 1.9.

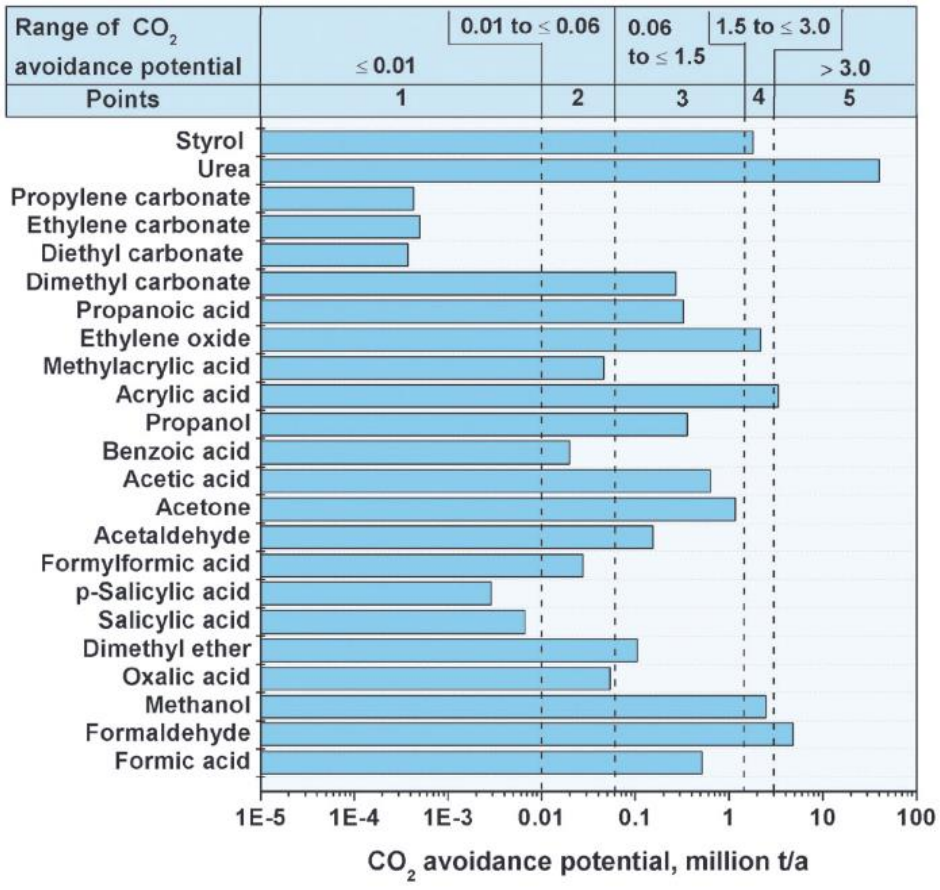

Figure 1.9. CO_2 avoidance potential for bulk chemicals within the EU for 2011. Reproduced from reference 26.

Facing this reality, it is likely that CCU for carbon-negative commodity chemicals production, while still worthwhile, can only play a supporting role in reducing global GHG emissions to acceptable levels.[26] However, CCU for the production of chemical fuels is estimated to significantly increase the potential of CCU in emissions mitigation to ca. 8.7 Gt per year.[96, 98] This is achieved by using excess renewable energy to drive renewable hydrogen production and convert CO_2 into chemical energy storage. CO_2-negative utilisation is also possible via this route by converting CO_2 into an excess quantity of fuels. However, the full scale and potential for this application remains less clear.[14, 98] It should be noted that the scale of carbon emitted from fossil fuels and industry is dwarfed by the flux of CO_2 back to land via photosynthesis in plants (440 Gt per year). However, only 2-3% of this carbon remains fixed (ca. 12 Gt per year), and only for several decades, as the remainder is re-emitted by plant and soil respiration.[98] Recent studies suggest that increasing the magnitude of CO_2 utilization via increasing uptake into soil and plant products may represent an important pathway for achieving net zero emissions.[98] However, as this thesis is primarily concerned with the development of materials for the conversion of CO_2 into chemical fuels, this concept will not be discussed further here.

1.4.5. CCU in renewable energy storage

Due to the threat of depletion and environmental consequences of carbonaceous fuels such as oil, coal, and natural gas, efforts are growing worldwide to shift the global energy infrastructure towards renewable sources.[99] Notable renewable energy technologies include wind, solar (thermal and PV), hydropower and geothermal, which must be developed to fuel demands for electricity, heat and transport.[14, 100] Significant investments in renewables are already being made, with the share of global energy demand being met by renewables expected to grow by one fifth to 12.4% of total worldwide demand from 2017 to 2023.[100] Growth in renewable energy production was noted to be more than 5% in 2017, as seen in Figure 1.10. This is 3 times greater than the growth in total fine energy consumption.[100] However, significant investments must still be made to entirely supplant traditional energy sources with renewables, and the ultimate composition of renewable energy generation remains to be seen.

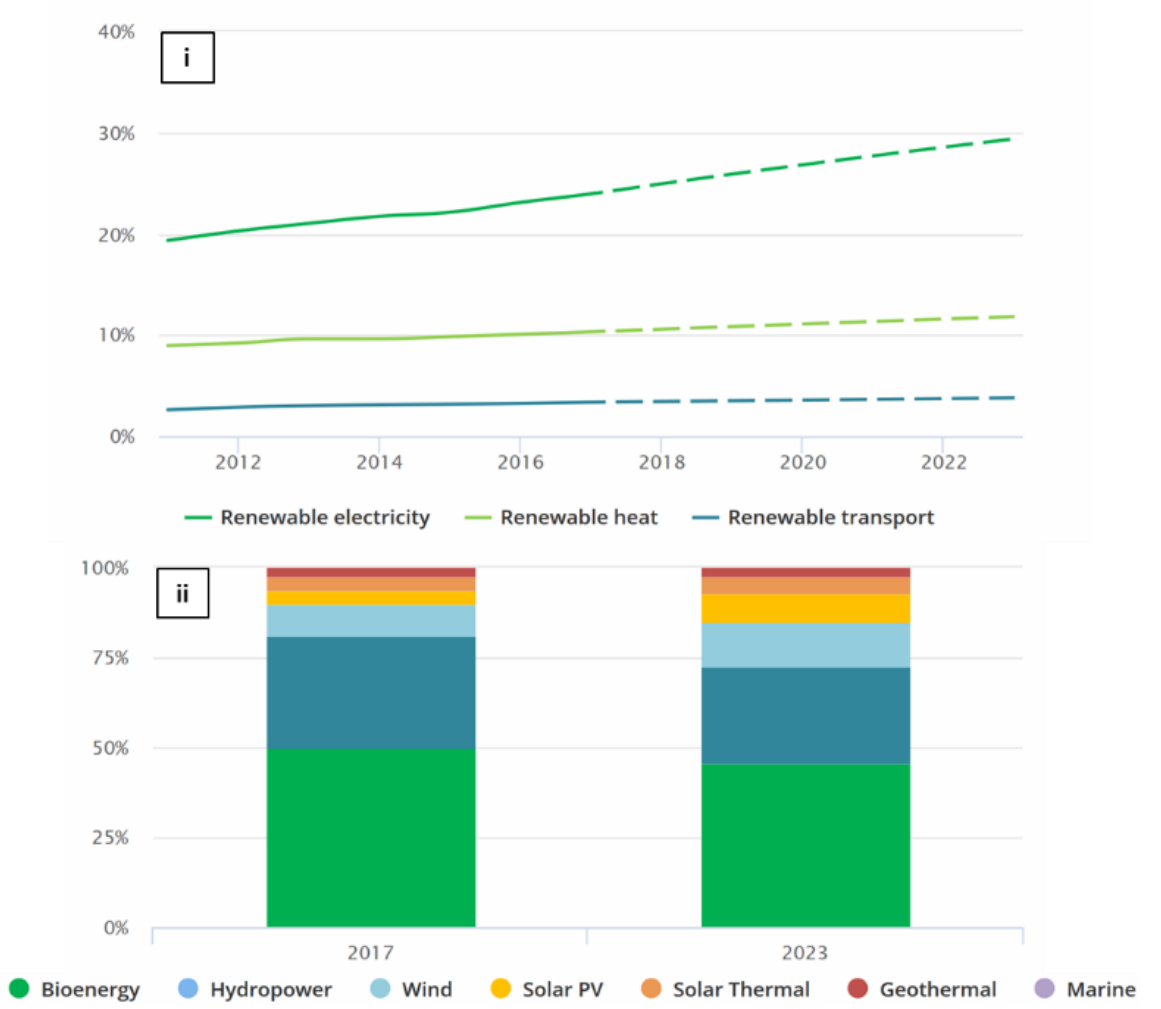

Figure 1.10. (i) Share of global renewable energy by sector and (ii) global renewable energy consumption by technology, 2017-23. Reproduced from reference 100.

A significant barrier to the viability of renewable energy technologies, particularly with respect to electricity generation, remains their intermittent supply patterns and matching this these with demand patterns.[35, 101, 102] A representation of these patterns is presented in Figure 1.11. To compensate for these mismatches in supply and demand, significant investment is required in energy storage technologies as it is estimated that a storage capacity of ca. 15-20% of annual load (ca. 2-3 months' worth) will be required in the future to utilize renewable energy on a global scale indefinitely.[103, 104]

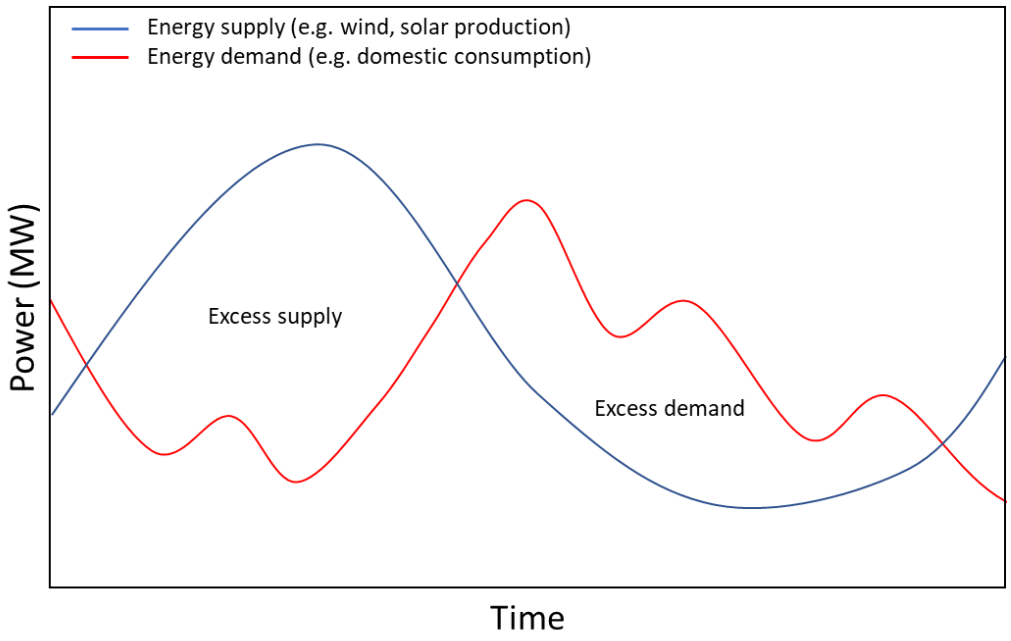

Figure 1.11. Example of daily renewable energy supply and demand patterns (abstracted). Inspired by reference 105.

A wide variety of storage technologies have been proposed to address this challenge, including fly wheels, batteries, compressed air energy storage (CAES), pumped hydro storage (PHS), and power-to-gas (P2G) technologies such as hydrogen production, FT and SNG production via electrolysis, among others.[35, 104, 106, 107] The storage capacities and discharge times for notable energy storage technologies are outlined in Figure 1.12. PHS plants are currently deployed worldwide, primarily due to technological maturity, representing ca. 99% of global storage capacity and 3% of global electricity production.[107] However, pumped hydro storage facilities are expensive to construct and maintain, and potential for expansion may be limited, as has already been noted in the UK.[107] Other storage technologies currently represent a much smaller segment of existing storage capacity and are generally considered to be at a lower level of technological maturity. These technologies may yet be appealing alternatives to pumped hydro, as significant storage infrastructure must still be constructed to achieve suitable capacity for the future, and no commercial technology exists at this time with suitable storage duration for seasonal storage, which will also be require to account for intermittent renewable energy production in the future.[107]

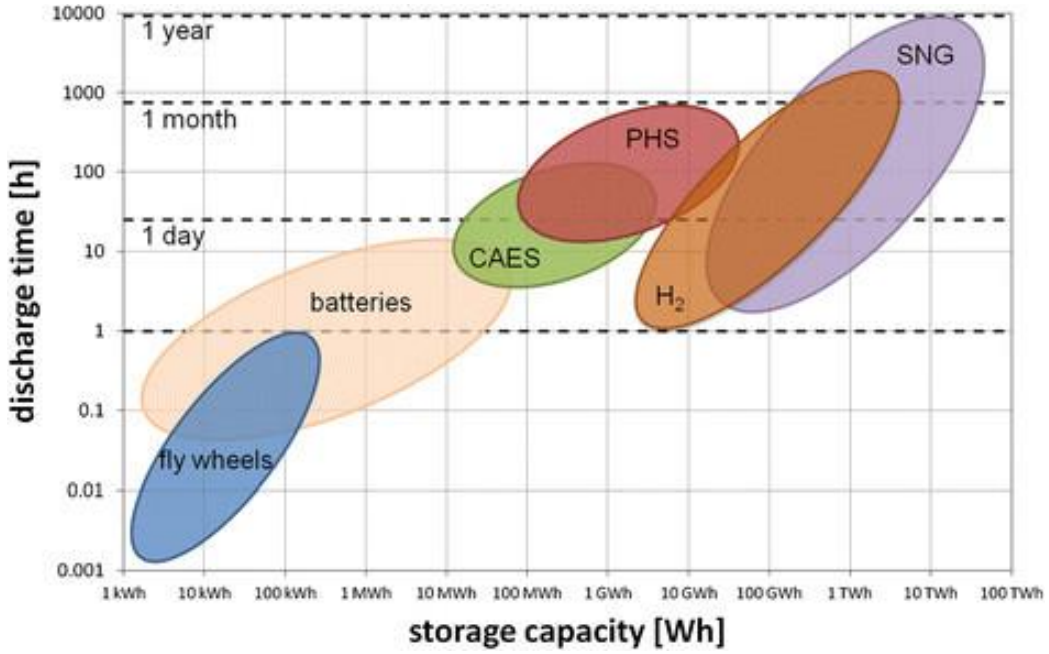

Figure 1.12. Storage capacity and discharge time for various electricity storage systems. Reproduced from reference 35.

CCU for bulk and fine chemicals has been noted to represent a limited potential in emissions reductions due to the small market for CO_2-derived products relative to the scale of global emissions.[26] However, CO_2 may yet play a role in the transition from traditional fuels to renewable energy through CCU for the production of carbon-neutral chemical fuels from excess renewable energy.[35, 90, 102, 103, 108] These fuels can be produced by using excess renewable energy to drive their synthesis when supply exceeds demand, thereby storing this excess renewable energy as chemical energy for future use, as seen in Figure 1.13. This does not reduce atmospheric CO_2 levels via permanent sequestration, though it allows for more effective emissions mitigation by renewable energy sources while fossil fuels remain prominent. Furthermore, it can play a role in the future energy storage required for widespread implementation of renewables, and may represent some sequestration potential in the form of energy storage beyond what is required.

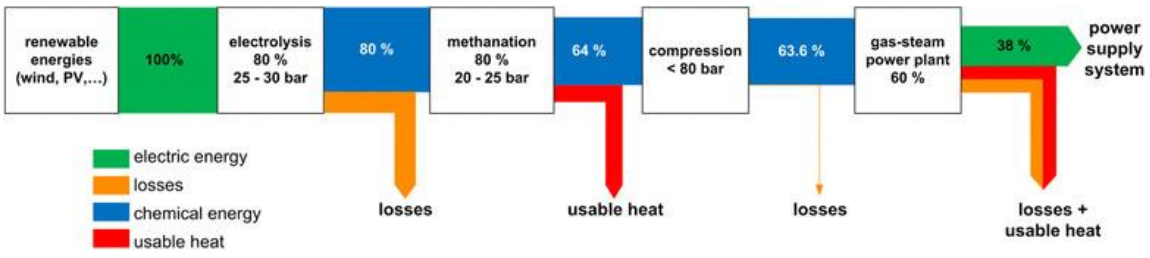

Figure 1.13. Sankey diagram for a proposed CO_2-to-methane P2G storage process. Reproduced from reference 35.

Methane (as SNG), hydrocarbons (from RWGS/FT), methanol and formic acid are the most prominent CO_2-derived energy storage molecules that have been discussed in this context.[35, 102, 103, 108-111] Formic acid has been proposed as a possible liquid hydrogen storage carrier, with potential integration into direct formic acid fuel cells to power the transport sector, though this technology remains at a low level of maturity.[43, 111] Methanol has been proposed as a combustible liquid fuel or fuel additive, which would again be beneficial in the transport sector where easily transportable liquid fuels are the industry standard. This technology is more mature than formic acid synthesis, with several notable CO_2-based methanol demonstration plants in operation.[14, 112] However, methanol possesses ca. 48% the energy density of gasoline (ca. 22 MJ kg^{-1} versus ca. 46 MJ/kg, respectively), and the scale of this technology remains relatively small compared to industrial requirements. CO_2-derived methane and liquid hydrocarbon fuels remain attractive targets, as much of the infrastructure for their use has already been built (e.g. natural gas pipelines), resulting in a large existing storage capacity and comparatively simple integration with existing technologies. Furthermore, the long-standing use of CO methanation and FT synthesis in industry may limit the amount of R&D required to apply CO_2 successfully in similar processes. CO_2 methanation in particular has seen increasing interest in academia and industry for its flexibility, storage capacity, storage duration, and potential round-trip process efficiency of ca. 38%, which would be useful for the generation and storage of electricity and district heating.[35] However, the solution for renewable energy production and storage that is easily compatible with the transport sector remains unclear.

1.5. **Motivation for this work**

In light of the clear challenge posed by increasing carbon emissions, depletion of conventional fuels, and difficulty in managing intermittent renewable energy sources, efforts are being mounted worldwide to supplant fossil fuels and improve the viability of renewable energy sources. According to the Climate Change Act 2008, the UK has committed to reducing its carbon emissions by 80% by 2050 to address this challenge,[113] and the Paris Agreement of 2016, signed by 174 states in addition to the European Union, has reaffirmed a global commitment to limiting warming to 1.5-2.0 °C.[114] While these goals are admirable and necessary, significant contributions from academia, government and industry will be required to achieve them and transition to a more sustainable energy infrastructure indefinitely.

It has been demonstrated that while chemical conversion of CO_2 into bulk and fine chemicals is desirable for its potential to generate value from CO_2, its potential to make a significant impact on atmospheric CO_2 concentrations is limited. This is due to discrepancies between the relatively small market for CO_2-derived products compared to the scale of CO_2 produced by modern human activity.[26] Therefore such CCU efforts are likely to play a supporting role in subsidising the cost of large-scale CCS operations. The conversion of CO_2 into chemical fuels may be attractive for more large-scale applications, however, as this route may support long-term, large-scale, carbon-neutral storage of intermitted renewable energy sources. This enhances their efficacy and potentially results in negative emissions by storing a surplus of fuel.

Effective conversion of CO_2 into such chemical fuels requires cost-effective, selective catalysts for CO_2 hydrogenation into methane, methanol, and longer hydrocarbons. Previously published Fe@CNT catalysts developed at the University of Bath have shown promise as highly active catalysts for combined RWGS/FT chemistry resulting in the hydrogenation of CO_2 into a distribution of CO and hydrocarbon products. While these catalysts are highly active, possess a novel structure, and are produced by a cost-effective CVD synthesis technique, the selectivity of their reactivity remains difficult to control.[68-70, 115, 116] Promoters and monolith support structures have been explored in attempts to enhance their activity and selectivity, resulting in enhanced activity and increased selectivity towards higher hydrocarbons, though complete selectivity of any product has yet to be achieved.[72, 116]

Herein, previous Fe@CNT studies are expanded upon by exploring modification of the CNT support structure through nitrogen addition, producing the first example of Fe@NCNT applied in CO_2 hydrogenation. The structure, stability, and reactivity of Fe@NCNT are explored, compared with Fe@CNT and further modified by the addition of promoter metals. The origins of the differences in their reactivity are probed through catalytic experiments, materials characterisation, and molecular dynamics simulations of their respective adsorption properties. This allows us to draw conclusions about the effect of nitrogen doping in catalytic materials designed for CO_2 hydrogenation, as well as synergistic properties between nitrogen doping in the CNT support and metal promoters on the catalyst surface that can be exploited to further influence catalyst activity and selectivity.

1.6. **Structure of the thesis**

This thesis is divided into eight chapters. The purpose and contents of each chapter have been summarised below.

- Chapter 1 introduces the evidence for anthropogenic climate change, followed by the descriptions, applications, benefits and limitations of various prominent CO_2 capture, storage and utilization technologies.
- Chapter 2 summarises the literature concerning the key concepts governing the synthesis, morphology, and reactivity of the catalytic materials and processes discussed in this work.
- Chapter 3 summarises the aims and objectives of this research.
- Chapter 4 outlines the experimental equipment, protocols, and theory applied to synthesize, characterise and test the catalytic materials explored in this thesis.
- Chapter 5 describes the synthesis, characterisation and activation of the Fe@NCNT catalyst supported by a comparison of its properties with those of Fe@CNT.
- Chapter 6 describes the reactivity of the Fe@NCNT catalyst under a variety of reaction conditions and a wide range of added metal promoters. A mechanistic analysis of the effect of nitrogen on CO_2 hydrogenation is provided, and applications in other novel catalytic processes are discussed.
- Chapter 7 builds upon the results obtained from the promoter experiments in Chapter 5 by conducting and in-depth study of Ru-Fe@NCNT as a CO_2 methanation catalyst with high activity and selectivity. Synthesis parameters, reaction conditions and the mechanism of methanation over Ru-Fe@NCNT are discussed.
- Chapter 8 concludes the thesis by summarising the work and key findings presented. Ongoing work is described followed by suggestions for future work that can be pursued to advance this research.

Chapter 2 – Literature review

This literature review summarises the theory and state of the art behind the key concepts governing the synthesis, morphology, and reactivity of the catalytic materials and processes discussed in this work. The key reactions employed in this research are first discussed to provide the reader with a basic understanding of their applications, the common catalyst used to drive them, and thermodynamic and kinetic models governing their operation. The synthesis, growth mechanisms, and nitrogen doping modes of CNT and NCNT materials are then outlined to provide suitable background on the carbonaceous support materials used in the Fe@CNT and Fe@NCNT catalysts. This is followed by a brief summary of the catalytic activity of the NCNT material itself to clarify the influence that the chosen support is capable of having on the CO_2 hydrogenation process. The literature review concludes with a summary of previous work on Fe@CNT, and previous examples of Fe@NCNT-type materials synthesised in literature (though it must be noted that this work remains the first example of their application in CO_2 hydrogenation catalysis).

2.1. The reverse water gas shift reaction

The WGS reaction has been used to produce hydrogen from carbon monoxide and water for the past century, as seen in Equation 2.1. In industry, this reaction is often used to upgrade the hydrogen content of syngas (a mixture of CO, H_2 and a small amount of CO_2 from steam methane reforming of natural gas) or water gas (an older name for syngas, which was originally produced by passing steam over red hot coke).[65, 85, 117] The resulting hydrogen is often used in applications such as the Haber process for ammonia production or the FT process for the production of hydrocarbons.[63]

$$CO + H_2O \leftrightharpoons CO_2 + H_2$$

Equation 2.1. The water gas shift reaction produces hydrogen and CO_2 by reacting CO with water.

$$CO_2 + H_2 \leftrightharpoons CO + H_2O$$

Equation 2.2. The reverse water gas shift reaction produces CO and water by reacting CO_2 with hydrogen.

The RWGS reaction allows for the production of CO and water from hydrogen and CO_2, as seen in Equation 2.2. While the WGS reaction has been extensively studied for its applicability in industrial hydrogen production, the RWGS reaction has received comparatively little attention. However, recent interest in the RWGS reaction has increased

as it may represent an appealing route for the conversion of thermodynamically stable CO_2 into CO as a more versatile intermediate molecule in efforts to reduce the impact of global CO_2 emissions.[118]

2.1.1. Catalysts and mechanism of the RWGS reaction

As the forward WGS reaction has received significantly more attention than the RWGS reaction, the current body of knowledge surrounding active WGS catalysts serves as a valuable starting point for further research into improved RWGS catalysis. There are four notable categories of forward WGS catalysts. These are the low temperature shift (LTS) catalysts, high temperature shift (HTS) catalysts, sour gas shift catalysts, and medium temperature shift (MTS) catalysts.[65] The LTS operates at a temperature range of ca. 200-250 °C and is typically catalysed by copper species, though other metals such as Ni have also been reported.[119, 120] The typical composition of a commercial LTS catalyst has been reported as ca. 32.7% CuO, 47% ZnO, and 11% Al_2O_3.[121] The upper temperature limit on LTS catalysis is generally considered to be due to the susceptibility of copper to sintering. Low temperatures can also be preferable, as they reduce the incidence of side reactions when forward WGS is the desired outcome. The HTS operates at a temperature range of ca. 300-450 °C and is typically catalysed by promoted iron oxide species. Typical commercial HTS catalysts are composed of ca. 80-90 wt. % Fe_2O_3 and 8-10 wt. % Cr_2O_3, with the difference consisting of promoters and stabilizers such as copper oxide, Al_2O_3, alkali, MgO, ZnO, etc.[64, 65] These catalysts are more stable against sintering and thus display higher activity than typical copper-based LTS catalysts at higher temperatures. However, their activity suffers comparatively in the LTS temperature range.[65] It is typically stated that iron oxides are the active phase for WGS (and RWGS) catalysis.[122, 123] Sour gas shift catalysts are typically composed of cobalt and molybdenum sulphides as the active species. This makes them suitable for use in sulphur-containing gas streams (sour gas) that would otherwise poison a typical WGS catalyst.[65] MTS catalysts have been a subject of investigation in the past in attempts to develop catalytic processes that operate between the LTS and HTS temperature ranges, at ca. 275-350 °C. While they are sometimes described using the distinct MTS moniker, in reality they are typically copper-zinc LTS catalysts that have been modified (often with iron oxide) to operate at marginally higher temperatures.[65] In addition to these primary WGS catalyst categories, in more recent years precious metal catalysts using gold and platinum have also been investigated for use in fuel cell applications.[65] It is worth noting

that because the reaction does not change molar totals, the effect of pressure on the reaction is minimal. However, industrial HTS reactors have been cited to operate at ca. 80 bar.[64]

The RWGS reaction has been investigated primarily using either (i) CuO/ZnO oxides modified by titania, zirconia, alumina and/or silica; (ii) iron-based catalysts modified from commercial HTS catalysts; or (iii) ceria-based catalysts both with and without precious metal promoters.[124] Because the RWGS reaction is favoured at higher temperatures and iron is also active in FT catalysis, HTS-type iron oxide catalysts form the basis of this investigation into combined RWGS/FT chemistry for CO_2 conversion. The mechanism of the RWGS reaction remains poorly understood and has been primarily studied over copper-based catalysts, though studies on Fe, Ni, Pd and Pt have also been conducted.[124, 125] The two most notable mechanisms discussed in literature are (i) the regenerative (redox) mechanism, in which oxygen transfers from adsorbed CO_2 to the catalyst or support before subsequently transferring again to adsorbed H_2 to yield CO and water; and (ii) the associative (formate) mechanism in which CO_2 and H_2 adsorb to form a formate intermediate at the catalyst surface.[124, 126] However, the reaction mechanism over iron oxide nanoparticles is yet to be categorically confirmed. In-depth *in situ* studies on the RWGS mechanism suggest that additional reaction routes may be possible, as seen in Figure 2.1.[127]

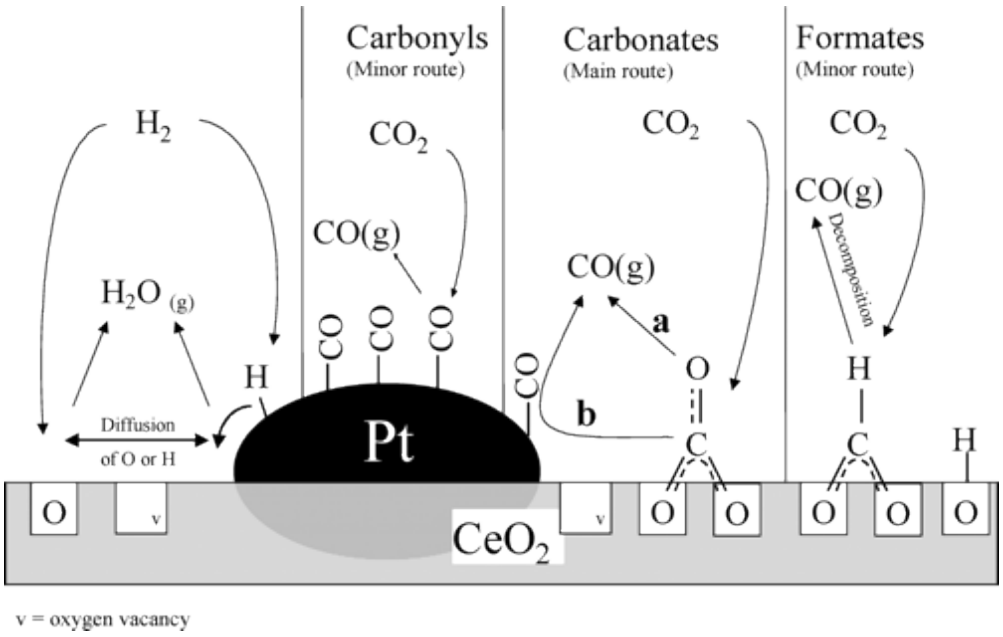

Figure 2.1. Proposed reaction pathways for the RWGS reaction over a 2% Pt/CeO_2 catalyst, as determined by combined DRIFTS-MS-SSITKA analysis. Reproduced from reference 127.

Using combined diffuse reflectance FT-IR spectroscopy (DRIFTS), steady-state isotopic transient kinetic analysis (SSITKA), and mass spectrometry (MS) analysis, Goguet *et al.*

achieved time-resolved simultaneous monitoring of the variation of the coverage of ^{12}C and ^{13}C-containing surface intermediates and the concentration of the gas-phase products ^{12}CO and ^{13}CO of the RWGS reaction over a 2% Pt/CeO_2 catalyst.[127] This investigation discarded the theory that formates are the primary intermediate formed during the reaction over this particular catalyst, as the isotopic exchange time for the observed formate species (ca. 600 sec) was more than an order of magnitude longer than that of the CO product (ca. 50 sec). While formates are likely to form to a limited extent, the authors instead suggest that the formation of surface carbonates is much more significant, and Pt-bound carbonyls may also be worth considering. However, similar investigations by Vesselli *et al.* subsequently supported the formate mechanism on a Ni(110) surface.[128] It is unclear to what extent these results can be considered analogous to the mechanism of RWGS chemistry on CNT- or NCNT-supported iron oxide nanoparticles, though they do illustrate the fact that much work remains to be done to generate a robust understanding of the RWGS mechanism using varied catalysts and reaction conditions.[129] Iron-based studies of the RWGS mechanism appear to be limited to theoretical and computational investigations at this time.[125, 130-132] These studies have been valuable in confirming the thermodynamic viability of CO_2 conversion using iron-based catalysts, as well as the importance of surface hydrogen coverage in effective CO_2 activation. However, they provide relatively limited insights into control of the RWGS reaction over iron oxide nanoparticles in real-world catalytic systems.

2.1.2. Thermodynamics and kinetics of the RWGS reaction

The RWGS reaction is thermodynamically favoured at high temperatures (ca. >800 °C) at 1 bar and a 1:1 H_2:CO_2 ratio. However, this can be influenced by increasing the H_2:CO_2 ratio of the feed gas or removing CO from the product stream to lower the temperature to increase CO_2 conversion, as seen in Figure 2.2.[124] This is significant, as excess H_2 is required in the feed stream for combined RWGS/FT processes to allow for subsequent hydrogenation of the RWGS-produced CO into hydrocarbons via FT. Furthermore, the subsequent FT reaction consumes CO, thereby increasing the efficiency of the process by shifting the equilibrium of the RWGS reaction towards products and increasing CO_2 conversion.[129]

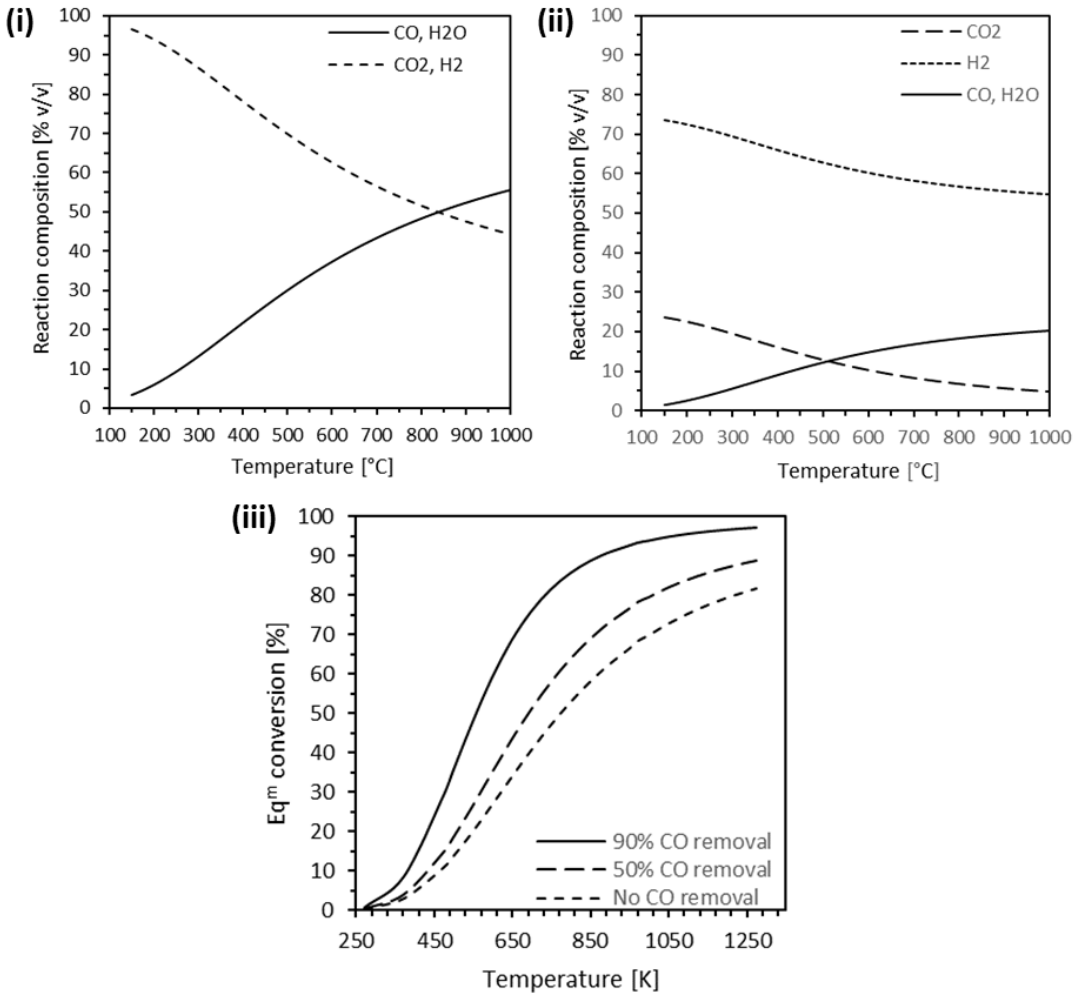

Figure 2.2. Thermodynamic equilibrium composition of the RWGS reaction from 150-1000 °C at 1 bar and (i) a 1:1 H_2:CO_2 ratio, (ii) a 3:1 H_2:CO_2 ratio. (iii) CO_2 conversion in the RWGS reaction at equilibrium and varying degrees of CO removal from 250-1300 K at 1 bar and a 3:1 H_2:CO_2 ratio. Reproduced from reference 68.

The kinetics of any process depend significantly upon the reaction mechanism, which is itself dependent upon the nature of the catalyst employed. Due to ambiguity surrounding the

mechanism of the RWGS reaction over carbon-supported iron oxide nanoparticles, consistent, relevant kinetic data is limited. Kinetic studies over copper surfaces and supported Cu/ZnO systems have agreed that the reaction order and rate limiting step vary with reaction conditions.[129] At low P_{CO2}/P_{H2} ratios the reaction is highly dependent upon P_{CO2}, though there are conflicting reports as to whether the limit for this dependence sits at $P_{CO2}/P_{H2} < 1/3$ or 1/10.[129] As P_{CO2}/P_{H2} increases to intermediate values, the reaction appears to become more dependent upon P_{H2}. At very low values of P_{H2} the reaction is dependent upon P_{H2} (approximately 2nd order) as the reaction requires adequate hydrogen surface coverage to form an active surface. Dissociation of CO_2 on the Cu atoms is considered to be the rate determining step, though the probability of CO_2 dissociation is two orders of magnitude greater on H-adsorbed Cu surfaces than clean surfaces. At very high values of P_{CO2}/P_{H2}, the rate is again linearly dependent upon P_{CO2}. This information may be useful in aiding our initial consideration of mechanistic and kinetic models of the RWGS reaction over the CNT-supported iron oxide nanocatalysts employed in this research. However, it must be emphasized that bespoke studies are required to gain a more thorough understand of the mechanism and kinetics of RWGS catalysed by the specific materials investigated in this thesis. Furthermore, it is critical to consider that the presence of concurrent FT chemistry on the surface of the catalyst during our CO_2 hydrogenation testing may further influence the mechanism and kinetics of the initial RWGS step. Examples of initial rate expressions for the RWGS reaction over a commercial Pt/Al_2O_3 catalyst are highlighted in Equations 2.3-2.4.

$$r_0 = \frac{k_s P^0_{CO_2} P^0_{H_2}}{(1 + K_{CO_2} P^0_{CO_2} + K_{H_2} P^0_{H_2})^2}$$

Equation 2.3. Initial rate expression for the RWGS reaction over a commercial Pt/Al_2O_3 catalyst for the associative mechanism. k_s is the rate constant for the surface reaction between adsorbed reactants. K_x is the adsorption equilibrium constant for reactant *x*. P^0_x is the initial partial pressure of reactant *x*. Reproduced from reference 126.

$$r_0 = \frac{k_1 (C_S + C_{OS}) P^0_{CO_2} P^0_{H_2}}{(\frac{k_1}{k_2}) P^0_{CO_2} + P^0_{H_2}}$$

Equation 2.4. Initial rate expression for the RWGS reaction over a commercial Pt/Al_2O_3 catalyst for the redox mechanism. Only the redox mechanism was found to be plausible over the tested catalyst. k_1 and k_2 are the rate constants for the sequential oxygen transfer steps. C_S and C_{OS} are the concentrations of the vacant and occupied active sites, respectively. P^0_x is the initial partial pressure of reactant *x*. Reproduced from reference 126.

2.2. **The Fischer-Tropsch process**

FT chemistry, sometimes referred to as FT synthesis or the FT process, is a series of chemical reactions that was originally developed by Franz Fischer and Hans Tropsch in 1926.[133] It is a catalytic process that allows for the conversion of syngas (a mixture of CO and H_2) into a mixture of products that can be refined into synthetic fuels, lubricants and petrochemicals. The syngas used in FT processes is typically derived from gasification of coal or biomass, or reforming of natural gas. The products generated from FT chemistry are sometimes referred to as synthetic crude oil (syncrude) and may require further refining to provide final products, similar to conventional crude oil.[134]

$$nCO + (2n + 1)H_2 \rightarrow C_nH_{2n+2} + nH_2O$$

Equation 2.5. The Fischer-Tropsch process produces hydrocarbons and water by reacting CO and hydrogen.

The FT process has been extensively studied since its discovery, as it allows for access to industrial organic chemistry from simple starting materials.[133] FT-based fuels, lubricants and petrochemicals are more complex and expensive to produce relative to similar product generated from conventional crude oil. This is due to the additional chemical processing required to produce syncrude from syngas, while conventional crude oil can be inexpensively extracted from the earth on a large scale. However, historically there have been several strategic, logistic and economic driving factors that have been significant enough to drive investment into applied FT chemistry. Most notably these investments have occurred at times when crude oil supplies could not be guaranteed (e.g. Germany in 1935-1939 to prepare for World War II, or South Africa in 1955-1993 to combat limited crude oil imports during the apartheid era). Other driving forces include the necessity of liquifying gaseous energy sources for ease of transportation, or economic incentives for converting low value, low energy density raw materials into higher value products.[134] Such processes are often referred to as gas-to-liquid (GTL) technologies. FT chemistry is still employed industrially today, as seen in Figure 2.3.

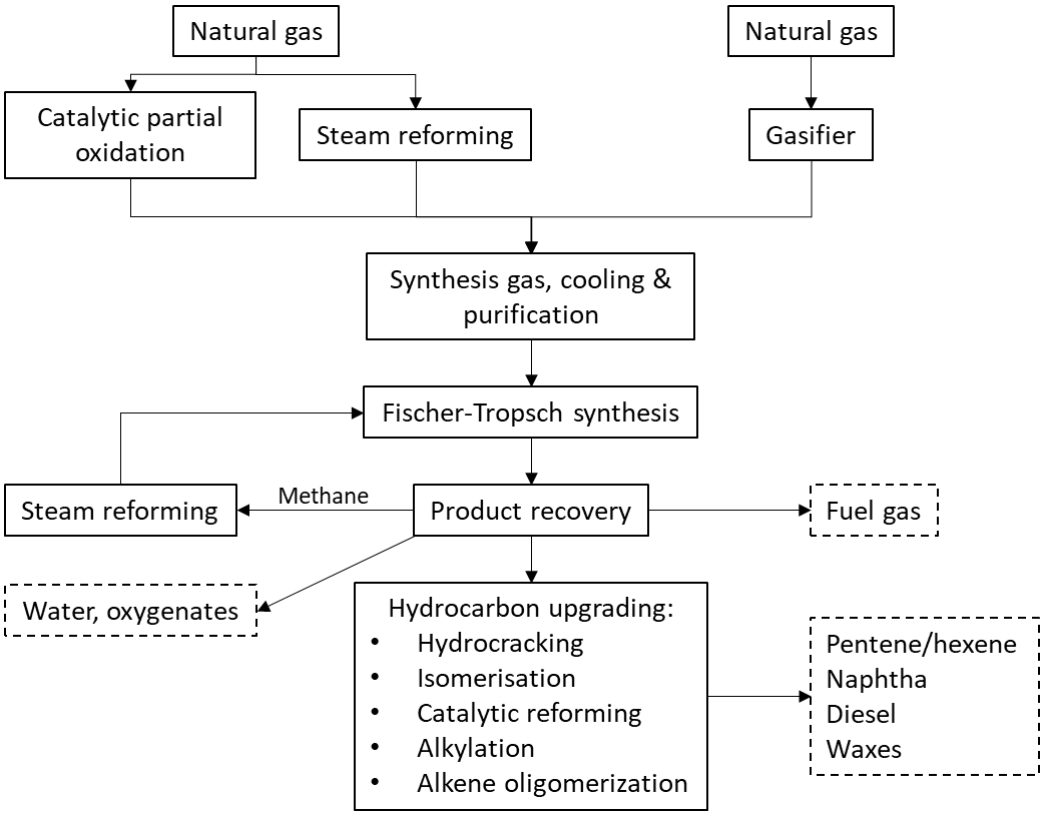

Figure 2.3. Overall scheme for a typical industrial FT process. Adapted from reference 81.

Notable examples of modern industrial FT processes include the Sasol Advanced Synthol process with a capacity of 120,000 bbl/day in South Africa, and the Shell Middle Distillate Synthesis process with a capacity of 140,000-260,000 bbl/day in Qatar.[134] As the world grapples with the challenges of renewable energy storage and emissions mitigation, FT chemistry has received renewed interest as a potential low-carbon energy storage mechanism, though this concept appears largely confined to academic discussion at this time.[35, 81, 124]

2.2.1. Catalysts and mechanisms of the FT process

Catalysts and mechanisms for the FT process have been extensively documented due to its historical significance and widespread industrial implementation.[124, 133-135] Similar to the RWGS reaction, the FT process is often noted to operate at several distinct sets of conditions. These are the High-Temperature Fischer-Tropsch (HTFT) and Low-Temperature Fischer-Tropsch (LTFT) syntheses. The HTFT process typically operates at ca. 300-350 °C and elevated pressures over fused iron catalysts in a fluidised bed reactor.[133, 134, 136] The LTFT process typically operates at ca. 220 °C and elevated pressures over precipitated iron or supported cobalt catalysts in a fixed bed reactor.[133, 134] Typical pressures for FT synthesis

range from 10-40 bar.[137] Iron-based HTFT catalysts form the basis of the FT component of the combined RWGS/FT catalysts investigated in this work. This is primarily due to the synergistic activity of iron in both RWGS and FT chemistry, combined with the thermodynamic necessity of operating at HTFT temperatures, as this is approximately the point at which the RWGS reaction becomes favourable at the relevant H_2:CO_2 feed gas ratio and subsequent CO consumption from FT. The Hägg carbide (χ-Fe_5C_2) has been frequently cited as the active phase in FT synthesis, though other carbides such as Fe_2C have also been discussed.[138, 139] Alkali- and platinum-group promoter metals have often been used to enhance the activity and selectivity of iron-based HTFT catalysts. Their enhanced activity is attributed to greater basicity originating from the promoter metals, resulting in improved CO_2 adsorption, easier iron reduction and overall greater reducing potential from the catalyst.[72] Cu, K, Mn, Cr and Zn are also significantly investigated, though these appear to be primarily applied to enhance the activity of precipitated iron catalysts during synthesis.[72, 74, 134, 140] A wide variety of other metals have been explored as FT catalysts. Fe, Co, Ni, Ru and Os are said to be the most active, with Re and Rh also displaying moderate activity. Only Fe and Co are industrially employed, however, as they represent both the best performance and the lowest cost.[134]

Mechanistically speaking, the FT process is thought of as a complex surface polymerisation reaction.[138] As such, the reaction proceeds via sequential initiation, propagation and termination steps, the nature of which determines which final products are generated.[134] The possible reaction pathways that exist during FT synthesis have been outlined in Figure 2.4.

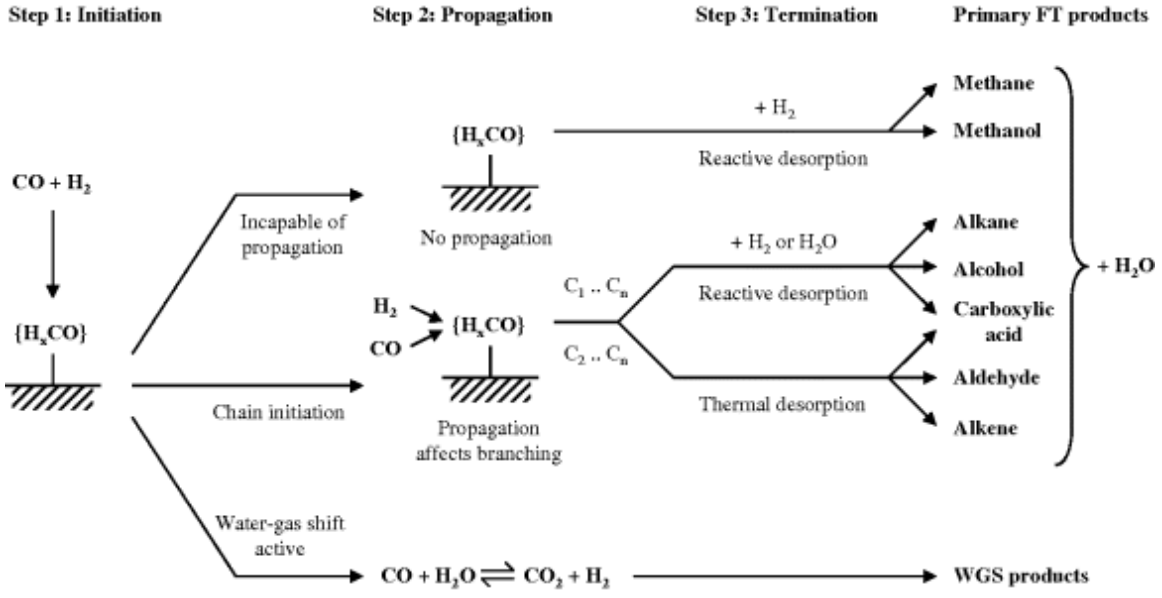

Figure 2.4. The reaction network of the catalytic Fischer-Tropsch process. Reproduced from reference 134.

Initiation occurs with adsorption of CO and H_2 at the catalyst surface, and it is said that this step is the most important step in determining which propagation pathways become accessible.[134] Upon initial adsorption, CO is not yet a chain initiator and must be bound, dissociated and partially hydrogenated to allow for chain initiation. The nature of the initiation intermediate may be such that it precludes propagation, as is found during syngas-to-methanol synthesis, or it may instead lead to water gas shift conversion.[134] A variety of mechanisms have been proposed for FT initiation and propagation, the most notable of which are the CO insertion mechanism, the carbide/alkyl mechanism, the alkenyl mechanism and the enolic mechanism.[124, 134, 135, 141] Further details on these mechanisms, their chemistry and respective initiators and monomers has been summarised in Table 2.1. The alkyl mechanism is the most generally accepted and experimentally supported mechanism at this time.[141-144] However, it does not easily explain the formation of oxygenates, suggesting that multiple mechanisms likely take place at the catalyst surface with oxygenates instead forming as a result of CO insertion or an alternative mechanism.[145] Whatever the precise identity of the propagation mechanism, the process always occurs such that oxygen cannot become bound to more than one carbon, and branching of the carbon chain is possible.[134] This gives rise to two significant implications about the FT process. Namely, that (i) hydrogenation of the CO-derived intermediate that propagates the chain must occur at some stage during the propagation phase of the reaction, and (ii) at some point during the propagation there must be two carbons from the chain that are attached to the catalyst in such a way that growth is possible from either carbon.[134]

Table 2.1. Formation chemistry of monomer and initiator during FT reaction, reproduced from reference 124. Full mechanistic schemes available from Saeidi *et al.*

Mechanism type	Monomer species	Formation chemistry of monomer	Initiator species	Formation chemistry of initiator
Enolic	*X-C-OH* *|* *H*	$2X+H_2 \rightarrow 2(X-H)$ $X+CO \rightarrow X-CO$ $X-CO+X-H \rightarrow X-COH+X$ $X-COH+X-H \rightarrow X-CHOH+X$	–	–
CO insertion	X-CO	$X+CO \rightarrow X-CO$	$X-CH_3$	$2X+H_2 \rightarrow 2(X-H)$ $X+CO \rightarrow X-CO$ $X-CO+X \rightarrow X-C+X-O$ $X-C+X-H \rightarrow X-CH+X$ $X-CH+X-H \rightarrow X-CH_2+X$ $X-CH_2+X-H \rightarrow X-CH_3+X$
Formate	CO	–	X-OH	$2X+H_2 \rightarrow 2(X-H)$ $X+CO \rightarrow X-CO$ $X-CO+X \rightarrow X-C+X-O$ $X-O+X-H \rightarrow X-OH+X$
Carbide	$X-CH_2$	$2X+H_2 \rightarrow 2(X-H)$ $X+CO \rightarrow X-CO$ $X-CO+X \rightarrow X-C+X-O$ $X-C+X-H \rightarrow X-CH+X$ $X-CH+X-H \rightarrow X-CH_2+X$	–	–
Alkyl	$X-CH_2$	$2X+H_2 \rightarrow 2(X-H)$ $X+CO \rightarrow X-CO$ $X-CO+X \rightarrow X-C+X-O$ $X-C+X-H \rightarrow X-CH+X$ $X-CH+X-H \rightarrow X-CH_2+X$	$X-CH_3$	$2X+H_2 \rightarrow 2(X-H)$ $X+CO \rightarrow X-CO$ $X-CO+X \rightarrow X-C+X-O$ $X-C+X-H \rightarrow X-CH+X$ $X-CH+X-H \rightarrow X-CH_2+X$ $X-CH_2+X-H \rightarrow X-CH_3+X$
Alkenyl	$X-CH_2$	$2X+H_2 \rightarrow 2(X-H)$ $X+CO \rightarrow X-CO$ $X-CO+X \rightarrow X-C+X-O$ $X-C+X-H \rightarrow X-CH+X$ $X-CH+X-H \rightarrow X-CH_2+X$	$X-CH=CH_2$	$2X+H_2 \rightarrow 2(X-H)$ $X+CO \rightarrow X-CO$ $X-CO+X \rightarrow X-C+X-O$ $X-C+X-H \rightarrow X-CH+X$ $X-CH+X-H \rightarrow X-CH_2+X$ $X-CH+ X-CH_2 \rightarrow X-CH=CH_2+X$
Alkylidene Hydride methylidyne	X-CH+X-H	$2X+H_2 \rightarrow 2(X-H)$ $X+CO \rightarrow X-CO$ $X-CO+X \rightarrow X-C+X-O$ $X-C+X-H \rightarrow X-CH + X$	$X=CH-CH_2-X$	$2X+H_2 \rightarrow 2(X-H)$ $X+CO \rightarrow X-CO$ $X-CO+X \rightarrow X-C+X-O$ $X-C+X-H \rightarrow X-CH+X$

The final phase of the reaction is the termination step. This step is the most important in determining product selectivity, as this is where chain growth and the addition of functional groups is controlled.[134] The termination process can be induced by either (i) thermal desorption or (ii) reactive desorption.[134] Thermal desorption occurs as a result of weakened bonds between the catalyst and the surface intermediate. It is only possible for C_2 and longer

intermediates, and the product is an unsaturated alkene (olefin) or aldehyde. Reactive desorption results from a reaction that breaks the bonds between the catalyst and the surface-bound intermediate. It is possible for C_1 and longer intermediates, taking place primarily via hydrogenation and producing either an alkane (paraffin) or alcohol.[134]

The product distribution of a given FT reaction is typically described using the Anderson-Schulz-Flory (ASF) model. The ASF model relates the hydrocarbon product selectivity of the reaction to its chain growth probability, α.[81] A value of α closer to 1 is associated with a higher probability of the reaction forming new hydrocarbon chains and adding to existing chains, while a value closer to 0 is associated with processes that favour short product chains due to early termination. More specifically, α = 0 will favour methanation, while α = 0.4-0.6 will favour short chain olefins, and paraffins and α = 0.9 will favour diesel and gasoline production, as seen in Figure 2.5.

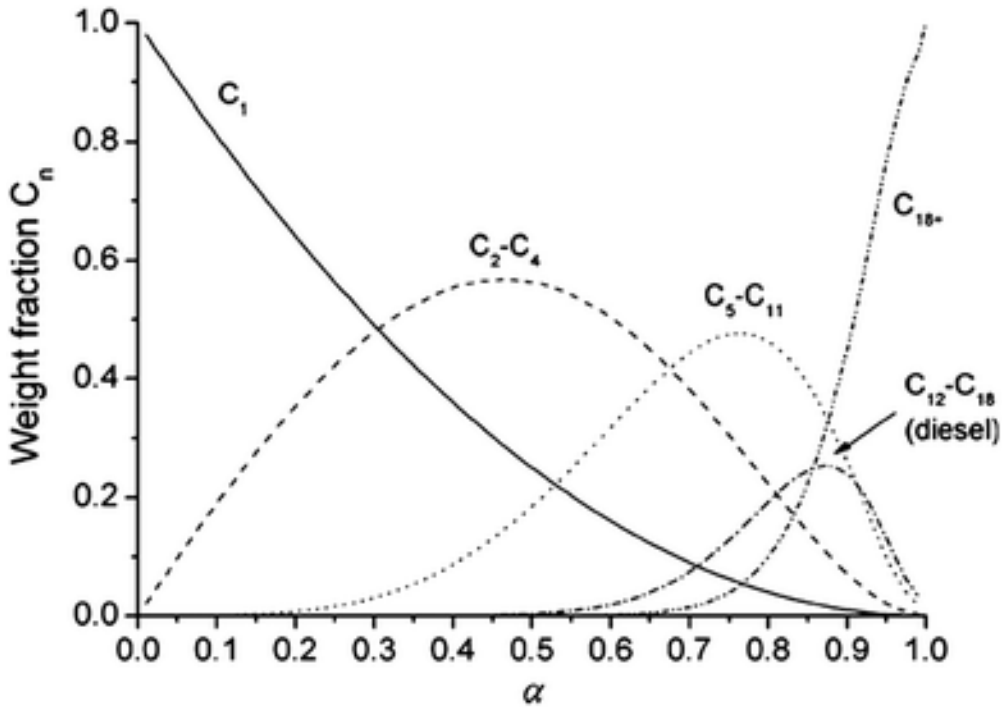

Figure 2.5. The ASF distribution of the FT process. Reproduced from reference 81.

The ASF model is expressed by Equation 2.6. This allows for α to be calculated from the hydrocarbon product distribution of any given FT experiment or process.

$$\log\left(\frac{W_n}{n}\right) = n\log(\alpha) + constant$$

Equation 2.6. The mathematical expression of the ASF model. Where *n* is the number of carbon atoms in a given hydrocarbon, W_n is the weight fraction of a hydrocarbon with carbon number *n*, and α is the chain growth probability of the process.

2.2.2. Thermodynamics and kinetics of the FT process

The Fischer-Tropsch process is irreversible, and therefore the rate of the reaction generally benefits from increased temperature and pressure. However, it has been shown that these reaction parameters also influence the final product distribution away from the ideal values predicted by the ASF distribution model.[146] Specifically, increasing temperature decreases the observed value of α, while increasing pressure increases the observed value of α, as seen in Figure 2.6. Increasing the H_2:CO feed ratio further affects the product distribution by decreasing α as the feed ratio increases.[146] It is therefore critical to balance these experimental parameters in addition to effective catalyst design in order to achieve an appropriate performance with respect to both the rate of the reaction and production of the desired hydrocarbon species.

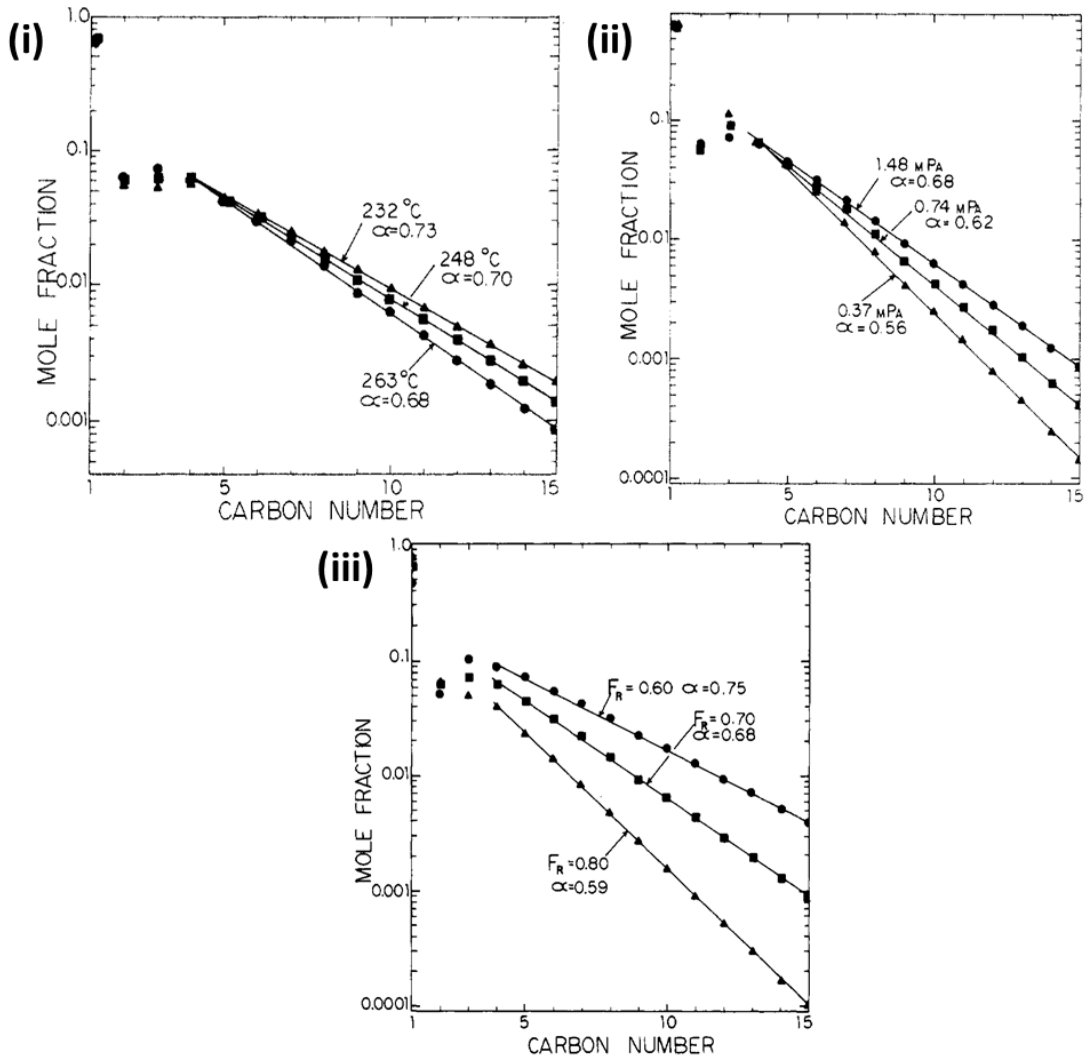

Figure 2.6. The effect of (i) temperature, (ii) pressure and (iii) feed composition on the product distribution of the FT process. Reproduced from reference 146.

2.3. **Combined RWGS/FT for production of hydrocarbons from CO_2**

Combined RWGS/FT chemistry allows for the conversion of CO_2 into hydrocarbons by coupling two well-established chemical processes together into a novel mechanism for energy conversion and storage. The process of converting CO_2 and electrolysed hydrogen into fuel for subsequent combustion is a large energy sink in practical terms. However, concern for climate change and increased investment in variable renewable energy sources are providing new societal, political and economic incentives that may justify large scale implementation of such technology, which would increase the efficiency of renewable energy technologies (and thus improve their GHG mitigation potential faster) by providing a large scale energy storage mechanism that allows for easy integration with the existing energy infrastructure while being nearly CO_2-neutral.

2.3.1. Developing catalysts for combined RWGS/FT

As has been mentioned in the prior sections discussing the RWGS and FT reactions specifically, these reactions can be catalysed individually by a wide variety of metallic species. However, in order to maximize the efficacy of the catalyst when combining these processes it is necessary for the catalyst to support the chemistry of both reactions simultaneously.[147] Furthermore, the catalyst should be able to take advantage of the lower reaction temperatures that become possible as a result of CO removal in the coupled process.[68, 69] Iron, cobalt, copper, nickel and ruthenium have been the subject of most investigations into such CO_2 conversion processes.[124, 148] While nickel and ruthenium are significantly active, they are generally considered to proceed via Sabatier chemistry, which produces predominantly methane rather than the range of hydrocarbons generated by FT. Copper catalysts proceed via a methanol intermediate and are therefore not considered true RWGS/FT processes.[149, 150] Cobalt and iron (often promoted by additional metals such as K, Mn, Pd, Pt, etc.) are noted to be active in both RWGS and FT, and have received the most research attention, likely due to the relatively large number of established commercial catalysts available for the WGS and FT processes.[74, 81, 151, 152] However, it should be noted that while commercial catalysts for the WGS and FT processes have provided a valuable starting point for combined RWGS/FT investigations, they are limited in their applicability and there is significant room for research into specialised RWGS/FT catalysts. This is predominantly due to the fact that WGS catalysts have not been optimized for RWGS

chemistry, and FT catalysts have been designed to suppress WGS activity, which is required for adequate activity in a combined RWGS/FT process.

Cobalt has displayed limited activity for the conversion of CO_2 into longer hydrocarbons, with iron-based catalysts often resulting in the best performance.[153] Thus, iron has been chosen as the active species to be investigated in this work, as it remains active for both reactions at temperatures of ca. 300-400 °C, where combined RWGS/FT processes have been noted to perform well.[72] Furthermore, previous research from the University of Bath has shown that residual iron nanoparticles (embedded into the graphitic walls of MWCNT forests after catalysing their growth) are capable of high activity in subsequent CO_2 conversion enhanced by beneficial particle-support interactions.[70] This allows for investigation into novel catalytic CO_2 reduction materials and results in a facile catalyst production process.[71, 72, 116] The significance of MWCNT and the specifics of these materials are discussed in greater detail in subsequent sections.

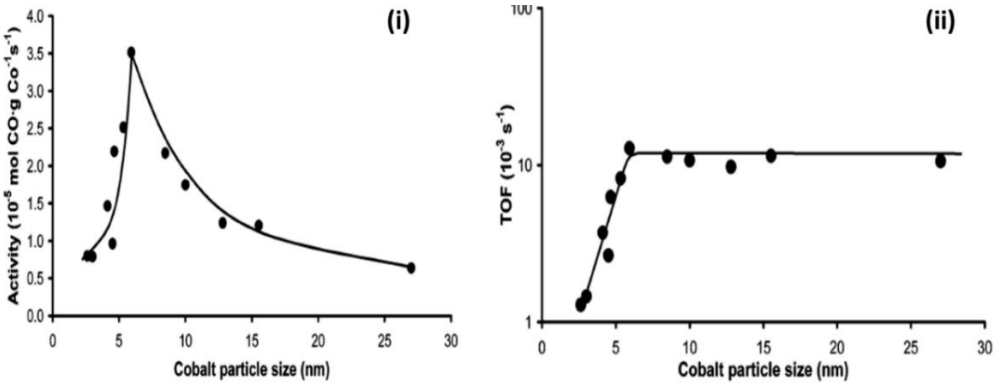

Figure 2.7. (i) CO conversion activity and (ii) catalyst TOF with respect to particle size in a pure FT process. Reproduced from reference 154.

The importance of nanoparticle size and particle-support interactions is also worth noting when attempting to develop an active RWGS/FT catalyst. Nanoparticles have been shown to display high activity for WGS and FT catalysis. While a clear understanding of size effects is yet to be established, it is generally accepted that catalyst activity is significantly influenced by particle size. Catalyst activity itself is often measured using (i) activity, or the rate of reactant conversion per gram of active metal or catalyst loading, and (ii) turn over frequency (TOF), or the intrinsic activity of the catalyst active sites. The size of catalyst particles has been shown to affect both of these parameters in Co-based FT catalysts. Activity appears to peak using particles of ca. 7 nm and TOF decreases at smaller sizes, as seen in Figure 2.7.[154] The decrease in activity observed in particles below 7 nm is initially surprising, as smaller particles are expected to afford a higher reactive surface-area-to-volume ratio.

The product distribution was also observed to shift towards methane at smaller particle sizes, which was attributed to increased H_2 coverage on the smaller particles and irreversible CO binding at the particle corner sites. Similar effects have also been observed for iron particles.[155] Particle-support interactions further affect activity and selectivity by modulating the shape and electronic properties of the catalytic particles. Strong particle-support interactions result in flatter particles when deposited by wet impregnation or incipient wetness, and may also serve to make the particles more difficult to reduce.[155] Examples of iron particles on supports with strong particle-support interactions (e.g. SiO_2 and Al_2O_3) have been shown to result in decreased FT activity relative to more weakly interacting supports (e.g. graphitic supports and SiC).[155-162]

2.3.2. Thermodynamic and kinetic considerations in RWGS/FT

The thermodynamic equilibrium and kinetics of a combined RWGS/FT process depends upon complex, largely synergistic interactions between the equilibria, kinetics and mechanisms of the two reactions individually. As has been previously discussed, consuming the CO product from the initial RWGS step to feed the subsequent FT reaction shifts the equilibrium of the RWGS process towards products at lower temperatures (as seen in Figure 2.2).[68, 69] This can be considered as synergistic cooperation between the two reactions where the activity of both processes is enhanced. The thermodynamic equilibrium of an entirely methane-selective RWGS/FT process is outlined in Figure 2.8.

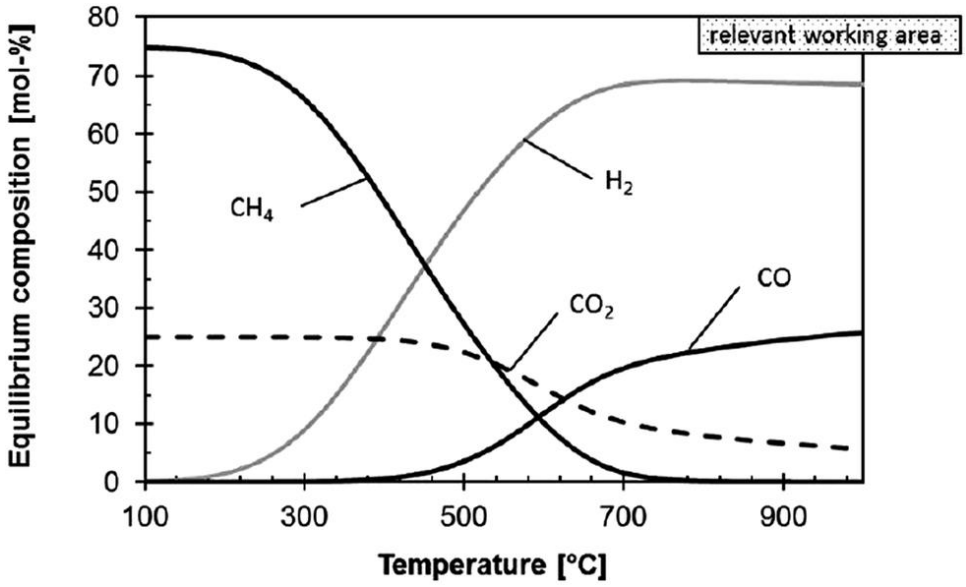

Figure 2.8. Thermodynamic equilibrium of a CO_2 conversion process proceeding via a CO intermediate at H_2:CO_2 feed gas ratio of 3:1. Reproduced from reference 118. The "relevant working area" label refers to the represented temperature range of 100-1000 °C, which clearly indicates the transition to thermodynamically favourable hydrocarbon production at a pressure of 0.1 MPa.

Furthermore, the hydrocarbon selectivity may shift to favour the formation of longer hydrocarbons as the process becomes viable at lower temperatures, in accordance with the behaviour of the isolated FT process detailed in Figure 2.6.[69, 146] Similarly to the isolated FT process, the hydrocarbon distribution of combined RWGS/FT processes has been observed to depend upon the ratio of reactants in the feed gas. Increasing the H_2:CO_2 ratio has been noted to favour CO_2 conversion and methane selectivity, with a ratio of 4:1 being stoichiometrically ideal for methane production. Decreasing the H_2:CO_2 ratio favours the production of longer hydrocarbons by starving the reaction of hydrogen, and a ratio of 3:1 is typically used in literature as this affords a desirable balance of CO_2 conversion and longer hydrocarbon selectivity.[67] Interestingly, decreasing pressure further increases selectivity towards longer hydrocarbons in combined RWGS/FT processes – an opposite trend compared to what is expected in isolated FT.[67, 146] Furthermore, selectivity towards longer hydrocarbons is often observed to increase with increasing time on stream in iron-based catalysts, suggesting increased generation of FT-active sites in the catalyst as the process evolves.[67]

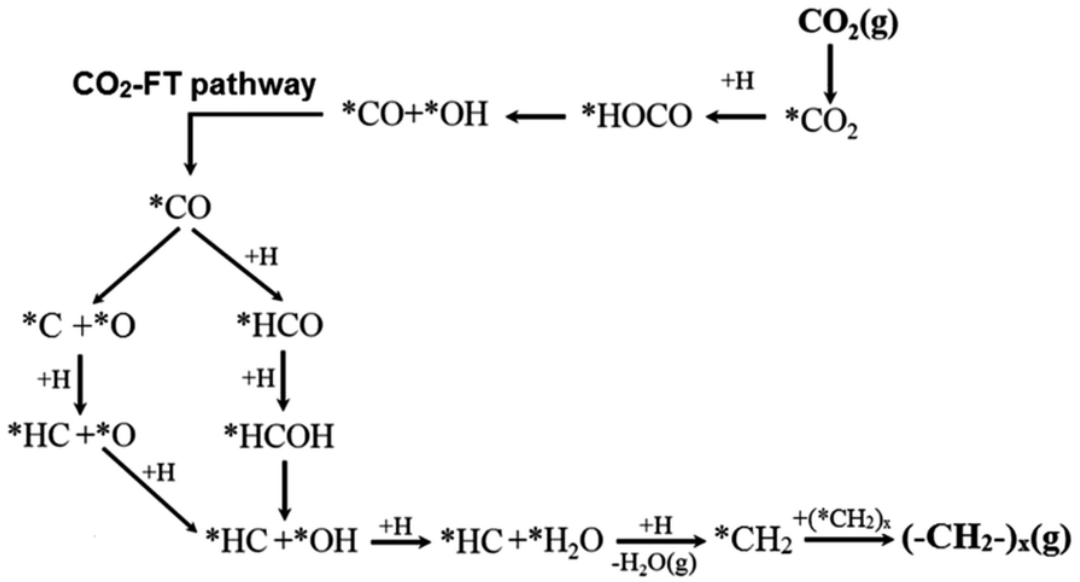

Figure 2.9. Schematic representation of the proposed CO_2-based Fischer-Tropsch mechanistic pathway. Reproduced from reference 153.

Comprehensive kinetic understanding of combined RWGS/FT processes remains limited due to the complex network of mechanistic possibilities that must be considered when developing kinetic models, as seen in Figure 2.9.[153] In all cases, CO_2 is initially converted into CO via RWGS, which then forms activated CO intermediates (CO*) that can be reduced to hydrocarbons via either associative or dissociative pathways, as previously discussed. The

stability of the CO* intermediates formed determines whether the molecule will desorb or undergo further reduction.[153] It is important to note that this requires the presence of different types of active sites (RWGS-active and FT-active) on the catalyst surface, and the relative abundance of these sites must likely be balanced to facilitate effective cooperation between the reactions.

2.3.3. A note on catalyst deactivation

Deactivation of the iron nanoparticle catalysts is a critical process that takes place during combined RWGS/FT catalysis, inhibiting the long-term activity of the catalyst and potentially affecting the product distribution of the reaction. Deactivation of supported iron nanoparticle catalysts in RWGS and FT chemistry is generally noted to occur via several common mechanisms. Specifically, (i) particle sintering and/or agglomeration, (ii) carbon deposition on the catalyst surface via the Boudouard reaction (iii) transformation of the active iron species into other inactive species, and (iv) sulphur poisoning. Particle sintering and agglomeration are known to reduce catalyst activity by increasing the size of the catalyst particles through ripening or motion across the catalyst support, thereby reducing the number of active sites available for catalysis due to surface-area-to-volume ratio effects.[163, 164] Carbon deposition is said to reduce activity by obscuring the catalytic particles beneath graphitic carbon deposits.[165, 166] Transformation of the iron species has been shown to impact the activity of pure FT catalysts due to the conversion of FT-active χ-Fe_5C_2 sites into Fe_3O_4, which is not active for FT.[167] However, it is unclear to what extent this affects combined RWGS/FT catalysis as the resulting iron oxides may contribute to RWGS activity. Sulphur is a widely known poison for industrial FT catalysts, though this process can largely be excluded from consideration in this thesis due to the high purity CO_2 and H_2 feed streams used for testing.

2.4. **Carbon nanotubes**

CNT are an allotrope of carbon in which an sp^2 hybridised network of carbon atoms takes the form of a tube with a diameter on the nanometre scale, typically with a high aspect ratio. Due to their numerous desirable properties, CNT have become a subject of intense research for applications ranging from construction to electronics, catalysis and beyond.[168-171] Their significance is evidenced by the large quantity of publications referencing them since their initial synthesis in 1991 – more than 200,000 publications to-date.[172] CNT-type materials are typically categorised into two notable groupings; single-walled carbon nanotubes (SWCNT) and multi-walled carbon nanotubes (MWCNT), as seen in Figure 2.10.

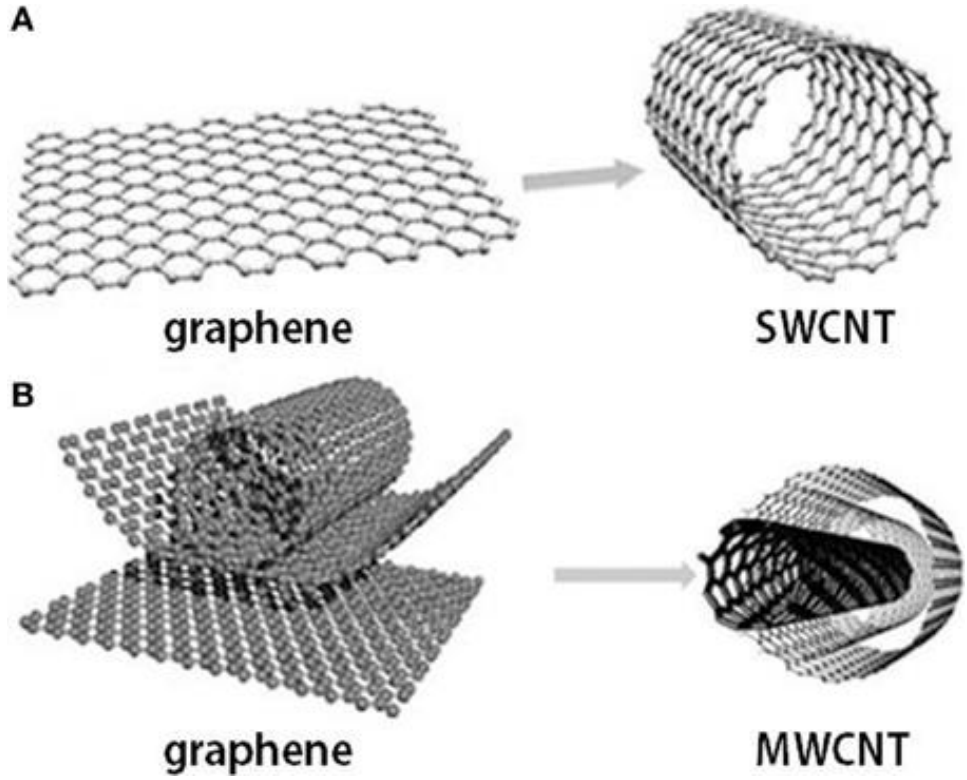

Figure 2.10. 3-dimensional representations of (A) SWCNT and (B) MWCNT. Reproduced from reference 173.

SWCNT are commonly defined as a single layer of sp^2 hybridized carbon atoms, similar to pristine graphene, rolled into a hollow cylinder, often with a diameter on the order of 1 nm.[171, 174] MWCNT are therefore often considered as an arrangement of multiple concentric SWNT with increasing diameter, fitted inside one another.[171, 175] The number of walls in MWCNT can vary from two (double-walled nanotubes) to several tens, reaching an external diameter up to ca. 100 nm. As with graphene, the interlayer distance in MWCNT is often ca. 3.4 Å.[171, 174, 175] The size and wall count of CNT-type materials directly influence their material properties, as represented in Figure 2.11. It is worth noting that a similar class of materials known as graphitic nanofibres (GNF) is also frequently discussed in literature, though these materials differ from CNT-type materials in that they do not possess a hollow core. While they are similar to CNT-type materials, GNF-type materials do not play a role in the work conducted for this thesis and therefore will not be further discussed.

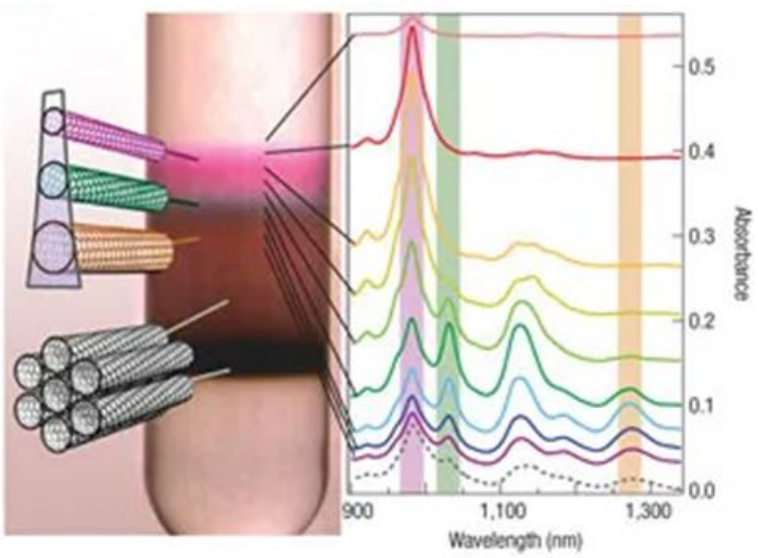

Figure 2.11. A CNT density gradient illustrating the different properties of differently sized CNT. Reproduced from reference 176.

In this work, MWCNT represent the fundamental support material for the iron nanoparticle catalysts that facilitate RWGS/FT chemistry for CO_2 hydrogenation. This section summarises their common synthesis techniques, proposed growth mechanisms, desirable properties and the notable safety concerns and best practices associated with their use.

2.4.1. Notable synthesis techniques

CNT have been reportedly synthesised via numerous routes, as seen in Figure 2.12. All syntheses share three notable ingredients: (i) a carbon source, (ii) catalyst, and (iii) energy input. Synthesis methods are often classified as being either "high temperature" or "low temperature," depending on the physical state of the carbon source employed.[174] High temperature methods typically involve the sublimation of graphite, which does not occur below 3200 °C, followed by rapid condensation of the sublimated carbon atoms in a chamber with a strong temperature gradient. Low temperature methods typically rely on the decomposition of a gaseous or liquid carbon source, which occurs at relatively lower temperatures (ca. 600-1200 °C).[174] Notable high temperature techniques include laser ablation and arc discharge. However, these are rarely applied in modern research due to cost and limitations in scalability, and are therefore not discussed further in this thesis.

Figure 2.12. Current methods of CNT synthesis. Reproduced from reference 175.

Catalytic chemical vapour deposition (cCVD) is a low temperature synthesis technique, which is now the standard method for industrial CNT production.[175, 177] Compared to the high temperature methods discussed previously, which were the first methods used to reliably produce CNT,[172, 178, 179] cCVD allows for easier scale-up and superior control of

properties such as CNT length, diameter, orientation, purity and density, while providing a yield between 20-100% by weight.[175, 180] Due to the flexibility of the CVD technique, numerous derivative techniques have been developed to allow for lower synthesis temperatures (down to 480 °C)[181] and the production of hybrid materials and surface modifications. The most notable example of these is plasma enhanced CVD (PECVD), which has itself has been developed into several variations including radio frequency (RF-PECVD), direct current (DC-PECVD), diffusion (DPECVD) and microwave (MWPECVD).[175] cCVD techniques typically produce MWCNT, though an increasing number of examples of SWCNT produced via cCVD are being reported in literature.[175, 182]

In cCVD synthesis, a metal catalyst (typically Fe, Co or Ni, though many metals have been reported)[174, 177] is deposited onto a suitable substrate or support (typically a SiO_2 or Al_2O_3 surface), as seen in Figure 2.13.[175, 183] This can be achieved by either coating the substrate with the catalyst beforehand or generating the catalyst *in situ* by depositing the catalyst onto the substrate during the CVD process, which is often referred to as floating catalyst CVD (FCCVD).[174] While the former allows for greater control over catalyst and tube growth orientation and morphology, the latter allows for a simpler overall manufacturing process.[174, 184]

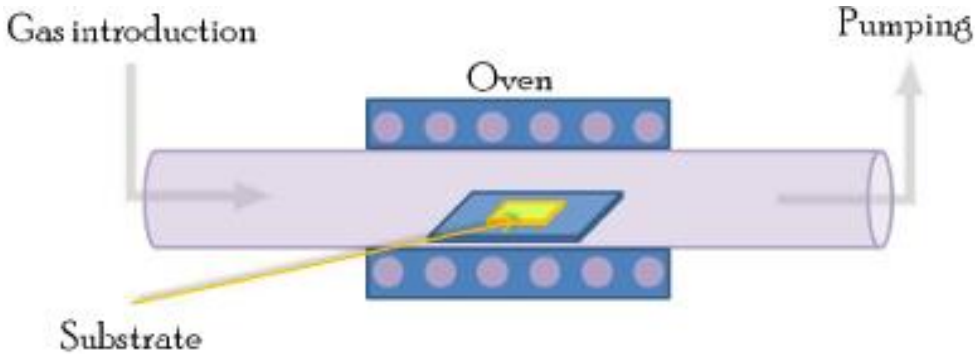

Figure 2.13. Schema of the cCVD synthesis. Reproduced from reference 174.

A carbon source is introduced either as a gaseous hydrocarbon (e.g. methane, ethylene or acetylene) or an aerosol of a liquid hydrocarbon (e.g. benzene, n-hexane, xylene, or toluene). This carbon source is typically diluted into an inert carrier gas stream (e.g. nitrogen, helium or argon) and flowed over the catalyst at temperatures of 600-1200 °C and pressures of 1-10 bar.[174, 175] The temperature required depends upon the thermodynamic stability of the carbon source, with methane requiring higher temperatures (ca. >850 °C) due to its relative stability, and sources such as acetylene and ethylene allowing for lower temperatures (ca. 500-750 °C and 650-850 °C, respectively), as seen in Figure 2.14. A high flowrate (500

sccm or more) is often used, as this dilutes the carbon source and suppresses the number of walls formed on the catalyst.[177] Hydrogen is often included in the gas stream if the catalyst is introduced *in situ* as a metallocene complex (e.g. ferrocene, cobaltocene, nickelocene; ferrocene is most common due to its high activity and stability in air) dissolved in the organic solvent carbon source to aid in the decomposition of the catalyst precursor into the desired catalytic nanoparticle on the substrate.[185] Once deposited, the catalyst then serves to aid the decomposition of the carbon source while acting as a nucleation site for CNT growth.[186]

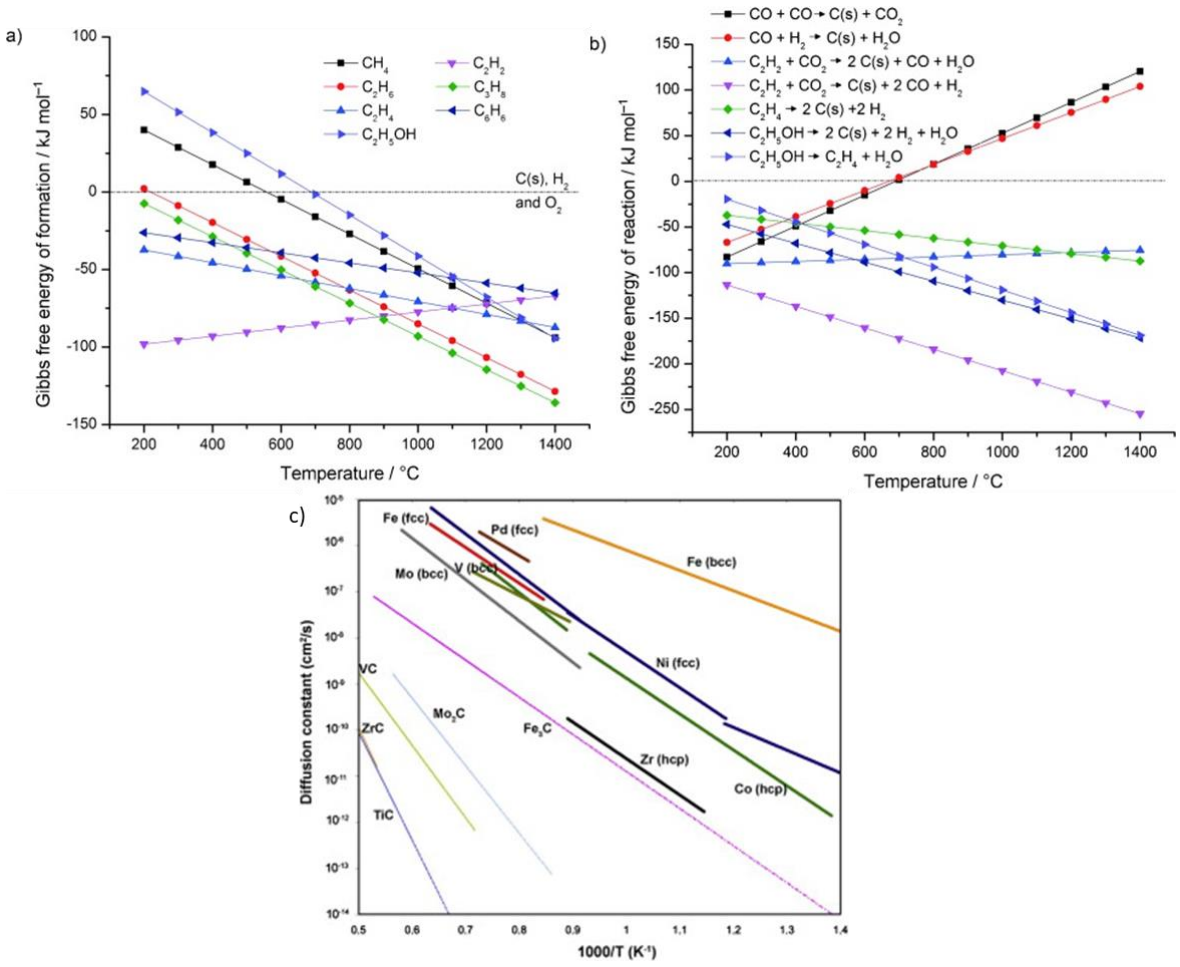

Figure 2.14. a) Gibbs free energies of formation for various carbon precursors. The energies are normalized to the number of carbon atoms in the precursor and correspond to its pyrolysis. b) Gibbs free energies of typical reactions: CO disproportionation, water gas shift, oxidative dehydrogenation of acetylene, and pyrolysis of ethanol. The energies are normalized to the number of solid carbon atoms. Reproduced from reference 186. c) Bulk diffusion constants of carbon in various metals and metal carbides as a function of temperature. Reproduced from reference 177.

Regardless of the synthesis method employed, CNT products always contain a variety of defects and impurities which must be removed to obtain a more uniform, high-quality sample.[175] The most common impurities noted in literature are undesired residual catalyst metals, amorphous carbon material, and structural defects such as bends and kinks caused

by disorder in the sp^2 lattice and deviation in growth morphology as a result of excess metal particles interfering with CNT growth from the initial nucleation point.[187] The most common purification techniques include: microfiltration for the separation of CNT from amorphous and graphitic carbons, metal clusters and polyaromatic carbons based on size/aspect ratio exclusion; oxidation in air at temperatures of 400-750 °C to remove amorphous and graphitic carbons by oxidation into CO_2 (though it can be difficult to selectively oxidize these graphitic impurities without destroying or shortening the CNT due to their similar thermal stabilities); and acid oxidation to etch away undesired carbonaceous and metallic contaminants more selectively without substantial loss of the CNT.[187] This acid treatment is the preferred purification technique employed in industry to produce high purity CNT without carbonaceous or residual metal impurities.[179, 187] However, it must be noted that applying strong acids (e.g. HNO_3, H_2SO_4, $HClO_4$, and HPO_4) in this method has the potential to generate covalent adducts on the CNT sidewall which further modify the structure and reactivity of the final product. For this reason, acid treatment is also often used as the starting point for further attempts at surface modification.[187]

In this work, an aerosol-assisted FCCVD method is employed to produce the Fe@CNT, Fe@NCNT and derivative catalyst materials from a precursor solution of ferrocene in toluene or acetonitrile. A representative schematic of the experimental apparatus is presente in Figure 2.15. This method has been chosen due to its simplicity, flexibility, and ability to produce CNT decorated with iron nanoparticles embedded into the tube walls by adding an excess of ferrocene into the precursor solution. While these nanoparticles would be considered impurities if the target product were pure CNT, in this work the same metal particles that catalyse CNT growth can later be activated for combined RWGS/FT catalysis. Due to their integration with the CNT support material during synthesis, they allow for strong particle-support interactions and improved hydrogen spill over from the particle to the CNT support material.[70] Hence, a thermal purification procedure is used to activate the catalyst by removing unwanted graphitic and amorphous carbon while exposing the metal particles for catalysis. The standard acid treatment purification method is comparatively unsuitable due to its capacity for etching away the desired metals.

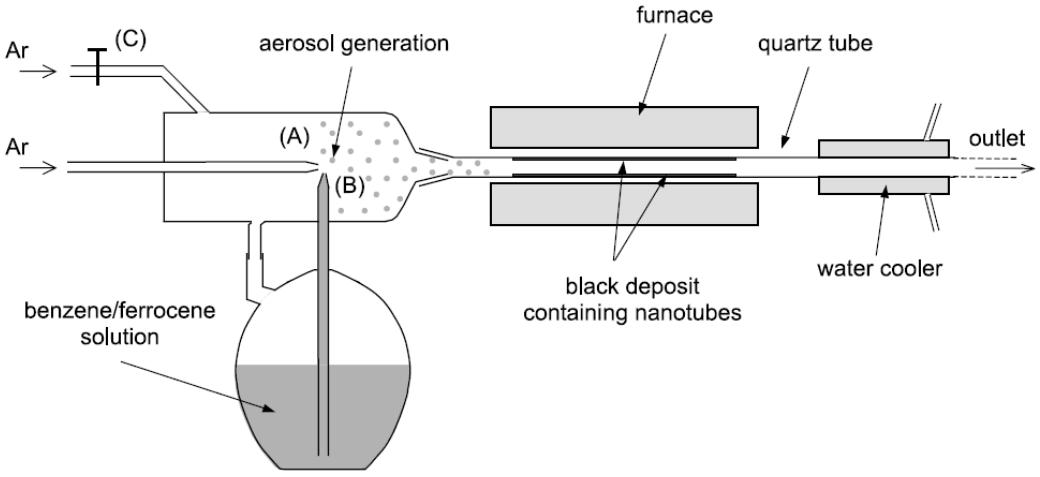

Figure 2.15. Schematic of an aerosol-assisted FCCVD synthesis similar to the apparatus employed for this work. Reproduced from reference 188.

2.4.2. CNT CVD growth mechanism

The mechanism for CNT growth is a topic of significant discussion in academia. Baker *et al.* were the first to develop a model for the growth of carbon nanofibers in the 1970's.[189-191] The model originated from the observation that catalytic particles were often located at the tip of a nanofiber, with one side chemically bonded to the solid carbon.[186] It was therefore proposed that the vapour-solid-liquid (VLS) model, originally developed by Wagner and Ellis to explain the growth of Si whiskers, could also explain the growth of carbon filaments.[192] Schematics of the VLS mechanism and the alternative VSS mechanism are presented in Figure 2.16. In the VLS mechanism, a carbon-containing precursor adsorbs and dissociates on the catalyst particle to form elementary carbon atoms. These atoms then dissolve into the bulk of the nanoparticle to form a metastable liquid carbide and diffuse through the particle before finally precipitating as solid carbon to form a nanofilament (e.g. nanotube, nanorod, etc.) on the opposite side of the particle.[186]

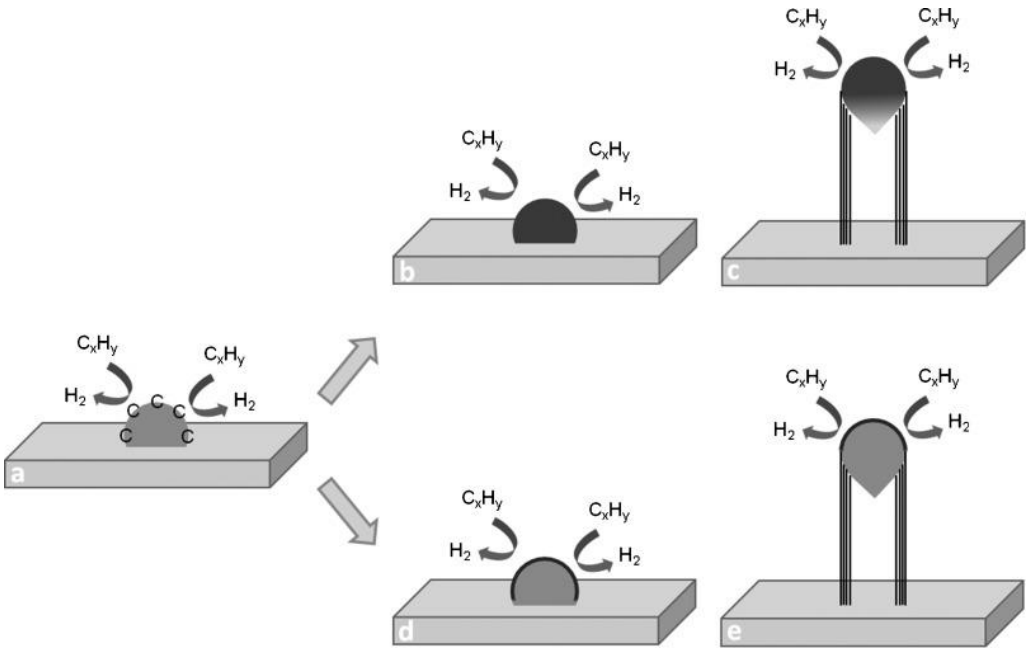

Figure 2.16. The three steps involved in the VLS mechanism: a) decomposition of the carbon-containing precursor on the surface of the catalyst particle; b) diffusion of carbon atoms through the particle as a solid solution; and c) precipitation of carbon at the metal-support interface and formation of a nanofiber or a nanotube. In an alternative VSS mechanism, carbon species diffuse only on the surface of the catalyst particle (d–e). Reproduced from reference 186. It should be noted that while this figure illustrates a tip-growth mechanism, both tip- and base-growth are possible.[193]

Activation energies for the growth of nanofibers have been measured to be in good agreement with previously determined values for the dissolution of carbon into relevant metals such as Fe and Co.[186] This gave the VLS mechanism significant credibility, and is in good agreement with more recent studies on the kinetics of CNF and MWCNT growth on iron.[194, 195] However, its validity has also been challenged, as the driving force behind the diffusion of carbon through the catalyst remains unclear.[196-201] Baker *et al.* propose that the thermal gradient generated across the particle by the exothermic decomposition of the carbon precursor and the endothermic precipitation of solid carbon drives the diffusion process.[189] However, this does not account for growth when the decomposition of the precursor is endothermic, as with alkanes, and additionally does not explain why CNT are hollow.[186] In light of this discrepancy it has been subsequently proposed that carbon diffusion occurs only at the surface of the catalyst particles, which has since been supported by numerous *in situ* studies using HRTEM and XPS.[186] These studies also suggest that the active phase in CNT growth is metallic iron, with only a small amount of subsurface iron carbide present during catalysis. This surface diffusion growth mechanism has been dubbed the vapor-solid-solid (VSS) mechanism, which is more substantiated by evidence than the VLS mechanism but does not appear as prominently in literature.[186] It is worth noting that while the diffusion of

carbon through the catalyst is generally considered to be the rate limiting step, it has been shown that when thick, dense mats or forests of CNT are grown, the mass transport of gaseous reagents to the catalyst can become the rate limiting step instead.[202]

During this growth process, a large number of variables determines the final morphology of the CNT product, as seen in Figure 2.17. Factors such as the crystal lattice of the catalyst, the size of the catalyst particles, the supply (availability) of carbon to the surface, the nature of the growth support material, the solubility of the carbon source in the chosen catalyst, and general reaction conditions such as temperature and flow rate all influence the size, chirality (metal/semiconductor ratio), length, defect density, number of walls, and orientation of the final CNT material.[177] For the purposes of this work, the principles governing the diameter of the nanotubes and catalyst particles is of particular interest, as tubes and particles with smaller diameters represent a greater surface area for catalysis and hydrogen spill over to enhance catalyst activity.[70] Furthermore, it has been noted that turnover frequency increase notably, accompanied by a significant shift in product distribution, when iron carbide particles decrease below 7 nm in FT synthesis.[155] This makes particle and tube size an attractive target for manipulation in the development of Fe@CNT and Fe@NCNT.

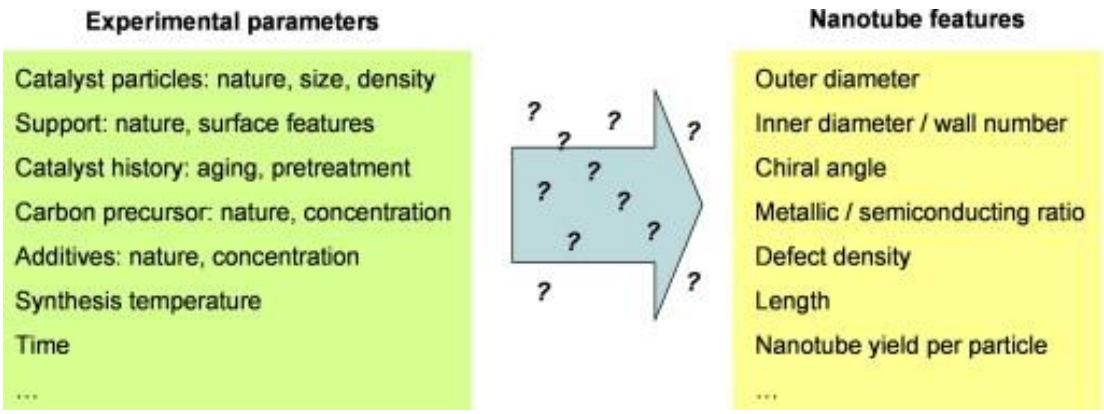

Figure 2.17. Input parameters and output features of carbon nanotube growth by cCVD. Reproduced from reference 177.

Due to the mechanics of the VSS growth process, the diameters of the particles and nanotubes are inextricably related, as seen in Figure 2.18.[203-205] CNT diameter is generally accepted to be linearly dependent upon the catalyst particle diameter. However, it should be noted that for a given particle, temperature effects and other reaction conditions will also influence the resulting tube diameter, with higher temperatures generally resulting in wider tubes with greater crystallinity.[177, 206] Carbon supply (i.e. the amount of carbon available to the catalyst during growth) strongly influences the nanotube diameter distribution, though

contradictory reports suggest that the influence of carbon supply is variably dependent upon the growth conditions of each individual system.[177] Numerous groups have reported that nanotube diameter decreases as a result of reduced carbon feedstock flux or pressure.[207-209] The opposite trend has also been reported by several groups,[210, 211] while others have reported an optimal carbon supply range for the production of small-diameter CNT at a given temperature.[212] Gaseous additives have also been reported to influence tube diameter, notably by increasing tube size through the increased addition of CO_2 into the feed stream.[213] This further supports reports elsewhere that the nature of the carbon and metal precursor also influences tube diameter. Substituted ferrocenes (most notably dimethylferrocene) have been noted to decrease mean tube diameter by ca. 50% compared to unsubstituted ferrocene,[214] and low carbon supply has been noted to produce tubes with fewer walls.[215-217]

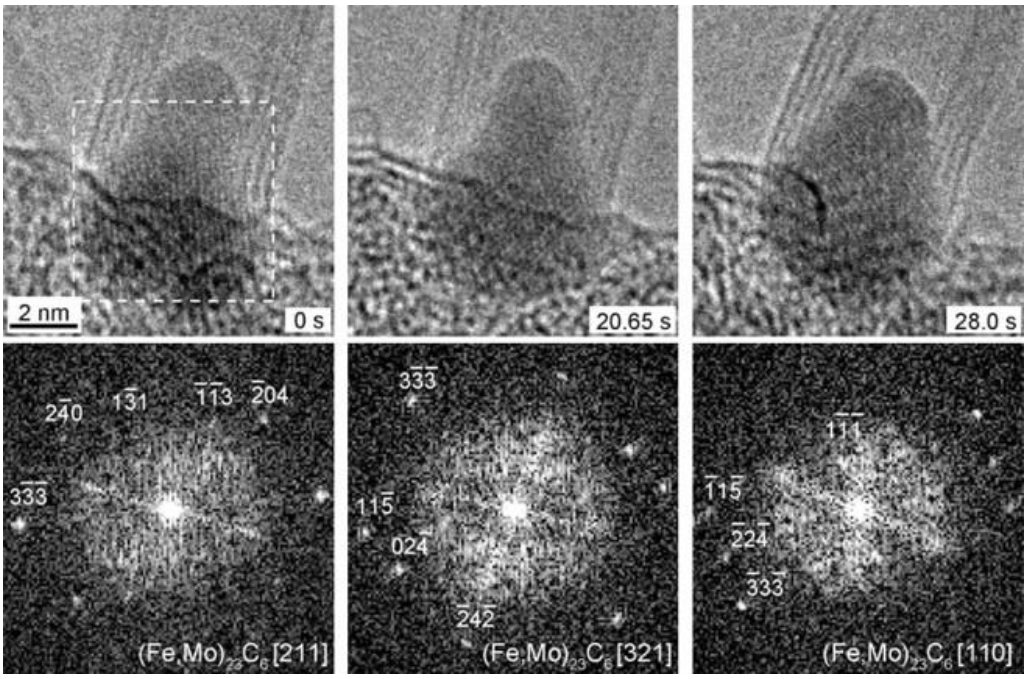

Figure 2.18. *In situ* Environmental Transmission Electron Microscopy observation of the growth of a four-wall CNT from a fluctuating catalyst nanoparticle of (Fe,Mo)23C6-type structure, reproduced from reference 218. This demonstrates the relationship between particle and tube diameter, as well as the malleable nature of catalyst particles during CNT synthesis.

While variables governing the diameters of CNT in CVD have been studied in-depth, relatively little work has been carried out on influencing the size of the FCCVD catalyst particles *in situ*. Researchers investigating the controllable synthesis of CNT materials consider these particles to be an impurity in the sample, rather than a source of valuable catalytic sites for further reactions as they are considered to be in our studies of Fe@CNT and Fe@NCNT. Even less work has been carried out to study the growth of the superfluous metal particles that form on the walls of CNT during FCCVD synthesis. While these particles

are thought to play an important catalytic role in Fe@CNT for RWGS/FT catalysts, they do not serve to enhance the ordered CNT growth mechanism during FCCVD, which is thought to be primarily governed by tip- or base-located particles. As a result, while manipulating catalyst particle size in Fe@CNT and Fe@NCNT during FCCVD may be a powerful tool for influencing their reactivity, determining methods to do so remains a significant challenge.

It should be noted that the nature of the support material can also significantly influence the activity and character of the CNT growth catalyst.[177, 183] Oxide supports (e.g. Al_2O_3, MgO, SiO_2, TiO_2, ZrO_2, ZnO) are commonly used to prevent diffusion of the metal catalyst into the support. For example, SiO_2 is preferable to pure Si, as metals have been noted to diffuse into pure Si to form metal silicides, which are not active for CNT growth, as seen in Figure 2.19.[219] For these oxide supports, the effect of the substrate on the CNT growth process is typically discussed in the context of the strength of the catalyst-support interactions. Strong catalyst-support interactions result in lower catalyst growth activity and can be attributed to two different phenomena: (i) modification of the electronic structure of the catalyst particle (i.e. stabilisation) by the oxide support via charge transfer and (ii) the physical encapsulation of the particles by a thin layer of oxide support.[220] Depending on the nature of the substrate material, different interaction effects may dominate the relationship between the metal and the support. The two prominent interactions to consider are: (i) the electronic interaction corresponding to the charge redistribution at the metal-oxide interface and (ii) the chemical interaction corresponding to atom diffusion at the metal–oxide interface.[220] For conducting oxides (e.g. TiO_2, ZrO_2, ZnO), charge redistribution is long range and driven by the difference of Fermi energies. For insulating oxide supports (e.g. Al_2O_3, MgO, SiO_2), chemical reactions (e.g. redox and alloy formation) are confined at the interface and are notably driven by the differences of electronegativity between metals.[177] While these interactions reduce catalytic growth activity, they can also result in reduced particle coarsening (thus influencing the particle size distribution) as catalyst particles are less free to move on the substrate surface.[221]

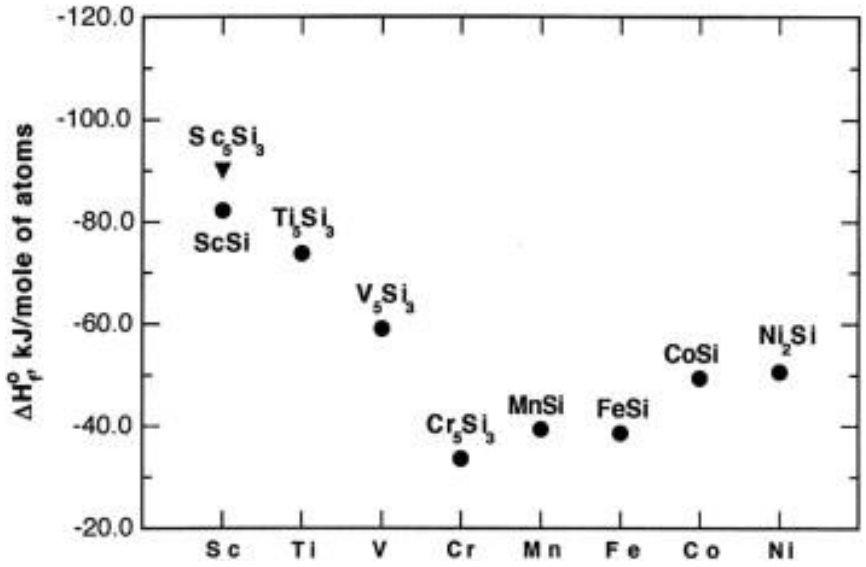

Figure 2.19. Standard enthalpies of formation for several relevant 3d transition metal silicides. Reproduced from reference 177.

Several notable deactivation mechanisms exist for CNT growth catalysis. Interestingly, these mechanisms are often related to the size of the produced particles and tubes, as seen in Figure 2.20. They are: (i) particle coarsening (sintering) due to either Ostwald ripening or migration coalescence, resulting in particles that grow too large to grow nanotubes (i.e. they become underfed by the carbon supply due to their size);[222] (ii) deactivation of metal particles due to either over-feeding (resulting in encapsulation by a carbon layer) or under-feeding (resulting in inactive particles) of carbon through sub-optimal carbon supply; (iii) physical encapsulation of metal particles due to diffusion into the support; and (iv) formation of alloys due to chemical affinity towards the support.[174] While these mechanisms are distinct phenomena, they are highly interconnected. It is important to be aware that attempts to manipulate any single variable in the FCCVD growth process are likely to have affect a significant number of other variables in the process.

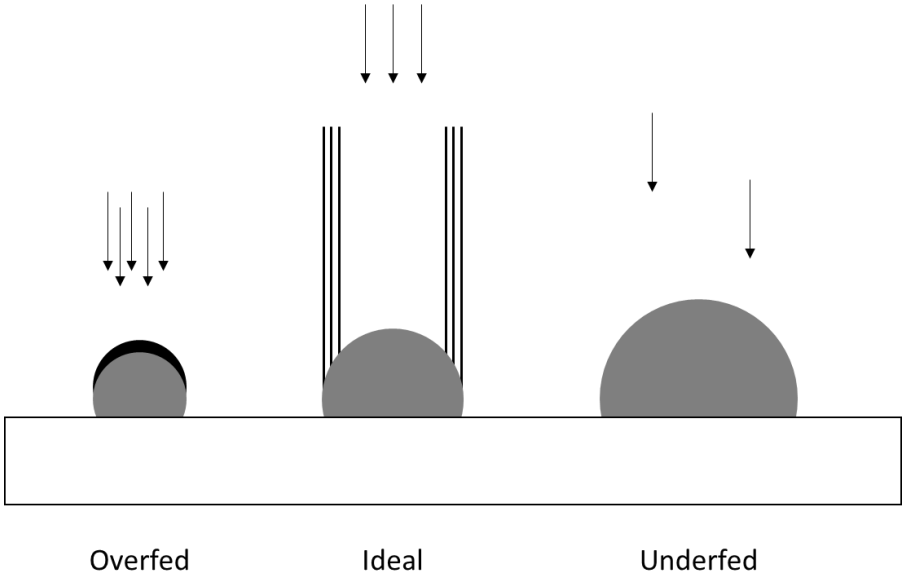

Figure 2.20. Proposed model of particle activation/deactivation as a function of particle size and carbon supply. Adapted from reference 207.

2.4.3. CNT as catalyst support structures

CNT possess a number of desirable properties that have already seen them applied commercially in the fields of energy storage (e.g. consumer lithium ion batteries), coatings and films (e.g. fouling-resistant paints for ship hulls), and composite materials (e.g. improved wind turbine blades) with many more applications on the horizon.[223] They are also desirable in the field of chemical catalysis as support materials for catalytic transition metal nanoparticles. As catalyst supports, CNT have been noted to be particularly attractive for their high surface area, tuneable structure (e.g. diameter, porosity and surface composition), and significant chemical and thermal stability. Their surface area (ca. 400-900 and 200-400 $m^2\ g^{-1}$ for SWCNT and MWCNT, respectively) is appealing as it allows for a high surface area to volume ratio for deposition and dispersion of catalytic metal nanoparticles.[171] Their tuneable diameter allows for control over specific surface area and porosity, and may also influence electronic interactions between the CNT p_z orbitals and the d orbitals of their supported nanoparticles, which have been found to decrease inversely with nanotube curvature.[224] Typical porosities, surface areas, and decomposition temperatures of CNT-type materials and similar carbon-based nanomaterials are detailed in Table 2.2.

Table 2.2. Adsorption properties and thermal stability of CNT, GNF, activated carbon and graphite. Reproduced from reference 171.

Type of Carbon	Porosity ($cm^3 g^{-1}$)	Surface area ($m^2 g^{-1}$)	Decomposition temp. in air (°C)
SWNT	Microporous, V_{micro}: 0.15–0.3	400–900	~800
MWNT	Mesoporous, V_{meso}: 0.5–2	200–400	~650
GNF	Mesoporous, V_{meso}: 0.5–2	10–200	~600–900
Activated carbon	Microporous	700–1200	~500–600
High SA graphite	Mesoporous	60–300	~800

Surface composition can be additionally modified through the addition of surface heteroatom species such as sp^3 hybridised nitrogen and oxygen groups (i.e. NO_3^- groups and epoxides) by e.g. acid treatment.[187, 225] These groups can act as additional anchoring sites for the deposition and dispersion of catalytic metal nanoparticles, which otherwise rely primarily upon surface defects to stabilise them on the CNT surface.[78, 171, 224, 226, 227] It should be noted that several studies indicate a significant difference in the reactivity of CNT-supported nanoparticles depending on whether they are located on the inner or outer surface of the CNT, notably due to restricted movement of the nanoparticles and reactants in the tube, stabilising the particles against sintering and potentially leading to the production of longer hydrocarbons in FT catalysis.[160, 161, 228, 229] The chemical stability of CNT makes them suitable for a wide range of reaction conditions, including stability in acidic and basic environments.[171] Their relative thermal stability makes them suitable for high temperature catalytic applications, though are also combustible, which allows for facile recovery of precious metals from the CNT support as well.[171] It has been noted that amount of residual catalyst metals in the sample can decrease this stability.[171]

However, while the advantages of CNT as a catalytic support material are evident, there are also several significant complications associated with their use. First, CNT remain relatively expensive compared to conventional supports such as alumina, silica and activated carbon.[230] This price is expected to decrease with time as larger and larger quantities of CNT enter the market for other applications, though CNT must show significant benefits over conventional catalyst support materials if they are to become a prominent material in commercial catalysis.[223, 230] Second, CNT often require significant pretreatment prior to catalysis to remove residual CNT growth catalyst metals and deposit the desired catalysts for subsequent reactions.[171, 187] Finally, CNT powders have proven themselves to be difficult to handle in

conjunction with conventional reactor designs. CNT powders suffer from significant pressure drop in packed bed reactors, and their electrostatic behaviour makes them prone to airborne dispersion. This makes them significantly hazardous when considered in conjunction with the long-term health concerns associated with their inhalation.[231]

2.4.4. CNT safety concerns and best practices

Despite increasing efforts in research and production of CNT-based materials, the potential health effects associated with CNT exposure remain poorly understood.[232, 233] Indeed, the number of publications investigating the toxicity of CNT-type materials pales in comparison to publications concerning their novel properties and application, as seen in Figure 2.21.

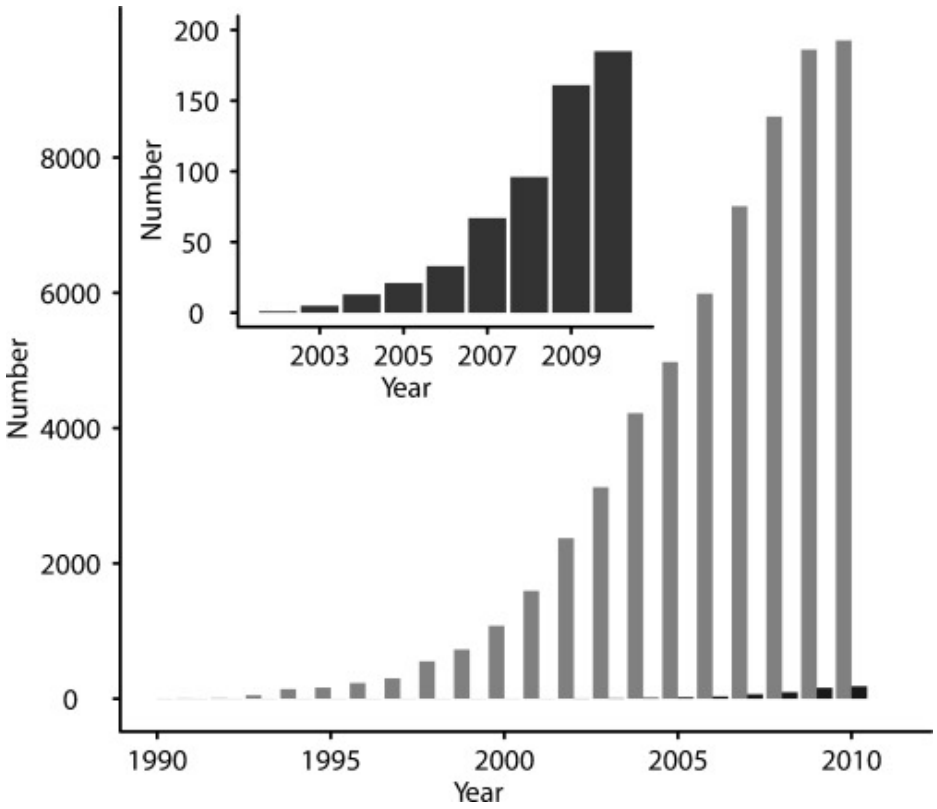

Figure 2.21. Number of publications in the ISI Web of Science database identified with the keyword ‘carbon nanotubes’ (grey bars) and ‘carbon nanotubes toxicity’ (black bars) from 1990-2010. Reproduced from reference 233.

The possible routes for CNT to enter the human body during handling are via the lungs (e.g. inhalation), the gastro-intestinal tract (e.g. ingestion), and the skin (e.g. absorption through the epidermis).[233] Of these, inhalation is the most likely, as CNT often exhibit a tendency towards electrostatic dispersion, resulting in airborne CNT particulate matter in the vicinity of their use. Initial studies on the toxicology of MWCNT focused on the effects of aerosolised MWCNT in mice, and found that MWCNTs induced airway fibrosis in

sensitized and MWCNT-exposed mice 14 days after exposure at 100 mg m^{-3}.[234] It was also shown subsequently that similarly aerosolized MWCNTs could reach the sub-pleura of pathogen-free C57L6 mice after 6 h following a single exposure of 30 mg m^{-3}.[235] While these studies were critical starting points in the toxicological study of CNT, it should be noted that they are considered unrealistic due to the large doses and aerosolised nature of the CNT, which are unlikely to occur in a typical handling environment.[233] A landmark study by Poland *et al.* indicated that long, stiff MWCNT are capable of carcinogenic toxicity in humans via a similar mechanism as asbestos.[236] This is attributed to MWCNT conforming to the "fibre paradigm," i.e. because they are (i) biopersistent and non-biosoluble; (ii) thin enough to enter cells (i.e. <5 μm); and (iii) have a length of at least 15 μm.[233] Long, straight MWCNT similar to those used in this study, particularly MWCNT-7, appear to be the most hazardous due to their ability to pierce cells and their apparent resistance against phagocytosis, as seen in Figure 2.22.

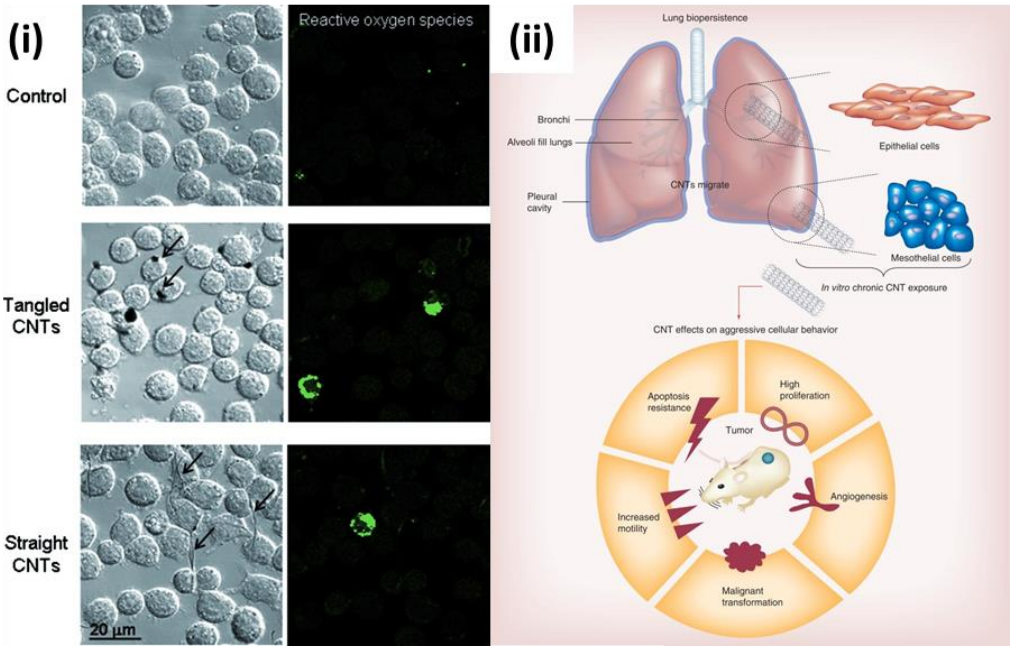

Figure 2.22. (i) Light microscopy images of J774A1 'macrophage-like' cells treated for 30 min with different CNTs (15 μg mL^{-1}) and stained for reactive oxygen species (green). The tangled CNTs appear to be readily phagocytosed (black arrows) whereas the straight CNTs are incompletely taken up by the cells (black arrows). Reproduced from reference 236. (ii) Lung models for carcinogenesis studies and chronic effects of carbon nanotube exposure on aggressive cellular behaviours. Reproduced from reference 237.

Residual metals in CNT likely contribute to their toxicity. Short, iron-rich MWCNT have been shown to possess a significant cytotoxic effect, and removing residual iron particles has been recommended as a method to reduce the toxicity of MWCNT.[238] Furthermore, hair loss, oxidative stress, depletion of glutathione, an increase of dermal cell number, and skin

thickening have been associated with skin contact for CNT with residual iron particles.[239] Dermal toxicity is another area of concern, as it has been shown that 0.2-0.6 mg of processed SWCNT were deposited on workers' gloves following a HiPCO production process.[233] Further studies on the dermal toxicity of SWCNT indicate that there is a dermal hazard associated with CNT exposure and that the dermal response is primarily inflammatory in nature.[237] Functionalisation of CNT has been noted to further affect their toxicity, frequently with reduced toxicity observed for carboxyl- and amino-functionalised CNT. It is unclear whether this reduced toxicity is a result of reduced bioactivity for individual CNT as a result of functionalisation, or whether it is instead caused by an increased tendency towards agglomeration after functionalisation, as agglomerated CNT have been noted to be less toxic than individual tubes.[240] The toxicity of N-doped CNT similar to those employed in this work has been sparsely studied, though evidence suggests that Fe- (2.0-2.5 wt. %) and N-doped (2-4 at. %) CNT prepared from ferrocene in benzylamine are less toxic than their pure CNT counterparts, and were not deemed to be toxic to mice when administered at doses of ≤1 mg/kg.[241] Ultimately, however, due to the huge amount of variation in length, diameter, residual metals, wall number, and chemical composition between otherwise "similar" CNT materials, comparing results between different studies and identifying studies where only one significant CNT variable has been altered remains a challenge. While a number of excellent reviews are available on the toxicology of CNT materials, the most unanimous conclusions drawn by these publications are that (i) CNT materials likely possess several mechanisms for toxicity and carcinogenicity in humans, with long, straight MWCNT posing a carcinogenic risk similar to asbestos, and (ii) that more stringent studies are required to develop a consistent framework with which to evaluate the toxicity of these materials.[233, 239, 242-244]

Given the current state of knowledge regarding the toxicity of MWCNT materials similar to those employed in this work, it is of the utmost importance to prevent worker exposure to these materials. Several groups and organisations have attempted to establish suitable occupational exposure limits (OEL) for workers who handle CNT regularly. In 2010, Aschberger *et al.* derived an OEL of 1-2 μg m^{-3} for two different types of MWCNT. Also in 2010, the Bayer Schering Pharmaceuticals Institute of Toxicology derived an OEL of 50 μg m^{-3} for its Baytubes® MWCNT. In 2013, The United States National Institute for Occupational Safety and Health (NIOSH) recommended an 8 hour time weighted average OEL of 2 μg m^{-3} for MWCNT and 1 μg m^{-3} for carbon nanofibers. Finally, in 2018

Fukushima *et al.* used an extensive rat inhalation test to derive an OEL of 0.15 μg m^{-3} over 15 years and 0.05 μg m^{-3} over 45 years to protect workers from the most clearly carcinogenic MWCNT (MWCNT-7).[242, 243] Of course, mandatory use of appropriate extraction hoods, gloves, lab coats and particle masks is always expected to ensure that these conditions are met. Specifically, a TYVEK antistatic coat must be worn over the standard lab coat to ensure that CNT fibres are not transported outside of the workspace on the workers' clothes. Nitrile gloves must be used to prevent dermal exposure, and as of 2013 the US NIOSH and UK Healthy and Safety Executive (HSE) recommend a minimum of APF20- or FFP3-grade respirator masks when handling CNT materials as a suitable precautionary measure against spillages.[245-247] If CNT are likely to become airborne during use, a full-face, motorised respirator should be used. Furthermore, work with CNT should always be conducted in a HEPA filtered fume cupboard, which is safely vented outside wherever it is reasonable to do so.[245] CNT samples should be stored in airtight vessels to prevent unintentional spillages, and safety equipment such as masks and gloves should be stored separately from the CNT samples to avoid contamination. As best practice, the required respirator masks should be applied first and removed last when preparing to handle CNT. Furthermore, it is critically important to ensure that work is conducted in a negative pressure extraction environment to prevent any risk of exposure from the outset.

2.5. **Nitrogen-doped CNT (N-CNT, NCNT)**

Substitutional heteroatom doping has become a central topic of interest in CNT research, in attempts to gain greater control over the chemical and electrical properties of CNT materials.[225, 227, 248] Among possible candidates (e.g. B,[249-252] N,[227, 253-255] S,[256] F[257], P[258]) nitrogen displays several notable advantages such as flexible, simple synthesis techniques, and effective modulation of the graphitic structure while maintaining high conductivity.[227] This thesis largely concerns the effect of nitrogen doping in the CNT support structure of a CO_2 hydrogenation catalyst, and how this influence can be exploited to enhance our capacity for CO_2 utilisation. In this section, the synthesis, structure, properties and previous work using NCNT as supports for RWGS and FT catalysis are summarised.

2.5.1. Electronic and chemical properties of NCNT

Nitrogen can be incorporated into the graphitic CNT lattice in several bonding configurations, as seen in Figure 2.23.[259-261] When compared to carbon, nitrogen possesses an additional valence electron. This prevents nitrogen from integrating into the sp^2

hybridised graphitic lattice perfectly, resulting in lattice defects and unique electronic properties for different nitrogen atoms in the lattice depending on their bonding configuration. The possible nitrogen bonding configurations, their respective properties and resulting lattice vacancies have been outlined below.[227, 260, 262-264]

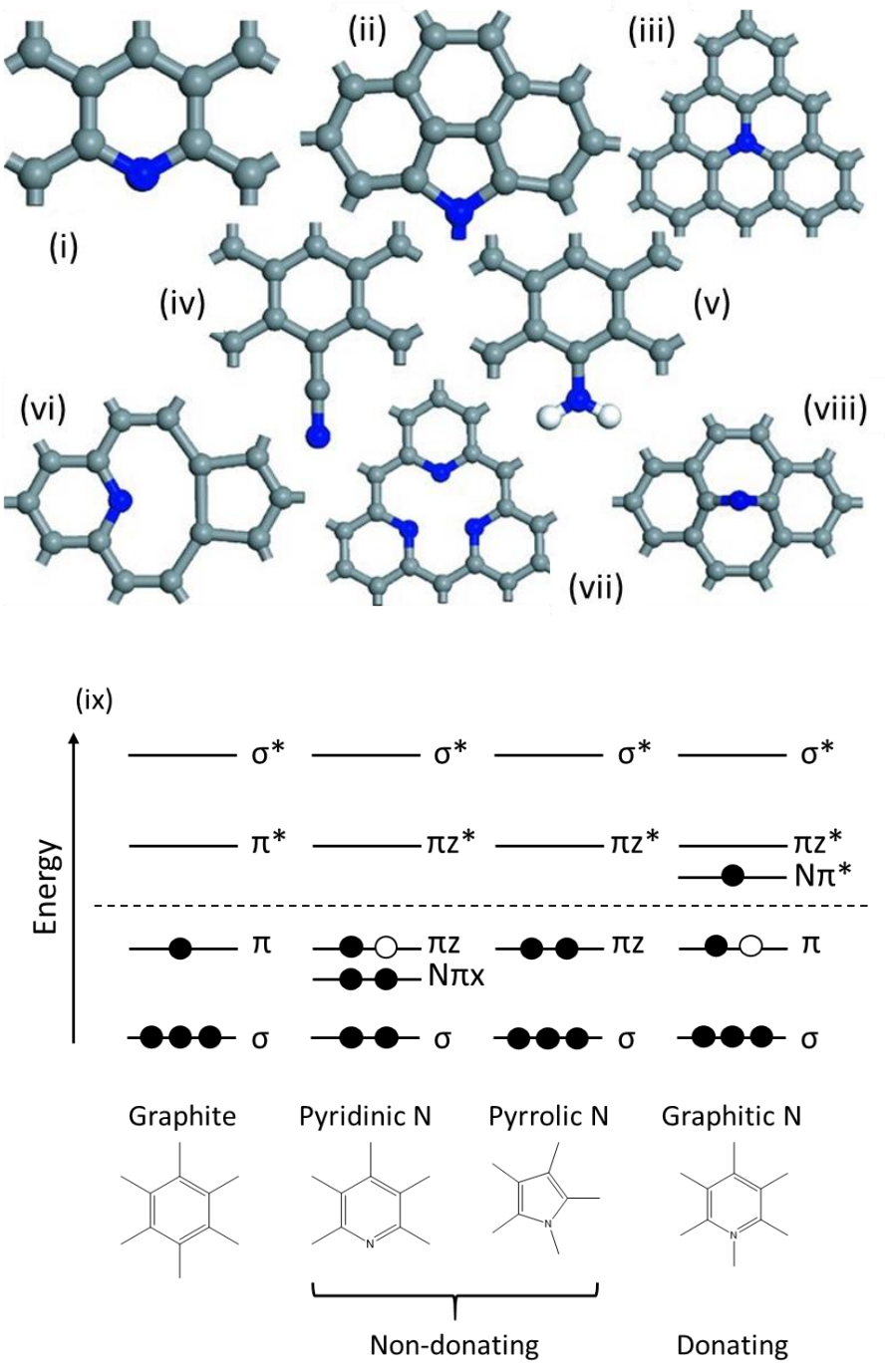

Figure 2.23. (i-viii) The bonding configurations of nitrogen incorporated into the graphitic CNT lattice, reproduced from reference [259]. (ix) Molecular orbital diagrams comparing the electronic structure of graphitic carbon versus possible nitrogen substitutes, inspired by reference 265.

i. **Pyridinic**, where the N atom is substituted into a 6 membered ring, contributing p-electrons to the aromatic π-system via sp^2 hybridised bonding to graphitic carbons. Two valence electrons take part in σ-bonding, two others form a lone pair, and the rest stay in the π-state. The lone pair on a pyridinic N may act as a Brönsted-Lowry base to become readily protonated in aqueous solutions or take part in base-catalysed reactions.

ii. **Pyrrolic**, where the N atom is substituted into a 5 membered ring. It retains sp^2 hybridisation through energetically favourable delocalisation of its lone pair into the aromatic π electron system.

iii. **Graphitic/Quaternary**, where the N atom replaces a graphitic carbon atom in the CNT lattice. Four out of five valence N electrons form σ- and π-bonds similar to C atoms; the remaining one electron forms a shallow donor state in the band gap of semiconducting SWCNT or is entirely delocalised in the π-system of graphene or metallic SWCNT. Other possible quaternary configurations include edge-located quaternary N, where nitrogen replaces a carbon in a 6 membered ring, but forms a terminal N—O or N—H bond rather than a fourth N—C bond that would otherwise continue the graphitic lattice.[260] In this instance, the quaternary N gains a formal positive charge as it is no longer fully stabilised by surrounding π electron systems.

iv. **Nitrile**, where the N atom experiences a terminal triple bond to a single-bonded carbon.

v. **Primary amine**, where the N atom is single-bonded to a CNT lattice carbon atom in addition to two hydrogen atoms.

vi. **Vacancy pyridinic doping complexes**, where the N atom is directly incorporated into an aromatic 6 membered ring in the CNT lattice, resulting in lattice defects elsewhere (there are multiple configurations within this bonding regime – for example see vii).

viii. **Interstitial divalent**, where the N atom is divalently incorporated into two 6 membered rings, joining two more together in the process.

In general, the additional electron density contributed by nitrogen incorporation is said to increase the reductive character and electron donation potential of N-doped graphitic materials versus their pristine counterparts, as seen in Figure 2.24.[266] However, each different nitrogen environment also gives rise to its own unique chemical properties that influences its role in catalysis. All C—N bonds experience charge redistribution with a weak

negative charge (δ^-) over the nitrogen and a weak positive charge (δ^+) over the carbon due to the difference in their electronegativities of 3.04 and 2.55 on the Pauling scale, respectively.[227] These dipoles have been noted to facilitate the first step of the catalytic oxygen reduction reaction (ORR) over N-doped graphene catalysts, by encouraging adsorption of O_2 to begin the process. In electrochemical ORR catalysis, dipoles aid the process further by the increasing in the local density of states around the Fermi level of N-doped graphitic carbons.[227] This facilitates charge transfer to the adsorbed O_2 molecule, reducing the energy barrier to dissociation. Graphitic/quaternary nitrogen is the most active in this facilitation of the ORR reaction, while pyridinic and pyrrolic nitrogen are noted to be less active. This is attributed to the presence of lone pair electrons in pyridinic and pyrrolic nitrogen, which hinder the initial adsorption of O_2 at the catalyst surface.[227] Graphitic nitrogen has been observed to be the most chemically stable of the three nitrogen environments.[267] Dipoles in the NCNT lattice also enhance interactions between NCNT and numerous solvents, notably causing them to disperse more readily than pure CNT.[268]

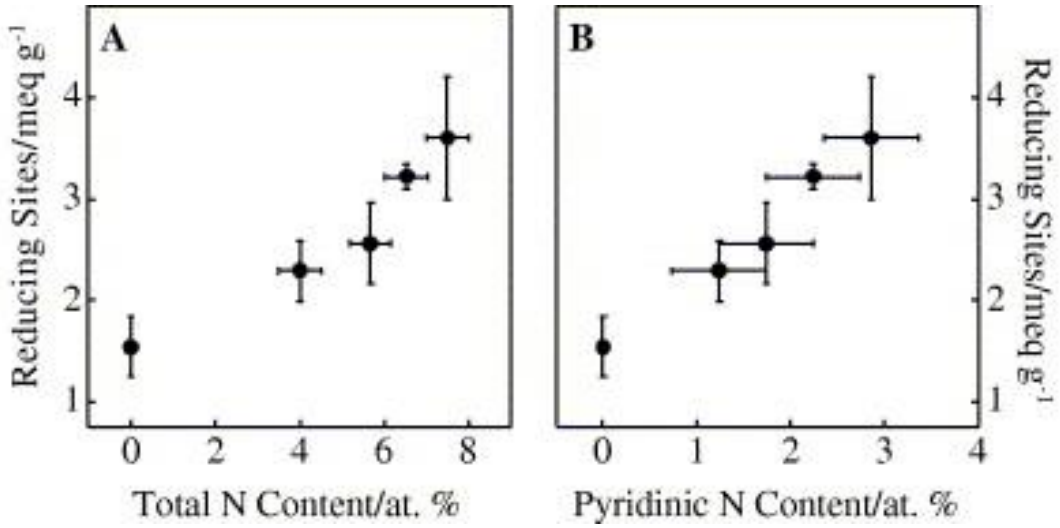

Figure 2.24. Number of reducing sites (meq g^{-1}) versus (A) total nitrogen content and (B) pyridinic nitrogen in NCNTs as determined by iodometric analysis. Reproduced from reference 266.

The aforementioned bonding modes and local C—N dipoles in NCNT represent attractive features to be exploited for novel chemical and catalytic applications. However, the vacancies and defects resulting from imperfect incorporation of nitrogen into the sp^2 lattice result in a decrease in the overall crystallinity, thermal and chemical stability of NCNT compared to similar pristine CNT.[262, 266, 269, 270] Common nitrogen concentrations reported for NCNT-based materials range from 1-10 at. %, with increasing nitrogen concentration resulting in decreased thermal stability of the material.[206, 262, 266, 270] It is therefore necessary

to balance the required stability of the NCNT material with the desired reactivity of its nitrogen sites in order to develop NCNT-based catalysts that are both active and durable.[271]

2.5.2. NCNT synthesis methods and mechanism

Nitrogen doping in CNT materials can be achieved by either *in situ* or post-treatment doping techniques.[187, 262] *In situ* techniques incorporate nitrogen directly into the CNT lattice during synthesis, while post-treatment techniques rely on surface modification of already-synthesized CNT. Whenever necessary in this thesis, N-doped CNT synthesised via *in situ* methods will be referred to as NCNT, while post-doped CNT will be referred to as N-CNT for clarity, though no formal distinction in naming convention has been made in literature. Common *in situ* synthesis methods are similar to the standard CNT synthesis techniques discussed above (e.g. CVD,[206] arc-discharge,[272] solvo-thermal,[273] laser ablation,[274] pyrolysis[248]), where nitrogen incorporation is achieved by adding a nitrogen source to the reaction and nitrogen integration occurs during CNT assembly. Of the *in situ* doping techniques, CVD remains the most investigated due to its potential for upscaling.[271] Post-doping techniques involve exposing pristine CNT to a nitrogen source (e.g. flowing ammonia) at elevated temperatures (ca. 400-1000 °C). Pretreatment of the CNT to introduce reactive oxygen groups (e.g. with nitric acid solution) has also been reported to facilitate more thorough nitrogen doping has also been reported.[78, 187, 275]

In this work, NCNT are primarily produced via *in situ* CVD doping using ferrocene as a floating catalyst dissolved in acetonitrile as a nitrogen- and carbon-containing precursor solution. This provides the benefit of facile catalyst synthesis, but also results in the same residual iron particles embedded in the NCNT surface that can later be applied in combined RWGS/FT catalysis. While a variety of N-containing organic solvents may be used, acetonitrile has been found to be the most versatile, producing NCNT consistently across a broad temperature range.[264] NCNT synthesis in this manner functions similarly to CNT CVD synthesis as described earlier. However, it has been noted that multi-walled NCNT CVD synthesis using iron nanoparticle catalysts results in “bamboo-like” compartments or segmentation along the internal tube bore rather than the hollow tubes observed in CNT without nitrogen doping, as seen in Figure 2.25.[206, 248, 253, 254, 264, 269-271, 276, 277]

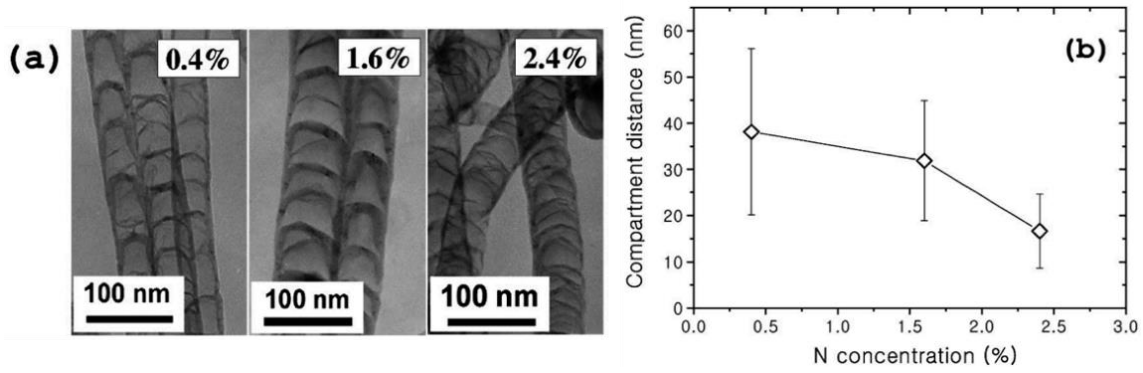

Figure 2.25. The degree of bamboo segmentation observed in CN_x nanotubes (NCNT) as a function of nitrogen content. Reproduced from reference 253.

The mechanism of formation for these bamboo-like segments is currently unconfirmed. However, results from independent studies have been corroborated to give an approximate description of the process. Several studies suggest that nitrogen acts as a surfactant during CNT growth, improving diffusion of carbon through the catalyst particle by reducing the energy barrier to diffusion.[278, 279] It is suggested that this results in partial encapsulation of the catalyst particle by the graphitic structure. Continued diffusion of carbon and nitrogen into the particle results in increasing strain in the graphitic shell until the particle is forcefully ejected from the shell, allowing for the process to be repeated as seen in Figure 2.26.[265] Bamboo-like structure is observed primarily in NCNT grown over iron catalysts, which has been suggested to be an effect of the stability of iron carbides, which may form favourably as carbon diffusion is enhanced along the exterior of the particle.[264, 266] This is said to reduce the vertical growth rate of NCNT relative to CNT, as it inhibits vertical carbon extrusion from the particle as more carbon is incorporated into the graphitic bamboo shell structures.[280]

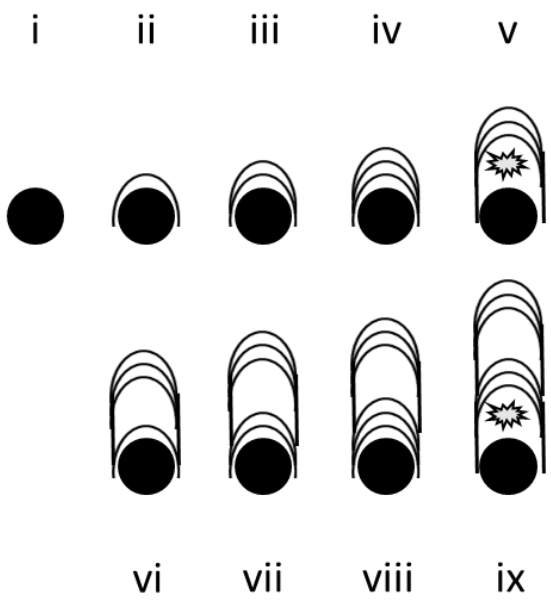

Figure 2.26. Proposed mechanism for the formation of bamboo-like segmentation in NCNT synthesised via CVD. Inspired by reference 265.

Controlling the individual properties of NCNT during CVD synthesis remains challenging. As with CNT, the individual properties of NCNT are significantly dependent upon each other such that altering a synthesis variable to target one material property is likely to influence numerous characteristics of the final product. In addition to all of the variables that must be considered when attempting to control the properties of pristine CNT during synthesis, NCNT synthesis requires the consideration of additional variables such as overall nitrogen content and the concentrations of each different nitrogen environment.[227, 280] Some progress has been made in targeting control of these properties. Several studies have shown that increasing temperature decreases the total nitrogen content (C/N ratio) of the NCNT product.[206, 264] This is attributed to the difference in ΔG_f for the relevant metal nitrides and carbides, with carbides becoming relatively more favourable at higher temperatures.[264] Increasing temperature has also been shown to increase the average tube diameter and decrease both nitrogen content and the ratio of pyridinic-to-graphitic nitrogen observed in the final product.[206, 264] Ferrocene concentration in the precursor solution has also been noted to influence nitrogen incorporation in NCNT. In NCNT grown via CVD of a ferrocene-in-acetonitrile precursor solution, increasing ferrocene concentration was shown to decrease the length and nitrogen content of the final product.[277] In NCNT grown via CVD of a ferrocene-in-pyridine precursor solution with added NH_3 in the carrier gas, increasing the NH_3 concentration during synthesis was shown to increase both the nitrogen and residual iron content of the final product.[266]

2.5.3. RWGS and FT over NCNT-supported iron particles

The reactivity of iron nanoparticle catalysts supported on N-doped CNT materials has been investigated in literature for the conversion of CO and CO_2.[78, 79, 227, 275] Notably, Lu *et al.* investigated the promoting effect of nitrogen doping into MWCNT on pure FT over supported iron nanoparticles.[281] NCNT with 3-5 at. % nitrogen with a ca. 1:1 ratio of graphitic and pyridinic N were synthesised via CVD and purified to remove the iron, cobalt and Al_2O_3 growth catalyst via reflux in 6M NaOH and 6M HCl solution at 110 °C for 4 h. Iron loadings of 2-15 wt. % were then achieved via incipient wetness of the desired amount of iron nitrate dissolved in distilled water, resulting in a particle size of ca. 7-8 nm. Nitrogen doping was observed to result in increased reducibility, basicity, activity, stability and olefin selectivity relative to a similarly prepared pristine CNT-based catalyst using 100 mg of catalyst at 300 °C, 1 bar, 4200 mL h^{-1} g^{-1}, and $H_2/CO = 1$. The increased activity and olefin selectivity were attributed to the intrinsic basicity of the nitrogen sites, which enhances CO adsorption and dissociation at the catalyst surface while encouraging desorption of short olefins. The enhanced reducibility of the N-doped catalyst was also credited for its improved activity due to easier formation of the FT-active Hägg carbide iron species (χ-Fe_5C_2). The enhanced stability of the catalyst was attributed to the anchoring effect of the nitrogen sites on the deposited catalyst particles, stabilising them against deactivation via coarsening.

Xiong *et al.* performed a similar investigation into the pure FT activity of iron particles supported on an N-CNT material.[275] The N-CNT support was produced by bubbling acetonitrile vapour over pristine CNT using an argon carrier gas at 100 sccm and temperatures of 700-900 °C, yielding N-CNT with a nitrogen content of 0.7-6.5 at. % and a ratio of ca. 3:1 graphitic to pyridinic N. Prior to nitrogen doping, the pristine CNT substrate had been grown in-house and purified of its iron, cobalt and $CaCO_3$ growth catalyst via treatment in 30% HNO_3 solution for 2 hours at room temperature. To achieving iron doping, the as-produced N-CNT supports were first further acid-treated under mild (30% HNO_3 at room temperature for 2 hours) and harsh (55% HNO_3 at 120 °C for 2 hours) conditions to introduce oxygen functionalities as further anchoring sites for the deposition of catalytic iron particles.[187] 10 wt. % iron doping was then achieved by dissolving the requisite amount of $Fe(NO_3)_3 \cdot 9H_2O$ and urea (1.5 mol per mol of Fe) in 20 mL deionised water and stirred for at 90 °C for 2 hours to allow for hydrolysis of the urea before drying. N-doping and harsh acid treatment were observed to decrease particle size while increasing dispersion, activity, olefin selectivity and C_{5+} selectivity. The increased activity and selectivity were attributed

to the smaller particle size (ca. 6 nm) and improved adsorption and dissociation of CO at the catalyst surface. Interestingly, N-doping decreased the reducibility of the material in this instance.

Finally, Chew *et al.* investigated the activity of iron nanoparticles supported on N-CNT materials in full RWGS/FT CO_2 hydrogenation following initial studies on pure FT over similar materials.[78, 162] The N-CNT support was produced via nitric acid vapour treatment of commercially-obtained pristine MWCNT at 200 °C for 24 hours to introduce oxygenated anchoring sites.[282] The oxygenated CNT were then treated under flowing ammonia (10 vol% NH_3 in He) at 400 °C for 6 hours to produce N-CNT with a nitrogen content of ca. 5.9 at. %, though the concentration of specific nitrogen environments was not stated. A theoretical iron loading of 40 wt. % was achieved via dry impregnation of ammonium ferric citrate in aqueous solution for 1 hour, resulting in iron particles of ca. 8-10 nm. N-doping was observed to increase reducibility, activity, olefin selectivity and C_{5+} selectivity relative to similar O-doped materials and an Fe/SiO_2 catalyst, though in many cases performance between the O-doped and N-doped samples were within a reasonable margin of error, and no comparison with pristine CNT-supported materials was provided.

These reports provide a valuable starting point to begin an investigation into the effect of nitrogen doping on the catalytic performance of CNT-supported iron particles on combined RWGS/FT CO_2 hydrogenation. Indeed, they suggest that nitrogen doping may be a valuable tool in enhancing the activity of these materials through enhanced particle-support interactions. However, existing studies remain limited in number, scope, comparability, and effective integration of the nitrogen, iron, and CNT support in the catalyst. The current state of the literature does little to account for the unique influence of different nitrogen environments in the CNT support, the limited integration between iron, nitrogen and the CNT support, and the mechanistic influence that nitrogen incorporation might have in the presence of competing simultaneous CO and CO_2 conversion reactions at the catalyst surface.

2.6. **Fe@CNT and derivative materials**

The work in this thesis builds upon previous studies of the Fe@CNT CO_2 hydrogenation catalyst,[70-72, 116] which relies on the residual iron nanoparticles used to catalyse the growth of MWCNT as active sites for combined RWGS/FT CO_2 reduction. The catalyst incorporates synergistic properties from iron nanoparticles, MWCNT supports,[70] and RWGS/FT chemistry.[68, 69] This affords a catalyst with a simplified manufacturing method,[72] and novel, noteworthy activity towards the reduction of CO_2 to hydrocarbons.[70-72] The investigations detailed in this thesis build upon these existing studies by determining the effect of nitrogen doping into the MWCNT support upon the activity of the N-doped catalyst (Fe@NCNT) in CO_2 hydrogenation. This section summarises the findings of previous publications from the University of Bath regarding the synthesis and catalytic activity of the Fe@CNT catalyst. Previous literature studies concerning the synthesis of similar Fe@NCNT-type materials are also summarised. While in theory any N-doped CNT produced via a typical iron-based FCCVD method might be considered as Fe@NCNT-type materials, there are no other reports in literature of the residual iron particles embedded in these materials being exposed and exploited for further reactivity. As such, this work constitutes the only example of turning these Fe@NCNT-type materials into the fully-realised Fe@NCNT catalyst by harnessing their iron particles as catalytic sites for CO_2 hydrogenation and other sustainable catalytic processes.

2.6.1. Fe@CNT

Investigations into the Fe@CNT CO_2 hydrogenation catalyst were originally published by O'Byrne *et al.* in 2013.[70] The catalyst was produced via an aerosol-assisted chemical vapour deposition method, resulting in a powder consisting of forests of MWCNT with residual iron catalyst growth particles embedded into their wall structure rather than doped onto the surface as had been previously reported. The particle diameters were noted to be ca. 31 ± 12 nm with tube diameters on the order of 25-75 nm. After CVD synthesis, the residual iron particles were noted to be obscured beneath a layer of graphitic carbon, which could be removed via thermal activation in air (as seen in Figure 2.27), thereby significantly increasing the activity of the catalyst.

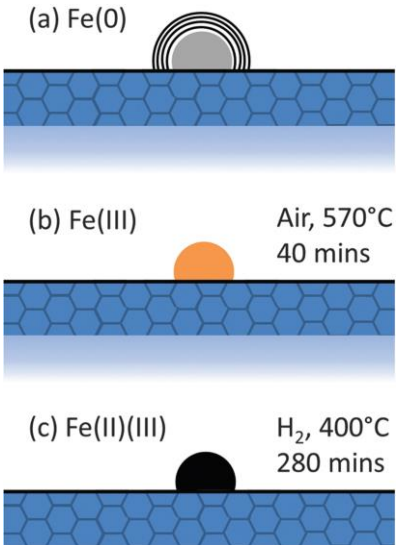

Figure 2.27. Oxidation states of (a) untreated iron nanoparticle coated in graphitic carbon (not to scale), (b) thermally oxidised nanoparticle with carbon layers removed, and (c) reduce particle treated with H_2. Reproduced from reference 70.

This deep integration of the catalytic iron particles and their MWCNT support materials resulted in notably superior CO and CO_2 hydrogenation performance relative to other Fe/C catalysts reported at the time.[70] This was attributed to improved hydrogen spillover from the metallic particles onto the CNT surface facilitated by the bridged connection between the CNT support and iron particles, thereby enhancing the reducing capabilities of the catalyst. The catalyst was analysed via SEM, TEM, EDS and XPS to elucidate the clear structure of Fe@CNT material and confirm the iron phases present during catalyst synthesis, activation, reduction and reaction. The catalyst was observed to consist of ca. 0.2 and 1.0 at. % iron loading at the surface, before and after activation, respectively, indicating the successful removal of the graphitic layer that initially obscured them. The phases of the iron were identified as predominantly metallic iron after synthesis, Fe(III) after activation, and a mixture of Fe(II) and Fe(III) after reduction. Tests were conducted using 0.4 g Fe@CNT powder in a packed bed reactor at 370 °C under a total flowrate of 8 sccm and a CO_2:H_2 ratio of 3:1 after an initial reduction under 50 sccm H_2 at 400 °C and atmospheric pressure for 3 hours.

Subsequent investigations into the Fe@CNT catalyst centred around supporting the catalyst on a cordierite monolith to improve process efficiency after initial investigations using a powder packed bed.[116] Mounting the Fe@CNT onto the cordierite monolith support was successfully achieved by using the cordierite monolith as a substrate during CVD synthesis, as seen in Figure 2.28. This was followed by a shorter thermal activation to avoid fully oxidizing away the thin Fe@CNT layer.

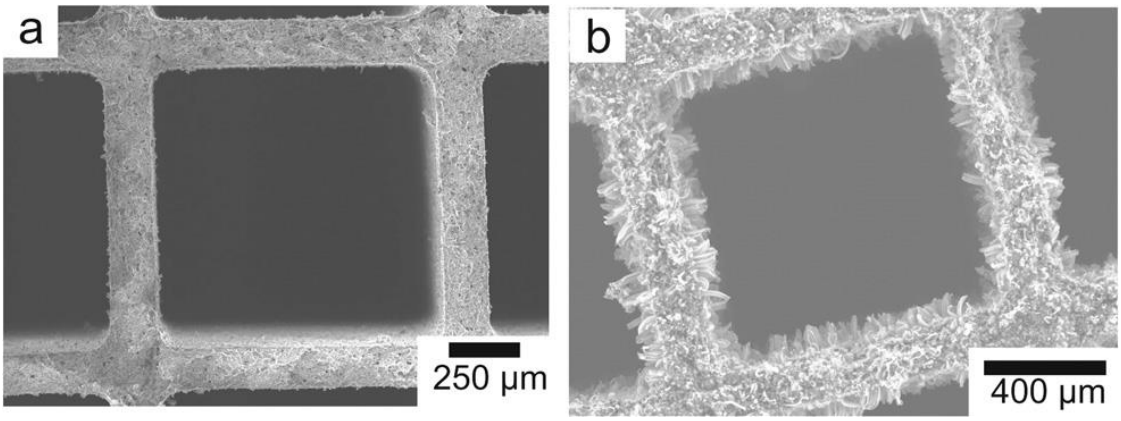

Figure 2.28. SEM micrographs of (a) bare cordierite monolith and (b) cordierite monolith coated with CNT layer. Reproduced from reference 116.

Fe@CNT-monoliths were determined to be stable at temperatures significantly above typical reaction conditions via TGA, with decomposition occurring above 500 °C under H_2 and above 600 °C under CO_2. CO_2 conversion performance was observed to suffer compared to the powder packed bed at atmospheric pressure, though similar conversions and superior rates of reaction were achieved at elevated pressures. Beyond the pressure of 7.5 bar, conversion did not increase further and the process was stated to become mass transfer limited rather than rate limited. Furthermore, catalyst stability was tested for 15 hours time on stream, during which conversion was observed to decrease by ca. 30%, though no shifts in product distribution were reported. This deactivation was attributed to a mixture of carbon deposition and iron particle sintering, as sulphur poisoning and conversion of the active phase could be excluded with some confidence, though conclusive evidence for any of these deactivation processes could not be established. Interestingly, *in situ* pXRD analysis of the monolith-supported catalyst revealed that a significant amount of Fe(0) was formed after the reduction step rather than the previously reported mix of Fe(II) and Fe(III). This was attributed to the greater penetration of pXRD into the sample relative to previous XPS studies, combined with the enhanced reducibility of iron particles encapsulated within the MWCNT at temperatures where particles supported on the tube exterior remain as oxides.

Prior to the investigations in this thesis, the most recent publication concerning the Fe@CNT catalyst was published by Mattia *et al.* in 2015 and consisted of efforts to optimise reaction conditions for the powder packed bed catalyst, as seen in Figure 2.29. Investigations into the effect of doping a variety of promoter metals onto the catalyst surface were also detailed and concluded with a full life cycle assessment (LCA) of the Fe@CNT to determine their real-world feasibility.[72] Ideal reaction conditions were confirmed to be a reaction temperature of

370 °C, flowrate of 8 sccm, reduction pressure of 5 bar, and reaction pressure of 7.5 bar. The target parameters for optimization were CO_2 conversion and selectivity towards (preferably long-chain) hydrocarbons. These findings served as a basis for determining the reaction conditions applied in this thesis. A variety of promoter metals were doped onto the surface of the Fe@CNT, including Na, K, Cs, Mg, Ca, Mn, and Pd. Of these, Na resulted in a desirable increase in CO_2 conversion and C_{5+} selectivity, though CO selectivity was also enhanced.

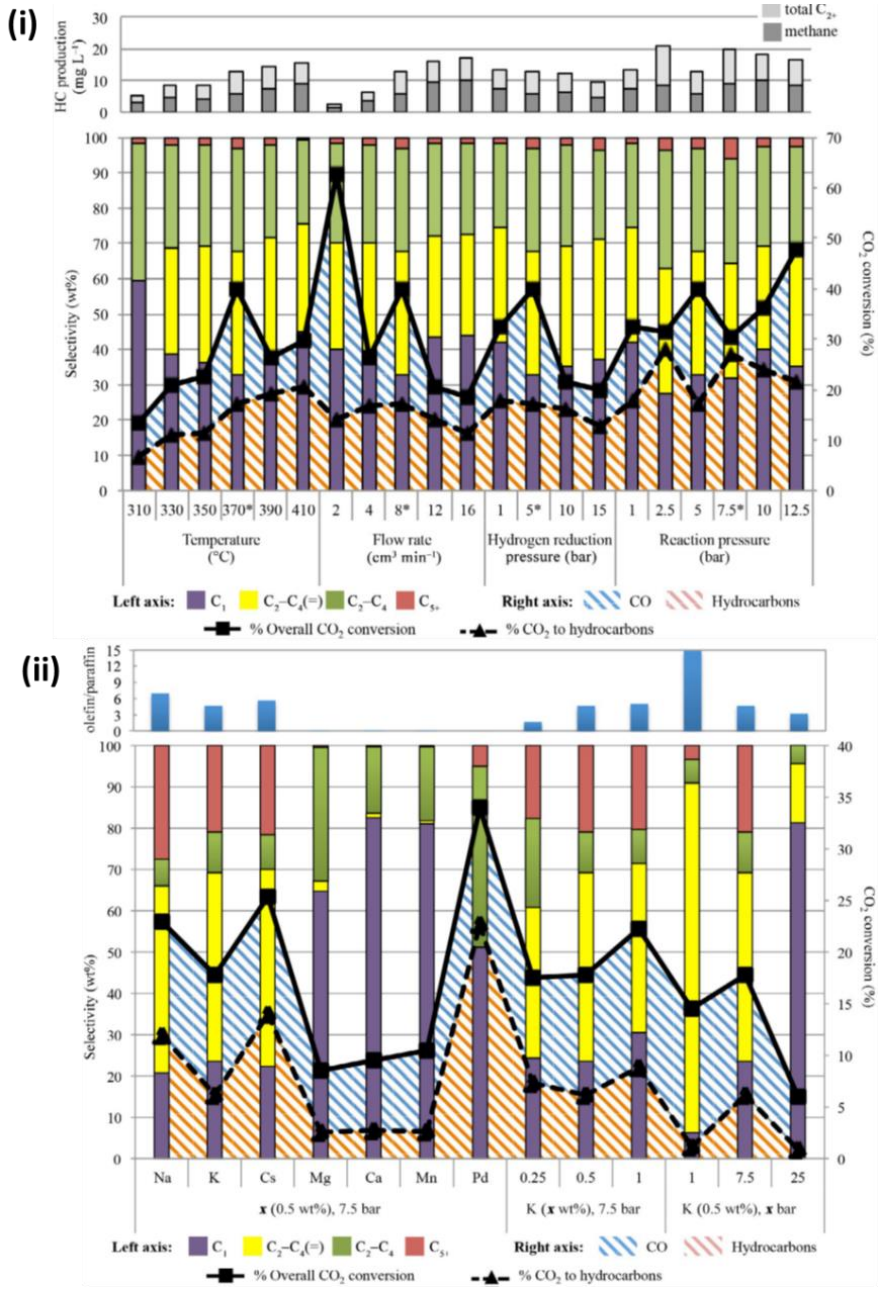

Figure 2.29. (i) CO_2-to-hydrocarbon conversion performance under a variety of reaction temperatures, flowrates, reduction pressures and reaction pressures. (ii) CO_2-to-hydrocarbon conversion performance when upon doping of the Fe@CNT with a variety of promoter metals at different metal loadings and pressures. Reproduced from reference 72.

The results of the LCA indicated that the impacts of materials sourcing, catalyst production and process operation could be approximately balanced by their offset in CO_2 mitigation. However, it was also overwhelmingly demonstrated that the renewable energy sources must be used to drive the process at an industrial scale in order for CO_2-neutral energy storage to be feasible.[72] The outcomes of these LCA studies are presented in Figure 2.30.

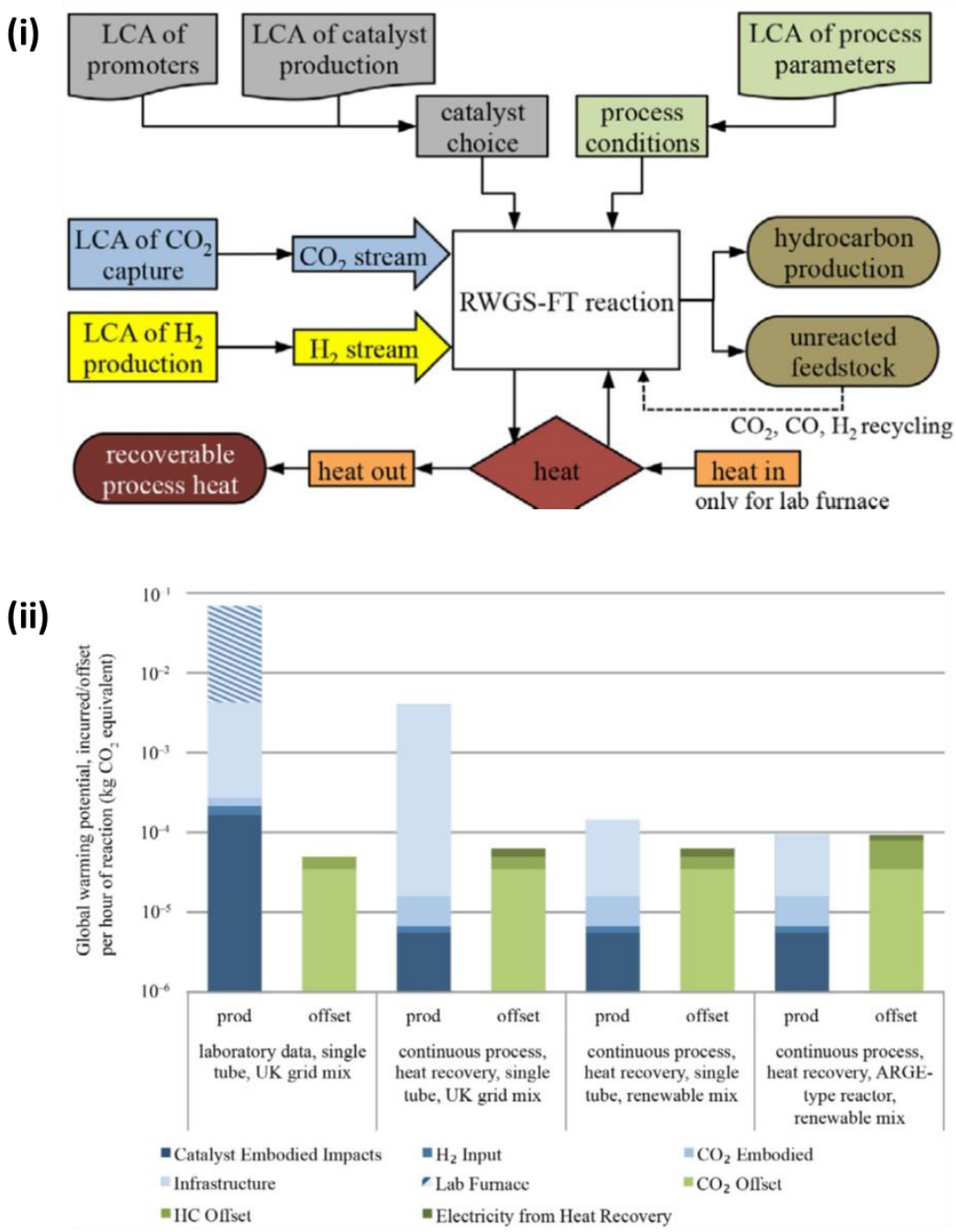

Figure 2.30. (i) Overview of LCA inputs and outputs when evaluating the environmental viability of the Fe@CNT-driven CO_2 conversion process. (ii) LCA results for the Fe@CNT-driven CO_2 conversion process showing the impact of catalyst production and process operation relative to the offset generated by the process at different scales and using different energy sources. Reproduced from reference 72.

2.6.2. Previous examples of Fe@NCNT

This thesis describes continued research into the Fe@CNT catalyst by exploring the effect of chemically modifying the underlying MWCNT support in RWGS/FT for the conversion of CO_2 into hydrocarbons. In order to maintain the simple synthesis and beneficial properties afforded by deep integration of the iron nanoparticles and CNT support in the Fe@CNT catalyst, any modification or substitution of heteroatoms into the CNT support structure must take place during the CVD synthesis process. Nitrogen doped Fe@CNT-type materials have been previously reported in literature.[206, 248, 253, 254, 264, 269-271, 277] Relevant findings from these studies have been summarised in detail in section 2.5. Indeed, any CNT or NCNT produced via a typical iron-based FCCVD method could be considered as Fe@CNT-type or Fe@NCNT-type materials. However, the final Fe@CNT or Fe@NCNT catalyst is defined by having suitably high enough iron content in the CVD precursor solution to generate a significant number of residual iron particles along the grown CNT, as well as the subsequent exposure of these iron particles from beneath the graphitic carbon layer to act as catalytic sites. To the best of our knowledge there are no known examples of the activated residual iron particles in Fe@NCNT-type materials being applied in thermochemical catalysis. As such, these studies constitute the first example of investigations into the reactivity of the fully realised Fe@NCNT catalyst.

Chapter 3 – Aims and objectives

3.1. Aims

The aim of the research detailed in this thesis was to contribute to the body of knowledge surrounding the catalytic conversion of CO_2 into chemical fuels. More specifically, it was intended to contribute to the development of novel and improved catalytic materials for the direct hydrogenation of CO_2 via coupled RWGS/FT chemistry. These aims were pursued by further iterating upon the material properties of the previously-published Fe@CNT catalyst, particularly through *in situ* nitrogen doping in the CNT support material. Desirable outcomes of these experiments included the successful production of novel CO_2 hydrogenation materials, improved catalyst activity in the RWGS/FT process, increased yield of high value olefins or long-chain hydrocarbons, and an improved understanding of the thermodynamic, kinetic, and mechanistic effects governing RWGS/FT chemistry.

3.2. Objectives

In order to achieve the aims of the research detailed in this thesis, a series of objectives was defined. These short, medium, and long-term objectives served to guide our research efforts and deconstruct the overarching aims of this project by categorising them into a series of approachable, related, and sequentially organised goals. The objectives of this research project have been outlined below:

Short-term objectives

- Achieve consistent synthesis of Fe@CNT and Fe@NCNT on a scale that is suitable for CO_2 hydrogenation testing
- Construct a suitable high-pressure CO_2 hydrogenation reactor
- Establish a reliable method for analysing and quantifying the products of CO_2 hydrogenation experiments via GC-MS
- Fully characterise the Fe@NCNT material to achieve a baseline understanding of its physical morphology and chemical composition
- Establish a suitable protocol for activation of the Fe@NCNT material to expose the embedded iron particles from underneath their graphitic layers for catalysis

Medium-term objectives

- Establish repeatability of previously published CO_2 hydrogenation data over Fe@CNT using the newly constructed high-pressure reactor
- Obtain an initial comparison of the reactivity of Fe@CNT and Fe@NCNT
- Determine the influence of reaction conditions upon the RWGS/FT process over Fe@NCNT
- Conduct a screening of potentially appealing promoter metals to identify desirable reactivity or synergistic effects arising from cooperation between the N-doping in the catalyst support and surface-doped promoter metals

Long-term objectives

- Fully characterise promising materials identified during promoter screening experiments
- Conduct further in-depth catalytic investigations of promising materials identified during the promoter screening studies (e.g. design of experiments targeting reaction conditions and promoter loading) for optimisation of desirable properties
- Investigate the mechanistic influence of N-doping upon the RWGS/FT process over Fe@NCNT
- Explore further *in situ* catalyst composition control methods (e.g. particle size and nitrogen content) to establish techniques for tuneable catalyst manufacturing

Logically defining and pursuing these objectives was critical in guiding research efforts and ensuring consistent, incremental progress during this project.

Chapter 4 – Materials and methods

This exploration of the catalytic conversion of CO_2 to hydrocarbons relies on a variety of synthetic and analytical techniques to develop and characterize novel catalytic materials, and assess their efficacy in catalysing RWGS/FT chemistry. This chapter summarizes the theory behind the techniques employed throughout this research and describes the specific methodologies employed during materials synthesis and catalytic testing.

4.1. Catalyst synthesis and characterisation

4.1.1. Chemical vapour deposition

CVD is a commonly employed laboratory and industrial scale technique for the synthesis of a wide variety of solid materials such as CNTs, graphene and thin films. In CVD processes, gaseous or vaporized reagents are dissociated, deposited and reacted in their atomized form over a heated or activated substrate surface such as quartz. This produces highly pure product materials with control at the atomic or nanometre scale, through the homogeneous reaction of gas phase reagents and/or the heterogenous chemical reactions that occur on or near the surface of the activated substrate.[283]

In this work, CVD was the most heavily employed materials synthesis technique for the production of Fe@CNT and Fe@NCNT. To produce Fe@CNT, 1.0 g ferrocene (FcH) was dissolved in 50 mL toluene to produce a CVD precursor solution of concentration 20 mg mL^{-1} FcH in toluene. 40 mL of the precursor solution was then injected at a rate of 10 mL h^{-1} into a quartz tube (25 mm ID × 28 mm OD × 122 cm L), loaded in a tubular furnace at 790 °C under a flow of 50 sccm H_2 and 400 sccm Ar. A schematic representation of this process is presented in Figure 4.1.

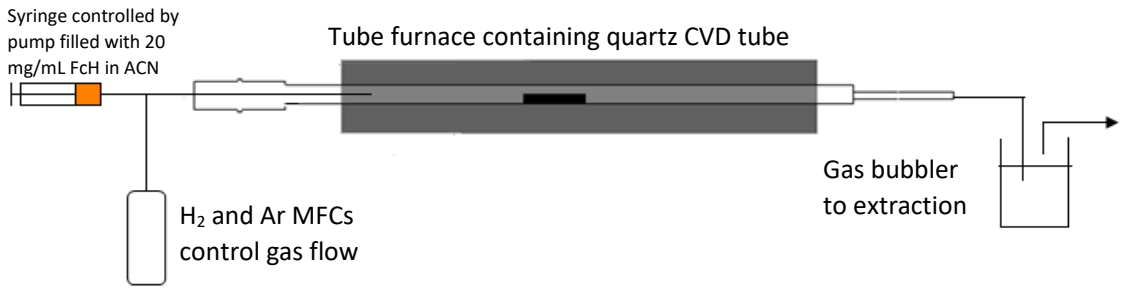

Figure 4.1. Schematic of a the Fe@NCNT synthesis process in the tubular CVD reactor.

After 4 hours of CVD injection, the raw catalyst was readily retrieved from within the quartz tube by scratching the interior cavity of the quartz tube with an elongated spatula. While the quartz tube itself was ca. 120 cm long, Fe@NCNT were only grown between 35-55 cm from the inlet of the tube, corresponding to the region of the tube located in the hot zone of the furnace. While black carbonaceous deposits were clearly visible along a greater length of the tube, these have been shown to consist of graphitic and amorphous carbon rather than CNT due to inadequate temperatures for CNT synthesis outside of the hot zone. A 40 mL injection synthesis typically yielded ca. 1.5 g of catalyst. To minimize error due to variance between catalyst batches, a stock of ca. 10 g was produced before beginning catalytic trials, and progressively topped up every 3 reactions.

In this synthesis process, the FcH and toluene solution acts as a carbon and iron source, and the argon acts as an inert carrier gas to deposit the vaporized solution evenly along the interior of the quartz tube. The hydrogen gas assists in the high temperature decomposition of the FcH in the vaporized solution. This results in the deposition of iron nanoparticles along the quartz surface. These iron particles form a solid solution, allowing them to dissolve carbon from the vaporized precursor to nucleate the growth of the Fe@CNT.[185] Thus, in order to produce Fe@NCNTs, the same experimental procedure was employed with the sole exception of replacing toluene in the precursor solution with acetonitrile (ACN) to act as a source of both carbon and nitrogen during the CNT growth process, resulting in a nitrogen-doped CNT support structure.

4.1.2. Catalyst wet impregnation

Impregnation has been commonly used to load catalytic species onto or into porous materials to produce a wide variety of supported catalysts,[284] and is often a first choice when attempting to synthesize or screen novel supported catalysts due to its simplicity in execution, scalability, and the relatively small amount of waste produced.[285] The technique can be broadly categorized into two notable variants, namely standard wet impregnation (WI) and pore volume impregnation (PVI), sometimes also referred to as incipient wetness impregnation (IWI) or dry impregnation (DI). All impregnation techniques rely on the initial preparation of a catalyst- or precursor-containing loading solution, in which the desired amount of catalyst (e.g. pre-synthesized metal nanoparticles) or catalyst precursor (e.g. an inorganic metal salt) is dissolved or dispersed according to the desired metallic loading of the final supported catalyst material. This loading solution is then mixed with the desired

amount of the porous support material to decompose the catalyst precursor and deposit the catalytic species onto the surface of the support (e.g. by initial sonication to aid in dispersion of the materials, following by an extended stirring period; often 24-48 hours). The resulting mixture is then dried to remove the solvent, leaving behind the supported catalyst as a product. The most commonly used solvent for inorganic salts is water because of the high solubility of many precursors. Methanol is also employed due to its beneficial solubility. To prevent premature deposition of the metal precursor in bulk solution, concentrations below (super)saturation are required.[285]

In standard WI, the amount of solvent used is in excess to the pore volume of the support material, resulting in a mixture that is more easily stirred but contains a relatively lower concentration of the catalyst or precursor compared to PVI. In PVI, the amount of solvent used to prepare the loading solution matches the pore volume of the support material (this volume is often experimentally determined by adding pure solvent to the desired amount of the support material dropwise, observing its absorption into the support until saturation has been reached and slight pooling is observed on the surface). This results in a thick, dry slurry containing a relatively higher concentration of the catalyst or precursor compared to standard WI. Which method should be chosen depends on the solubility of the catalyst or precursor in the chosen solvent, and the desired properties of the resulting catalyst, as the strong capillary forces acting on the high concentration loading solution in PVI can assist in depositing catalytic species more deeply into the porous support.[285]

In this work, standard WI was used to dope promoter metals such as ruthenium and sodium onto the surface of pre-synthesized Fe@NCNTs prior to activation. It was also used to dope iron nanoparticles of various sizes and morphologies onto commercially obtained carbon nanotubes and a variety of novel porous support materials. WI was chosen over PVI to ensure that all of the chosen metal precursors and nanoparticles were evenly dissolved and dispersed through prolonged stirring with the catalyst support to minimize the effect that differences in solubility and particle size might have on the impregnation process. Additionally, because RWGS/FT catalysis takes place primarily at the exterior surface of the nanotube support, rather than in the internal cavity, increased metal impregnation inside the nanotubes through PVI was not a desirable outcome.

To deposit promoter metals onto the surface of existing Fe@NCNTs, a variety of potentially beneficial promoters was first identified. Promoters were primarily evaluated by their

potential to increase the α values and olefin-paraffin ratios of our product distributions in combined RWGS/FT catalysis. Precursor salts of these metals corresponding to 0.5 wt. % promoter metal loading were then dissolved into 15 mL of either water or methanol, depending on the solubility of the precursor salt, and stirred for 24 hours with 0.5 g Fe@NCNT. The product was then heated at 115 °C for 2 hours to ensure the removal of any remaining solvent after stirring. The salts, solvents and weights employed have been summarized in Table 4.1.

Table 4.1. Summary of salts, solvents and loadings used in Fe@NCNT promoter screening.

Salt	Solvent	Loading /mg (0.5 g Fe@NCNT, 0.5 wt. %)
$Co(NO_3)_6.6H_2O$	methanol	12
$LiOAc.2H_2O$	methanol	24
$Pd(OAc)_2$	methanol	5
$RuCl_3$	methanol	11
Cs_2CO_3	water	6
$NaHCO_3$	water	9
$InCl_3$	water	5

To deposit pre-synthesized iron oxide nanoparticles onto the surface of pristine commercial carbon nanotubes (Sigma-Aldrich, MWCNT 50-90 nm diameter), the nanotube support first had to be oxidized with nitric acid to aid in their dispersion and provide anchoring sites for the subsequent iron nanoparticle doping step. 0.5 g CNT was dispersed in 200 mL 6 M nitric acid solution and stirred for 24 hours. The resulting slurry was collected and washed with deionised water under vacuum filtration until the washings were pH neutral. The solid was then washed again with toluene to remove any remaining water and dispersed in toluene with 5 wt. % of the desired iron particles. Fe_2O_3 was the primary species used for a brief study of the relationship between particle morphology and RWGS/FT activity. For Fe_2O_3 particles, a loading of 35 mg was used per 0.5 g CNTs to ensure that the amount of iron metal being added was equal to 5 wt. %. After stirring for 48 hours the slurry was collected again washed with acetone under vacuum filtration before being left to dry at 60 °C overnight.

4.1.3. Brunauer-Emmett-Teller surface area analysis

Surface area analysis measures the specific surface area (total surface of the material per unit of mass or volume) and pore size distribution of a material by employing the BET model. This provides a model for the monolayer physical adsorption of gas molecules on a solid surface, and follows from the Langmuir theory for monolayer molecular adsorption, extending it to multilayer adsorption under three key hypotheses. Namely, that gas molecules physically adsorb on a solid in layers infinitely, that gas molecules only interact with adjacent layers, and that the Langmuir theory can be applied to each layer, as seen in Figure 4.2.

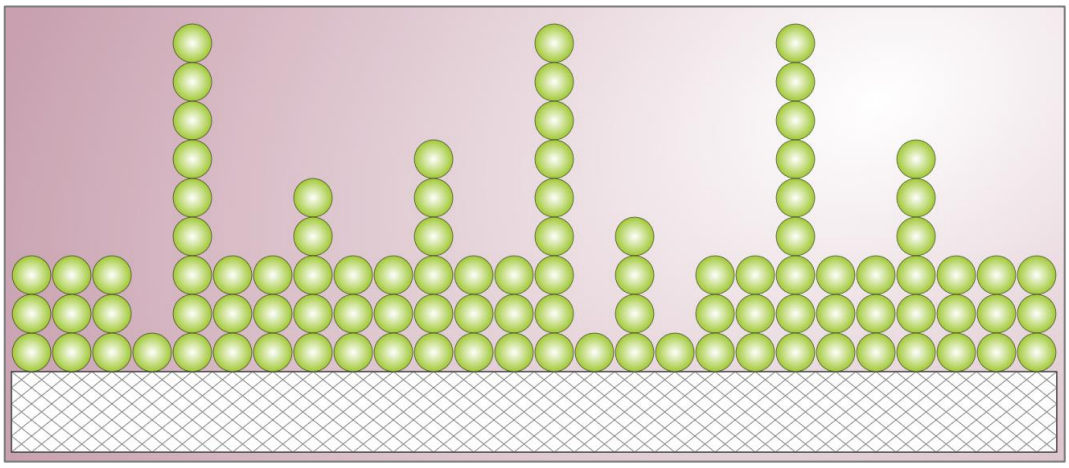

Figure 4.2. Multilayer gas adsorption on a solid surface, as modelled by BET theory. Reproduced from reference 286.

This gives rise to the BET isotherm equation (Equation 4.1), which allows for the surface area of the sample to be determined from the adsorption cross section of the adsorbing species.

$$\frac{V}{V_{mon}} = \frac{cz}{(1-z)(1-(1-c)z)}$$

Equation 4.1. The BET isotherm equation, where V is the adsorbed gas quantity, V_{mon} is the monolayer absorbed gas quantity, c is a constant which is large when the enthalpy of desorption from a monolayer is large compared with the enthalpy of vaporization of the liquid adsorbate, and $z = \frac{p}{p_0}$, where p is the equilibrium pressure and p_0 is the saturation pressure.

In this work, BET surface area analysis was used to determine the specific surface area of Fe@CNTs and Fe@NCNTs to compare their physical properties, as these may be useful in understanding the causes for similarities and differences in their catalytic activity. It is worth noting that it was difficult to assess the significance of surface area with respect to the reactivity of these materials, as it is unclear how much reactivity occurs on the outer surface of the nanotube versus inside the tube cavity. Surface area analysis was conducted in

conjunction with collaborators at the University of Bari, using a Pulse ChemiSorb 2750 Micromeritics instrument with N_2/He as a carrier gas at 273 K followed by heating to 923 K.

4.1.4. Raman spectroscopy

Raman spectroscopy is a powerful spectroscopic technique that allows changes in molecular state to be explored by examining the frequencies present in the radiation scattered by subject molecules. In Raman spectroscopy, an incident photon is scattered from a molecule with either an increase in frequency (if the radiation gains energy from the molecule) or with a lower frequency (if it loses energy to the molecule) to give the anti-Stokes and Stokes lines, respectively, as seen in Figure 4.3. Scattering without changes in frequency result in Rayleigh lines.[287] The difference between the frequencies of the scattered and incident radiation is determined by the transitions that take place within the molecule as a result of the impact of an incoming photon, and can thus be used to study molecular rotations and vibrations.

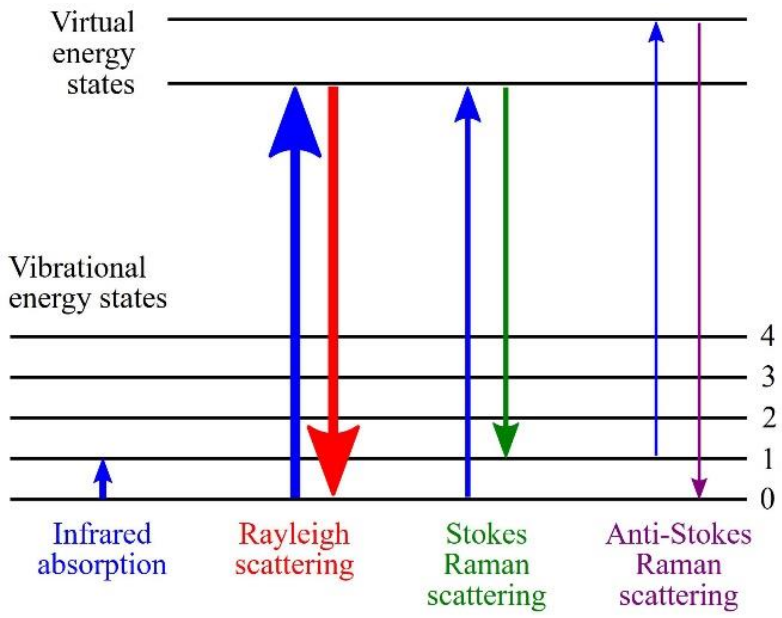

Figure 4.3. Energy level diagram representing the transitions observed in Raman spectroscopy. Line thickness in the transition arrows is roughly proportional to signal strength. Reproduced from reference 288.

Raman spectroscopy of carbon nanotubes can yield significant information regarding the structure, purity and integrity of a given sample by considering the relative magnitudes of several characteristic vibrations. These vibrations include the radial breathing mode (RBM) at ca. 200 cm^{-1}, the D band at ca. 1340 cm^{-1}, and the G' band at ca. 2600 cm^{-1}, as seen in Figure 4.4. However, the positions of these bands will shift depending on the frequency of the laser used.[289, 290]

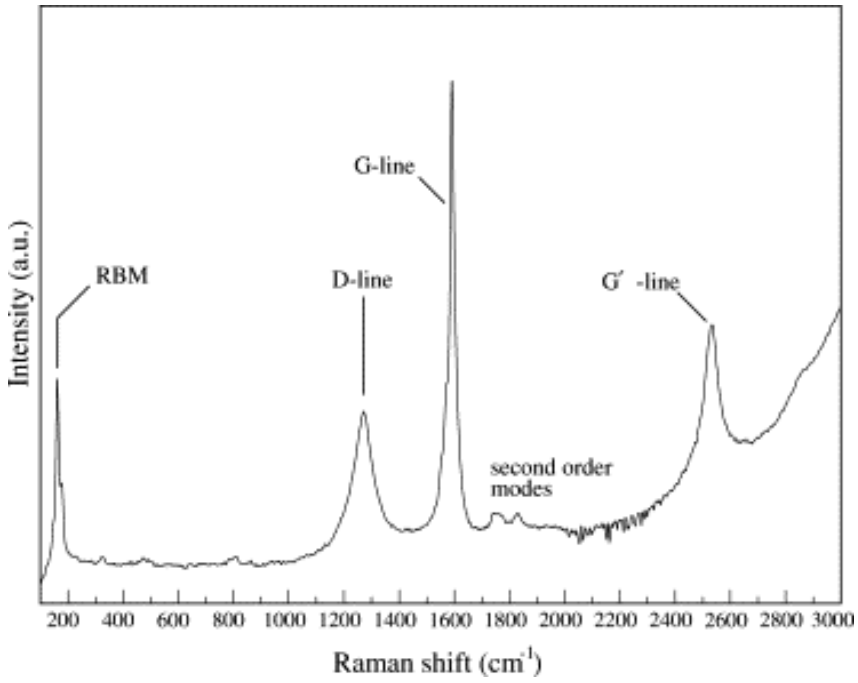

Figure 4.4. Characteristic features in the Raman spectra of CNT-based materials. Reproduced from reference 290.

The RMB is particularly characteristic of CNT with a small tube diameter of less than 2 nm. This band is thus more often observed in SWCNT, though it may also be observed in MWCNT if the inner tube diameter is less than 2 nm. However, the RMB has not been noted as a significant feature in the Raman spectra of Fe@CNT- or Fe@NCNT-based materials, as their outer tube diameters tend to range from 20-100 nm, with inner diameters typically no smaller than 10 nm. The group of peaks commonly referred to as the D band is typically associated with defects, disorder, impurities or damage to the integrity of the CNT lattice. Conversely, the group of peaks referred to as the G band corresponds to tangential vibration of the carbon atoms in a CNT sample, and thus its intensity is a good measure of graphitisation in the material. This band is seen as a single peak at 1582 cm^{-1} in graphite, with considerably lower intensity than in SWCNT and MWCNT. It is therefore possible to use the ratio of the D and G bands (often referred to as the I_D/I_G value of a sample) as a measure of the purity and integrity of the CNT lattice in a given sample, with a higher value

of I_D/I_G corresponding to greater disorder or impurity.[291] Finally, the G' band (sometimes referred to as the 2D band) is a second order harmonic overtone of the D band. The presence of this band in a sample indicates that there is long-range order in the sample, and its presence can thus be used to confirm the purity of the material as it is highly sensitive to defects in the CNT lattice. It has also been used in determining the diameter of SWCNT and MWCNT with relatively few walls.[292]

In this work, Raman spectroscopy was used to verify the successful synthesis and purity of CNT-based catalyst samples such as Fe@CNTs, Fe@NCNTs and their metal-promoted derivative materials. A Renishaw InVia system with a 532 nm laser was used to analyse all samples. For CNT-based materials, a laser power of 5% was employed with the standard exposure time to facilitate quick analysis without burning or damaging the sample during analysis. For NCNT-based materials, the laser power was reduced to 0.1% due to the decrease in the stability of the CNT lattice caused by nitrogen doping leading to significant decomposition under even 1% laser power. Consequently, the exposure time for NCNT-based samples was also increased substantially to 400 seconds to collect a clear Raman spectrum. Comparing the I_D/I_G ratios of 3 similar samples indicated a standard deviation in I_D/I_G measurements of ca. ± 0.01.

4.1.5. Scanning and Transmission Electron Microscopy

SEM and TEM are widespread microscopic techniques used in the imaging of nano- and micrometre-sized objects. Both techniques rely on bombarding the sample with a beam of electrons with a well-defined de Broglie wavelength to collect information, as seen in Figure 4.5. In SEM, this beam is focused into a fine point as small as 1 nm in diameter on the specimen surface, and scanned in a rectangular raster over the specimen. As the beam interacts with the sample, it produces secondary electrons, backscattered electrons and characteristic X-rays. These signals are collected by one or more detectors to produce the desired micrograph of the sample surface. Accelerating voltages in SEM vary from 50-30,000 volts, with a maximum resolution of approximately 1 nm.[287, 293] Field Emission Electron Microscopy (FESEM) is a variation on SEM that was also occasionally conducted in this work. While in normal SEM the electron beam is driven by a thermoionic electron beam gun, in FESEM the beam is driven by a cold cathode field emitter, which allows for improved resolution at lower accelerating voltages. In TEM, the electron beam is broader and static, with much higher accelerating voltages used (often 100-300 kV).[294] Electrons

from the beam penetrate through the sample and are collected behind the sample to produce the desired cross-sectional or plan view micrograph of the specimen, where denser or heavier areas of the sample appear darker. Atomic resolution is currently possible with TEM instruments.

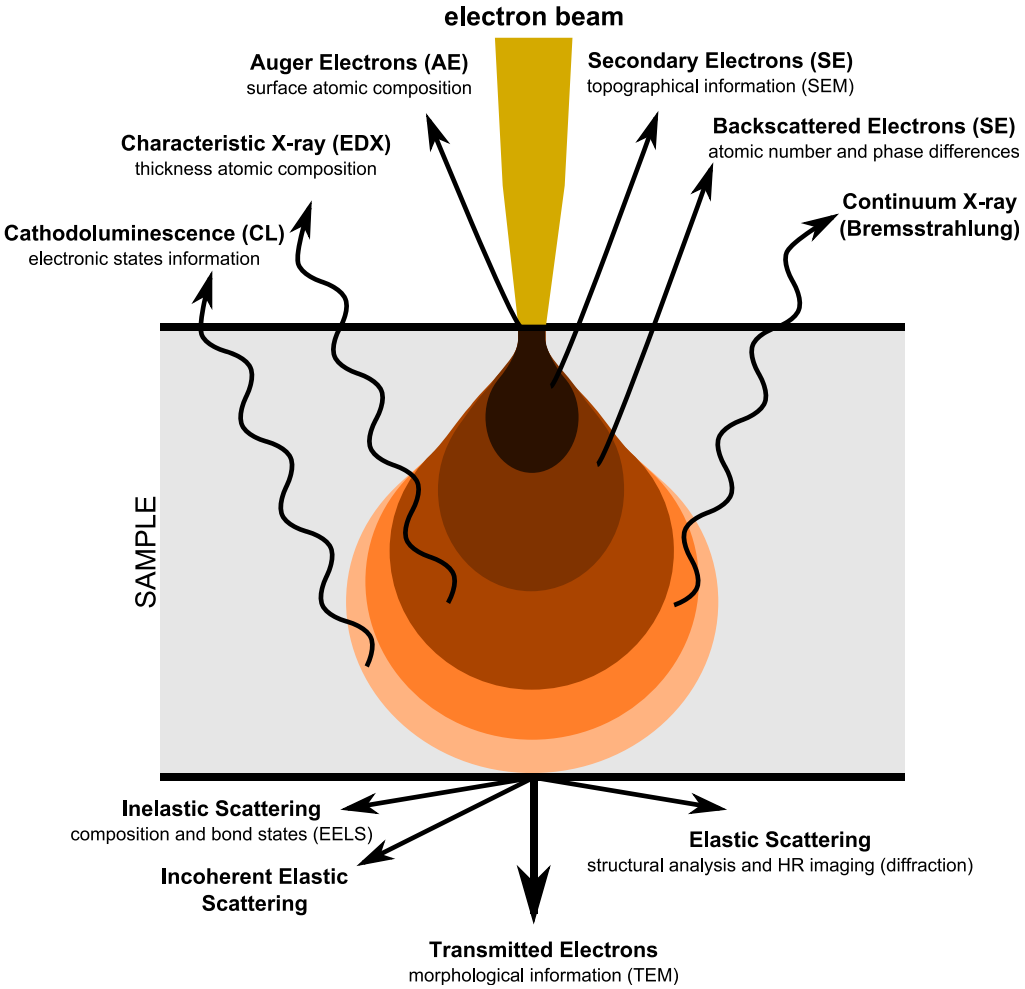

Figure 4.5. Schematic of electron-sample interactions in SEM and TEM. Reproduced from references 295.

In this work, SEM was typically used to image the catalyst in its powdered form to observe its micro-scale growth morphology (100-3,000 times magnification). Typically this produced micrographs of the highly-ordered CNT bundles after key steps in the process of producing and testing the catalyst (e.g. after synthesis, wet impregnation, activation, and catalytic testing) to determine the effect of each step on the overall integrity and morphology of the tubes in aggregate. TEM was used for high resolution imaging of individual tubes rather than the aggregated tube bundles observed via SEM (100,000-300,000 times magnification). TEM allowed for detailed analysis of catalyst tube and particle morphology, and was useful in confirming successful doping of nitrogen and promoter metals, producing particle and tube size distributions, determining appropriate conditions for catalyst

activation, and assessing damage to the catalyst throughout the process of producing and testing our materials. SEM analysis was conducted using a JEOL SEM6480LV in secondary electron imaging mode at an accelerating voltage of 10 kV, or a JEOL FESEM6301F at an accelerating voltage of 5 kV. TEM analysis was conducted using a JEOL JSM-2100PLUS at an accelerating voltage of ca. 200 kV.

4.1.6. Energy-dispersive X-ray spectroscopy

EDS (sometimes also referred to as EDX, EDXS, XEDS, EDXA or EDXMA) is a common analytical technique used in determining the elemental composition of a material sample. The technique makes use of the X-ray spectrum emitted by a solid sample bombarded with a focused beam of electrons to obtain a localized elemental analysis, as seen in Figure 4.6. By scanning the beam in a television-like raster and displaying the intensity of a selected X-ray line, elemental distribution maps can be produced and used in conjunction with topographical images produced by electrons collected from the sample surface to visually portray the position and quantity of elements in a sample.[296]

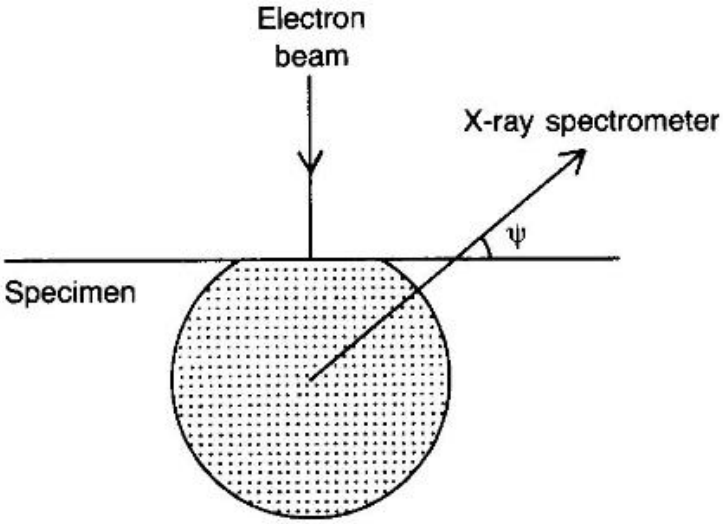

Figure 4.6. X-ray source region in EDS with path of X-rays through the sample to the spectrometer, where ψ is the take-off angle. Reproduced from reference 296.

In this work, EDS was used to determine the elemental analysis of catalyst samples. Most notably it was used to confirm successful nitrogen doping in Fe@NCNTs and distinguish between different metal nanoparticle species after doping Fe@CNTs and Fe@NCNTs with additional promoter metals. EDS analysis was conducted using a JEOL JEM-2100Plus transmission electron microscope with Oxford Instruments large area EDS detector and Aztec analysis software.

4.1.7. Temperature programmed desorption and reduction

TPD is a common analytical technique used in identifying and evaluating the strength of molecular adsorption modes on a solid surface. The technique relies on exploiting the different desorption activation energies of the observed adsorption modes to produce a spectrum of molecular desorption rates from the sample surface plotted with respect to temperature.[287] Typically, the desired sample is initially saturated with a desired adsorbate gas such as N_2, H_2, CO_2, etc. The sample is then placed under high vacuum, as seen in Figure 4.7, and the temperature is linearly raised across a desired temperature range. The rate of desorption of the adsorbate molecules is measured as a change in pressure, or may be coupled with a mass spectrometer for additional analysis of the desorbed species.[287, 297, 298]

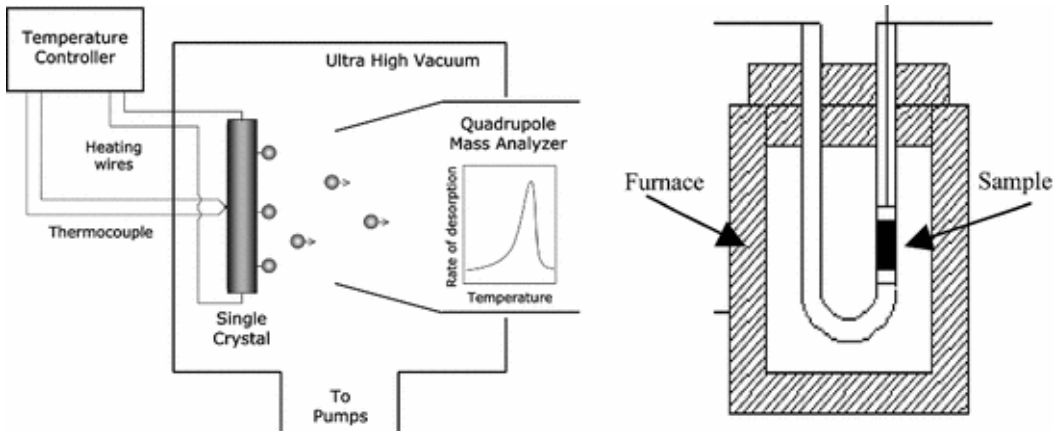

Figure 4.7. Schematic of a typical TPD experimental setup. Reproduced from reference 298.

When the temperature reaches the desorption activation energy of one or more of the adsorption modes present in the sample, a rapid increase in desorption is observed until the corresponding adsorption mode is depleted of adsorbate molecules and the observed desorption flux falls again. In this manner, the quantity strength of different adsorption modes in a single sample or across multiple samples may be compared, as an adsorption mode that desorbs at a higher temperature is considered to be adsorbed more strongly, and vice versa.

In this work, TPD was primarily used to compare the strength of adsorption of the reactant molecules H_2, CO, and CO_2 on Fe@CNTs and Fe@NCNTs to determine whether nitrogen doping in the catalyst support significantly influenced the attraction of these molecules to the catalyst surface. TPD analysis was conducted in conjunction with collaborators at the University of Cambridge, using a Micrometrics AutoChem II 2920 Automated Catalyst Characterization system. Samples of typically 0.05-0.1 g were saturated with the desired

adsorbate gas and then heated across the desired temperature range (typically 100-400 °C or 100-1,000 °C) at 10 °C min^{-1} to observe the relevant rates of desorption. These temperature ranges were chosen as they reflect the typical temperature ranges experienced by the analysed materials (0-1,000 °C for H_2, 0-400 °C for CO and CO_2) through the processes of catalyst synthesis and catalytic testing.

4.1.8. Thermogravimetric analysis

TGA is a thermal analysis technique used to characterize a wide variety of materials by measuring the amount and rate of change in the mass of a sample as a function of temperature or time in a controlled atmosphere such as a fixed flow rate of air or argon. By measuring the loss or gain of mass as a result of decomposition, oxidation or loss of volatiles such as moisture, TGA provides valuable information about the thermal and oxidative stability of a sample, as well as its composition. The technique is most commonly employed to determine information such as the composition of multi-component materials or blends, thermal stability, oxidative stability, estimated product lifetimes, decomposition kinetics, effects of reactive atmospheres on a material, filler content in materials, and moisture or volatiles content.[299] TGA may in some cases be coupled with a mass spectrometer (MS) to aid in identifying decomposition products and monitor their production with respect to temperature and time to provide further information on sample composition and the rate and mechanism of its decomposition.

In this work, TG-MS was used in conjunction with XPS and TEM to determine adequate activation conditions for the Fe@NCNTs to expose their iron particles for catalysis without damaging the NCNT support. The mass of the Fe@NCNT sample was monitored with respect to a temperature ramp, and CO_2 counts were additionally monitored in the MS to provide additional information on the decomposition products. By plotting the first derivative of these spectra, it was possible to determine the onset decomposition temperature of the Fe@NCNT sample. TGA was conducted using a Setsys Evolution TGA 16/18 from Setaram with Omnistar GSD 320 by Pfeiffer Vacuum mass spectrometer. In all cases, the TG-MS was prepared for analysis by rinsing the crucible with acetone, leaving it to dry and taring the balance prior to adding the sample. Approximately 10 mg sample was then added to the crucible and the temperature ramp was executed under 20 sccm air flow. Typically, samples were heated from 0-200 °C at 5 °C/min, and then ramped to their isotherm temperature at 1 °C/min. Decomposition was monitored for 1 hour before cooling.

4.1.9. X-ray photoelectron spectroscopy

XPS is a common technique used in analysing the atomic composition and chemical bonding observed at the surface of a material. Through this powerful technique it is possible to determine the elemental composition, empirical formula, chemical state and electronic state of elements in a sample.[300] XPS falls under a family of characterization techniques known as Photoelectron Spectroscopy (PES), which relies on measuring the ionization energy of electrons that are ejected from a molecule upon absorbing a photon of a known energy, referred to as photoelectrons, as seen in Figure 4.8.

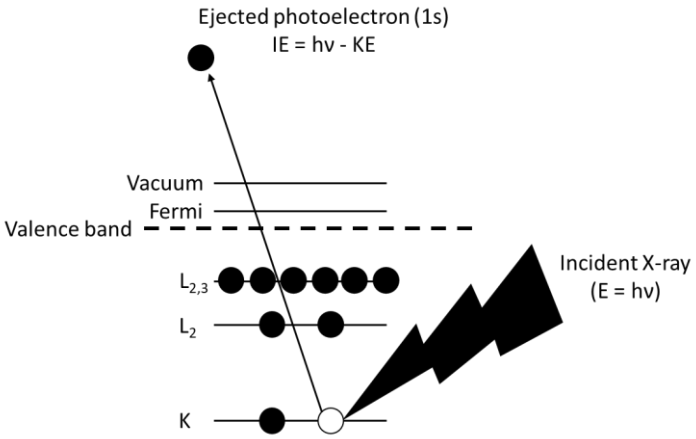

Figure 4.8. The photoemission process involved in XPS surface analysis. Discs represent electrons and bars represent energy levels with the material. Inspired by reference 301.

Because energy is conserved when a photon ionizes a sample, the sum of the ionization energy of the sample and the kinetic energy of the photoelectron must be equal to the energy of the incident photon, as seen in Equation 4.2. It is therefore possible to infer the energy, and thus also the character, of the orbital from which a photoelectron was ejected by measuring its kinetic energy and comparing it to the known energy of the incident photon. This interpretation is made possible through Koopman's theorem, which states that the ionization energy I_i is equal to the orbital energy of the ejected photoelectron. In actuality this is not entirely accurate, as the remaining electrons adjust their distributions when ionization occurs, though this approximation is critical in obtaining useful information from photoelectron spectra.[287]

$$h\nu = \frac{1}{2} m_e v^2 + I$$

Equation 4.2. The energy of an incident photon ($h\nu$) is shown to be equal to the sum of the kinetic energy of the ejected photoelectron ($\frac{1}{2} m_e v^2$) and the ionization energy of the molecular orbital from which the photoelectron was ejected (I).

Molecular ionization energies are on the order of several electron volts (eV), even for low energy valence electrons, so a minimum photon energy in the ultraviolet range is required to generate photoelectrons that can be analysed with PES techniques. When core electrons are studied, even higher energy photons are required to expel them. In this case X-rays are used, hence the ubiquity of XPS analysis. A critical characteristic of XPS analysis is that though the incident X-rays penetrate many microns into the sample, the inelastic mean free path (IMFP) of the ejected photoelectron determines the information depth of XPS analysis. The IMFP of the ejected photoelectrons varies from element to element, but is typically on the order of 1-3.5 nm. It is well established that the ca. 95% of the observed signal in XPS analysis comes from a depth of ca. 3 times the IMFP of the collected photo electrons. Thus, the information depth of XPS analysis is typically considered to be on the order of 1-10 nm, making it a true surface characterization technique that is not intended for analysing the bulk of a sample.[302]

In this work, XPS analysis was used to collect information about the quantity and chemical character of nitrogen, iron, carbon and other metal promoters that were present in our catalyst samples after synthesis, activation and catalytic testing. XPS was particularly useful in identifying suitable catalyst activation conditions, calculating the surface iron and nitrogen content of the catalysts after activation, and identifying any chemical differences that resulted through catalytic testing or doping additional promoters, such as catalyst deactivation due to carbon deposition or the formation of iron-promoter composites (or lack thereof) after promoter doping experiments. For all samples, a survey scan was collected to determine the overall elemental composition of the sample in at. % concentration. High resolutions scans of the C 1s, N 1s, O 1s, and Fe 2p orbital regions of the spectrum were also collected for all samples, with additional high resolution orbital region scans for added promoter metals when appropriate. These high resolution orbital regions scans made it possible to determine the chemical character of each element in the survey scan by deconvoluting the high resolution orbital scans into separate components (e.g. graphitic, pyridinic and pyrrolic nitrogen components in the N 1s region, or different iron oxidation states in the Fe 2p region). Calculating the areas under these deconvoluted component curves made it possible to quantify the at. % concentrations of each chemical species as well. This was achieved by multiplying the normalized area % contribution from each component in the orbital scan of an element with the overall at. % concentration of that element in the survey scan, as seen in Equations 4.3-4.4.

$$\frac{A_i}{\sum A_i} \times 100 = c_i$$

Equation 4.3. The normalized area percentage contribution of a given chemical component in a high resolution orbital region scan (c_i) is shown to be equal to the the area under that specific component's peak after deconvolution (A_i) divided by the total area under all component peaks in that orbital scan after deconvolution ($\sum A_i$) multiplied by 100.

$$\frac{c_i}{100} \times C_x = C_i$$

Equation 4.4. The at. % concentration of a given chemical component in a sample (C_i) is shown to be equal to the normalized area percentage contribution of that component in its high resolution orbital scan (c_i), divided by 100 and multiplied by the total at. % concentration of the element containing that chemical component in the survey scan of the material (C_x).

The survey scans were additionally used to estimate the surface iron loading of the Fe@NCNTs to determine how much iron was available for catalysis in terms of approximate iron nanoparticle weight loading at the surface. This was done by calculating the relative mass contribution of iron in the XPS survey scans, as seen in Equation 4.5. As has been discussed above, XPS information depth is limited to ca. 10 nm sample penetration, so the elemental compositions indicated by the survey scans were assumed to be roughly indicative of the composition of the tube surface rather than the tube interior or bulk of the sample. In actuality, however, with an average tube diameter 20-40 nm and an average tube wall of <10 nm, it is likely that XPS did probe beyond just the tube surface, including some contribution from the tube interior as well. These calculations yielded a rough surface iron loading of 4.5 wt. %, though due to the degree of sample penetration in the XPS, the amount of iron in these calculations is likely slightly overrepresented.

$$C_{W,i} = \frac{C_{at,i} \times MW_i}{\sum C_{at,i} \times MW_i} \times 100$$

Equation 4.5. The wt. % concentration of a given element in the survey scan of an XPS spectrum ($C_{W,i}$) is shown to be equal to 100 times the given at. % concentration of that element in the survey scan multiplied by its molecular weight ($C_{at,i} \times MW_i$), divided by the sum of the products of the at. % concentrations and molecular weights of all elements in the sample ($\sum C_{at,i} \times MW_i$).

XPS analysis was conducted using a Kratos Axis Ultra-DLD system through the Cardiff University XPS analysis facilities and Newcastle University NEXUS XPS facilities. All scans were run three times and averaged to minimize random error.

4.1.10. X-ray diffraction

XRD is a common analytical technique used for phase identification in crystalline materials, and can additionally be used to provide information on atomic spacing and unit cell dimensions. The technique produces diffraction patterns generated by constructive interference between monochromatic X-rays and a crystalline sample, which acts as a three-dimensional diffraction grating for X-ray wavelengths that are similar to the spacing between the planes of the sample's crystal lattice.[303] The X-rays are produced by a cathode ray tube that is filtered to produced monochromatic radiation. This is then concentrated and directed at the sample, as seen in Figure 4.9. The incident X-rays produce constructive interference upon interacting with the sample when the conditions of Bragg's Law are satisfied.

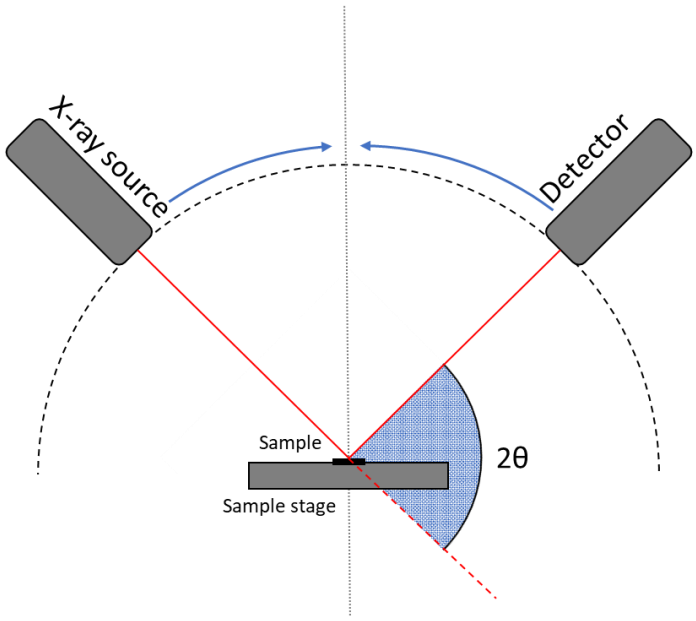

Figure 4.9. Schematic of a typical XRD analysis configuration. 2θ is the diffraction angle. Inspired by reference 304.

The sample is scanned across a range of 2θ angles to collect all possible diffraction directions from the lattice, which are then detected, processed, counted and plotted against 2θ to produce the XRD spectrum of the sample. The diffraction peaks may be converted into d-spacings to identify a crystalline material by matching them against a reference database, as each crystal structure will display a unique, characteristic set of d-spacings. This is achieved using Bragg's Law (Equation 4.6).

$$n\lambda = 2d \sin\theta$$

Equation 4.6. Bragg's Law relates the wavelength of electromagnetic radiation to the diffraction angle and lattice spacing in a crystal sample. n is the order of reflection, λ is the wavelength of the incident X-ray, d is the interplanar spacing of the crystal, and θ is the angle of incidence.

XRD can be additionally useful in determining the average particle size of nanoparticles in a sample using the Scherrer equation (Equation 4.7), which relates the average crystallite size in a powder to the broadening observed in its powder diffraction peaks.[305] Appropriate use of the Scherrer equation in this manner benefits from a sample with a narrow, unimodal size distribution, and requires users to carefully account for additional factors that contribute to peak broadening such as shape, size, strain, orientation, and instrumental broadening before beginning particle size calculations.

$$\beta_L = \frac{K\lambda}{L\cos\theta}$$

Equation 4.7. The Scherrer equation relates the size of crystallites in a solid to the broadening of a peak in a diffraction pattern. β_L is the line broadening at the full width at half maximum of the peak, K is a dimensionless shape factor constant that is typically on the order 0.9, λ is the wavelength of the incident X-ray, L is the average crystallite size in the sample, and θ is the usual Bragg angle.

In this work, XRD was primarily used to confirm the iron species present in catalyst samples throughout various stages of synthesis, activation and reaction. A Bruker D8 Advance with Vantec Detector using Cu K-α_1 radiation was used to analyse all samples, which were scanned in flat plate mode from 20-85° at a scan rate of 0.27° min^{-1} (4 hours per sample).

4.2. **Reaction equipment and analysis**

4.2.1. Catalyst activation and sample preparation

Before any Fe@CNT or Fe@NCNT-based materials could be tested for catalytic activity, they first had to be calcined to remove the thin graphitic carbon layer obscuring their iron particles and preventing them from participating in catalysis. To activate the catalyst in this manner, 0.47 g of the catalyst was loaded into a stainless steel calcination tube (0.5 inch OD × 0.451 ID × 6 inch L). This tube was plugged at one end with quartz wool (9-30 micron, H. Baumbach & Co Ltd) to prevent the catalyst from escaping while still allowing for air flow. For Fe@ NCNT-based materials, the tube was then heated in a muffle oven at 400 °C for 1 hour under a static air atmosphere, with a heating ramp rate of 10 °C min^{-1}. For any Fe@CNT-based materials, the same process was repeated, though the catalysts were instead heated to 570 °C for 40 min, as pure CNTs without nitrogen doped into the surface are known to be more thermally stable than NCNTs, which degrade faster when heated due to lattice defects introduced during nitrogen doping.[262]

Catalyst samples were prepared by loading the required amount of the desired catalyst (typically 0.4 g) into a stainless steel reaction tube (0.5 inch OD × 0.451 inch ID × 6 inch

L), which was plugged with quartz wool (9-30 micron, H. Baumbach & Co Ltd) at both ends to ensure that the catalyst powder rested securely in the middle of the tube. When catalyst dilution was necessary, the catalyst was diluted on a volume by volume basis with silicon carbide powder before mixture of powders was loaded into the reaction tube.

4.2.2. Catalyst testing and the high-pressure packed bed reactor

Once the reaction sample tube had been prepared it was then placed in the tubular furnace of the high pressure packed bed reactor and heated to 400 °C for 3 hours under a flow of 50 sccm H_2 at atmospheric pressure to reduce the catalytic metal sites and saturate the catalyst support with hydrogen. This allowed for the formation of the iron carbide species that catalyse the FT process to form hydrocarbons from CO, following the initial RWGS step. After reaction, these carbide species are not maintained and the particles return to their initial iron oxide state.

To begin the combined RWGS/FT process, the temperature was lowered to the desired temperature (typically 370 °C) and the was pressure gradually raised to the desired reaction pressure (typically 15 bar), while maintaining the desired reaction gas ratio (typically 3:1 H2:CO_2). A high overall flow rate (180 sccm) was employed during this step to facilitate pressurization of the reactor. When the desired pressure had been achieved, the flow rate was lowered to the reaction flow rate of 8 sccm. The reactor was left for 2 hours to equilibrate following pressurization, after which samples were taken hourly for 3 hours via a 50 mL SGE gas tight syringe with leur-lock fittings and analysed via GC-MS.

4.2.3. Gas chromatography-mass spectrometry analysis and calibration

GC is a common analytical technique for analysing compounds that can be vaporised without decomposition. Most commonly, GC is used to determine the purity of a substance or to separate and quantify the different components in a mixture. The principle behind GC is similar column chromatography and other chromatographic techniques such as HPLC and TLC. Components in the analyte are transported through the column by a mobile phase, and are separated from each other with respect to their retention time in the column, as seen in Figure 4.10. This separation is a function of their relative attraction to the stationary phase in the column and their boiling points.

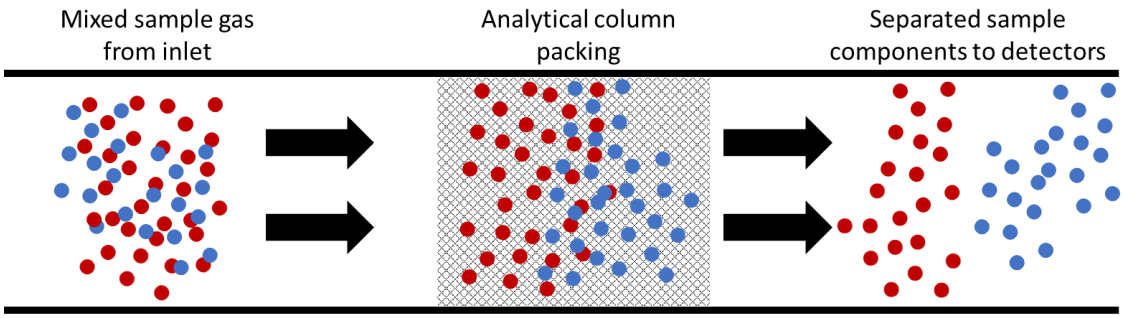

Figure 4.10. Gas separation in the GC column according to analyte interactions with the stationary phase. Inspired by reference 306.

In GC, a carrier gas is used as the mobile phase, typically an inert gas such as nitrogen or helium, while the stationary phase is often a microscopic layer of liquid or polymer on an inert solid support inside a length of glass or metal tubing referred to as the GC column, as seen in Figure 4.11. Interactions between the analyte gases and the stationary phase cause separation of the gases in the mixture, resulting in each component of the mixture to elute after a different retention time on the column.

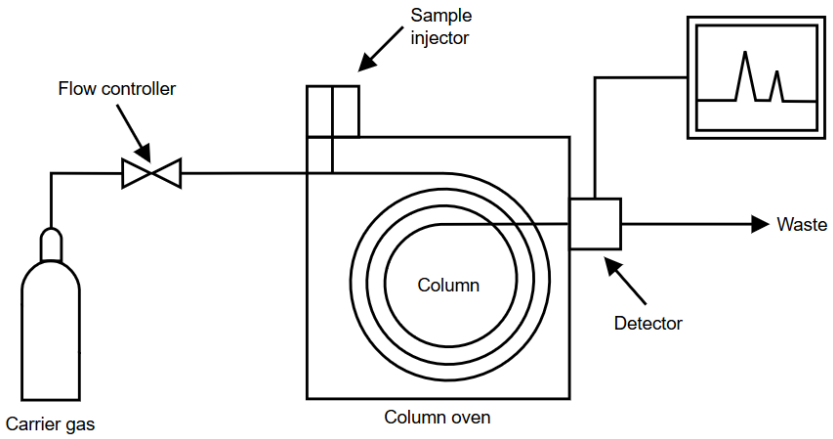

Figure 4.11. Schematic of a standard GC analysis set up showing the full process of sample injection, separation and quantification. Reproduced from reference 307.

The column is also typically placed inside an oven, providing temperature control over the analyte and thus influencing the strength of its interaction with the stationary phase. A higher temperature will typically weaken this interaction, resulting in a shorter retention time on the column. As such, establishing an effective GC method relies on effectively combining the flow of the mobile phase with an appropriate temperature ramp to provide good separation of the analyte components in an acceptable amount of time. GC analysis is often coupled with a mass spectrometer at the outlet to provide information on the mass of each eluent. This analysis configuration is referred to as GC-MS. The temperature ramp and retention times of key analytes in this work are outlined in Figure 4.12.

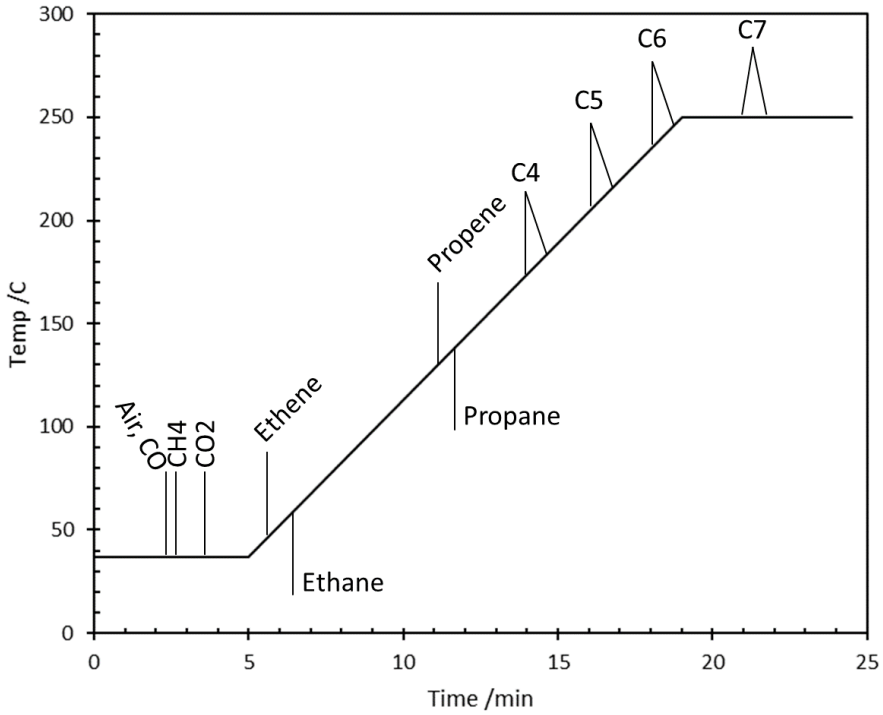

Figure 4.12. The temperature ramp used in this work with key retention times demarked.

In this work, GC-MS was used to separate and quantify the mixture of H_2, CO_2, CO, hydrocarbons and water produced by combined RWGS/FT catalytic testing. The reaction products were sampled from the reactor via a 50 mL SGE gas tight syringe with leur-lock fittings and injected into GC-MS instrument for analysis. An Agilent Technologies 7890A GC System with Agilent Technologies 5975C insert MSD with Triple-Axis Detector (MS, TCD, FID) was used as the GC-MS instrument. The installed column was an HP-Plot Q column. This is a polystyrene-divinylbenzene based column designed for separation of polar and a-polar compounds. While it is specifically intended separate C_1-C_3 hydrocarbons, CO_2, air, water and polar solvents, it is additionally capable of separating hydrocarbons in the range of C_1-C_7. However, it should be noted that nitrogen, oxygen, CO and Ar cannot be separated and all display similar retention times. This makes sampling particularly sensitive to error via contamination from air and makes the process of implementing an internal standard additionally complex, as the presence of air or a convenient internal standard gas such as argon at the same retention time as CO results in over-counting CO in the product distribution, and thus also overestimating CO_2 conversion.

To begin, it was necessary to determine the retention times and response factors of key components in the product gas composition. Knowing the approximate retention times of all possible products greatly expedites the data analysis process and additionally aids in the

identification of contaminants or unexpected by-products. Determining the response factor of each possible component greatly improves the accuracy of conversion and product analysis, as different gases will elicit different responses from the GC detector, even if they are at the same concentration in the mixture. The response factor of a component is determined by calculating the ratio the detector's response signal (e.g. peak area) with respect to a known concentration of the component (Equation 4.8). By calculating the response factor of each component at the detector, quantification analysis can be calibrated to account for this difference in detector response for different gas components. The response factors of key analytes in the work are highlighted in Table 4.2.

$$RF_i = \frac{A_i}{C_i}$$

Equation 4.8. The response factor of a component in a gas mixture (RF_i) is shown to be equal to the detector response (such as peak area) for that component (A_i) divided by the concentration of the component in the analyte mixture (C_i).

Table 4.2. Tabulated retention times, response factors and relevant detectors for quantification as determined by the calibration gas mixture.

Component	Retention time /min	Response factor	Detector
CO	2.813	3297300	TCD
CO_2	4.245	4270200	TCD
CH_4	3.072	34244112	FID
C_2H_6	7.791	71799521	FID
C_3H_8	12.876	132744357	FID
n-C_4H_{10}	15.557	178668655	FID

Retention times and response factors were determined by injecting a calibration gas containing 1% v/v CO, CO_2, CH_4, C_2H_6, C_3H_8, and n-C_4H_{10} in N_2. CO_2 and CO were detected and quantified via the TCD, while hydrocarbon were detected and quantified via the FID to ensure that components were detected with the highest possible sensitivity. The gas components eluted at different retention times with respect to their polarity on the column, with CO eluting first, methane eluting second, CO_2 eluting third, and all other hydrocarbons eluting afterwards with increasing retention times according to their carbon number. In later testing, olefins were observed to elute marginally faster than paraffins of the same carbon number, though their response factors were assumed to be identical. Response factors were

determined on a volume basis by calculating the ratio of the GC response to a component (its peak area) with respect to its known concentration. This was done in greater detail for CO_2 and CO by the plotting the response of each gas at known concentrations of 5.0, 33.3, 66.7, and 100 % v/v in H_2, as seen in Figure 4.13. The gradient of these plots was then used as more robust values for the response factors of CO_2 and CO in particular.

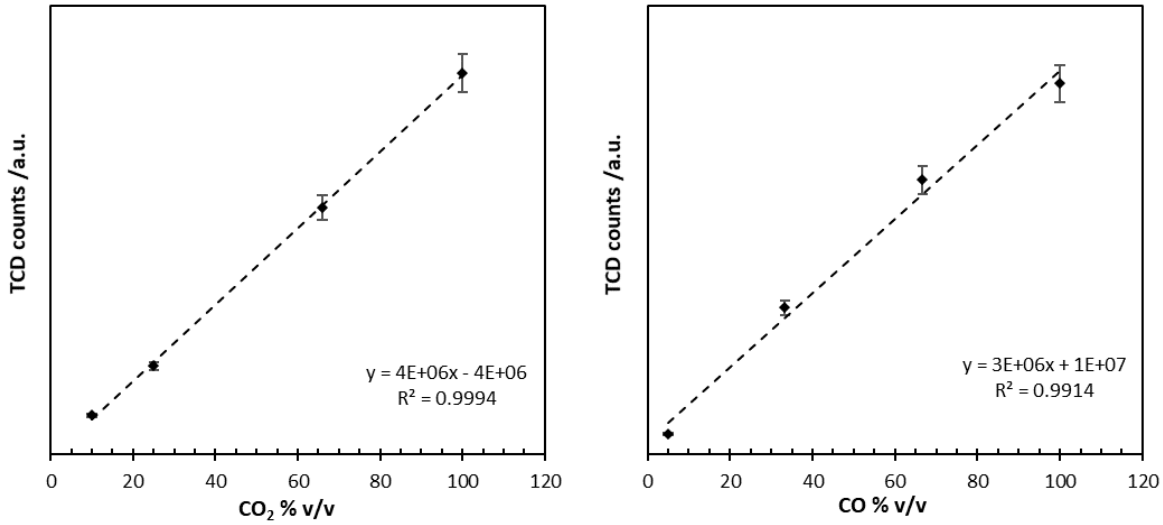

Figure 4.13. TCD calibration for CO_2 and CO at different partial pressures in H_2.

The response factors of hydrocarbons in the calibration gas mixture were additionally plotted with respect to their carbon number, as seen in Figure 4.14. Because the calibration gas did not contain hydrocarbons beyond a length of C_4, the gradient of this plot was then used to extrapolate response values for hydrocarbons up to a value of C_9.

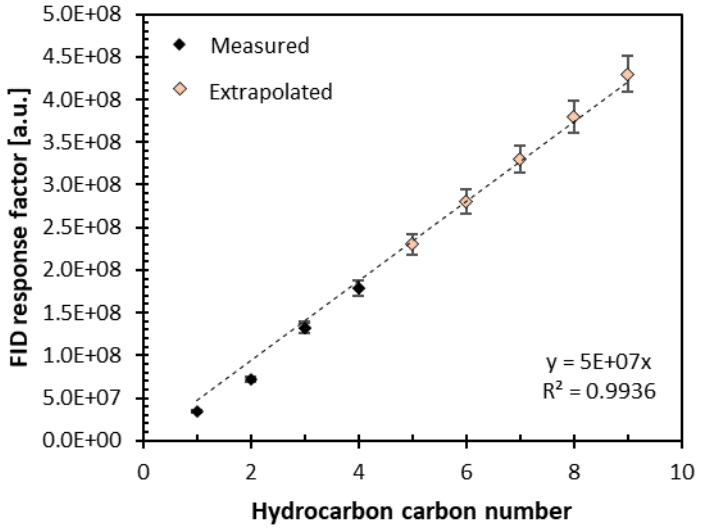

Figure 4.14. FID response factors of hydrocarbons in the product gas mixture plotted with respect to their number of carbons.

After performing these calibration steps, the composition of reaction samples could be quantified from GC-MS spectra by dividing the peak area of each component by that component's response factor to calculate its volume concentration (Equation 4.9). It should be noted that quantification of H_2 and water was not possible using the employed GC-MS method. H_2 cannot be detected when using He as the carrier gas, as the thermal conductivities of these two gases is too similar to be distinguished by the TCD. The use of nitrogen as the carrier gas would allow for the detection of H_2, though this would also reduce the effectiveness of the GC-MS detection and increase error in detecting CO due to their similar retention times. Water is detectable in the GC-MS trace, though the detector is sensitive to water and carrying out a calibration for accurate water quantification would involve introducing significant water to the detector, potentially resulting in damage. Thus, the quantification of H_2 and water were foregone in favour of accurate quantification of the carbon species in with a helium carrier gas instead.

$$C_i = \frac{A_i}{RF_i}$$

Equation 4.9. The concentration of a component in a gas mixture (C_i) is shown to be equal to the detector response (such as peak area) for that component (A_i) divided by the response factor of that component at a known concentration (RF_i).

4.2.4. Mass balance calculations and internal standard implementation

Understanding the mass balance of a reaction is critical in assessing the activity of a given catalyst and determining the fates of different reagents in a chemical process. Mass balance calculations may also be useful in identifying reactor malfunctions such as leaks, though this application is secondary to their value in reaction analysis and quantification. Mass balance calculations rely on the principle of conservation of matter (i.e. that matter cannot be spontaneously created or destroyed), and in their simplest form state that any mass that enters a system must either leave the system or accumulate within the system (Equation 4.10). When quantifying a chemical reaction, the term "mass" typically refers to the sum of the masses of all atoms entering the system. As the reaction occurs these atoms may rearrange into new molecules, though their total mass should remain unchanged.

$$Input = Output + Accumulation$$

Equation 4.10. The input of mass into a system is shown to be equal to the sum of the output of mass from the system and the accumulation of mass within the system.

In this work, mass balance calculations were used to determine and quantify the various reactive fates of CO_2 for each catalyst that was tested, as well as to quantify the productivity of each catalyst normalized with respect to an argon internal standard. This was done by comparing the volume concentration of different components in a reaction gas sample as determined by GC-MS with the known input feed gas flow rate of CO_2 (or sometimes CO for pure FT testing) and H_2 as determined by the MFCs on the high pressure packed bed reactor.

For a full mass balance analysis, it would have been necessary to quantify both H_2 and water in the GC-MS, though this was not possible due to complications in detecting H_2 when using a helium carrier gas, and the susceptibility of the GC-MS detector to water damage, as previously discussed. Thus, carbon balance calculations were used instead, as GC-MS analysis allowed for accurate quantification of all carbon species, and the carbon species formed could be easily related to H_2 consumption and water production through the known chemical equations for the RWGS and FT processes.

To begin, it was necessary to determine the molar flow rate of CO_2 and H_2 into the reactor using the known volumetric flow rate of the gases into the high pressure packed bed reactor as determined by the MFCs (typically 2 sccm CO_2 + 6 sccm H_2 = 8 sccm total flow rate), and the ideal gas law (Equation 4.11).

$$n_F = \frac{PV_F}{RT}$$

Equation 4.11. The ideal gas law relates the molar flow rate of a gas (n_F) to its volumetric flow rate (V_F) at a given pressure and temperature, assuming ideal gas behaviour.

It should be noted that different MFC manufacturers will sometimes use different conditions to define a "standard cubic centimetre." As such, it is necessary to understand how the chosen MFC defines an sccm unit in order to calculate its molar flow rate correctly.

The molar production of each carbon component in a gas sample could then be calculated by multiplying the % v/v concentration of the component as determined via GC-MS with the molar flow rate of CO_2 into the reactor (Equation 4.12).

$$n_{F,i} = n_{F,CO2\ in} \times C_i$$

Equation 4.12. The molar production of each component in a gas mixture ($n_{F,i}$) at the outlet of the high pressure packed bed reactor is shown to be equal to the product of the molar input flow of CO_2 in the feed gas ($n_{F,CO2\ in}$) and the % v/v concentration that component in the sample as determined by GC-MS (C_i).

CO_2 conversion was then calculated by comparing the molar carbon content in all detected carbon product components with the molar flow rate of CO_2 into the reactor (Equation 4.13).

$$\chi_{CO2} = \frac{\sum N_{C,product\ i} \times n_{F,product\ i}}{n_{F,CO2\ in}} \times 100$$

Equation 4.13. CO_2 conversion (χ_{CO2}) is shown to be equal to the sum of the molar productions all carbon products (hydrocarbons and CO) multiplied by the number of carbons they contain ($N_{C,product\ i} \times n_{F,product\ i}$), divided by the molar input flow of CO_2 in the feed gas ($n_{F,CO2\ in}$) multiplied by 100.

The carbon balance of a sample could then be similarly calculated by adding the molar flow of CO_2 out of the detector, as determined via GC-MS, into the numerator of the previous expression (Equation 4.14).

$$C_{bal} = \frac{n_{F,CO2\ out} \sum N_{C,product\ i} \times n_{F,product\ i}}{n_{F,CO2\ in}} \times 100$$

Equation 4.14. The carbon balance of a sample (C_{bal}) is shown to be equal to the sum of the molar flow of CO_2 out of the reactor as determined via GC-MS ($n_{F,CO2\ out}$), plus the molar productions of all carbon products multiplied by number of carbons they contain ($N_{C,product\ i} \times n_{F,product\ i}$), divided by the molar input flow of CO_2 in the feed gas ($n_{F,CO2\ in}$) multiplied by 100.

It should be further noted that throughout the course of this work, the gas syringe sampling method for collecting and injecting samples for GC-MS analysis was noted to be subject to error due to loss in volume from H_2 consumption and water production. A loss in H_2 volume during the reaction had the potential to cause oversampling of carbon species, as the sample in the syringe might contain greater than 25% v/v carbon species. This exceeded the initial concentration of carbon in the feed gas, often resulting in overstated conversion and carbon balances. This effect was observed particularly in samples with high conversion and greater selectivity towards long chain hydrocarbons, as more H_2 was consumed in these samples. To account for this, the pure H_2 feed gas was replaced with a 1% v/v Ar in H_2 mixture. While the H_2 volume decreased as a result of conversion, the Ar internal standard continued to flow at a constant rate, accumulating in the syringe in a similar fashion to the carbon species. Thus, the values for carbon balance and CO_2 conversion could be corrected by dividing them by ratio of Ar in the outlet gas versus the feed gas mixture (Equations 4.15-4.16).

$$C_{bal}{}' = \frac{C_{bal}}{D_{Ar}}$$

Equation 4.15. The corrected carbon balance ($C_{bal}{}'$) is shown to be equal to the uncorrected carbon balance (C_{bal}) divided by the ratio of Ar at the outlet of the reactor versus in the feed gas (D_{Ar}).

$$\chi_{CO2}{}' = \frac{\chi_{CO2}}{D_{Ar}}$$

Equation 4.16. The corrected CO_2 conversion ($\chi_{CO2}{}'$) is shown to be equal to the uncorrected carbon balance (χ_{CO2}) divided by the ratio of Ar at the outlet of the reactor versus in the feed gas (D_{Ar}).

As previously discussed, Ar elutes at a similar time to CO, N_2 and O_2. As such, the Ar internal standard contributes to error in the system by contributing to the CO signal in the TCD. This must be separately quantified by the MS detector to determine D_{Ar}, where its signal contribution can be separated from other contributions at the same retention time according to its mass-to-charge ratio (m/z = 40 for Ar), using the "Extract Ion IEC" function in the ChemStation analysis software (it should be noted that this Ar-specifc analysis file must be generated and saved under a different name in the sample directory before exporting the results for the rest of the sample to avoid overwriting it).

$$D_{Ar} = \frac{A_{Ar,out}}{A_{Ar,in}}$$

Equation 4.17. The ratio of the Ar content in the outlet stream versus in the feed gas (D_{Ar}) is shown to be equal to MS detector response signal for Ar at the outlet ($A_{Ar,out}$) divided by the MS detector response signal for Ar at the known inlet concentration ($A_{Ar,in}$).

Finally, to correct the CO signal in the TCD to account for the added contribution from the Ar internal standard, the Ar TCD signal must be subtracted from the total CO TCD peak (Equation 4.18). To do this, the TCD signal for 1% v/v Ar in H_2 was measured (this value was typically on the order of 2×10^6). This could then be used conjunction with D_{Ar} to estimate the Ar contribution to the CO TCD peak. A calibration curve was plotted using 100%, 50% and 33% Ar/H_2 mix in CO and CO_2 to ensure an accurate response from the internal standard in the MS detector. Comparing 3 repeated samples at 5 bar indicated an error in GC-MS species quantification of ca. ± 5%.

$$A_{CO}{}' = A_{CO} - A_{Ar,TCD,1\%} \times \frac{P_{H2}}{P_{CO2} + P_{Ar,H2}} \times D_{Ar}$$

Equation 4.18. The actual signal response for CO in the TCD, in the presence of the Ar internal standard ($A_{CO}{}'$) is shown to be equal to the uncorrected signal due to CO (A_{CO}), less the contribution from the CO peak from the Ar internal standard at 1% v/v in H_2 ($A_{Ar,TCD,1\%}$) multiplied by the contribution of the Ar/H_2 mixture to the feed gas stream ($\frac{P_{H2}}{P_{CO2}+P_{Ar,H2}}$), multiplied by the ratio of the Ar content in the outlet stream versus in the feed gas (D_{Ar}).

4.2.5. Reactor safety and adiabatic temperature rise calculations

The high-pressure packed bed reactor used for CO_2 hydrogenation testing in this thesis is pictured in Figure 4.15. Safety is of the utmost concern during combined RWGS/FT catalytic testing, and undoubtedly the most severe hazards encountered during this process are potential exposure to the CNT-based catalyst, leaks of hazardous gases such as H_2 and CO, and, in the worst case, runaway combustion of H_2 culminating in an explosion or open flame. Additionally, the heating cord used to maintain products in their gaseous state after the furnace outlet may short out if the internal wire comes in contact with the metal surface of the reactor, resulting in uncontrolled heating in excess of 700 °C. In this section, the risks and precautions taken to mitigate each of these hazards are outlined.

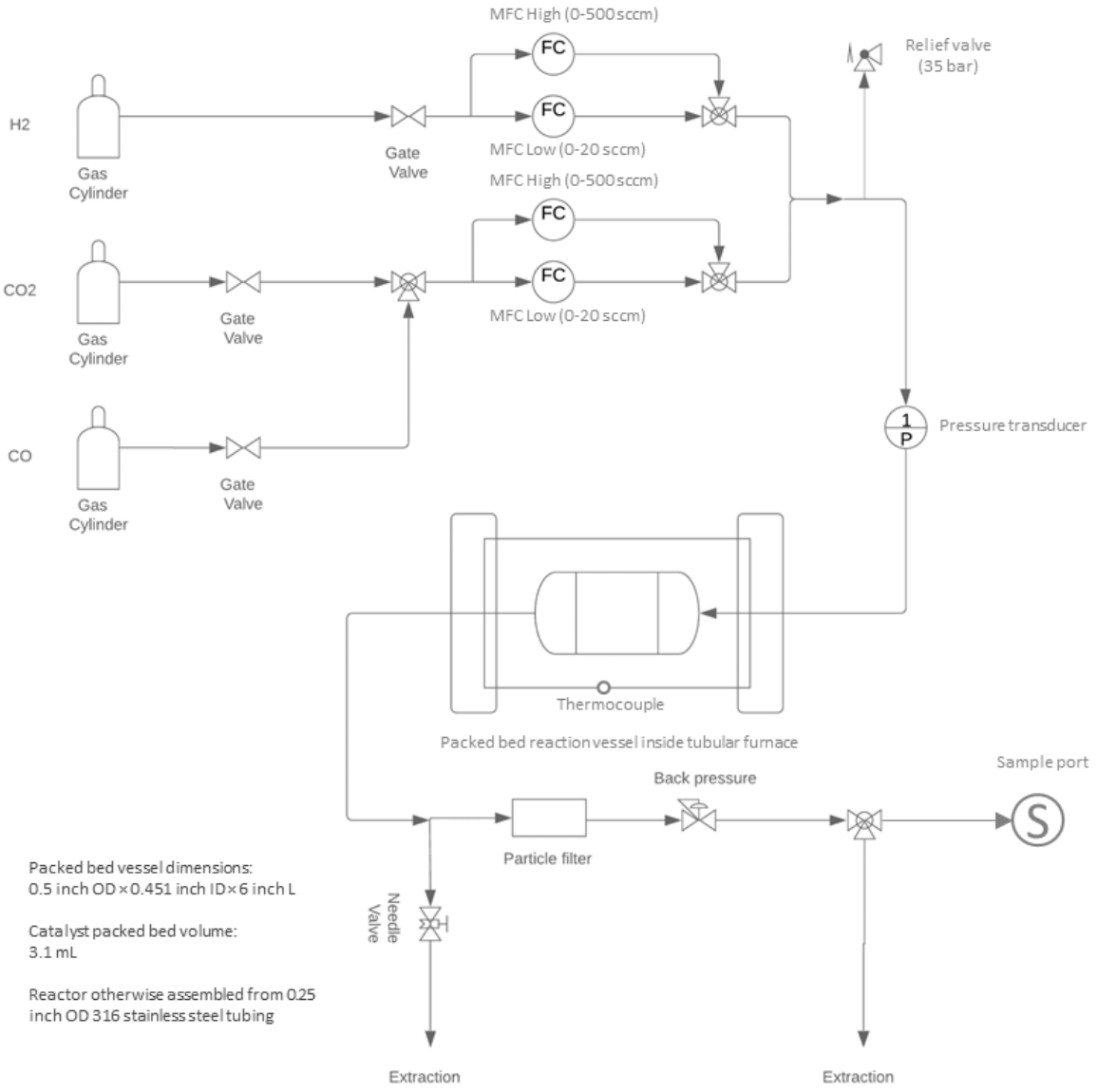

Figure 4.15. P&ID diagram of the high pressure CO_2 conversion reactor used in this work.

Detailed safety procedures and best practices concerning the handling of CNT-based materials have been outlined in section 2.4.4. During the catalytic testing process, the risk of exposure to the CNT-based catalyst is relatively limited compared to the processes of catalyst synthesis and activation. However, it is important to be aware that the typical quantity of catalyst loaded into the reaction tube (0.4 g) poses a significant hazard if it is improperly handled, dispersed, or inhaled. It is therefore recommended once again to refer to the previously described nanomaterials safety procedures before loading or unloading the reaction tube, keeping in mind that damage to the reactor could result in the additional hazard of catalyst exposure.

Leaks represent a significant cause for concern in any high pressure chemical application. In this instance, H_2 and CO represent the most significant leak hazards, as H_2 is highly flammable, and CO is a potentially fatal asphyxiant gas. Leaks are primarily mitigated during the reactor commissioning process. The reactor is filled with an inert gas such as Ar or N_2 and pressurized to several bar above typical reaction pressures. All joints on the reactor are then checked for leaks with snoop and tightened as appropriate. Whenever sections of the reactor are replaced or upgraded, this process must be repeated for any components that have been changed. At the typical reaction flow rate of 8 sccm and $P_{H2}/P_{CO2} = 3$, the amount of CO or H_2 that is likely to escape is very low and is unlikely to pose a significant threat as long as the reactor is placed in a large enough room with suitable extraction (such as a walk-in fume hood). A CO detector should be kept near the reactor at all times to identify potential leaks, and all gases should be fed to directly to the extraction when they are not being sampled. It is additionally worth noting that while H_2 has very low ignition energy of 0.017 mJ in air, which makes it much easier to ignite in the presence of a spark than typical hydrocarbon fuels, it is also extremely lightweight, which causes it to disperse very quickly and results in a much more localized flame if ignition does occur.

Finally, it is important to understand the adiabatic temperature rise in the reactor, as an increase in the reaction temperature not only affects reaction progress, but may eventually result in hazardous conditions in the reactor. In the case of combined RWGS/FT testing, a potential concern during prolonged testing is reaching the auto-ignition temperature of hydrogen in air (ca. 500 °C). If H_2 gas in the reactor were to reach this temperature and then leak from the reactor, it could produce an open flame and subsequent runaway reaction. By calculating the adiabatic temperature rise within the reactor as a result of the reactions (Equation 4.19), we are able to estimate the time required for the reaction to reach a potentially hazardous temperature.

$$T = T_0 + \frac{(-\Delta H_{rxn})\chi}{\sum \theta_i Cp_i}$$

Equation 4.19. Adiabatic temperature rise for a mole of gas reacted at a given temperature (T_0). ΔH_{rxn} is the enthalpy of reaction, χ is conversion, and $\sum \theta_i Cp_i$ is the sum of the mole fractions of the gases in the reaction multiplied by their specific heat capacity.

CO_2 methanation is the most exothermic process that can occur during combined RWGS/FT catalysis (-165 kJ mol^{-1}), so 100% CO_2 methanation was assumed as a worst-case scenario calculation for the adiabatic temperature rise. It was determined that at a typical flow rate of 8 sccm and P_{H2}/P_{CO2} = 3, the temperature increases by ca. 12.2 K hr^{-1}. Keeping this in mind, a test would need to run for ca. 10 hours before approaching the auto-ignition temperature of hydrogen in air under conservative conditions. Thus, the typical operating conditions and test duration of ca. 5 hours has been deemed safe to perform.

Chapter 5 – Fe@NCNT production

Several examples of Fe@NCNT-type materials (with nitrogen heteroatom and iron nanoparticle doping incorporated during synthesis) have been reported in the literature, as outlined in sections 2.5.2 and 2.6.2. However, no previous studies have utilised the residual iron particles embedded in the NCNT wall structure for CO_2 hydrogenation catalysis. In order to keep the synthesis and growth mechanism for the Fe@NCNT material as similar as possible to those of the previously studied Fe@CNT, the same CVD synthesis technique was employed with the exception of replacing toluene with acetonitrile in the precursor solution to act as a carbon and nitrogen source during NCNT growth process. The specifics of this synthesis process have been outlined in greater detail in section 4.1. This chapter first summarises the initial production, characterization and scale-up of the Fe@NCNT catalyst. After confirming the physical and chemical composition of the as-synthesised Fe@NCNT material, the chapter concludes with a study leading to the determination of suitable activation conditions to expose the residual iron particles for catalysis.

The work discussed in this chapter has been used to produce the following publication:

D. L. Williamson, C. Herdes, L. Torrente-Murciano, M. D. Jones and D. Mattia, *ACS Sustainable Chemistry & Engineering*, 2019, **7**, 7395-7402.

5.1. **Fe@NCNT synthesis and characterisation**

Fe@NCNT were produced using the same CVD synthesis technique outlined by Minett *et al.* to produce Fe@CNT,[70, 71] with the exception of replacing toluene with acetonitrile as the carbon- and nitrogen-containing solvent in the precursor solution. The specifics of this synthesis process have been outlined in greater detail in section 4.1. Initial synthesis efforts yielded ca. 400-500 mg catalyst as a black, spongy powder, as seen in Figure 5.1. This is typical for CNT materials produced via CVD, though the presence of black powder in itself does not confirm the successful production of the desired Fe@NCNT product. A wide variety of graphitic materials and amorphous carbon can be deposited with a similar appearance during CVD, without necessarily yielding nanotube arrays. A comprehensive suite of characterisation techniques was therefore employed to confirm the atomic composition and nanoscale morphology of the collected powder.

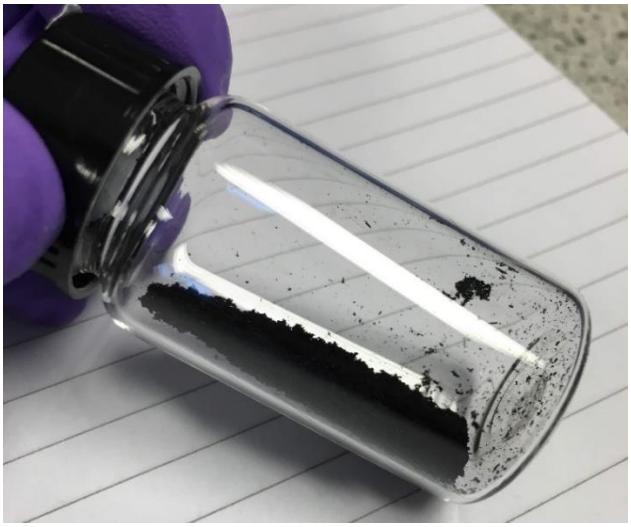

Figure 5.1. Typical initial synthesis yield of ca. 400-500 mg Fe@NCNT. The pictured sample vial has a maximum capacity of 20 mL.

5.1.1. Structural characterisation

SEM micrographs of as-produced Fe@NCNT revealed bundles and wisps of highly-aligned, vertically-grown forests of CNT fibres, as seen in Figure 5.2. This is in good agreement with previously published findings on the microscale morphology of the Fe@CNT catalyst.[71] While individual tube diameters and composition cannot be determined from SEM due to limited magnification, tube length was determined to be up to ca. 100 μm, corresponding to a CVD growth rate of ca. 100 μm/hour or 10 μm/mL of the CVD injected precursor solution.

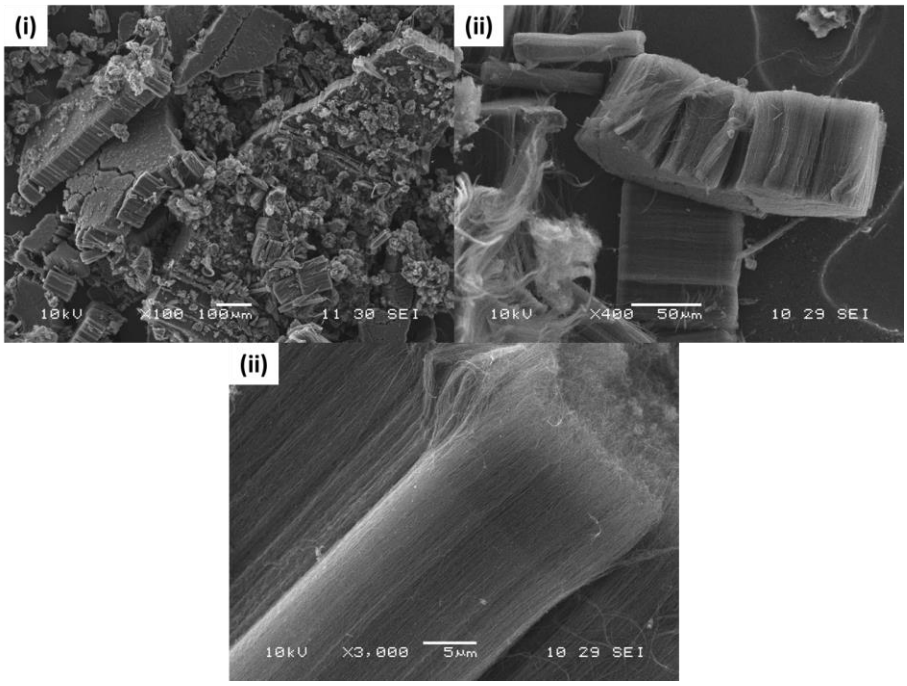

Figure 5.2. SEM micrographs of Fe@NCNT after synthesis at (i) 100, (ii) 400, and (iii) 3,000 times magnification.

Brief sonication (ca. 1-3 min) of the tightly packed bundles in ethanol dispersed them sufficiently to be individually visible in TEM. TEM micrographs of Fe@NCNT revealed clear MWCNT structures with a similar morphology and dimensions relative to the Fe@CNT produced via the same technique, as seen in Figure 5.3. Embedded iron nanoparticles were clearly visible along the length of the tube support structure, with elongated slugs of iron also occasionally occupying the interior tube bore. A noteworthy difference in morphology between the Fe@CNT and Fe@NCNT was the presence of clear graphitic compartmentalisation (sometimes referred to as bamboo segmentation) along the Fe@NCNT interior tube bore. This is in good agreement with previous studies, which have noted such segmentation to be characteristic of successful nitrogen incorporation into the MWCNT crystal lattice. These segmented structures are generally attributed to defects in the sp^2 hybridised carbon network that arise out of imperfect nitrogen incorporation, resulting in deviation away from the hollow bore structure observed in Fe@CNT.[206, 254, 266, 270, 277]

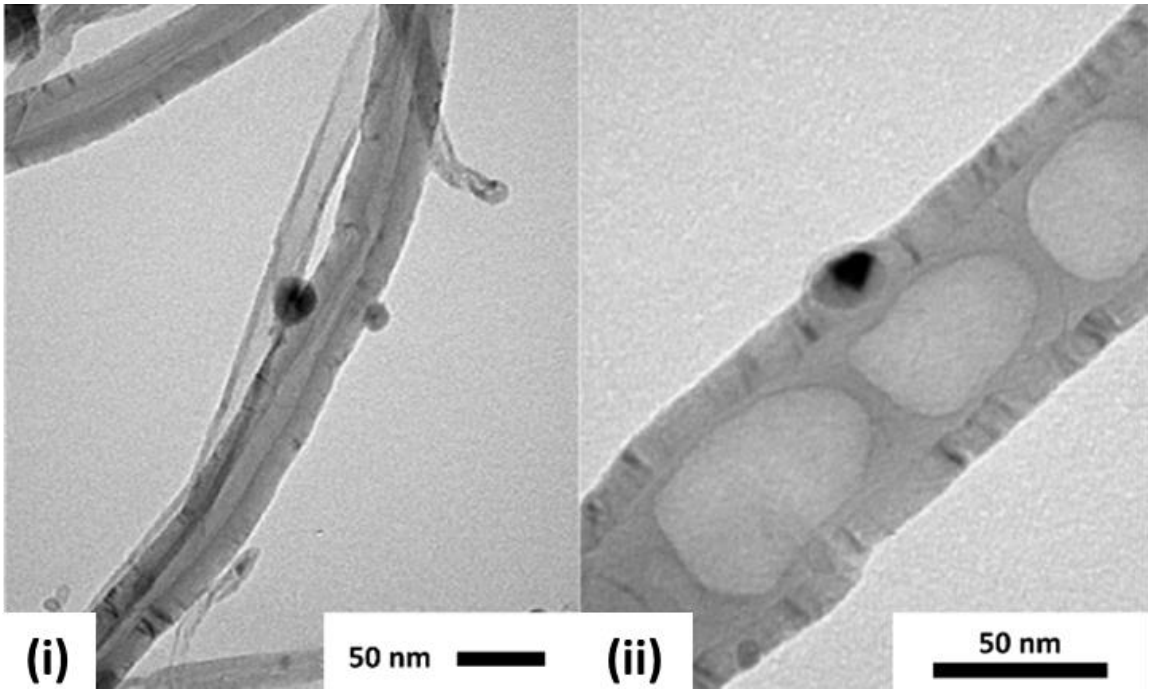

Figure 5.3. TEM micrographs, particle and tube size distributions of (i) Fe@CNT and (ii) Fe@NCNT after activation in air for 1 hour at 570 °C and 400 °C, respectively.

While characteristic bamboo segmentation served as a valuable initial indication of successful nitrogen incorporation in the MWCNT lattice, further characterisation was required to confirm the chemical composition of the Fe@NCNT product. HRTEM EDS maps confirmed the presence of carbon and nitrogen in the MWCNT support structure of the Fe@NCNT, as seen in Figure 5.4. Carbon appeared in significantly greater concentrations than nitrogen. This is in good agreement with previously reported syntheses of Fe@NCNT-type materials in literature, where nitrogen contents have typically been reported between 1-10 at. %.[206, 262, 266, 270] Crucially, nitrogen was observed to remain fixed in the CNT lattice even after activation to expose the catalytic iron particles for catalysis. Due to imperfect incorporation of nitrogen atoms into the sp^2 hybridised CNT network, they are less stably bound into the CNT structure than the graphitic carbons that comprise the rest of the lattice. The presence of nitrogen in the EDS maps of Fe@NCNT after activation confirmed that nitrogen was not entirely removed by the oxidative activation process, and the catalyst maintained some degree of nitrogen doping prior to its application as a CO_2 hydrogenation catalyst. Furthermore, oxidation of the embedded iron particles was evidenced by the presence oxygen mapped over the iron particles after activation.

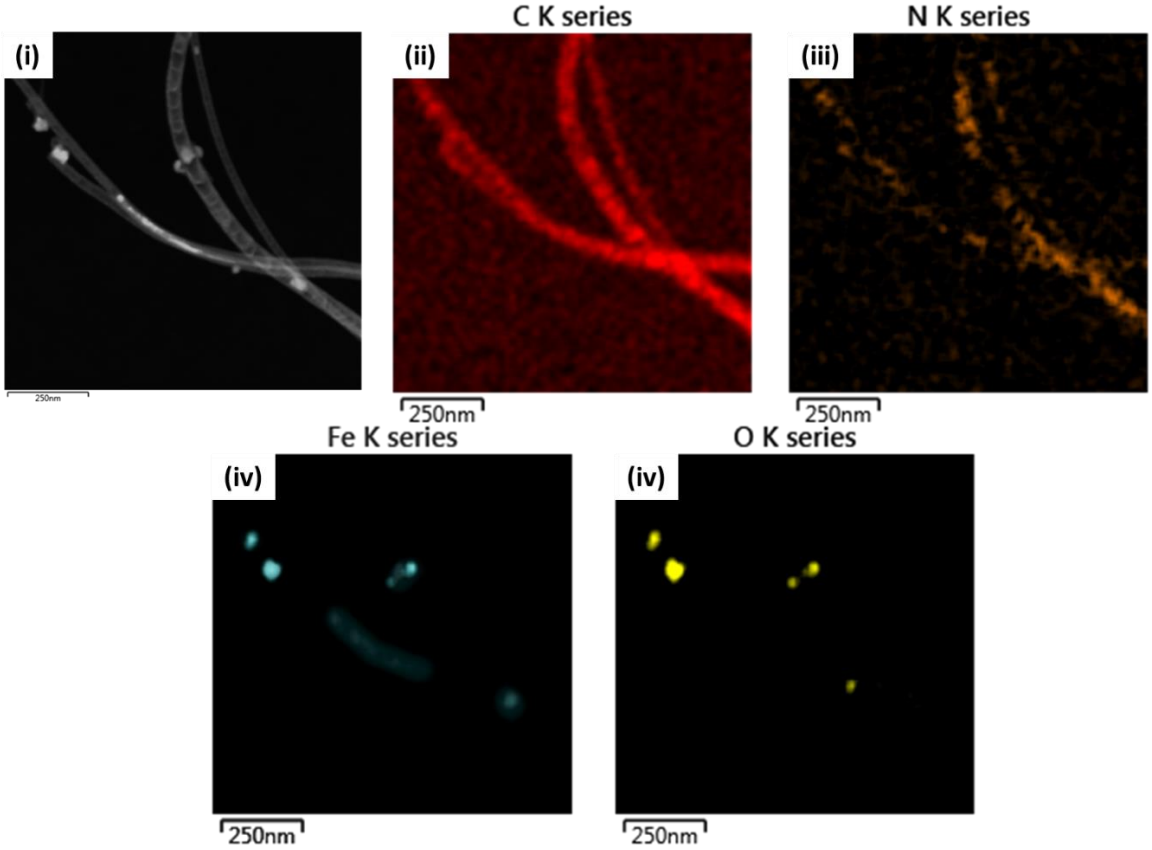

Figure 5.4. EDS maps of Fe@NCNT after activation at 400 °C in air for 1 hour. Maps display clear nitrogen doping along the CNT tube support structure and oxidation of the embedded iron particles due to activation.

5.1.2. Chemical characterisation

In addition to microscopy and EDS mapping, a variety of spectroscopic techniques was applied to investigate the chemical composition of the Fe@NCNT catalyst in greater detail. Raman spectroscopy of the Fe@NCNT catalyst displayed sharp peaks at 1354 cm^{-1} and 1597 cm^{-1}, as seen in Figure 5.5. These are assigned to the D and G bands, respectively. These peaks are typically observed in the Raman spectra of CNT-based materials.[270] The D band becomes more intense as the number of defects in the sample increases, and so the ratio of these peaks (I_D/I_G) is often used as a measure of the overall disorder in a sample. Fe@CNT display a low I_D/I_G value of 0.2, while I_D/I_G for Fe@NCNT is much larger at 0.9. This increase in I_D/I_G is an indication of nitrogen incorporation in the CNT lattice, as the number of defects in the lattice increases due to poor assimilation of nitrogen atoms into the sp^2 hybridized network. [206, 227, 254, 266, 270, 277, 308] The final feature at ca. 2666 cm^{-1} is the G' band, which is caused by two-phonon scattering processes that are free from the defect structures.[255, 309, 310] It is therefore suppressed in Fe@NCNT where defects are more prominent.

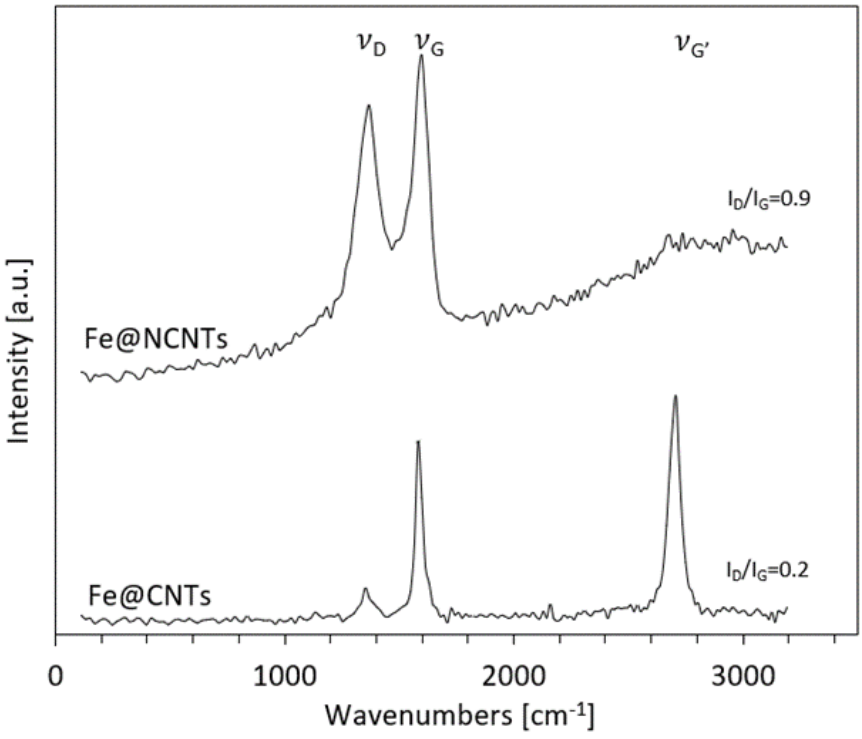

Figure 5.5. Raman spectra of Fe@CNT and Fe@NCNT after activation in air for 1 hour at 570 °C and 400 °C, respectively. I_D/I_G error is estimated to be ± 0.01.

XPS spectra further confirm the presence of ca. 3 at. % nitrogen in the Fe@NCNT sample, with ca. 1 at. % iron exposed for catalysis in both Fe@CNT and Fe@NCNT after activation. It should be noted that the surface iron and nitrogen content varied depending on the temperature of activation. Further details on the determination of the activation conditions to expose the iron nanoparticles are discussed in section 5.3. Fe 2p spectra of the Fe@NCNT suggest the formation of Fe_8N and $Fe_{16}N_2$ after synthesis, as seen in Figure 5.6. This is evidenced by peaks at 707.2, 708.0, and 710.5 eV.[311] These peaks shift to 707.5, 709.9, and 711.3 eV after oxidation in air to expose the iron particles for catalysis, suggesting the formation of Fe(0), Fe(II) and Fe(III) as a mix of Fe_2O_3 and Fe_3O_4 and metallic iron, respectively.[312, 313] A similar shift has been observed for the iron carbides in Fe@CNT.[70] N 1s spectra for Fe@NCNT display peaks at ca. 398.8, 401.3, and 404.4 eV, corresponding to the presence of pyridinic, graphitic and physisorbed N_2 or N–O species, respectively.[227, 266, 270, 275] These peaks initially appear at a ratio of 1:2:1 after synthesis, though this shifts to a ratio of 1:3:0 as the pyridinic, chemisorbed and physisorbed peaks are suppressed during the thermal activation process. This suggests that the nitrogen species in the CNT lattice consist primarily of graphitic nitrogen prior to catalytic testing. This may be significant, as different nitrogen environments have been noted to encourage different reactivity due to discrepancies in electron availability (e.g. graphitic nitrogen forms a shallow donor state, while the valence electrons in pyridinic and pyrrolic nitrogen sites remain confined to the π_z orbital).[79, 227, 265]

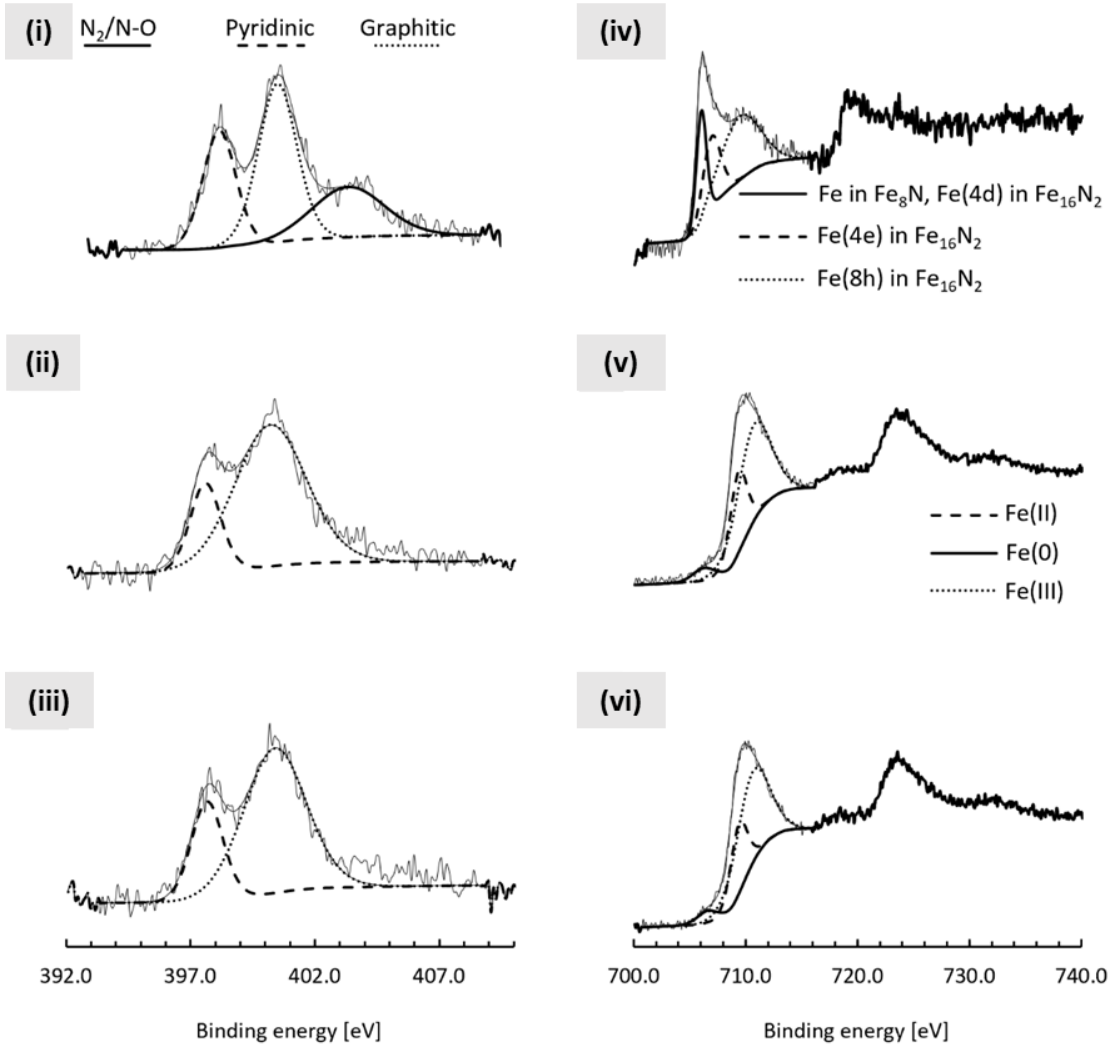

Figure 5.6. XPS spectra of Fe@NCNT N 1s region (i) freshly synthesized, (ii) activated at 400 °C in air for 1 hour, and (iii) after a typical CO_2 reduction reaction. Fe@NCNT Fe 2p region (iv) freshly synthesized, (v) activated at 400 °C in air for 1 hour, and (vi) after a typical CO_2 reduction reaction.

Varying the CVD synthesis temperature of Fe@NCNT indicated that nitrogen content may decrease with increasing synthesis temperatures, as seen in Table 5.1. This is in good agreement with previously reported trends in literature.[206, 266] However, no clear temperature dependence was observed in the concentrations of the individual nitrogen species.

Table 5.1. XPS composition of Fe@NCNT synthesised at varying CVD hold temperatures after activation at 400 °C in air for 1 hour.

T_{synth} [°C]	C [at. %]	N [at. %]	O [at. %]	Fe [at. %]
650	89.3	3.4	6.3	1.0
700	87.6	3.6	7.7	1.1
750	88.7	3.1	7.1	1.0
790	90.9	2.7	5.2	1.2

pXRD further confirmed similarities in the morphology and iron species of Fe@CNT and Fe@NCNT, as seen in Figure 5.7. Both materials exhibit reflections at ca. 26.4° corresponding to the CNT support structure. Reflections at 30.5°, 35.8°, 43.4°, 54.1°, 57.6°, and 62.5° confirm the presence of Fe_3O_4 in both materials,[314] while reflections at 24.2°, 30.4°, 33.3°, 35.8°, 41.0°, 49.6°, 54.1°, 57.6°, 62.5°, and 63.9° confirm the presence of Fe_2O_3.[315] Iron carbides are also weakly visible as a characteristic grouping of overlapping peaks between 40° and 50°.[316] Fe@CNT appear to have more intense reflections from Fe_2O_3, which is likely an effect of the higher activation temperature (T_{act}) required to expose the iron particles for catalysis due to the greater thermal stability of the Fe@CNT (T_{act} = 570 °C) compared to Fe@NCNT (T_{act} = 400 °C).[70] Further justification of this difference in activation conditions is discussed in section 5.3. Beyond this difference, which is itself mitigated during catalyst reduction prior to catalysis,[116] pXRD suggests similar iron species between the iron particles of Fe@CNT and Fe@NCNT, with limited effect on the particles due to nitrogen doping. Reducing the Fe@NCNT sample resulted in suppression of the iron oxides and clear evolution of metallic iron characterized by reflections at 44.9° and 64.9°.[317] This is in good agreement with previous XRD studies of the Fe@CNT material.[116]

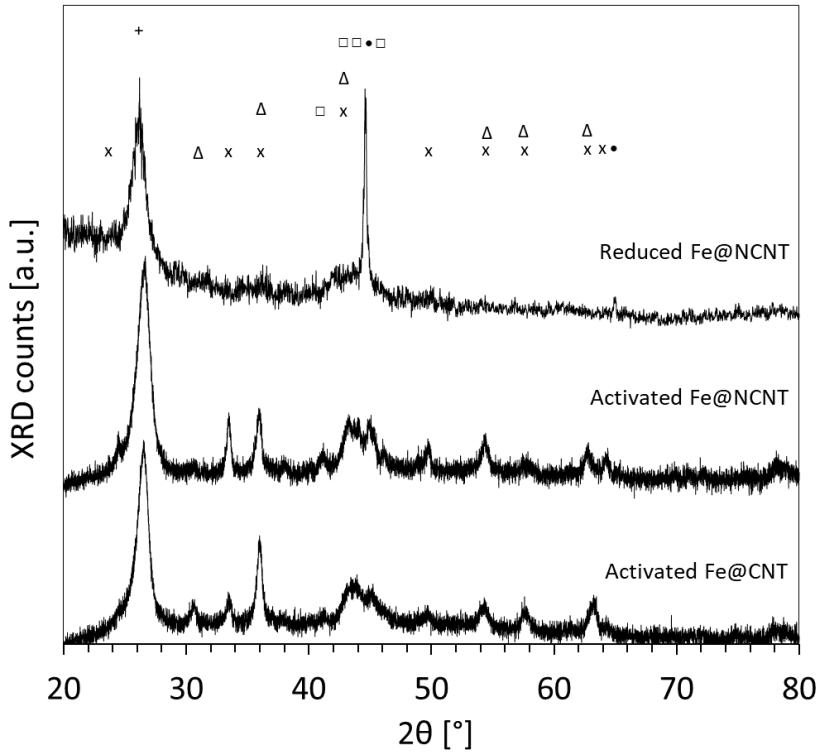

Figure 5.7. pXRD spectra of Fe@CNT and Fe@NCNT after activation at 400 °C (or 570 °C for Fe@CNT) in air for 1 hour. Fe@NCNT after reduction in 50 sccm H_2 at 400 °C and atmospheric pressure are also included. Spectra indicate the presence of the CNT support (+), Fe_2O_3 (x), Fe_3O_4 (Δ), iron carbides (□), metallic iron (•).

5.2. **Fe@NCNT scale-up**

While initial attempts at synthesising the Fe@NCNT material were successful, CVD injections using 10 mL of the ferrocene-in-acetonitrile precursor solution generated low yields of ca. 400-500 mg. Such yields represented enough catalyst to perform a single CO_2 hydrogenation experiment per catalyst synthesis run when applied under previously reported conditions used in the testing of the Fe@CNT.[70, 72] This significantly limited experimental workflow and the frequency of catalytic experiments. It was therefore determined that the Fe@NCNT production process should be scaled up to produce more catalyst per CVD synthesis run. This section outlines the results of several approaches taken to increase Fe@NCNT production yield. Initial efforts involved increasing the substrate surface area by loading quartz beads into the CVD tube in the hot zone of the furnace, while subsequent efforts attempted to increase yields by increasing the CVD injection volume and run duration to maintain a sustained injection rate over a longer period of time.

5.2.1. Catalyst growth on quartz beads

Efforts to increase the yield of each Fe@NCNT synthesis initially centred around increasing the CVD quartz substrate surface area for deposition. This was achieved by loading the CVD tube with quartz beads (Multi-Lab Ltd, 6 mm OD × 6 mm L) in the furnace hot zone. These experiments were conducted at the very outset of this research, prior to establishing a reliable procedure for the production of Fe@NCNT. Therefore, scale-up over quartz beads was largely attempted using Fe@CNT, with the intention of applying an established scale-up process to Fe@NCNT production once both procedures had matured. A map of the furnace hot zone has been previously shown to correspond to increased thickness of the carbon layer, as seen in Figure 5.8. This makes proper placement of the quartz beads critical for scale-up. Quartz beads were loaded between 35-55 cm in the CVD furnace, corresponding to the area that experiences the most reliable temperatures and the greatest CNT deposition. The typical Fe@CNT synthesis process was then executed, and the Fe@CNT product could then be retrieved as a black powder coating the quartz tube wall and the surface of the quartz beads substrate.

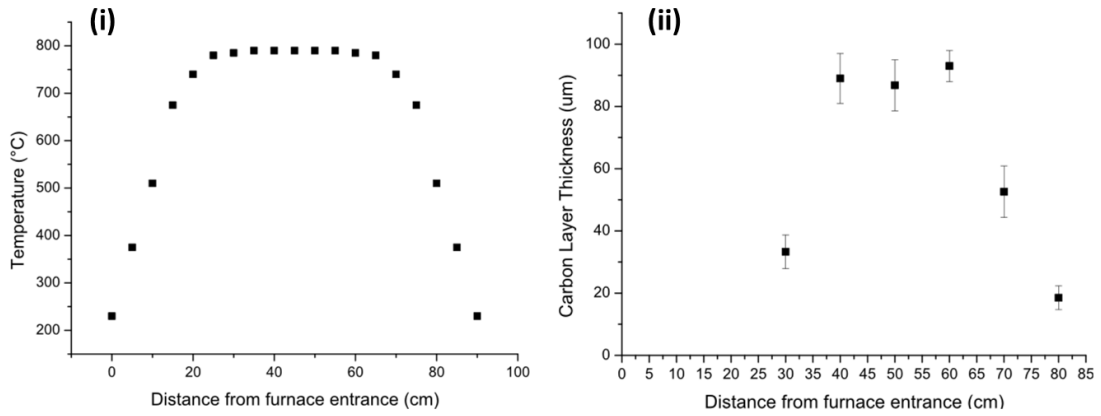

Figure 5.8. (i) Map of temperature against distance from the furnace entrance, and (ii) variation in carbon layer distance in relation to distance from the furnace entrance. Reproduced from reference 71.

While collection and activation of the Fe@CNT powder deposited on the quartz tube wall could be easily achieved using previously reported techniques,[70] the Fe@CNT deposited on the quartz beads could not be reasonably removed from the surface of the beads on a scale required for catalyst testing by scraping with a spatula. The Fe@CNT-beads were instead activated while still supported on the beads using the milder conditions that have been reported for Fe@CNT supported on cordierite monoliths (470 °C for 10 min in ambient air).[116] This was determined to be necessary after attempts to activate the Fe@CNT-beads using the same conditions as the Fe@CNT powder (570 °C for 40 min in ambient air) resulted in significant decomposition of the Fe@CNT-beads, oxidizing away the carbon support and leaving a red iron dust deposit behind on the previously blackened beads, as seen in Figure 5.9. Conversely, activation under the same conditions as the Fe@CNT-monoliths resulted in a significant amount of catalyst remaining on the beads without quantitative oxidation. This is likely due to the significantly greater availability of oxygen for the thin layer of Fe@CNT deposited on the quartz beads relative to the bulk powder when packed into the typical calcination tube. The activated Fe@CNT-beads were then collected by sonication in methanol for 30 min to dislodge the deposited Fe@CNT from the beads. The resulting Fe@CNT-in-methanol slurry was then transferred into a round bottom flask to remove the remaining methanol using rotary evaporation.

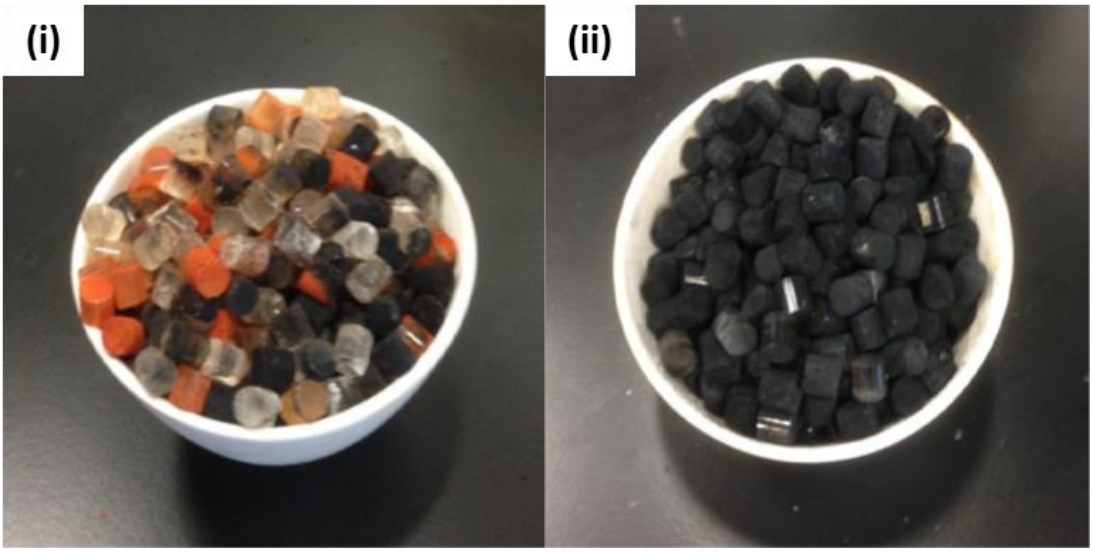

Figure 5.9. Fe@CNT-beads activated at (i) 570 °C for 40 min, and (ii) 470 °C for 10 min.

Comparison of the Fe@CNT-beads with the Fe@CNT deposited on the quartz tube wall via SEM and TEM revealed familiar bundles of Fe@CNT grown on both substrates, as seen in Figure 5.10. This initial assessment suggested that the loaded quartz beads were in fact capable of supporting the growth of Fe@CNT similar to those deposited on the quartz tube wall, thereby increasing yields per Fe@CNT synthesis run. However, further analysis of Fe@CNT-beads was required to confirm that they displayed a similar degree of crystallinity and chemical composition when compared with Fe@CNT deposited on the quartz tube wall.

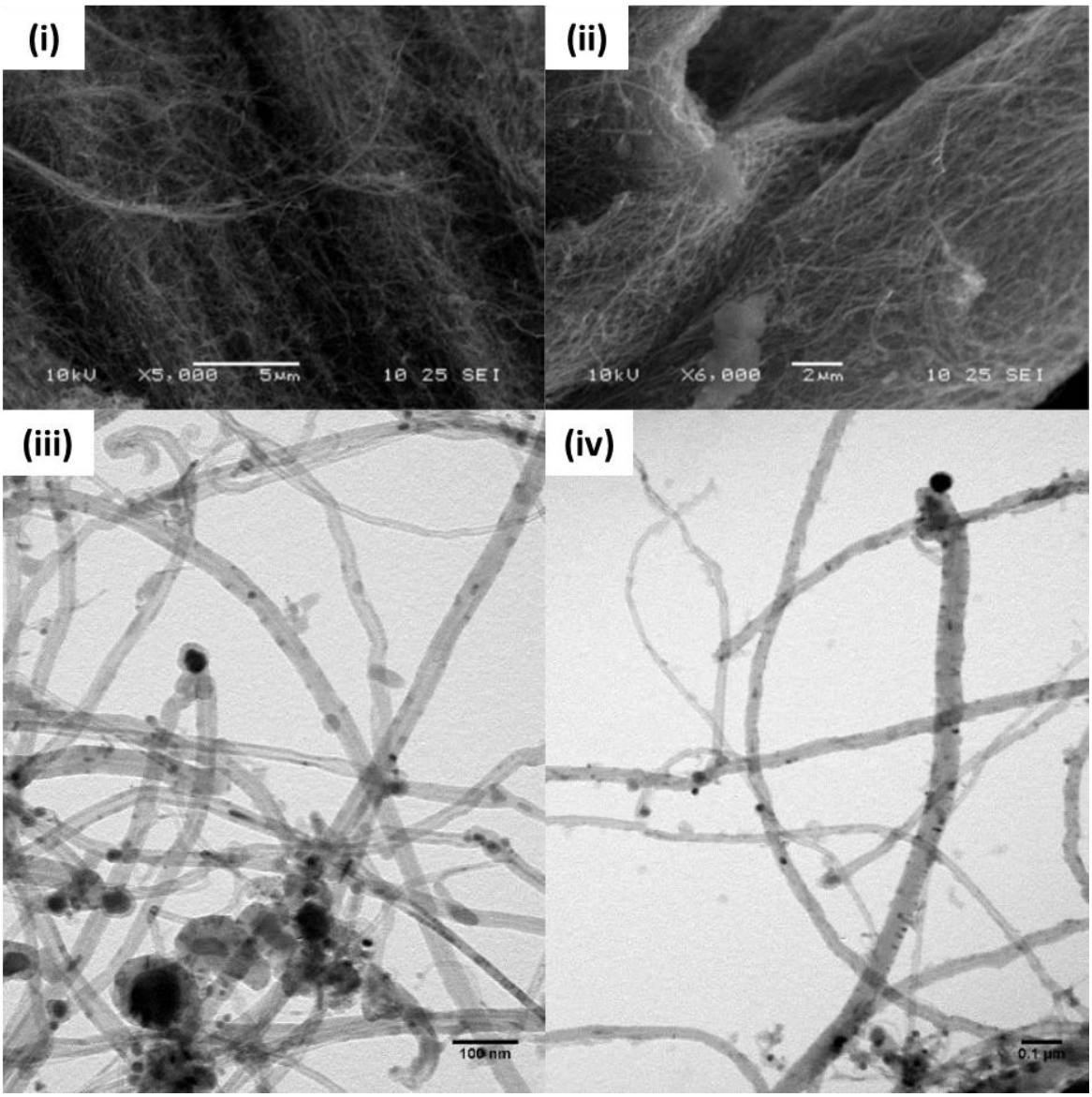

Figure 5.10. SEM and TEM micrographs of activated Fe@CNT retrieved from (i, iii) the quartz tube wall, and (ii, iv) the quartz beads substrate after activation and collection via sonication in methanol.

Interestingly, the Fe@CNT-beads displayed a lower I_D/I_G ratio in Raman analysis when compared with Fe@CNT collected from the quartz tube wall, as seen in Figure 5.11. The I_D/I_G ratios were calculated to be 0.49 and 0.78 for Fe@CNT collected from the quartz beads and quartz tube wall, respectively. This was unexpected, and suggests a greater degree of crystallinity in the Fe@CNT-beads. Furthermore, both of these I_D/I_G ratios are greater than the previously recorded value of 0.2 for Fe@CNT synthesized without any beads present in the quartz tube. The greater crystallinity of the Fe@CNT-beads relative to the wall-grown Fe@CNT suggests that the collection and activation process for the Fe@CNT beads may be more effective at purifying the sample than the processes used to collect and purify the wall-grown Fe@CNT. It may also be possible that the presence of quartz beads in the quartz tube

inhibits the regular supply of carbon to the Fe@CNT growing on the bottom half of the quartz tube, below where the beads rest, thereby impeding their ability to grow pure Fe@CNT. Overall, however, it appears that the mere presence of quartz beads within the quartz tube itself results in poorer crystallinity in the Fe@CNT sample when compared with Fe@CNT deposited on the quartz tube wall without any added quartz beads.

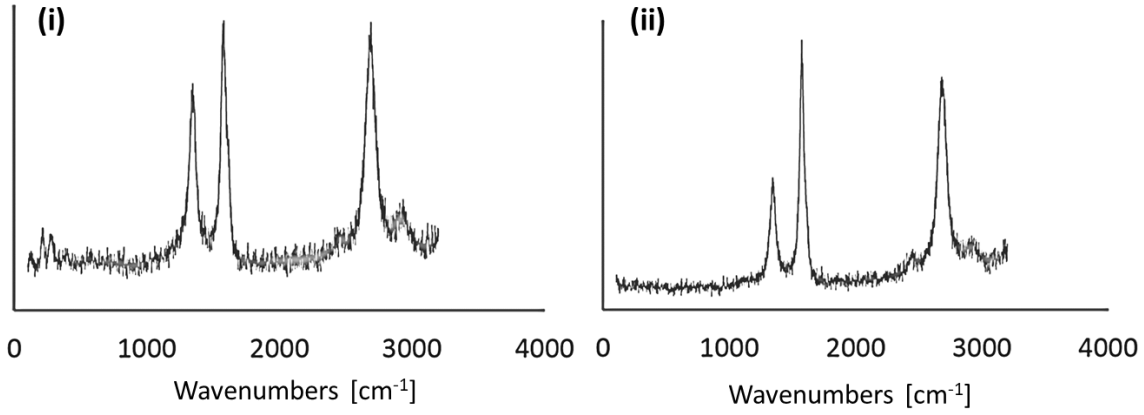

Figure 5.11. Raman spectra of activated Fe@CNT deposited on (i) the quartz tube wall, and (ii) the quartz beads substrate after activation and collection via sonication in methanol.

When comparing the stability of Fe@CNT-beads versus Fe@CNT grown on the quartz tube wall, both samples displayed similar rates and profiles of decomposition in air, as seen in Figure 5.12. A larger mass percentage remained after the decomposition of the Fe@CNT-beads, which was attributed to a larger amount of quartz contamination present in the sample. This increased quartz contamination likely originated from chipping of the beads into the sample during the sonication process, resulting in quartz shards that are difficult to separate from the bulk powder. Despite different degrees of crystallinity observed in the Raman spectra of these materials, TGA suggested similar that both samples possessed similar thermal stability. This might support the theory that the larger I_D/I_G ratio observed for the Fe@CNT grown on the quartz tube wall was largely due to greater amorphous carbon deposition on the tube wall due to impeded carbon supply caused by the presence of the quartz beads in the CVD tube. This amorphous carbon is likely to decompose early in the TGA ramp without a significant mass contribution, though even a small amount could impact the I_D/I_G ratios observed via Raman spectroscopy.

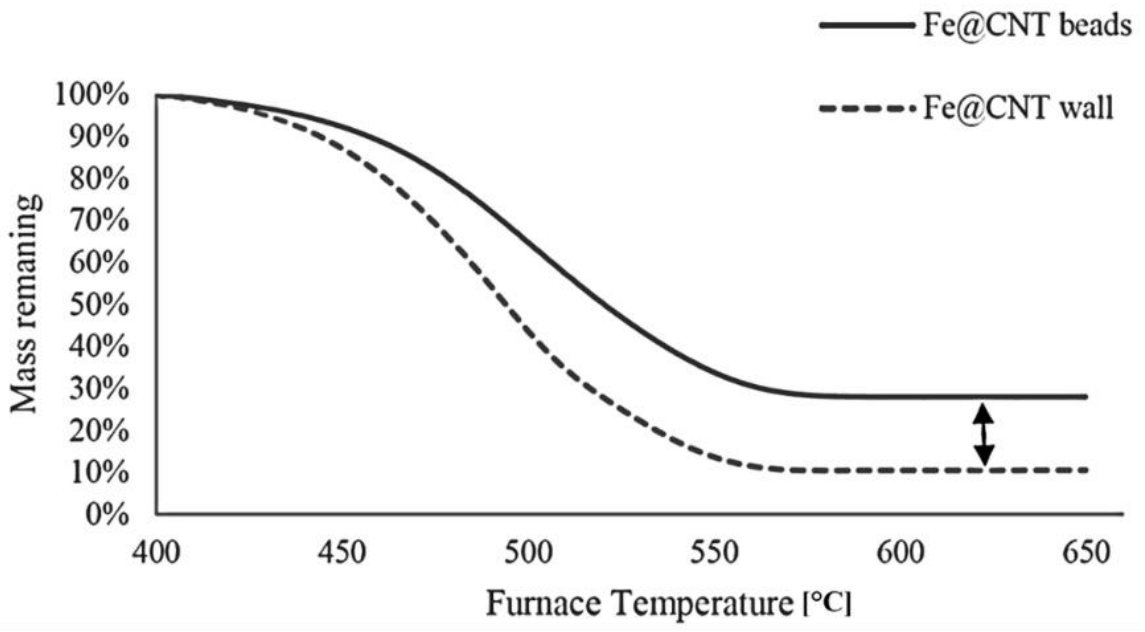

Figure 5.12. TGA decomposition profile of Fe@CNT grown on quartz beads versus the quartz tube wall in air.

Synthesizing Fe@CNT using beads in the CVD tube resulted in a positive, but limited increase in overall production capacity. The yield of Fe@CNT synthesized with beads ranged from 445-726 mg, with an average yield of ca. 590 mg compared to typical yields of ca. 400-500 mg without beads, as seen in Table 5.2. This represented an average increase of 18-48%. However, the process of producing Fe@CNT with beads required significantly increased time, processing, and generated a significant amount of methanol solvent waste while occasionally providing no increased yield at all. Furthermore, while microscopy confirmed the presence of Fe@CNT-type materials grown on the quartz beads, variability in the Raman spectra of Fe@CNT-beads samples, wall samples, and samples deposited without any beads present gave rise to concerns over the purity and consistency of samples produced in the presence of the quartz beads substrate. As a result, it was concluded that a simpler and more reliable method for scale-up should be pursued.

Table 5.2. Synthesis yields of Fe@CNT grown with beads and without beads.

Sample run	**Specific mass yield [g]**			**Total mass yield**
	Beads	Wall 35-55 cm	Wall 55+ cm	**[g]**
1	N/A	0.30	0.01	0.31
2	0.54	0.15	0.01	0.71
3	0.33	0.10	0.02	0.45
4	0.43	0.10	0.20	0.73
5	0.52	0.11	0.01	0.64
6	N/A	0.38	0.04	0.42
7	0.37	0.07	0.02	0.46

5.2.2. Increased CVD injection time and volume

Subsequent efforts to scale-up Fe@NCNT production centred around increasing the CVD injection volume and run duration. This allowed for sustained injection rate over a longer period of time in hopes of depositing more CNT in the furnace hot zone. The total injection volume and hold time was progressively increased to the maximum volume that could be injected by the syringe/pump system (40 mL). The Fe@NCNT yield was measured with each 10 mL increase in injection volume, as seen in Figure 5.13.

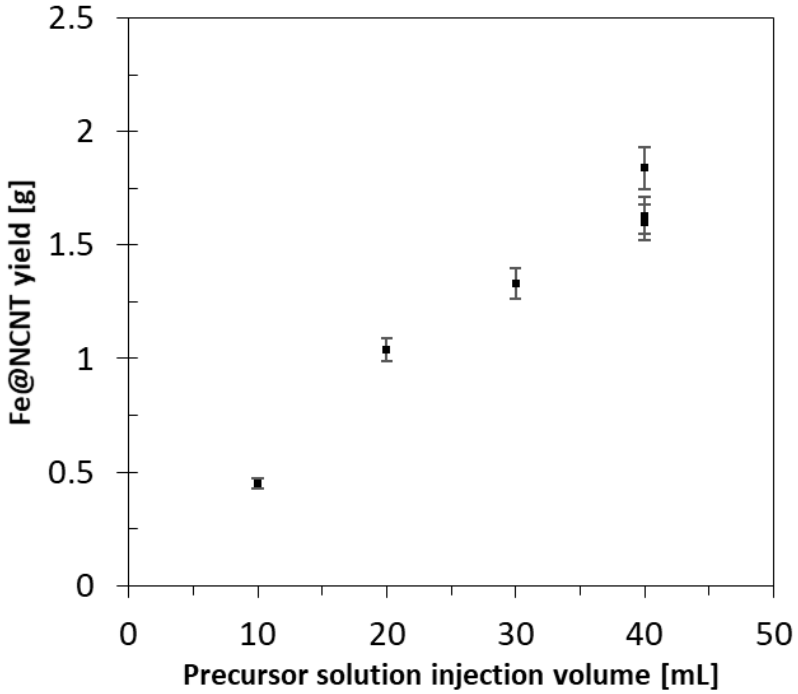

Figure 5.13. Fe@NCNT yield using different injection volumes. A constant injection rate of 10 mL hr^{-1} was used.

Fe@NCNT yield increased approximately linearly with increased injection volume, though some diminishing returns may have been present as the average yield decreased from 0.045 g mL^{-1} when injecting 10 mL to 0.040 g mL^{-1} when injecting 40 mL. The increased bulk yield per synthesis using a 40 mL injection volume represented a significant improvement in work flow efficiency, as seen in Table 5.3. It allowed for the execution of 3 CO_2 hydrogenation reactions per catalyst synthesis run compared to 1 reaction per 1-2 synthesis runs using the original 10 mL injection method, with a similar day-long reaction time when factoring in time for furnace ramp-up and cooldown.

Table 5.3. Fe@NCNT bulk yield, specific yield, and corresponding number of CO_2 hydrogenation tests achievable per CVD synthesis run using different injection volumes.

Injection volume [mL]	Fe@NCNT yield [g]	Specific yield [g mL^{-1}]	CO_2 reactions per synthesis
10	0.45	0.05	1
20	1.04	0.05	2
30	1.33	0.04	2
40	1.84	0.05	3
40	1.63	0.04	3
40	1.60	0.04	3

When analysed using SEM and TEM, the Fe@NCNT samples displayed similar morphologies regardless of CVD injection volume, as seen in Figure 5.14. Similar bundles of tubes with comparable diameters, shapes, embedded iron particles and characteristic bamboo segmentation were observed in all samples. However, a potential difference was noted in the thickness of the deposited Fe@NCNT layer, which appeared to increase from ca. 100 μm using a 10 mL injection to ca. 400 μm using a 40 mL injection. This was an unexpected but reasonable result, as increasing the duration of the deposition process logically increases the length of the deposited tubes rather than resulting in more nucleation sites for the Fe@NCNT growth process. There is little reason to assume that the chemical composition of the catalyst should change significantly with increasing tube length, however. This suggested that this increased injection volume technique might allow for successful scale-up of Fe@NCNT production without significantly altering the composition of the catalyst.

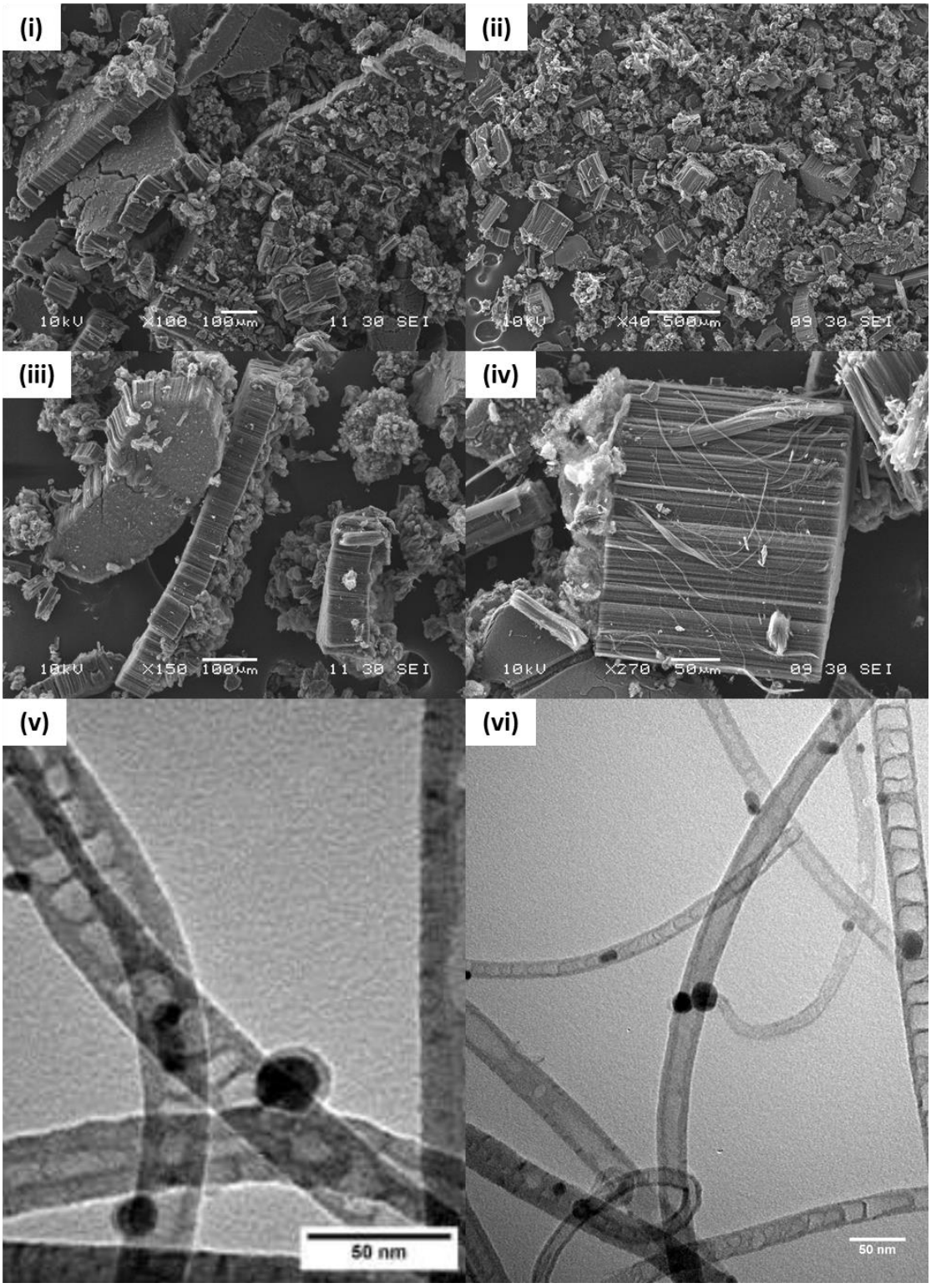

Figure 5.14. SEM and TEM micrographs of Fe@NCNT synthesised using (i, iii, v) a 10 mL synthesis injection, and (ii, iv, vi) a 40 mL synthesis injection.

Subsequent Raman analysis of Fe@NCNT synthesised with different injection volumes displayed similar peak positions and I_D/I_G ratios across all samples, as seen in Figure 5.15. This confirmed a similar degree of crystallinity (and disorder) in the produced materials regardless of injection volume, and further supported the viability of upscaling with increased injection volume. Additionally, syntheses conducted using a 40 mL injection volume displayed good repeatability, with consistent peak positions and I_D/I_G ratios across multiple synthesis runs.

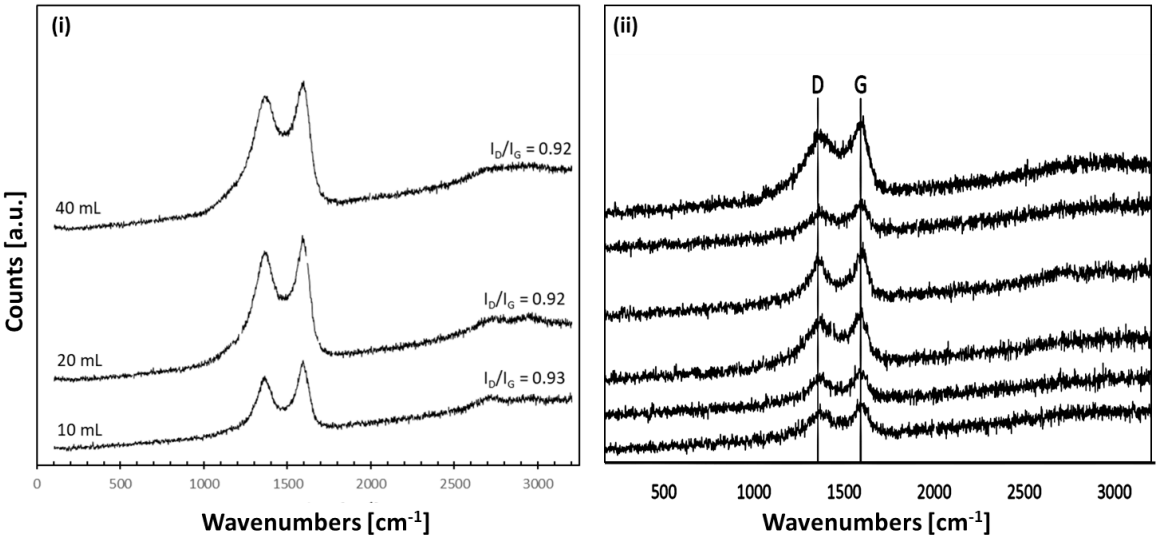

Figure 5.15. Raman spectra of (i) fresh Fe@NCNT samples synthesised at using different CVD injection volumes, and (ii) repeated syntheses using a 40 mL injection volume. I_D/I_G error is estimated to be ± 0.01.

Furthermore, limited differences were observed in the chemical compositions of samples produced from a 10 mL injection versus a 40 mL injection, as seen in Table 5.4. While using a larger injection volume appeared to slightly reduce nitrogen content in the final material, sample consistency appeared also appeared to be more uniform, with less variation between different scan sites in the same sample. As such, it was determined that increasing Fe@NCNT production via the use of larger injection volumes and longer hold times was capable of producing a consistent product without notable drawbacks. The up-scaled synthesis protocol using a 40 mL injection volume was used for the production of all Fe@NCNT samples going forward.

Table 5.4. Chemical composition of unactivated Fe@NCNT produced via 10 mL and 40 mL injection volumes, as determined via XPS.

		Composition [at. %]			
Sample	**Scan**	**C**	**N**	**O**	**Fe**
10 mL	1	94.6	3.1	2.1	0.2
	2	93.7	2.1	4.1	0.2
	3	93.5	4.1	2.2	0.2
40 mL	1	94.3	2.7	2.8	0.2
	2	94.4	2.8	2.6	0.2
	3	94.1	2.6	3	0.3
Avg 10	--	93.9	3.1	2.8	0.2
Avg 40	--	94.3	2.7	2.8	0.2
Stdev 10	--	0.6	1.0	1.1	0.0
Stdev 40	--	0.2	0.1	0.2	0.1

5.3. **Fe@NCNT activation conditions**

It has been previously determined that the catalytic iron particles in Fe@CNT-type materials remain obscured beneath a thin graphitic carbon layer directly after synthesis, as seen in Figure 5.16. This layer prevents them from participating CO_2 hydrogenation must therefore be removed via calcination in air to activate the catalyst prior to CO_2 hydrogenation. Activation at 570 °C for 40 minutes has been shown to sufficiently remove the graphitic layer in Fe@CNT, resulting in ca. 1 at. % iron exposure as determined by XPS.[70] However, due to lattice defects that form as a result of nitrogen doping in Fe@NCNT, their thermal stability is decreased and milder activation conditions must be applied to expose similar levels of iron without destroying the catalyst.

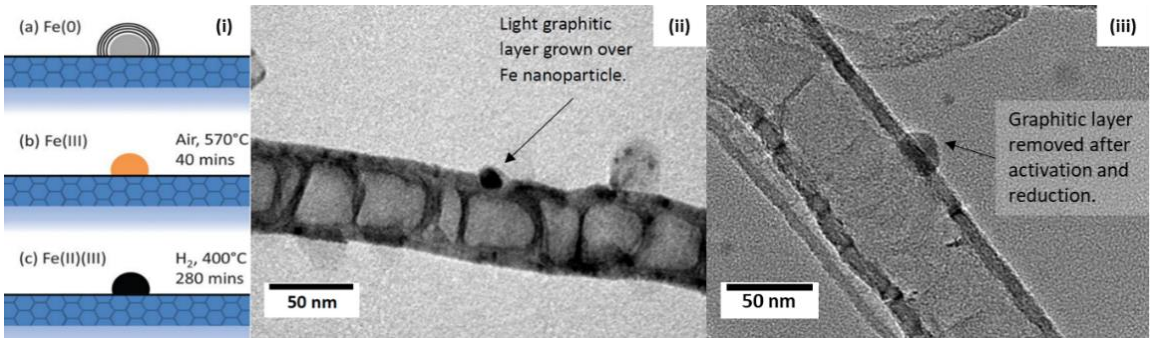

Figure 5.16. (i) Schematic illustrating the oxidation states of the iron nanoparticles in Fe@CNT (a) as synthesised, (b) following thermal activation, and (c) following reduction prior to catalytic testing. Removal of the protective graphitic layer during the activation step is clearly communicated. (ii) TEM micrograph of freshly synthesized Fe@NCNT clearly exhibiting the presence of a similar graphitic layer over the iron nanoparticle. Reproduced from reference 70. (iii) TEM micrograph of activated and reduced Fe@NCNT illustrating the removal of the graphitic layer after activation and a similar sample morphology after reduction.

5.3.1. Determining thermal stability and iron exposure

TG-MS, TEM and XPS were used to determine suitable activation conditions for the Fe@NCNT. The decomposition of Fe@NCNT was monitored in air via TG-MS in an attempt to identify a distinct decomposition temperature for the graphitic layer prior to the onset of decomposition for the NCNT support material. The TG-MS profile of Fe@NCNT in air is presented in Figure 5.17. The rate of mass loss began increasing significantly at ca. 300 °C until peaking at ca. 415 °C. No distinct decomposition mode for the graphitic layer was detected in either the mass loss or CO_2 counts over the range of tested activation temperatures. This suggests that either the decomposition of the graphitic layer is too small to be detectable, or the graphitic layer has a similar thermal stability to the NCNT support and must therefore be removed through a quick activation procedure that serves to expose the iron particles before the NCNT support can be significantly damaged. Thus, TGA was used primarily to determine the onset temperature for Fe@NCNT decomposition in air, which could in turn be used to inform a rough range of activation temperatures that could be probed in conjunction with TEM, XPS and catalytic testing to establish a more precise activation procedure.

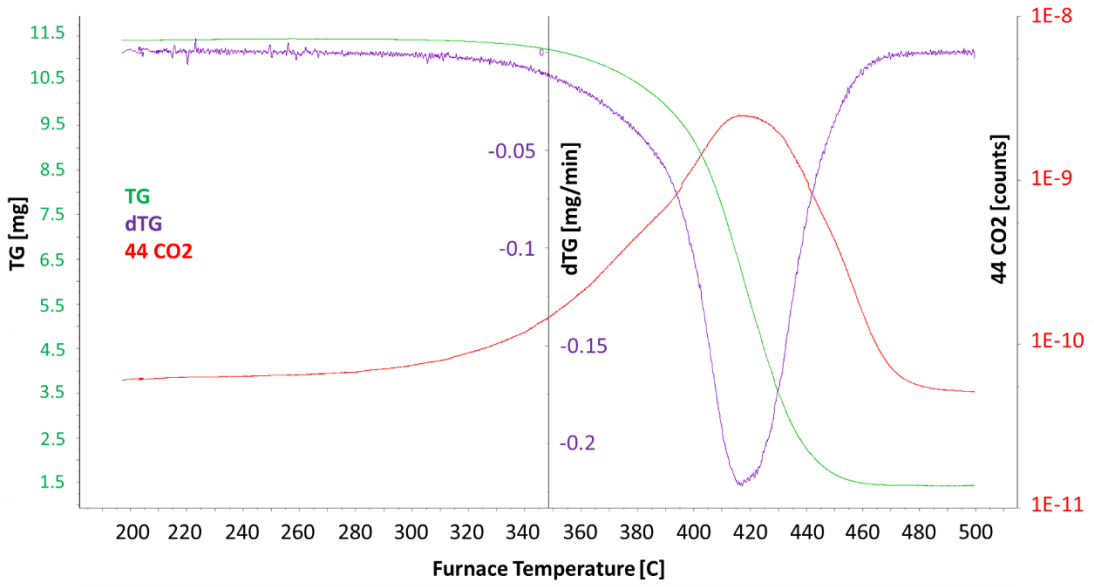

Figure 5.17. Mass loss and CO_2 counts of Fe@NCNT from 280-420 °C, as measured via TG-MS. TG refers to the measured mass, dTG refers to the rate of change in the measured mass, and 44 refers to CO_2 counts registered by the detector.

TEM micrographs were subsequently corroborated with XPS analysis of Fe@NCNT at different activation temperatures to monitor iron exposure and the integrity of the NCNT support after a 1 hour activation procedure. TEM micrographs indicated limited degradation to the Fe@NCNT structure up until 420 °C. At this point significant iron particle agglomerates became visible and the NCNT support became visibly degraded as the oxidation conditions became too severe, as seen in Figure 5.18.

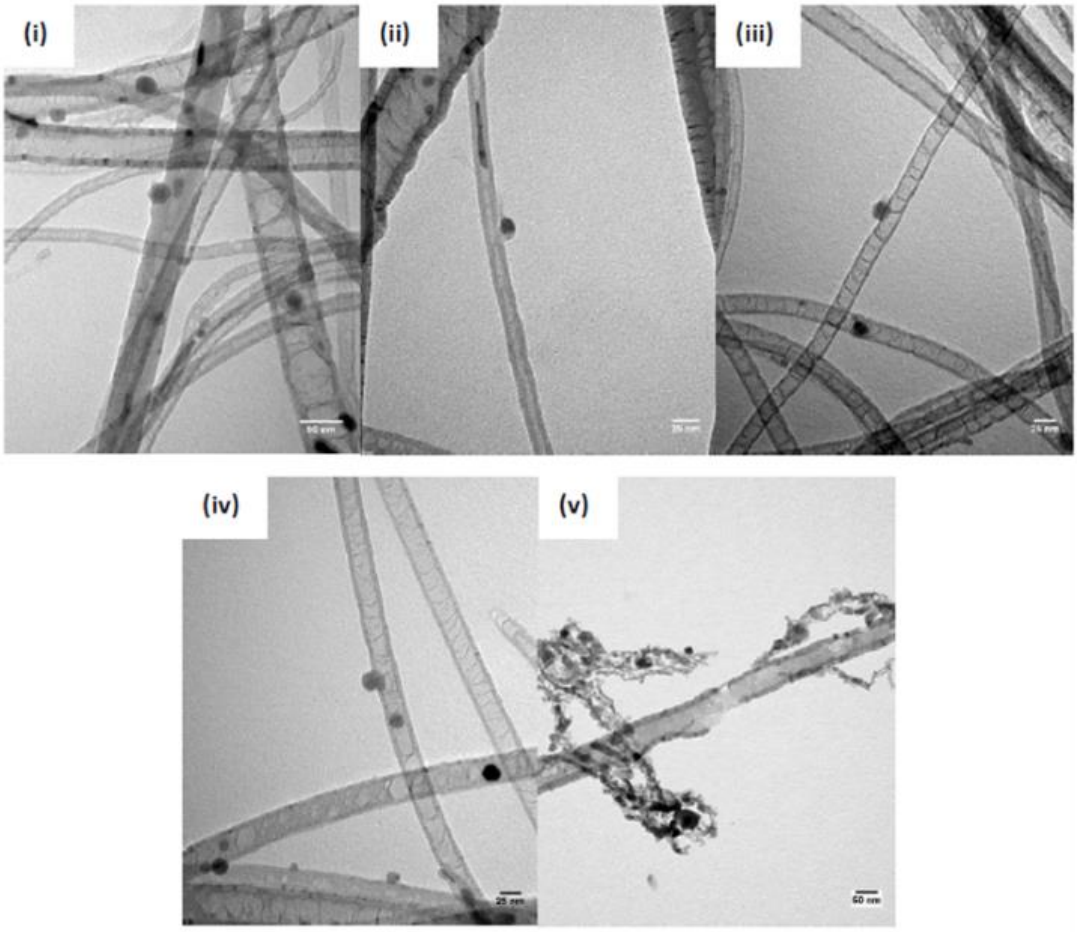

Figure 5.18. TEM micrographs of Fe@NCNT showing increased degradation and disintegration with increasing activation temperature. Samples were activated in air for 1 hour at (i) 340 °C, (ii) 360 °C, (iii) 380 °C, (iv) 400 °C, and (v) 420 °C.

Stability of Fe@NCNT up to 400 °C corresponded well with XPS analysis of samples activated at different temperatures, as seen in Figure 5.19. Increasing activation temperature appeared to increase average iron and carbon content while decreasing nitrogen content. The increase in iron is attributed to increased exposure of the iron nanoparticles from beneath their graphitic layers up until a maximum of ca. 1 at. % iron content, corresponding to ca. 4.5 wt. % iron at the surface. This corresponds well with previously reported surface iron content in Fe@CNT.[70] However, it should be noted that while the surface iron content is measured at ca. 1 at. % via XPS, the total metallic iron content of the catalyst is noted to be ca. 10-20 wt. % after complete oxidation via TG-MS. This discrepancy is due to the substantial amount of iron present in the CNT interior bore, which is not detected by the surface-level penetration of XPS in the sample. The decrease in nitrogen from 4 at. % after synthesis to ca. 3 at. % after activation at 400 °C is attributed to the loss of more weakly bound nitrogen species such as pyridinic nitrogen and surface-adsorbed N_2 and N—O species.[227, 264, 266, 270, 275] This in good agreement with the relative decrease of these species in the N 1s region of the XPS spectrum after activation, as previously discussed. Interestingly, oxygen content was ca. 3 at. % after synthesis, increasing to ca. 5 at. % after activation and remaining roughly constant or decreasing slightly to ca. 4.5 at. % at 400 °C.

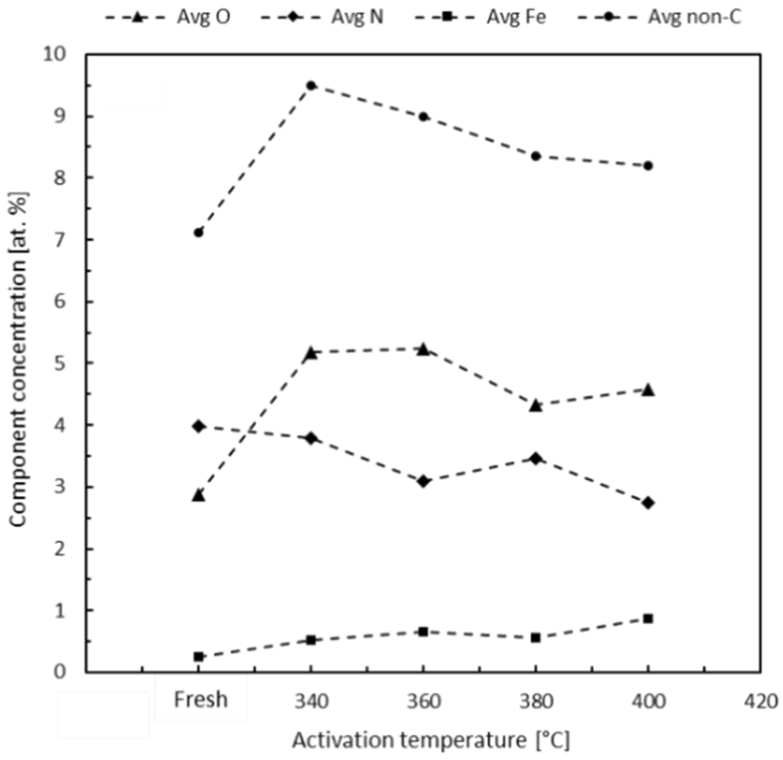

Figure 5.19. Effect of activation temperature on Fe@NCNT composition, as determined via XPS.

The initial oxygen content after synthesis is unexpected and suggests some degree of oxygen functionalisation during the CVD process. The CVD synthesis tube is ensured to be airtight using a subaseal and parafilm and flushed many times with argon prior to Fe@NCNT production, and it is unlikely that so much oxygen would correspond to oxidation of the small amount of iron that is initially exposed in the sample after synthesis. Thus, the origin of this initial oxygen content remains unclear but may be indicative of some amount of quartz contamination in the XPS sample or unexpected oxygen contamination during synthesis. The increase in oxygen content is expected, as this corresponds with iron oxide formation as the nanoparticles are exposed and oxidised during the activation process. It is noteworthy, however, that oxygen content remains roughly constant or decreases slightly with increasing activation temperature, even as more iron is exposed and oxidised by the activation process. This suggests a release of oxygen from the sample that matches or outpaces iron oxide formation during activation. While the exact origin of this oxygen release remains unclear, it is possible that this corresponds to the desorption of surface oxygen and N—O species. Removal of impurities such as physisorbed H_2O, and sintering of iron oxide particles to reduce their surface area my also reasonable causes. The increase in overall carbon content is likely a relative increase, observed as a result of nitrogen and oxygen loss in the samples as the activation temperature increases.

5.3.2. Effect of activation conditions on reactivity

In order to probe the effect of activation temperature on catalytic activity, an initial screening of Fe@NCNT activated at different temperatures were applied in CO_2 hydrogenation, as seen in Figure 5.20. An uncalcined sample was also tested for comparison, displaying negligible activity as expected (less than 2% conversion at all reaction temperatures). While catalyst activation resulted in a significant increase in activity relative to the uncalcined sample, there was little difference in performance between any of the activated samples aside from the sample activated at 380 °C. This sample consistently displayed greater conversion and marginally improved hydrocarbon selectivity at all reaction temperatures. However, no notable difference in catalyst composition or morphology could be determined via Raman, TEM or XPS. This abnormal peak activity was therefore attributed to experimental error. An activation temperature of 400 °C for 1 hour was eventually chosen as the activation temperature to use for Fe@NCNT going forward. This resulted in similar performance relative to catalyst activated other temperatures, and displayed a similar level of iron exposure as determined via XPS (ca. 1 at. %). Maintaining similar exposed iron contents

between Fe@CNT and Fe@NCNT in such a manner was intended to allow for more reasonable attribution of any differences in reactivity between them to the presence or absence of nitrogen in the catalyst support, rather than differences in their catalytic iron species or metal loading.

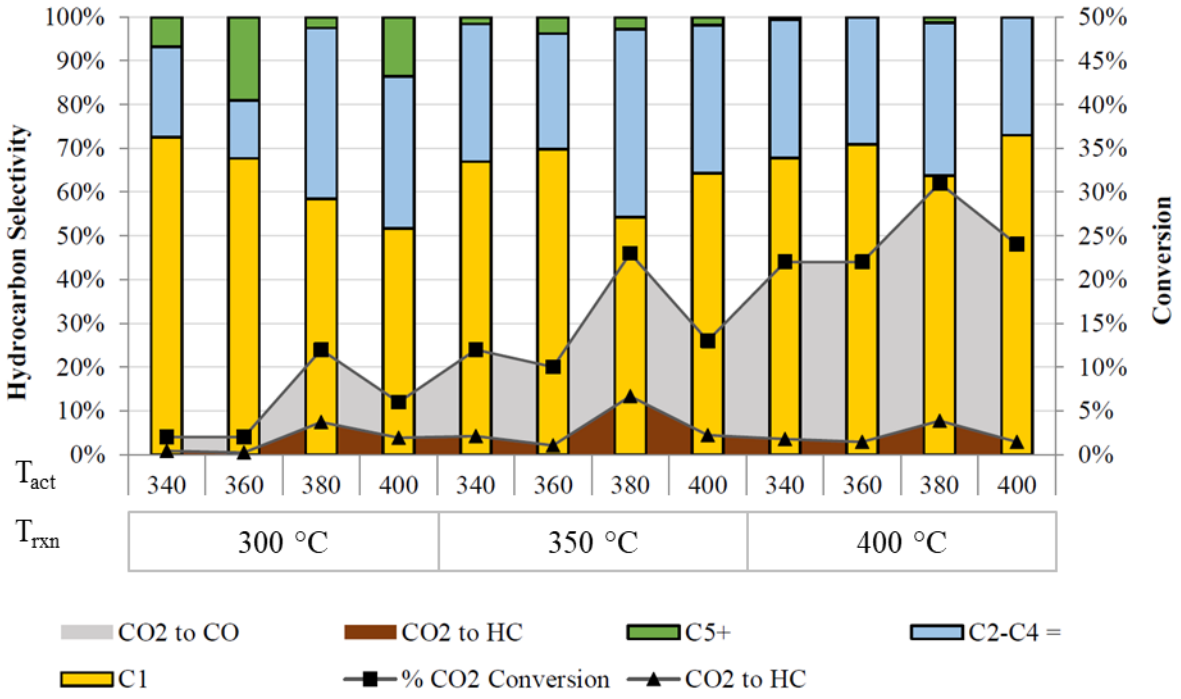

Figure 5.20. Conversion and product selectivity for catalysts activated at different temperatures. In all cases, 0.4 g Fe@NCNTs were reduced for 3 hours at 300 °C under 20 sccm H_2 and 1 bar, then reacted at 300 °C, 350 °C, and 400 °C under 5 sccm CO_2 and 15 sccm H_2 at 1 bar. The reactor was allowed to equilibrate for 1 hour between each temperature change. Carbon balances for all samples were calculated to be between 100-110 %. CLC refers to the calcination temperature used to activate the samples. Quantification error is estimated to be ± 5%.

Chapter 6 – Fe@NCNT reactivity

A successful technique for the production of Fe@NCNT and valid activation conditions to expose their catalytic iron sites have been described in Chapter 5. Chapter 6 therefore concerns the results of investigations into the unique reactivity of Fe@NCNT when applied in CO_2 hydrogenation. Notable differences between Fe@CNT and Fe@NCNT, enhanced reactivity arising from the addition of promoter metals, and the mechanistic implications of these findings are discussed here.

Section 6.1 discusses the reactivity of pristine Fe@NCNT when initially compared with Fe@CNT, to establish a baseline estimation of the effect of nitrogen doping prior to any further process optimisation. The effects of reaction conditions such as temperature and pressure upon the RWGS/FT process over Fe@NCNT are subsequently discussed. A full screening of relevant promoter metals is also detailed, in order to identify synergistic relationships between the iron nanoparticles, promoter metals at the catalyst surface, and nitrogen doping in the CNT support. The results of these promoter screening studies culminate in a full design of experiments investigating the combined effects of reaction conditions and sodium promoter content in the Fe@NCNT.

Section 6.2 discusses the mechanistic implications of the observed reactivity of Fe@NCNT in RWGS/FT CO_2 hydrogenation. Further characterisation of the material is conducted to determine the effect of nitrogen doping on the adsorption properties of reactant molecules at the catalyst surface. This characterisation is supported by further catalytic testing and molecular dynamics simulations to verify the differences in reactant adsorption observed between Fe@CNT and Fe@NCNT. The chapter concludes with section 6.3, which summarizes several ancillary studies on *in situ* CVD particle size control during Fe@CNT and Fe@NCNT production, and a collaboration investigating the capabilities of Fe@NCNT in sustainable oxalic acid production.

The work discussed in this chapter has been used to produce the following publications:

D. L. Williamson, C. Herdes, L. Torrente-Murciano, M. D. Jones and D. Mattia, *ACS Sustainable Chemistry & Engineering*, 2019, **7**, 7395-7402.

M. Ventura, D. Williamson, F. Lobefaro, M. D. Jones, D. Mattia, F. Nocito, M. Aresta and A. Dibenedetto, *ChemSusChem*, 2018, **11**, 1073-1081.

6.1. **Fe@NCNT reactivity and promotor addition**

Upon determining valid conditions for the activation of the Fe@NCNT catalyst, the reactivity of the catalyst was thoroughly investigated. This section first discusses an initial comparison of the Fe@NCNT catalyst with Fe@CNT under previously tested CO_2 hydrogenation conditions.[70, 72] This serves to determine a baseline influence of nitrogen doping in the catalyst support. The effect of temperature and pressure are subsequently discussed, followed by a screening of potentially interesting promoter metals and a full design of experiments to evaluate the influence of temperature, pressure and sodium promoter loading upon Fe@NCNT reactivity.

6.1.1. Initial comparison of Fe@CNT and Fe@NCNT

To establish a baseline understanding of the influence of nitrogen doping in the CNT support, the reactivities of Fe@NCNT and Fe@CNT were initially compared, as seen in Figure 6.1. Conditions were chosen based upon previously established experiments investigating Fe@CNT,[70, 72] which were optimised to provide high conversion, hydrocarbon production and olefin selectivity. Readers should note that detailed instructions concerning interpretation of the CO_2 conversion and product selectivity plots presented throughout this thesis (e.g. Figure 6.1) are located in Appendix 3.

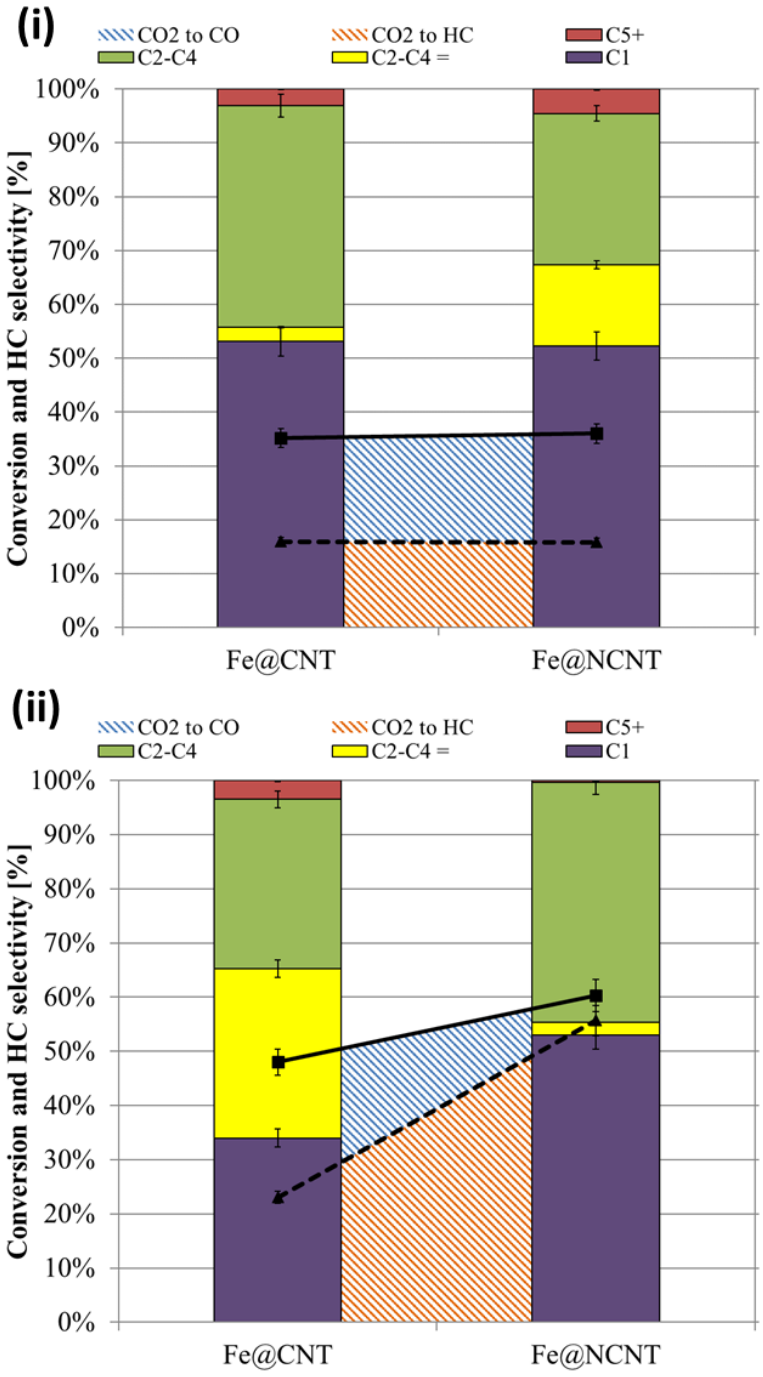

Figure 6.1. Comparison of Fe@CNT and Fe@NCNT reactivity at (i) 1 bar, and (ii) 15 bar. Aside from pressure, reaction conditions were fixed at 370 °C, 8 sccm, a 3:1 H_2:CO_2 feed gas ratio, and 0.4 g catalyst. Quantification error is estimated to be ± 5%.

At 1 bar, Fe@CNT and Fe@NCNT display nearly identical conversion, hydrocarbon production and selectivity, aside from a slightly increased ratio of olefin to paraffins observed over Fe@NCNT. These values are in good agreement with previously published CO_2 conversion and product selectivity over pristine Fe@CNT.[70] While this confirmed good repeatability between our reaction setup and previous protocols, the lack of variance between

Fe@CNT and Fe@NCNT was unexpected and suggested limited influence from nitrogen doping. At an elevated pressure of 15 bar, however, reactivity and selectivity shifts significantly and a distinct effect from nitrogen doping is observed. CO_2 conversion and methane selectivity increases substantially using Fe@NCNT, while olefin, CO, and long-chain hydrocarbon selectivity are significantly diminished.

When considering these results in the context of competing RWGS and FT reactions at the catalyst surface, this data provides initial evidence that nitrogen doping serves to enhance RWGS activity and initial FT conversion. At low pressure, this effect appears limited. The RWGS and FT reactions proceed at a similar rate regardless of nitrogen doping, with largely identical product distributions. The greater olefin production observed over Fe@NCNT could arise from electronic modulation of the catalytic iron particles due to nitrogen doping.[227, 265] However, the previously discussed XPS and XRD analysis of the iron species in Chapter 5 suggest negligible differences in iron species between Fe@CNT and Fe@NCNT. The slight difference in olefin production at atmospheric pressure is therefore more likely to be within experimental error. At 15 bar, the influence of pressure appears more pronounced over Fe@NCNT than Fe@CNT. The significant decrease in CO selectivity suggests that Fe@NCNT are more capable of consuming CO for FT conversion than Fe@CNT. This increased rate of CO consumption increases overall CO_2 conversion by shifting the equilibrium of the RWGS reaction further towards products, in addition to the already beneficial effect of pressure upon the RWGS reaction. However, the increase in methane selectivity, decrease in olefin production, and decrease in C_{5+} selectivity suggest that nitrogen doping also serves to inhibit further chain growth via subsequent FT polymerisation steps. As a result, Fe@NCNT provide increased CO_2 conversion and overall hydrocarbon production, but generate fewer valuable olefins and long-chain hydrocarbon products than Fe@CNT.

6.1.2. Effect of reaction conditions on unpromoted Fe@NCNT

The effects of temperature (Figure 6.2) and pressure (Figure 6.4) upon CO_2 hydrogenation over Fe@NCNT were subsequently investigated. Temperature has a significant effect upon the rates of both the RWGS and FT reactions, with the RWGS reaction becoming more thermodynamically favourable at higher temperatures.[68] However, the FT process favours production of more valuable long-chain hydrocarbons at lower temperatures.[146] Selectivity towards CO is also expected to increase at lower temperatures due to reduced FT activity. For this reason, the reaction temperature must be carefully tuned to balance high conversion with desirable hydrocarbon selectivity.

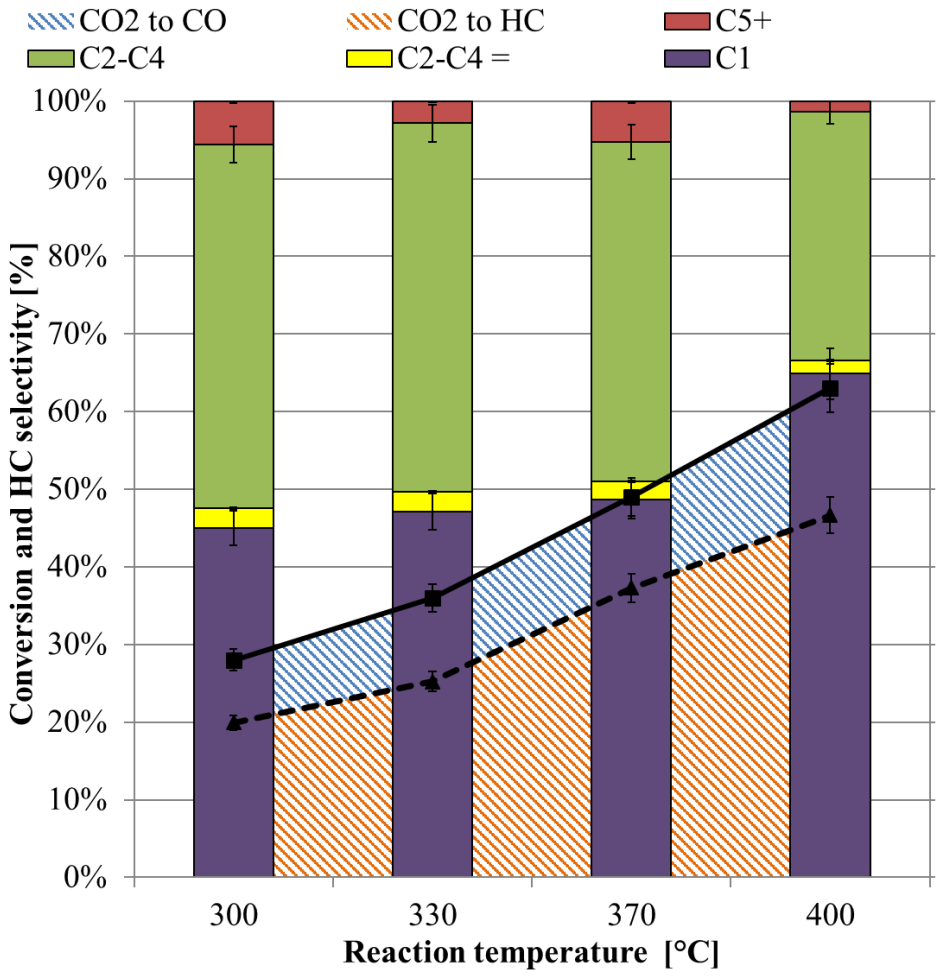

Figure 6.2. Effect of reaction temperature on the CO_2 hydrogenation performance of Fe@NCNT from 300-400 °C at 5 bar, 8 sccm, and a 3:1 H_2:CO_2 feed gas ratio. Quantification error is estimated to be ± 5%.

A reaction pressure of 5 bar was maintained while investigating the effect of temperature upon the Fe@NCNT CO_2 hydrogenation process. This was to done to ensure that some degree of the nitrogen influence observed in the initial Fe@CNT comparison experiments would be observed while varying temperature, without overshadowing the influence

temperature entirely as might occur at a high pressure of 15 bar. As expected, CO_2 conversion increases with reaction temperature from 300-400 °C. The product distribution of the process remains relatively constant between 300-370 °C. This suggests a limited benefit to maintaining a lower reaction temperature to target long-chain hydrocarbon production. Above 370 °C, CO selectivity remains similar while methane selectivity increases significantly. As a result, further catalytic testing was maintained at 370 °C in order to achieve high CO_2 conversion without tending towards methane production.

The continued increase in CO_2 and CO conversion over the tested temperature range of 300-400 °C suggests that both the RWGS and FT reactions remained rate limited up to (and possibly beyond) 400 °C. The observed activation energies (ΔE_a) of both reactions can therefore be estimated from the Arrhenius plot of the observed rate constants (k_{obs}) of the reactions at the measured temperatures versus 1000/T, as seen in Figure 6.3. Values for k_{obs} at each temperature are obtained from the observed rate of reaction (r_{obs}) and the observed reactant concentrations at each temperature. r_{obs} is defined as the moles of reactant (CO_2 for RWGS and CO for FT, respectively) converted per gram of catalyst per second (μmol $g_{Fe@NCNT}^{-1}$ s^{-1}). Values for r_{obs} and the reactant concentrations are experimentally obtained via GC-MS analysis of the product gases at each temperature. The true reaction orders of these processes remain unclear (both individually and combined). Therefore, the reactions are assumed to be first order with respect to each of their reactants in these calculations.

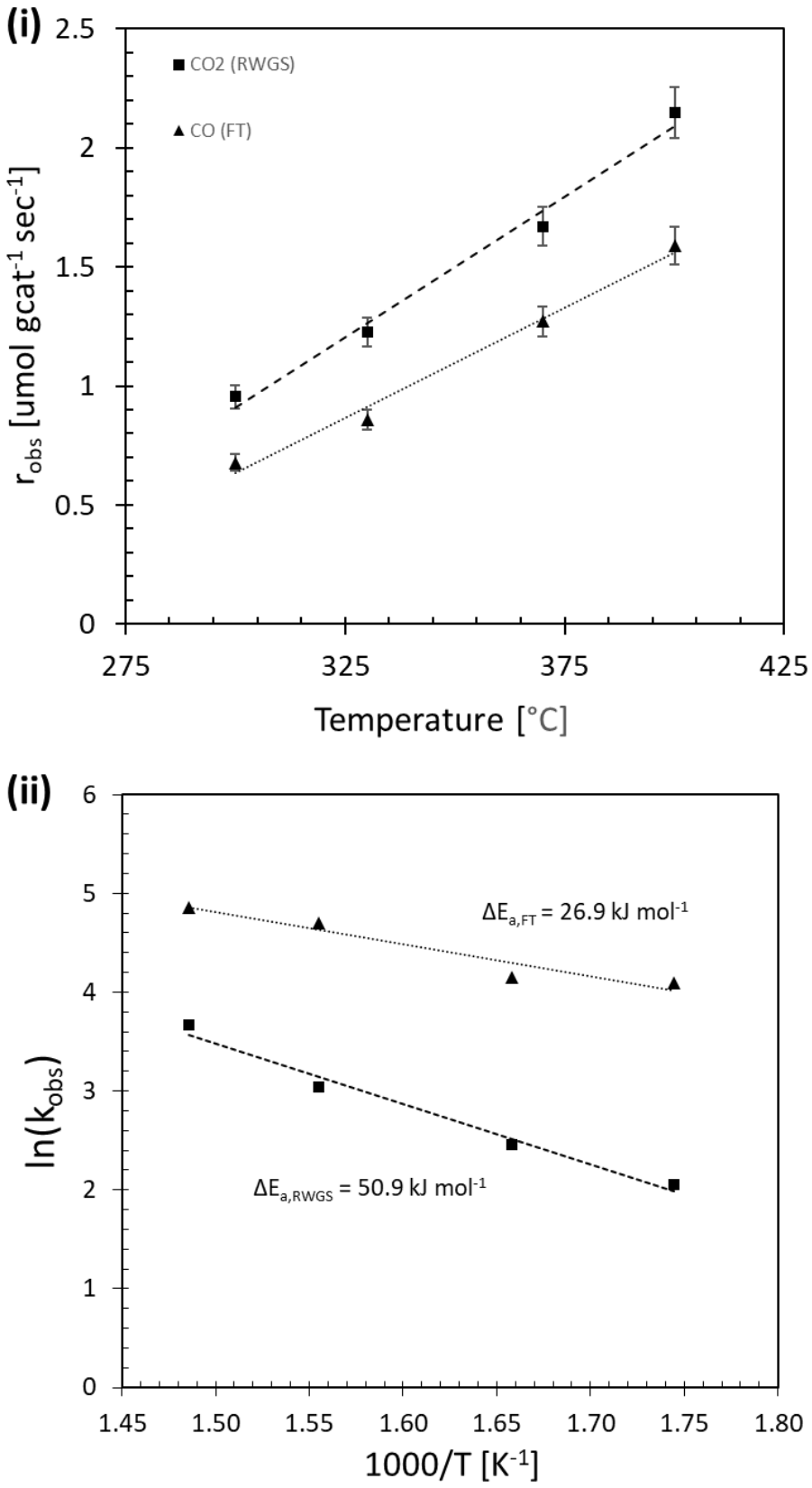

Figure 6.3. (i) Observed rates of reaction for the RWGS and FT processes over Fe@NCNT from 300-400 °C. (ii) Activation energies of the individual RWGS and FT reactions over Fe@NCNT from 300-400 °C.

The observed activation energies are $\Delta E_{a,RWGS}$ = 50.9 kJ mol^{-1} and $\Delta E_{a,FT}$ = 26.9 kJ mol^{-1}. It is noteworthy that the FT process appears to occur more readily than the RWGS reaction, but depends on the initial RWGS reaction taking place in order for FT to occur at all. This is in good agreement with the low CO selectivity observed over Fe@NCNT. Furthermore, these values are notably low when compared with literature. Activation energies for the RWGS reaction range from 40-120 kJ mol^{-1} over a variety of catalytic metals.[63, 166] Activation energies for the FT process have been cited as ca. 63-89 kJ mol^{-1} over iron catalysts.[166] This suggests that Fe@NCNT are highly suited for catalysing both processes, while being particularly amenable to FT catalysis. The observed rate of reaction ranges between r_{obs} = 0.97-2.14 $\mu mol_{CO2}\ g_{Fe@NCNT}^{-1}\ s^{-1}$. This is twice the rate of reaction of a previously reported Fe@CNT-monolith catalyst at 300 °C and 7.5 bar, and comparable to performance at 400 °C and 7.5 bar.[71] Furthermore, this matches or exceeds high literature values over other iron catalysts, even using harsher conditions and more efficient reactor designs (e.g. CSTR).[73, 74, 77, 318] However, this is significantly lower than the rate of ca. 38.15 $\mu mol_{CO2}\ g^{-1}\ s^{-1}$ reported by Chew *et al.* over a post-doped Fe/N-CNT catalyst.[78] It should be noted that a high flowrate of 50 L hr^{-1} and pressure of 25 bar were used in those experiments, and product selectivity significantly favoured CO production. It is likely that Fe@NCNT would display a higher rate of reaction under similar conditions, and significant process optimisation remains to be done to exploit their ideal performance. Care should be taken not to confuse the observed rate of reaction, r_{obs}, with the true or maximum possible rate of reaction in the current, unoptimized system. A wide variety of confounding factors may be masking the true rate of reaction (e.g. mass transfer limitations, heat transfer limitations, pressure drop, etc.).

Pressure plays an equally important role in influencing the rate and selectivity of the RWGS/FT process. Added pressure primarily affects the FT reaction, increasing the rate of reaction and favouring longer hydrocarbon production.[146] The FT process is irreversible and therefore does not possess a pressure-dependent equilibrium. Pressure increases the rate of the RWGS reaction and may influence the equilibrium if water is removed from the product stream (e.g. by condensation). The effect of increasing pressure from 1-25 bar can be seen in Figure 6.4. CO_2 conversion increases steadily with pressure until 15 bar, at which point it stabilises at ca. 60%. Hydrocarbon selectivity also increases with pressure until 15 bar, at which point it stabilises at ca. 90%. This suggests that the FT process experiences a greater pressure dependence than the RWGS reaction. Olefin selectivity remains significantly below

50% in all cases, oscillating between a low value of 10-20% as soon as pressure increases above 1 bar. Interestingly, C_{5+} selectivity appears to decrease with pressure. This is in direct conflict with the expected relationship between pressure and long-chain hydrocarbon production.[146] The origins of this unexpected reactivity are explored further in section 6.2. A pressure of 15 bar was noted to result in a desirable balance between CO_2 conversion, hydrocarbon selectivity, and relatively mild conditions.[64, 137] As such, 15 bar was frequently used as the reaction pressure in subsequent testing in hopes of achieving high CO_2 conversion and low CO selectivity while investing further means of modulating the hydrocarbon product distribution.

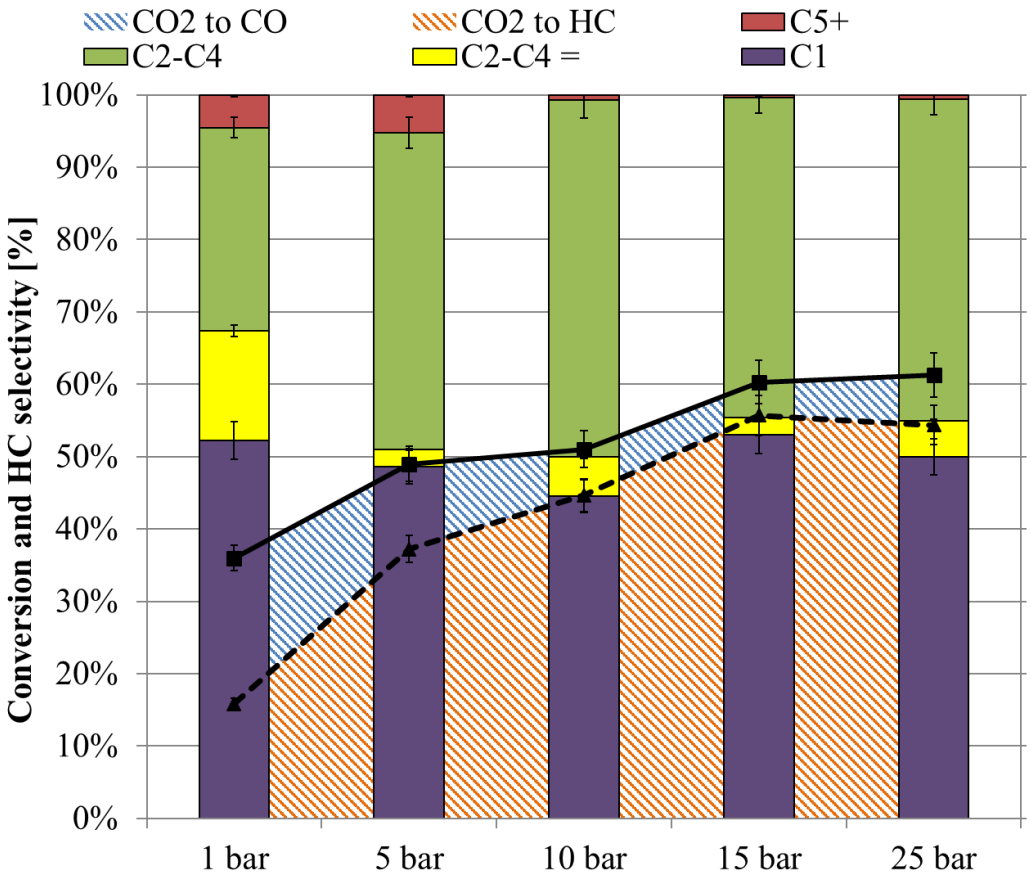

Figure 6.4. Effect of pressure on the CO_2 hydrogenation performance of Fe@NCNT. Aside from pressure, reaction conditions were fixed at 370 °C, 8 sccm, and a 3:1 H_2:CO_2 feed gas ratio. Quantification error is estimated to be ± 5%.

It should be noted that pressure drop across the catalyst bed likely influenced the outcome of these CO_2 hydrogenation experiments. Figure 6.5 shows the pressure drop measured across a reactor filled with various cordierite monolith supports, including monolith-supported Fe@CNT, compared with an equivalent mass of Fe@CNT powder. This shows that the powder packed bed experiences a significantly greater influence from pressure drop

relative to a supported catalyst. Furthermore, significantly more process optimisation is required to establish a kinetic model of the process where mass transfer limitations do not play a significant role. While the present investigations into Fe@CNT and Fe@NCNT are valuable in establishing the influence of nitrogen doping in the MWCNT support, it is likely that activity and selectivity could be further improved by testing the catalyst in an optimised, supported form rather than in a powder packed bed.

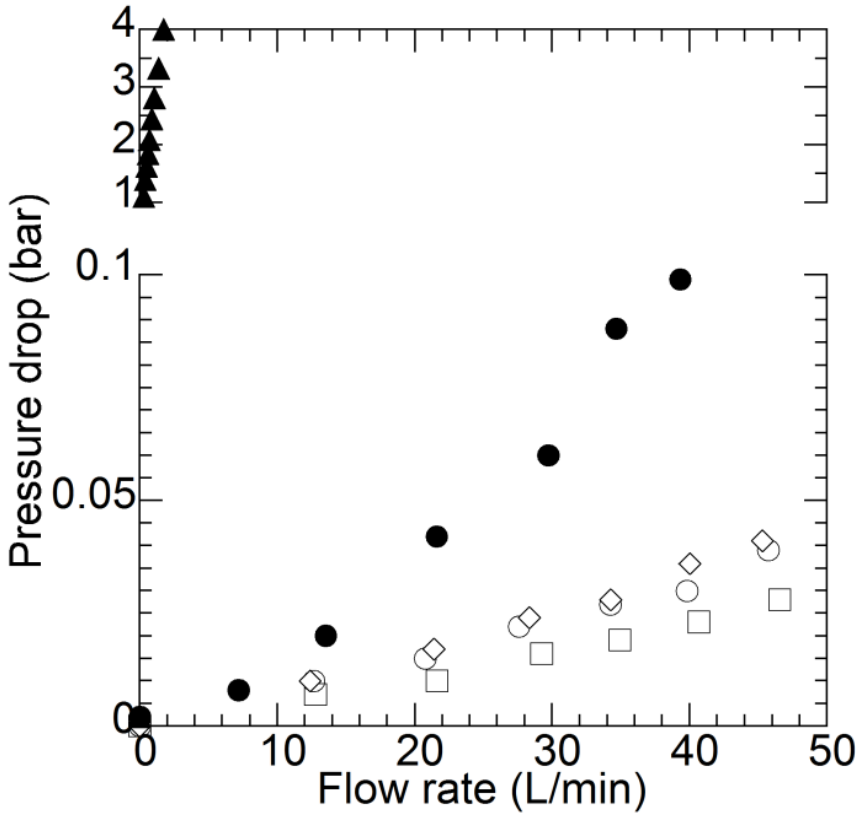

Figure 6.5. Pressure drop over a 10 cm × ½ inch Swagelok™ tube filled with: (○) 10 × 1 cm bare cordierite monolith; (◊) 10 × 1 cm CNT coated cordierite monolith; (●) 10 × 1 cm alumina washcoated cordierite monolith; (□) empty reactor tube; and (▲) equivalent mass of CNT powder in packed bed configuration. Reproduced from reference 71.

6.1.3. Effect of promoter addition

Alkali- and platinum-group promoter metals have often been used to enhance the activity and selectivity of iron-based HTFT catalysts. Their enhanced activity is attributed to greater basicity originating from the promoter metals, resulting in improved CO_2 adsorption, easier iron reduction and overall greater reducing potential from the catalyst.[72] Cu, K, Mn, Cr and Zn are also significantly investigated, though these appear to be primarily applied to enhance the activity of precipitated iron catalysts during synthesis.[72, 74, 134, 140] A variety of promoters were therefore added to Fe@NCNT via wet impregnation and screened to identify synergistic reactivity between the iron, nitrogen, and promoter dopants, as seen in Figure 6.6. Dopants were considered attractive if they might decrease CO and methane selectivity, or increase CO_2 conversion, long-chain hydrocarbon production, and the ratio of olefins to paraffins. Previous investigations into promoted Fe@CNT were used as a basis for this screening.[72] These studies revealed that Cs and Na were the most effective alkali promoters for Fe@CNT, resulting in enhanced CO_2 conversion, olefin production, and C_{5+} selectivity when compared with other alkali species. Pd resulted in the greatest increase in CO_2 conversion of all of these promoters, though olefin production and C_{5+} selectivity suffered comparatively.

Cs, Na and Pd were therefore selected as promoters for the present screening study over Fe@NCNT. Co, In, Li, and Ru were also screened, as these have not been previously investigated as promoters over Fe@CNT-type catalysts but also possess potentially desirable reactivity. Co is commonly used in commercial FT catalysts, and might therefore enhance the activity of Fe@NCNT by providing additional active sites. In has been noted to improve the reducibility of Fe-based FT catalysts due to improved H_2 spill-over, and has been posited to improve FT activity similar to Cu through the "Knight's move" relationship (though the low melting point of In may present a significant practical limitation).[319] Li was investigated for its potential to enhance the basicity of the catalyst similar to other alkali metals. Finally, ruthenium is a well-known CO and CO_2 methanation catalyst on its own, and the addition of an Ru component during synthesis has been previously shown to enhance both CO_2 conversion and long-chain hydrocarbon production over an Al_2O_3-supported iron catalyst.[75] The results of the promoted Fe@NCNT screening studies have been outlined in Figure 6.6.

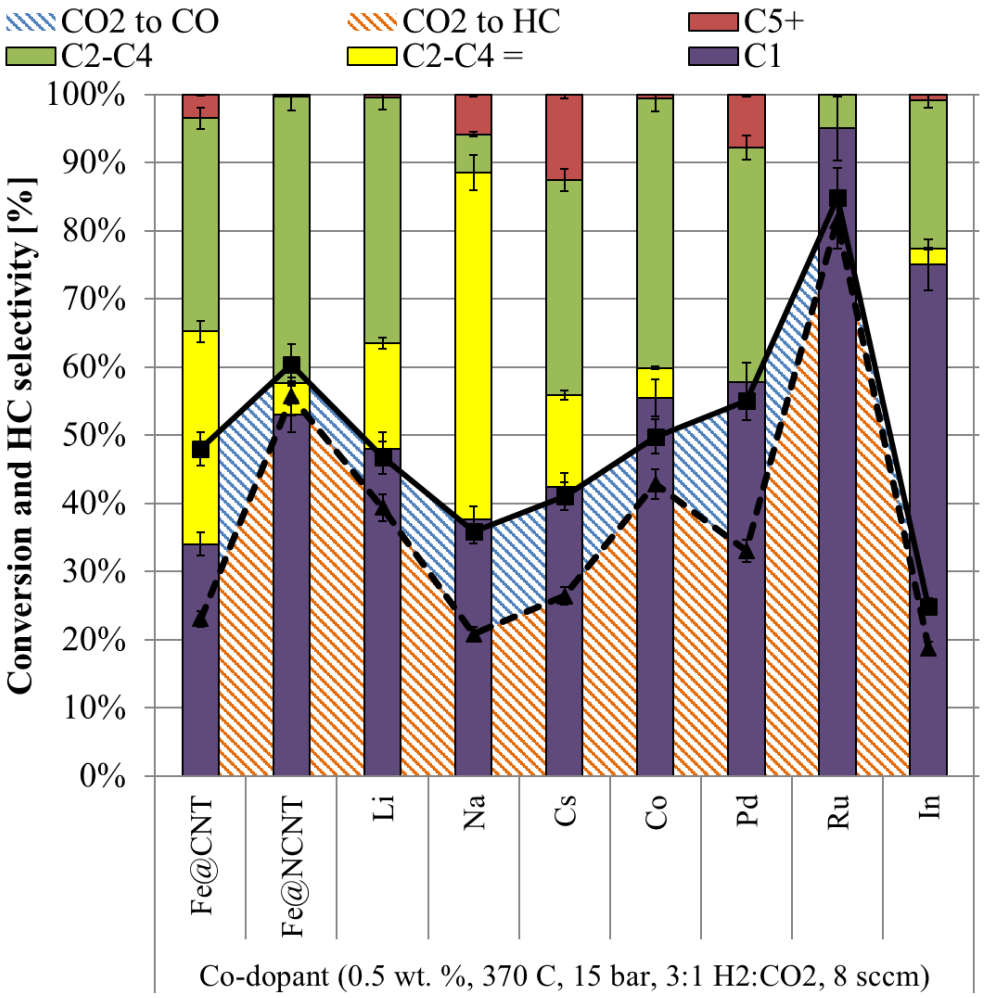

Figure 6.6. Effect of promoter addition on the CO_2 hydrogenation performance of Fe@NCNT. * indicates that Ru was tested at 1.0 wt. % loading rather than 0.5 wt. %. Quantification error is estimated to be ± 5%.

Interestingly, all promoted Fe@NCNT samples displayed a decrease in CO_2 conversion of at least 10% when compared with unpromoted Fe@NCNT. Ru-Fe@NCNT was the only exception to this trend, displaying an increase of ca. 25% over unpromoted Fe@NCNT with nearly quantitative conversion to methane. Among the alkali-promoted samples, an apparent trade-off between CO_2 conversion and desirable product selectivity was observed. Li-Fe@NCNT displayed a moderate decrease in conversion and increase in CO selectivity, while the hydrocarbon product distribution remained similar to Fe@NCNT aside from a slight increase in olefin production. Na-Fe@NCNT and Cs-Fe@NCNT displayed further decreased CO_2 conversion and increase CO selectivity compared to Li-Fe@NCNT, with a more notable shift in hydrocarbon products. Both Na-Fe@NCNT and Cs-Fe@NCNT tended towards higher hydrocarbon production than either Li-Fe@NCNT or unpromoted Fe@NCNT, though Na-Fe@NCNT slightly favoured olefin production, while Cs-Fe@NCNT slightly favoured the production of C_{5+} hydrocarbons. Co-Fe@NCNT displayed

greater CO selectivity than unpromoted Fe@NCNT in addition to decreased CO_2 conversion and a similar hydrocarbon product distribution. Pd-Fe@NCNT displayed a small decrease in CO_2 conversion, as well as significant increases in CO and C_{5+} hydrocarbon selectivity. Finally, In-Fe@NCNT displayed the least desirable performance of all samples, with a low CO_2 conversion of ca. 25% and a significant tendency towards methane production.

The results of this screening further emphasize the potential significance of competition between the RWGS and FT reactions at the catalyst surface. While FT-driven CO consumption is known to result in higher equilibrium CO_2 conversion,[68, 69] in these screening experiments, further propagation of the FT hydrocarbon polymerisation appears to come at the expense of CO_2 and CO utilization. Figure 6.7 plots CO_2 conversion and CO selectivity versus α for the screened promoted Fe@NCNT samples. Samples with greater values of α (i.e. more potent FT chain growth catalysts) display both decreased CO_2 conversion and increased CO selectivity (or decreased CO consumption). While this was not an expected result, it might be intuited by considering that longer hydrocarbon species occupy the catalyst surface longer per mole of product than shorter hydrocarbons. This inhibits the adsorption of new CO reactants, hence the increased CO selectivity and subsequent decrease in CO_2 conversion. This may explain why the relationship between α and reactant conversion appears to hold more strongly for CO selectivity than CO_2 conversion, as the decreased CO_2 conversion is a secondary effect of inhibited CO consumption. No evidence of such a relationship between CO conversion and α has been identified in literature studies of pure FT catalysts. As such, this build-up of CO at higher α values in combined RWGS/FT catalysis appears to be an effect of operating the reactions simultaneously.

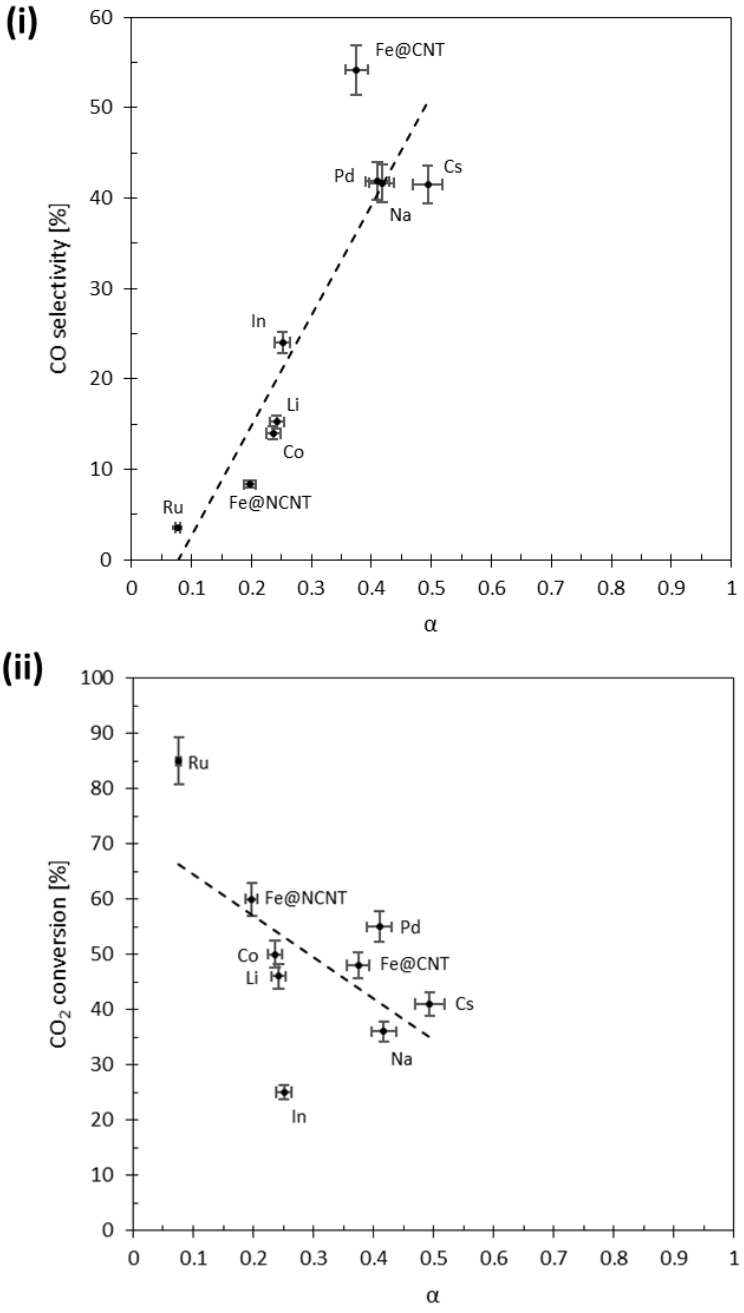

Figure 6.7. (i) CO_2 conversion, and (ii) CO selectivity plotted versus α for the screened promoted Fe@NCNT samples.

Despite this observation, Na-Fe@NCNT and Ru-Fe@NCNT were identified as valuable subjects for further investigation. A full design of experiments targeting temperature, pressure and sodium loading was devised to exploit the increased olefin production observed over Na-Fe@NCNT. Ru-Fe@NCNT were subsequently probed to optimize their high methanation potential using a relatively small amount of ruthenium. The results of the Na-Fe@NCNT design of experiments have been outlined in the following section, while the results of investigations into Ru-Fe@NCNT have been detailed in Chapter 7.

6.1.4. Sodium design of experiments

C_{2-4} olefins are critical reagents for a wide variety of chemical processes, particularly within polymer production. They are therefore an alternative valuable target product if high energy density fuels such as gasoline, kerosene and diesel are not achieved. Na doping in the previously described promotor screening studies resulted in a significant increase in these desirable olefin products. However, this increase in desirable olefins was accompanied by decrease in CO_2 conversion and an increase in undesirable CO selectivity. As such, the design of experiments matrix was structured with a sodium loading range below the initial screening loading of 0.5 wt. % (0-0.5 wt. %) to determine whether any lower sodium loading might afford a similar high olefin production without sacrificing CO_2 and CO conversion. Temperature and pressure were varied equally above and below their tested values in the promoter screening studies to gain greater insights into their influence on a wider range of the reaction space. The selected temperature and pressure ranges were additionally chosen to reflect typically suitable ranges for the RWGS and FT processes that are achievable with our experimental apparatus (330-410 °C, 1-29 bar). The design of experiments matrix has been outlined in Table 6.1. The results of the design of experiments investigations have been summarised in Figures 6.8-6.11.

Table 6.1. Design of experiments matrix to determine the effects of temperature, pressure and sodium loading upon conversion and selectivity of RWGS/FT chemistry over Fe@NCNT.

Expt. No.	Temperature /°C	Pressure /bar	Na /wt. %
1	350	8	0.125
2	350	8	0.375
3	350	22	0.125
4	350	22	0.375
5	390	8	0.125
6	390	8	0.375
7	390	22	0.125
8	390	22	0.375
9	370	15	0.25
10	330	15	0.25
11	410	15	0.25
12	370	1	0.25
13	370	29	0.25
14	370	15	0
15	370	15	0.5

Based upon these design of experiments investigations, the relationships between temperature, pressure, sodium loading, CO_2 conversion, hydrocarbon selectivity, olefin production, and C_{5+} selectivity were estimated, as seen in Figures 6.8-6.11. Conversion of CO_2 and CO suffered as a result of sodium doping. Increasing sodium loading resulted in increased temperature and pressure requirements to achieve comparable conversion and hydrocarbon selectivity when compared with unpromoted Fe@NCNT. Maximum conversion and hydrocarbon yield of 60% and 90%, respectively, were achieved at 350 °C and 12.5 bar over unpromoted Fe@NCNT. 370 °C and 10 bar were noted to be optimal conditions for overlap between maximal conversion, hydrocarbon production and C5+ selectivity over unpromoted Fe@NCNT. No such combination of high CO_2 conversion and hydrocarbon yield appeared to be possible over 0.5 wt. % Na-Fe@NCNT in the tested temperature and pressure ranges. However, increasing Na loading appeared to lower the temperature requirement for olefin production and C_{5+} selectivity in the FT products. Despite otherwise inferior conversion and selectivity, sodium-promoted samples displayed superior olefin production when compared with unpromoted Fe@NCNT, with olefin:paraffin ratios reaching as high as 4:1 at 0.5 wt. % sodium loading below 340 °C and 2 bar. However, the low temperatures and pressures required to achieve this high olefin:paraffin ratio result in a modest maximum olefin yield of only ca. 14%.

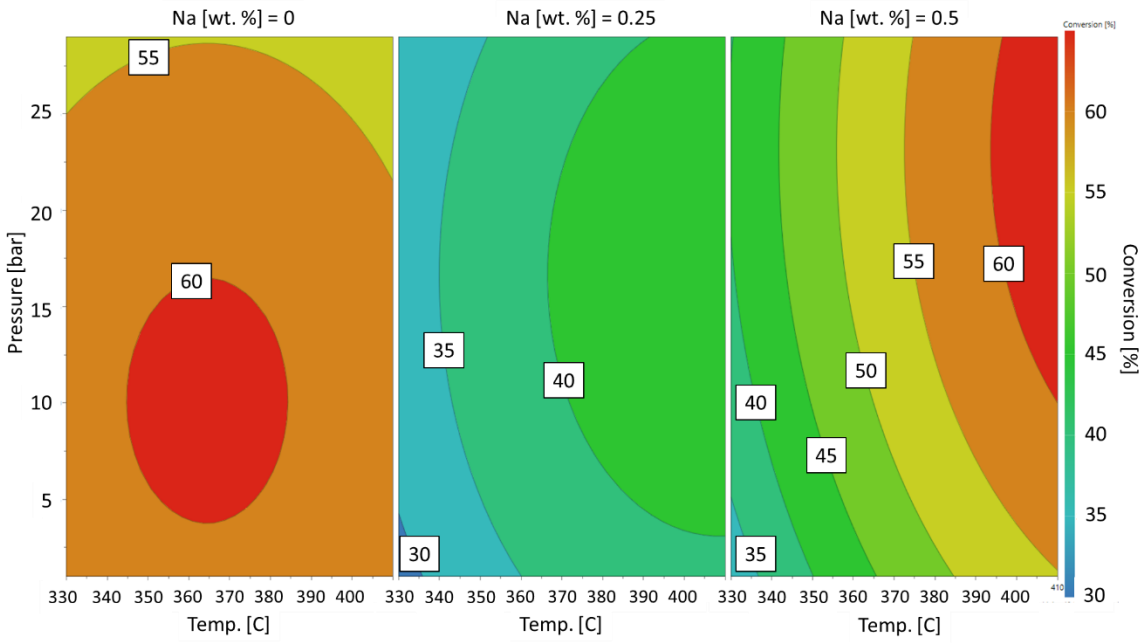

Figure 6.8. The dependence of conversion upon temperature, pressure, and sodium loading, as established during the design of experiments.

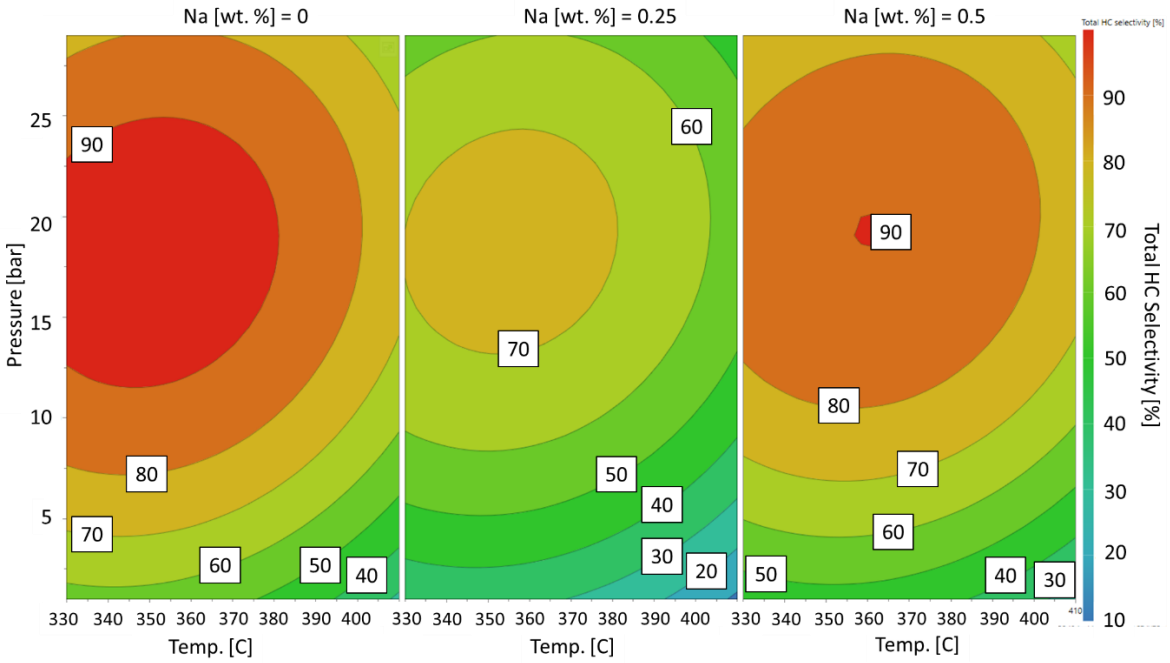

Figure 6.9. The dependence of total hydrocarbon selectivity upon temperature, pressure, and sodium loading, as established during the design of experiments.

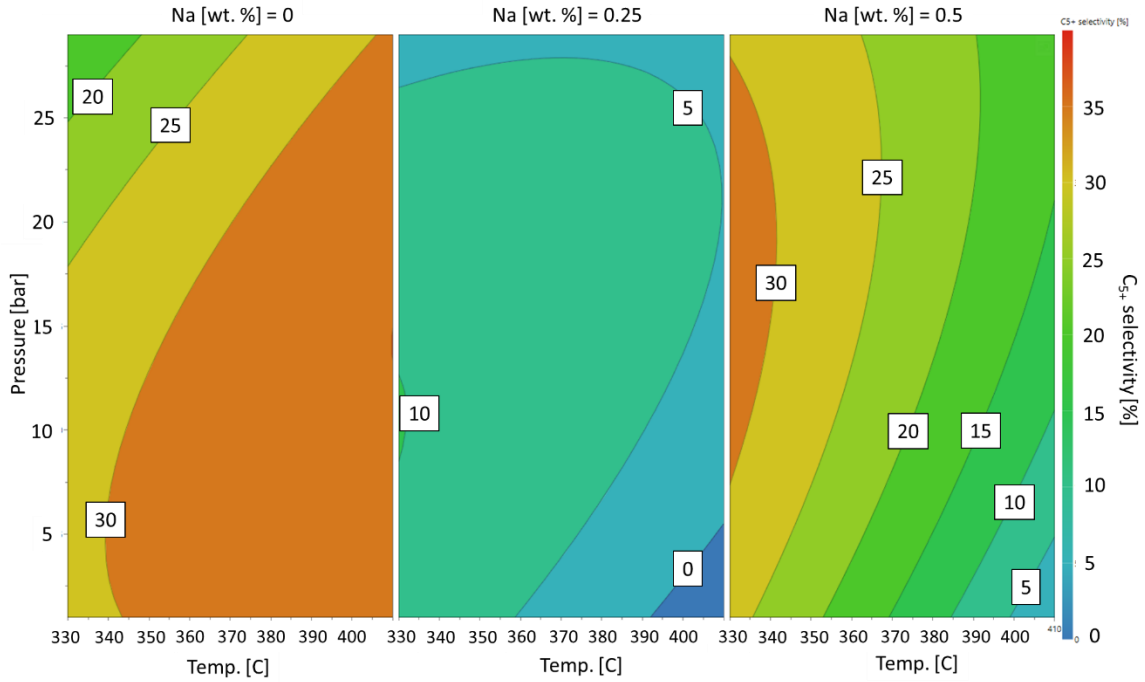

Figure 6.10. The dependence of C_{5+} selectivity upon temperature, pressure, and sodium loading, as established during the design of experiments.

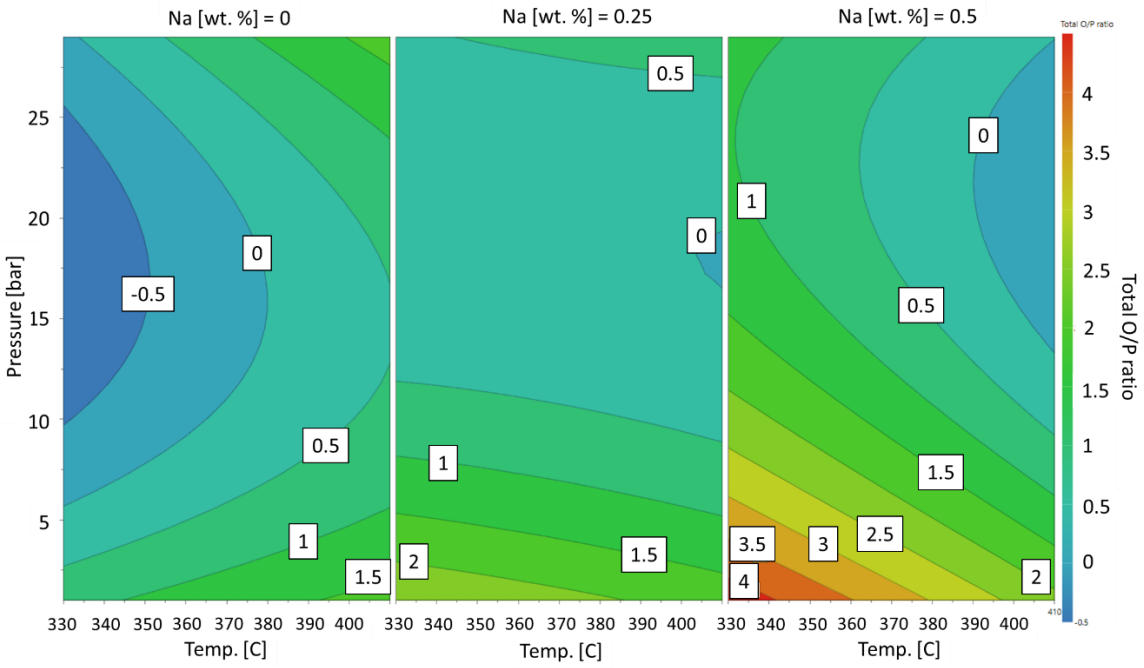

Figure 6.11. The dependence of the total olefin/paraffin ratio in hydrocarbon products upon temperature, pressure, and sodium loading, as established during the design of experiments.

While this design of experiments was valuable in clarifying of expected trends during RWGS/FT testing, the value of sodium promotion in the tested range was limited. In fact, the decrease in conversion and hydrocarbon production in sodium-promoted samples suggests that the presence of sodium inhibits the beneficial effects of nitrogen doping upon the mechanism of CO_2 and CO conversion over unpromoted Fe@NCNT. The increased basicity afforded from the Na promoter would be expected to have a beneficial effect on all of the targeted process variables (conversion, hydrocarbon yield, C_{5+} selectivity, olefin:paraffin ratio). However, in practicality only C_{5+} and olefin production were aided, while conversion and total hydrocarbon yield were inhibited by Na promotion, directly countering the influence of nitrogen doping in the original Fe@NCNT catalyst.

These results unfortunately suggest that there is no combination of temperature, pressure and Na loading that can achieve high conversion, hydrocarbon production and olefin or C_{5+} selectivity over the tested range. Furthermore, it does not seem likely that a higher sodium loading will achieve more desirable results, as conversion and total hydrocarbon yield are directly inhibited by the presence of sodium in the sample. However, while the resulting model displays a reasonable fit with experimental observations, the predictability of the model remains poor, as seen in Figure 6.12. R^2 (sometimes "R-squared") represent the fit of the generated model to the provided experimental data. Better fits tend towards a maximum value of 1 as the model and the data approach parity. Q^2 (sometimes "Q-squared") represents

the predictability of the model when comparing its prediction of the data under similar conditions with the no-model assumption (mean response of the training set). Similarly to R^2, models with better predictability will also tend towards a maximum value of 1. In general, R^2 will increase as more data points are provided, regardless of the quality of the data. Conversely, Q^2 may decrease with increasing data input if the provided data is noisy, as model prediction requires good data to build an accurate model of that data.

R^2 values for Figures 6.8-6.11 range from 0.66-0.84, implying a reasonable but imperfect fit between the design of experiments model and experimental data. However, Q^2 values are extremely low at -0.2 for all target parameters. This suggests that either a more robust data set was necessary to improve predictability, or a more fundamental understanding of the process was required to identify additional factors influencing RWGS/FT activity over Fe@NCNT. As such, further experiments were devised to develop a clearer understanding of the mechanistic influence of nitrogen doping upon the activity of Fe@NCNT, and determine how sodium promotion might inhibit this influence.

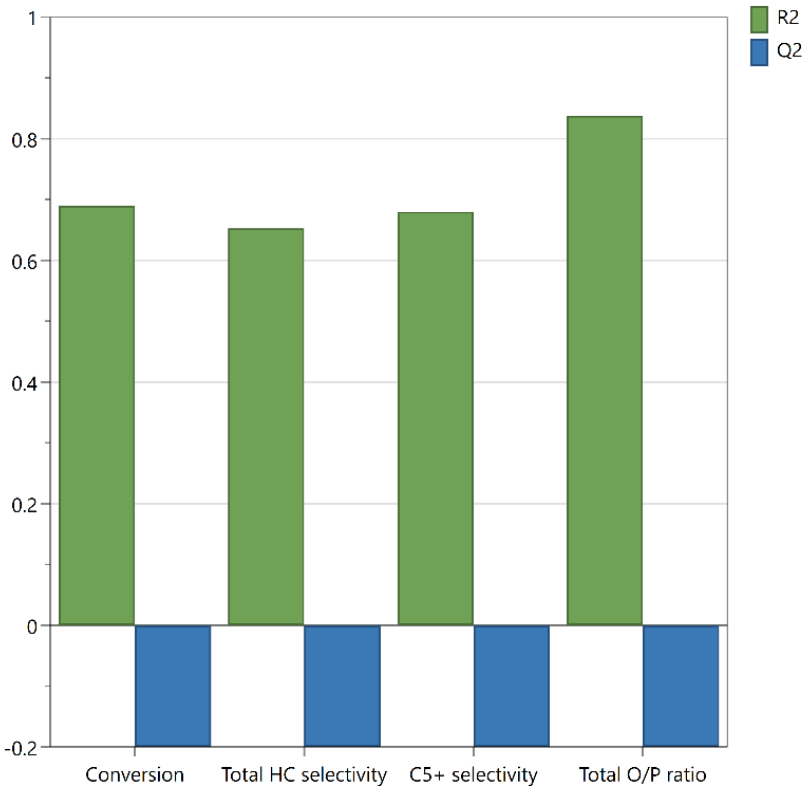

Figure 6.12. Summary of model fit for probed variables in the design of experiments.

6.2. **Evaluation of the Fe@NCNT reaction mechanism**

The increase in CO_2 conversion and decrease in CO selectivity and α values observed over Fe@NCNT compared to Fe@CNT represents a clear influence from nitrogen upon the RWGS/FT reaction mechanism. More specifically, it appears that nitrogen incorporation enhances both CO_2 and CO conversion (i.e. facilitates both RWGS activity and initial CO conversion via FT), but inhibits further polymerisation of the FT intermediates into longer hydrocarbons. This relationship was further evidenced during promoter screening studies in section 6.1.3, where promoters that increased the basicity of the catalyst (e.g. alkali metals) reversed the influence of nitrogen doping by increasing α, as expected according to similar studies of promoted Fe@CNT,[72] but also unexpectedly decreased conversion of CO_2 and CO. As such, the mechanistic effect of nitrogen doping was investigated further in hopes of optimising the catalyst for high RWGS and FT activity without sacrificing α values in the process.

Existing studies concerning the influence of nitrogen doping upon the RWGS and FT activity of CNT-supported metal particles have suggested that nitrogen incorporation leads to improved conversion, reducibility and particle dispersion.[78, 79, 227, 259, 275] This has been attributed to increased overlap between the metal 3d orbitals and excess π-electron density in the graphitic plane. Nitrogen heteroatoms are known to act as anchoring sites for metal nanoparticles during wet impregnation, and their additional electron density is said to enhance catalyst reducibility; particularly from the shallow donor state provided by graphitic nitrogen species.[187, 227, 265] However, these studies are significantly limited in that they have focused exclusively on the effect of nitrogen doping in pure FT synthesis, or have only investigated catalysts where the nitrogen heteroatoms and iron nanoparticles have been post-doped onto an existing CNT support separately.[78, 79, 92, 275, 320] The strength of particle-support interactions in such materials is known to play a critical role in modulating the activity of the catalytic metal particles.[80, 129, 156, 158-161] Furthermore, direct incorporation of iron particles in the CNT support during synthesis (as in Fe@CNT and Fe@NCNT) has been shown to enhance activity due to increased hydrogen spill-over afforded by the bridged particle-support structure that exists in these materials.[70] As a result, existing studies of RWGS and FT chemistry over N-CNT-supported iron particles suffer from limited applicability to combined RWGS/FT catalysis for CO_2 utilisation, sub-optimal integration of nitrogen and iron in the CNT support, and a potentially significant influence from variable

particle-support interactions that mask the intrinsic influence of nitrogen doping upon the RWGS and FT processes.

The sections below detail investigations into the influence of nitrogen doping in Fe@CNT and Fe@NCNT. These studies provide novel insights into the intrinsic effect of nitrogen incorporation upon the RWGS and FT processes for CO_2 hydrogenation. Specifically, they isolate the influence of nitrogen more clearly than existing studies by eliminating concerns over variable particle-support interactions, as the iron particles are incorporated directly into the support in both materials. Furthermore, they represent the most cohesive integration of all three key elements of the catalyst (iron, nitrogen and CNT support) yet reported, and provide the clearest depiction of the influence of nitrogen doping yet reported for full CO_2 hydrogenation, as previous studies have only investigated the isolated FT process.

6.2.1. Reactant adsorption properties and MD simulations

Existing studies of N-CNT-supported metal nanoparticles for RWGS and FT catalysis suggest that nitrogen doping serves to enhance catalyst reducibility, activity and long-chain hydrocarbon production.[78, 79, 275] This is attributed to additional electron density from the nitrogen heteroatom enhancing the basicity of the support and increasing electron donation to the catalyst particles.[79, 227, 265] However, XPS and XRD comparisons of Fe@CNT and Fe@NCNT (as seen in Chapter 5) do not indicate any discernible difference in iron species as a result of nitrogen incorporation after activation and reduction. Furthermore, the enhanced electron donation described in literature would be expected to result in both increased activity and higher α values rather than the observed shift towards lower values of α over Fe@NCNT.[79, 275] As such, alternative explanations for this deviation from expected reactivity were explored. The influence of local C—N dipoles upon reactant adsorption was identified as potentially significant. Charge redistribution across adjacent C and N atoms has been observed to attract and activate O_2 molecules, making nitrogen-doped CNT's potent catalysts for the oxygen reduction reaction.[227, 321, 322] It is therefore conceivable that a similar effect might be observed for the CO_2 and CO reactants in the RWGS and FT processes over similar materials.

CO is inherently polar with a relatively weak dipole moment of 0.122 D and an atypical charge distribution, where the carbon possesses a weak negative charge and the oxygen possesses a weak positive charge.[323, 324] This provides an opportunity for attraction between the asymmetrical charge distributions on the carbon and oxygen atoms in CO upon reaching

close proximity to the weak positive and negative charges on adjacent carbon and nitrogen atoms in the NCNT support. CO_2, on the other hand, does not possess a dipole moment due to its linear, symmetrical structure. However, CO_2 is notably quadrupolar, with a quadrupole moment of -1.4×10^{-39} C m^2.[325] Despite its lack of a dipole moment, its quadrupolar nature belies charge separation and electronic structure that affords surprisingly polar properties. For example, CO_2 is capable of acting as a Lewis acid or Lewis base in studies of its solvation behaviour, with experimental and theoretical studies supporting its participation in conventional and unconventional hydrogen bonds.[326] This has been previously exploited to afford selective CO_2 capture over other non-polar molecules (H_2, N_2, CH_2) in flexible 3D coordination polymer networks.[325] Furthermore, the presence of other polar and asymmetrically charged bodies (e.g. CO or C—N bonds) in close proximity may result in induced dipoles in the CO_2 molecules. This suggests further opportunities for attraction between the CO_2 reactant and asymmetrical charges on local C—N dipoles in the NCNT lattice. It should be noted that wherever "C—N dipoles" are discussed in this thesis, the term refers to this asymmetrical charge distribution across adjected C and N atoms in the NCNT lattice. Dipole moments for the overall nitrogen bonding modes (e.g. graphitic, pyridinic, pyrrolic) are theoretically possible, but expected to tend towards zero due to their integration into the overall carbon-based nanotube macrostructure.[327]

To probe the interactions between reactants and nitrogen sites in the catalyst support, the adsorption properties of reactants were compared over Fe@CNT and Fe@NCNT. The acidity, basicity and BET surface area of both materials were initially investigated, as seen in Table 6.2. Both materials displayed similar BET surface areas of ca. 80 m^2 g^{-1}. This is consistent with typically reported values for the surface area of MWCNT.[71] Fe@CNT displayed higher overall CO_2 and NH_3 adsorption capacity, which may be due to the bamboo structure preventing adsorption along the interior tube bore in Fe@NCNT. Interestingly, nitrogen incorporation appeared to increase the acidity of Fe@NCNT. This is unexpected, as nitrogen doping is generally stated to increase the basicity of the catalyst, especially considering that Fe@NCNT are composed of predominantly electron-donating graphitic nitrogen according to XPS.[79, 265] The origin of this increased acidity remains unclear, though it may contribute to explaining the decreased α values observed over Fe@NCNT, as more basic supports and alkali promoters typically result in increased α values. However, if that were the case, the increased CO_2 and CO conversion over Fe@NCNT would remain unexplained, as a less basic support would also be expected to result in decreased overall

activity. This increased acidity may also be a consequence of testing the acidic and basic sites of activated catalysts rather than reduced catalysts, where the acidity of the oxidised iron particles (which is affected by variance in particle size and surface area) masks the enhanced basicity of the catalyst support after nitrogen doping.

Table 6.2. BET surface area and characterisation of acidic/basic sites for Fe@CNT and Fe@NCNT after activation in air at 570 °C (40 min) and 400 °C (60 min), respectively.

Catalyst	Ads_{CO2} [mL g^{-1}]	$Ads_{CO2,\ strong}$ [mL g^{-1}]	Ads_{NH3} [mL g^{-1}]	$Ads_{NH3,\ strong}$ [mL g^{-1}]	Strong n_{acid}/n_{base}	SA_{BET} [m^2 g^{-1}]
Fe@CNT	0.55	0.55	2.25	1.99	3.6	78
Fe@NCNT	0.40	0.39	1.94	1.85	4.6	81

The reducibility and adsorption properties of CO_2 and CO over both materials were subsequently investigated, as seen in Figure 6.13. H_2 TPR, CO_2 and CO TPD spectra indicate that the iron particles in both materials experience a stepwise reduction from Fe_2O_3 to Fe(0), and Fe@NCNT are more easily reduced than Fe@CNT, as expected.[78] Furthermore, it appears that CO_2 and CO adsorb more strongly to the catalyst surface in Fe@NCNT. CO chemisorption has been observed to occur at ca. 400 °C over Fe/CNT in literature.[79] Thus, peak ζ has been attributed to chemisorbed CO and peak ε has been attributed to physisorbed CO. While the desorption of chemisorbed CO appears largely unchanged between samples (ca. 395 °C), physisorbed CO desorbs at a notably higher temperature in Fe@NCNT. Stronger chemisorption by CO_2 at nitrogen sites is also observed in Fe@NCNT, where only physisorption is observed in Fe@CNT.[79]

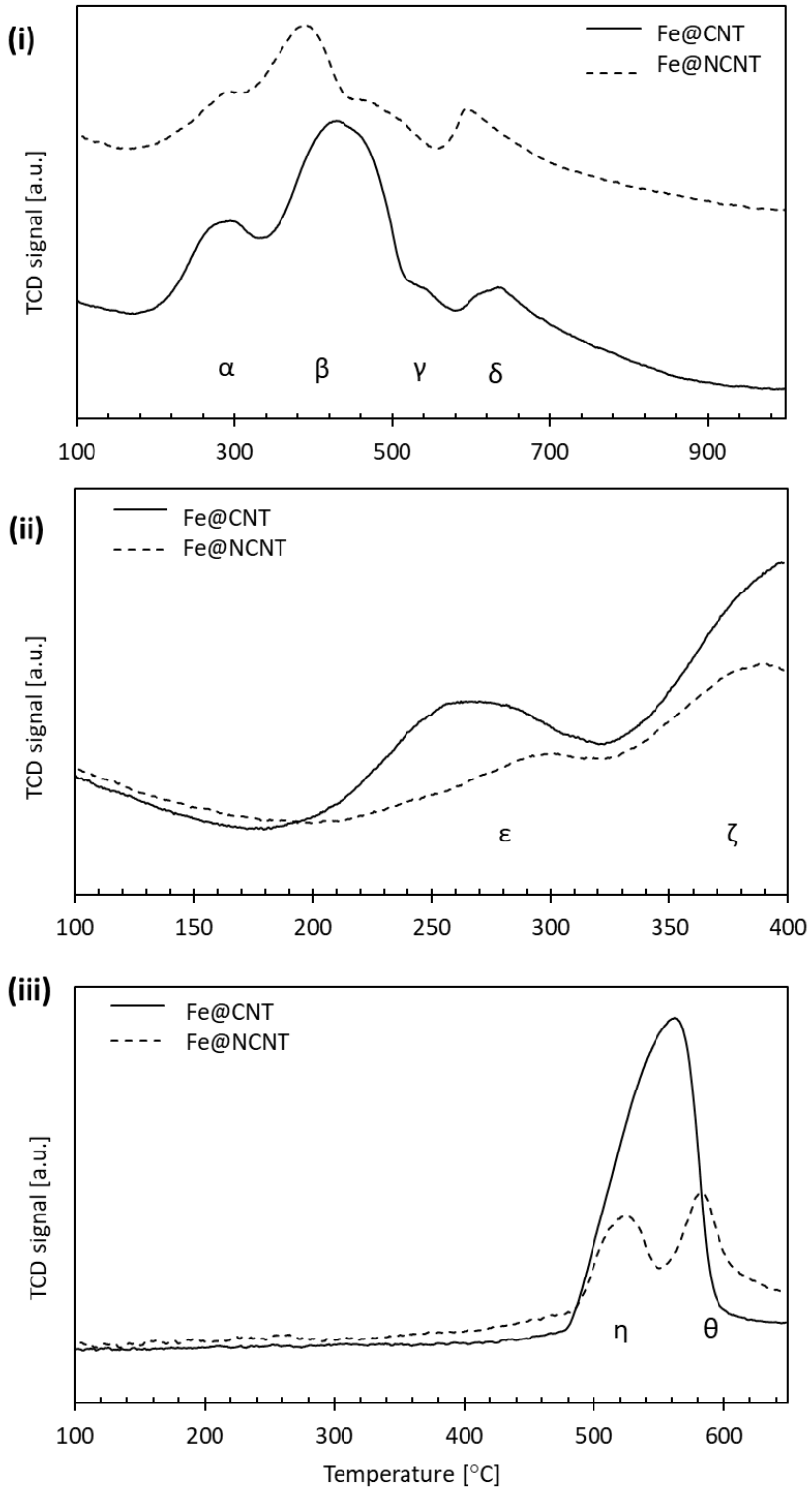

Figure 6.13. (i) H_2 TPR profiles of Fe@CNT and Fe@NCNT, where α = Fe_2O_3→Fe_3O_4, β = Fe_3O_4→Fe(0), γ = Fe_3O_4→Fe(0) via FeO, and δ = gasification of the CNT support. (ii) CO TPD profiles of Fe@CNT and Fe@NCNT, where ε = physisorbed CO and ζ = chemisorbed CO. (iii). CO_2 TPD profiles of Fe@CNT and Fe@NCNT, where η = physisorbed CO_2 and θ = chemisorbed CO_2.

This increased attraction is mirrored in molecular dynamics simulations of the 3:1 H_2:CO_2 feed gas adsorption process. Representative segments of Fe@CNT and Fe@NCNT were modelled based on their composition and morphology as observed via TEM and XPS, as seen in Figure 6.14. The simulation cell was then filled with CO_2 and H_2 molecules at the appropriate temperature (370 °C), pressure (15 bar), and concentration to represent the initial introduction of the feed gas to the catalyst. The reactant species were subsequently left to adsorb to the catalyst surface under the influence of Lennard-Jones potential and constant coulombic charges between all components in the system. Full details of the software, parameters, models, and forcefields used to achieve these simulations can be found in Appendix 2. A full detailed simulation methodology is freely available in the Supplementary Information for D. L. Williamson, C. Herdes, L. Torrente-Murciano, M. D. Jones and D. Mattia, *ACS Sustainable Chemistry & Engineering*, 2019, **7**, 7395-7402.

The author would like to provide explicit thanks and credit to Dr Carmelo Herdes of the University of Bath Department of Chemical Engineering for his work in configuring and performing these simulations. While establishing the concept and parameters of these simulations was a joint effort, the simulations presented in this thesis were set up and executed entirely by Dr Herdes.

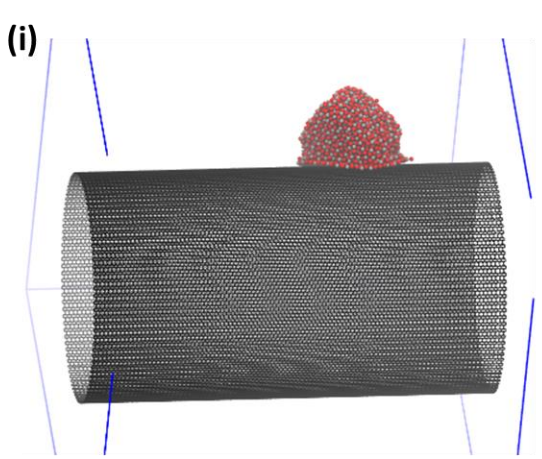

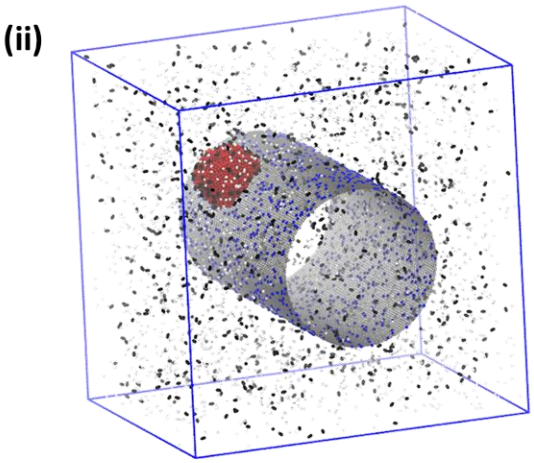

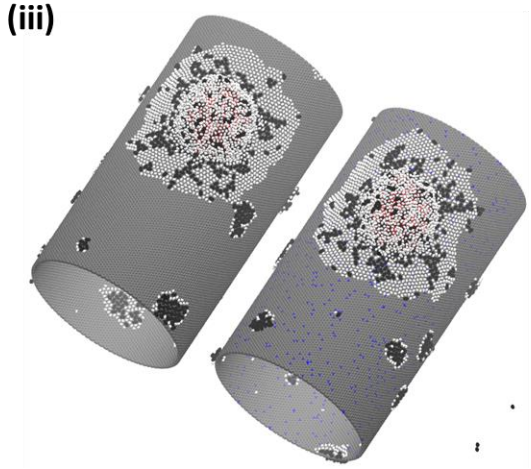

(iv)

Pair interaction	Contribution [%]	
	CNT	NCNT
CO_2 - Catalyst	4.10	5.31
H_2 - Catalyst	2.84	3.06
H_2 - CO_2	1.19	1.10
CO_2 - CO_2	1.22	1.14
H_2 - H_2	1.15	1.09

Figure 6.14. (i) Simulated Fe@CNT prior to adsorption simulations. (ii) Initial state of adsorption simulation cell containing a simulated Fe@NCNT and initial concentrations of H_2 and CO_2. (iii) Final state of adsorption simulations over Fe@CNT and Fe@NCNT. (iv) Percentage contribution to the potential energy (LJ + coulombic) of selected simulation pairs upon adsorption, directly before reaction.[328]

While the time to reach equilibrium was similar over both materials, interactions between CO_2 and the catalyst surface are notably stronger in Fe@NCNT, and a slight smoothing effect can be observed in the equilibration of reactants on the N-doped catalyst (Figure 6.15). This suggests a more ordered adsorption process over Fe@NCNT. As CO_2 and CO possess a quadrupole and dipole moment, respectively, the local C—N dipoles generated through nitrogen doping are likely sources of this enhanced attraction. Furthermore, it must be noted that the hydrocarbon products of this hydrogenation do not possess such dipoles, and are therefore at a relative disadvantage in terms of attraction to the catalyst compared to new CO_2 and CO reactant molecules. This may serve as an explanation for both the increased RWGS and initial FT activity, as well as the decreased α values observed over Fe@NCNT. While CO_2 and CO are more readily adsorbed for reaction over Fe@NCNT, this increased attraction could also result in more rapid displacement of less polar FT intermediates in favour of new CO_2 and CO coordination, thereby inhibiting further chain growth.

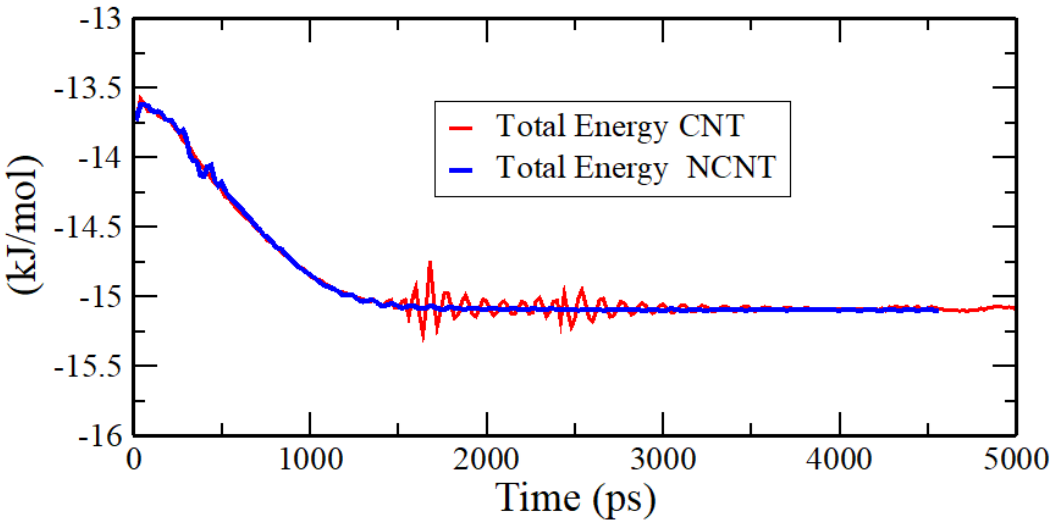

Figure 6.15. Simulated 3:1 H_2:CO_2 feed gas adsorption energies on surface of Fe@CNT and Fe@NCNT.

Alternatively, the increased acidity of Fe@NCNT may also be a source of their inhibited chain growth activity. While local C—N dipoles attract CO_2 and CO to the catalyst surface, the relatively lower basicity of Fe@NCNT compared to Fe@CNT may prevent the production of higher hydrocarbons that is typically observed over more basic catalysts.

6.2.2. Obscuring nitrogen sites during RWGS/FT catalysis

The reactivity of Fe@NCNT was noted to revert back to resembling Fe@CNT after the addition of alkali promoters in the initial promoter screening outlined in section 6.1 (reiterated by Figure 6.16). Based upon the adsorption properties of CO_2 and CO over Fe@CNT and Fe@NCNT observed in section 6.2.1, this effect of alkali promotion might be explained by a decrease in the acidity of Fe@NCNT to more resemble Fe@CNT. Alternatively, this might be a result of obscuring the local C—N dipoles in the catalyst support through M^+ coordination and particle formation over the nitrogen heteroatoms by the dissolved alkali metal cations during wet impregnation. The reactivity of Na-Fe@NCNT was therefore revisited. At 0.5 wt. % loading, conversion and product selectivity once again reverted to resemble that of Fe@CNT.

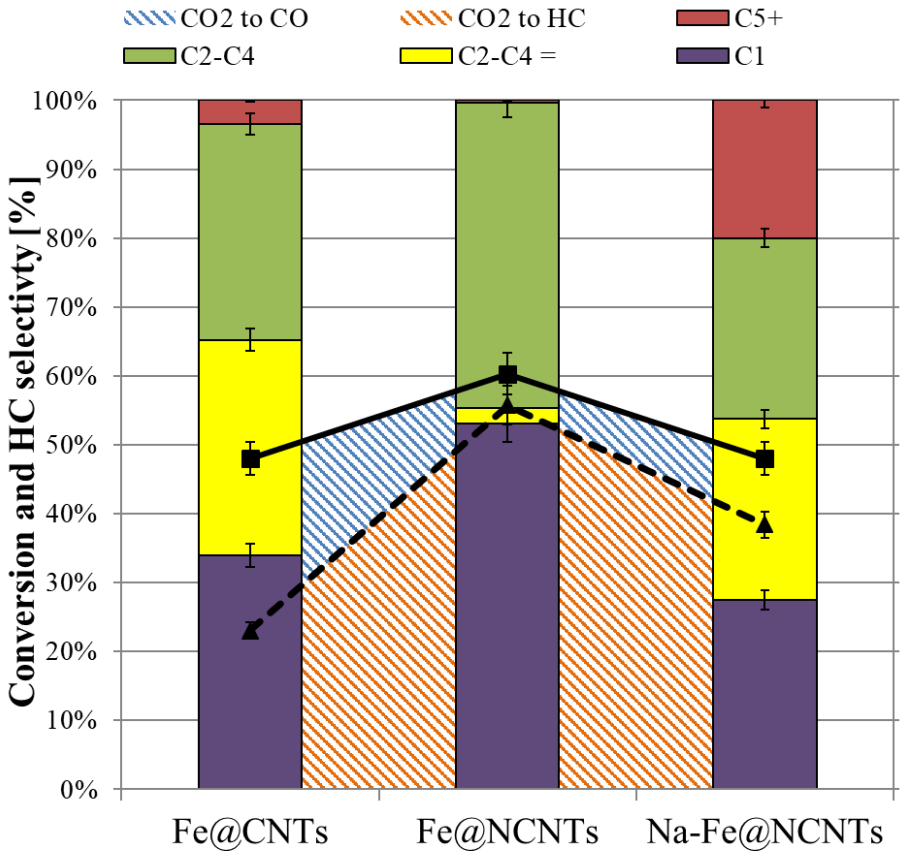

Figure 6.16. Effect of obscuring nitrogen sites via Na^+ coordination during wet impregnation. Quantification error is estimated to be ± 5%.

While the increased basicity arising from sodium doping likely plays a role in increasing long-chain hydrocarbon production, this does not explain the observed decrease in CO_2 and CO conversion. If local C—N dipoles play a role in increasing reactant attraction to the catalyst surface, as suggested by TPD and MD simulations, then this decrease in activity

could be explained by obfuscation of these dipoles through Na^+ coordination during wet impregnation. As such, the presence of Na^+ coordination was investigated via EDS and XPS.

EDS maps of Na-Fe@NCNT revealed the clear presence of carbon and nitrogen throughout the MWCNT structure, as expected, as seen in Figure 6.17. The presence of Na particles was also clear, if more diffuse, indicating Na deposits lightly dispersed along the length of the NCNT support. The visibility of nitrogen and carbon is understandably greater than that of the sodium deposits, as nitrogen and carbon are present throughout the entirety of the NCNT wall structure, while a relatively small amount of dispersed sodium is present only at the NCNT surface. While these EDS maps confirmed successful dispersion of sodium along the NCNT, they did not provide sufficient evidence of obscured nitrogen sites Na^+ coordination. XPS analysis of the sodium species was therefore conducted to clarify the nature of their adsorption on the surface.

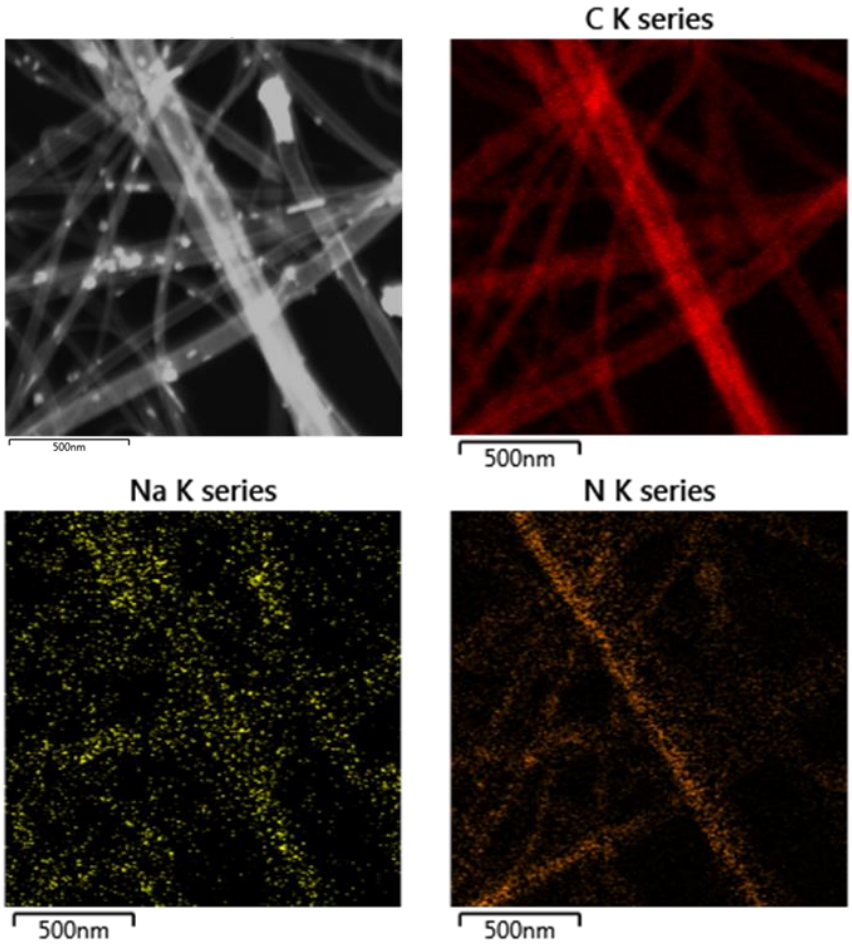

Figure 6.17. EDS maps of Na-Fe@NCNT confirming the presence of lightly dispersed sodium particles obscured nitrogen sites along the catalyst surface.

Deposition of Na^+ to obscure surface nitrogen sites was further supported by XPS analysis, as seen in Figure 6.18. After initial Na doping via wet impregnation, all Na in the sample exists as Na^+, evidenced by a single peak at 1071.5 eV. In previous publications it has been shown that pure Na(I) in the form of fresh cleaved single crystal NaCl exhibits a characteristic Na 1s peak at 1071.1 eV.[329] This peak shifts to 1072.0 eV for Na^+ stabilised by the presence of a negatively charged counterion.[330] The Na^+ peak shift to 1071.5 eV for Na-Fe@NCNT following wet impregnation can therefore be taken as evidence of weaker $N^{\delta-} \rightarrow Na^+$ interactions between nitrogen sites and their obscuring Na^+ species. Following activation at 400 °C in air for 1 hour, ca. 50% of the Na^+ is converted to Na_2O_2 (1073.2 eV), while half remains stabilised as Na(I) (1071.2 eV).[331] Fe 2p regions of Na-Fe@NCNT and Fe@NCNT after activation at 400 °C in air for 1 hour show similar iron compositions across both samples. Na-Fe@NCNT display a greater presence of both Fe(III) and Fe(0), while Fe@NCNT display a greater presence of Fe(II). These differences in composition are likely affected by variance in the samples and margin of error in the XPS measurement rather than electronic perturbations in the iron caused by Na doping. It is unlikely that the Na-Fe@NCNT would possess the greatest concentrations of both the most and least reduced metals species if Na doping significantly enhanced or inhibited the reducibility of the iron.

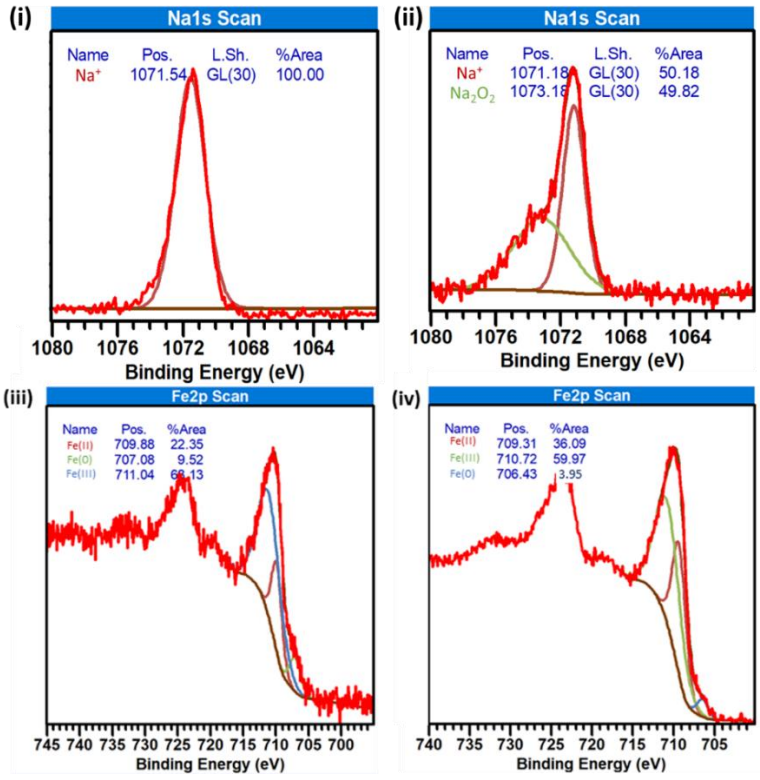

Figure 6.18. XPS Na 1s regions of Na-Fe@NCNT (i) directly after sodium doping and (ii) after activation at 400 °C in air for 1 hour. XPS Fe 2p regions of (iii) Na-Fe@NCNT and (iv) Fe@NCNT after activation at 400 °C in air for 1 hour.

It appears likely that the increased CO_2 and CO conversion and decreased α values observed over Fe@NCNT are caused by increased attraction of the dipole-containing reactants and that catalyst surface. However, it is also likely that increased acidity in Fe@NCNT plays a role in controlling their reactivity, particularly with respect to limiting the production of long-chain hydrocarbons. Unfortunately, it is unlikely that the high conversion activity of Fe@NCNT can be easily exploited without sacrificing the production of higher hydrocarbons in the process. However, further modulation of the nitrogen species in the catalyst support may represent an opportunity to maintain the presence of local C—N dipoles while enhancing the basicity of the catalyst further.

6.3. **Additional reactivity studies**

While this thesis primarily concerns the influence of nitrogen doping upon the reactivity of Fe@NCNT when applied in RWGS/FT catalysis for CO_2 hydrogenation, additional studies were carried out to probe several other potentially interesting aspects of Fe@CNT and Fe@NCNT reactivity. Most notably, the activity of Fe@NCNT as a pure FT catalyst was briefly investigated; the potential for *in situ* Fe@CNT particle size control during CVD synthesis was explored; and a collaboration concerning the reactivity of Fe@CNT, Fe@NCNT, and V-Fe@CNT for sustainable oxalic acid production was published. The motivations and results of these ancillary studies have been briefly outlined in the sections below.

6.3.1. Fe@NCNT in FT catalysis

Upon observing the enhanced CO_2 and CO conversion over Fe@NCNT in RWGS/FT catalysis and exploring the influence of local C—N dipoles in enhancing this reactivity, the value of Fe@NCNT as a pure FT catalyst was called into question. CO is significantly more polar than CO_2, and so a feedstock containing only CO rather than CO_2 might be expected to display further enhanced reactivity over Fe@NCNT. Furthermore, previous studies into pure FT reactivity over N-CNT-supported iron particles have indicated increased C_{5+} selectivity as a result of nitrogen incorporation.[79, 275] These studies have used post-doped nitrogen and iron species on pre-synthesised MWCNT supports. As such, Fe@NCNT represented a potential improvement over these materials due to their bridged particle-support structure and integration of all elements of the catalyst during synthesis.

Fe@NCNT were applied in pure FT synthesis at various pressures and their activity was monitored over time, as seen in Figures 6.19-6.20. The feed gas composition was changed from H_2 and CO_2 at a ratio of 3:1, respectively, to a composition of H_2 and CO at a ratio of 2:1, respectively, as the additional H_2 required for the initial RWGS CO_2 conversion was no longer necessary.

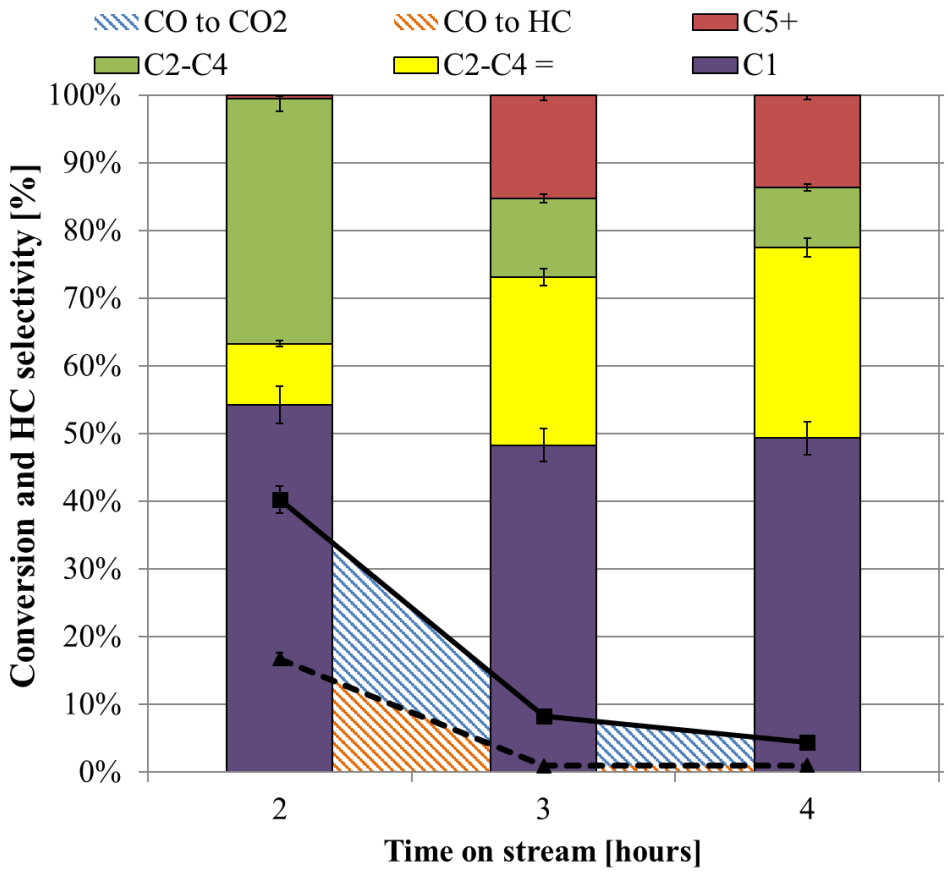

Figure 6.19. FT and WGS activity of Fe@NCNT at 1 bar, 370 °C and a 2:1 H_2:CO feed gas ratio (total flowrate = 8 sccm). Quantification error is estimated to be ± 5%.

Regardless of pressure, CO_2 production via the forward WGS side reaction increased with time on stream. The observed CO_2 and hydrocarbon production can be explained as an effect of interactions between the FT and WGS reactions. The H_2 and CO feed gas initially encourages the production of hydrocarbons and water via FT. The water product from the FT process then reacts with CO in the feed gas via WGS to produce the observed CO_2, as well as additional H_2. As such, the FT process can be considered as feeding the WGS reaction with the water required for its operation. The WGS reaction leeches CO from the feed gas, but also partially feeds the FT process by recycling hydrogen in the FT water product.[332] An equilibrium is achieved between water production from FT, CO consumption via WGS and

H_2 production via WGS. This implies a limited maximum hydrocarbon yield from FT based on the WGS activity of the catalyst.

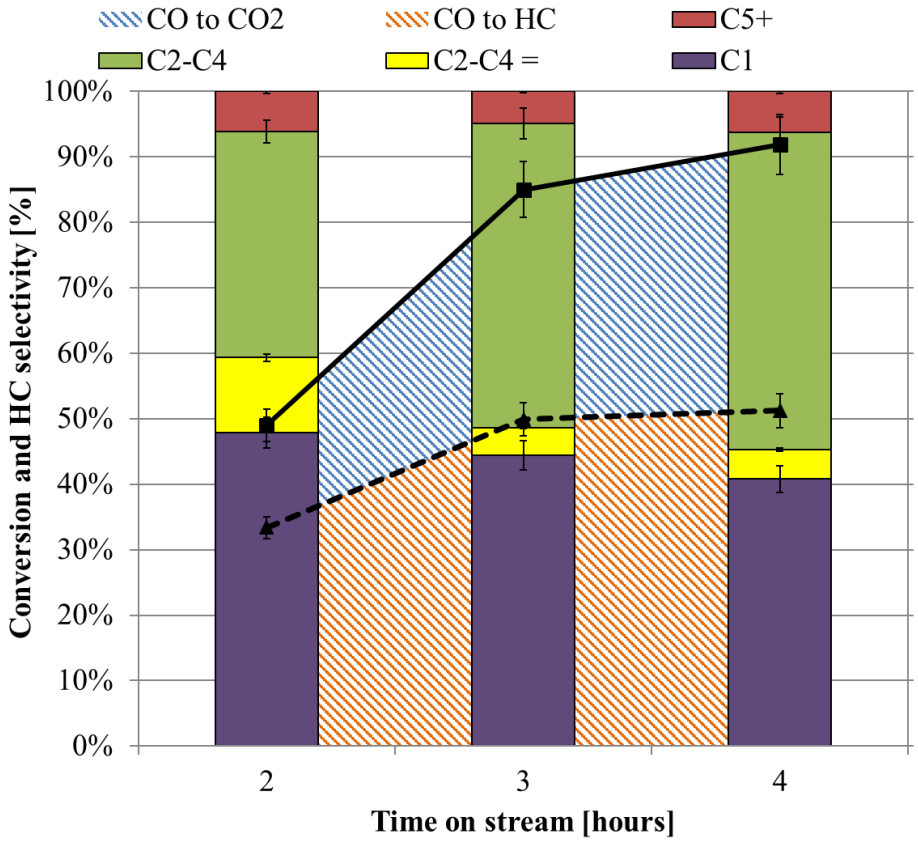

Figure 6.20. FT and WGS activity of Fe@NCNT at 15 bar, 370 °C and a 2:1 H_2:CO feed gas ratio (total flowrate = 8 sccm). Quantification error is estimated to be ± 5%.

The distribution of hydrocarbons produced via FT varied slightly with pressure with ca. α = 0.48 at 1 bar and α = 0.42 at 15 bar. This is notably higher than the α values observed for Fe@NCNT in RWGS/FT catalysis of ca. α = 0.20, and is consistent with reduced α values observed when applying FT catalysts in CO_2 hydrogenation. Olefin production was significantly higher at low pressure, which is consistent with the pressure dependence established during the sodium promoter design of experiments outlined in section 6.1.4. Overall CO conversion varied significantly with pressure and time on stream. At a low pressure of 1 bar, conversion decreased rapidly between 2-4 hours on stream. CO conversion decreased from an initial high of ca. 40% to an eventual minimum of ca. 5%. At the increased pressure of 15 bar, the opposite trend was observed. CO conversion increased from an initial low of ca. 49% to an eventual maximum of ca. 92%.

Iron FT catalysts experience deactivation due to several known mechanisms. Specifically, these are (i) poisoning (primarily due to sulphur in the feed gas), (ii) carbon deposition (via

the Boudouard reaction), (iii) sintering of catalyst particles, and (iv) oxidation of the FT-active iron carbides into WGS-active magnetite. The partial pressure of water in the reaction is significant in affecting this deactivation, as a higher water concentration increases the rate of catalyst oxidation.[332] The catalyst deactivation process occurs gradually, and is generally observed to take place over a period of tens of hours or days rather than the relatively short duration of these experiments. As such, the opposite CO conversion trends observed here are likely a result of the processes taking several hours to reach steady state rather than a significant contribution from catalyst deactivation at low pressure. As such, the third sample at each pressure should be considered the most reliable indication of catalyst performance under the tested conditions. These samples are compared more directly in Figure 6.21. In this context, the increased conversion at higher pressure is an expected result. Interestingly, the product distribution appears to be split into a roughly 1:1 ratio of hydrocarbons and CO_2. This suggests that the catalyst is approximately equally active for the WGS and FT processes. This is desirable for its intended application in combined RWGS/FT chemistry, but generally undesirable for pure FT catalysts.

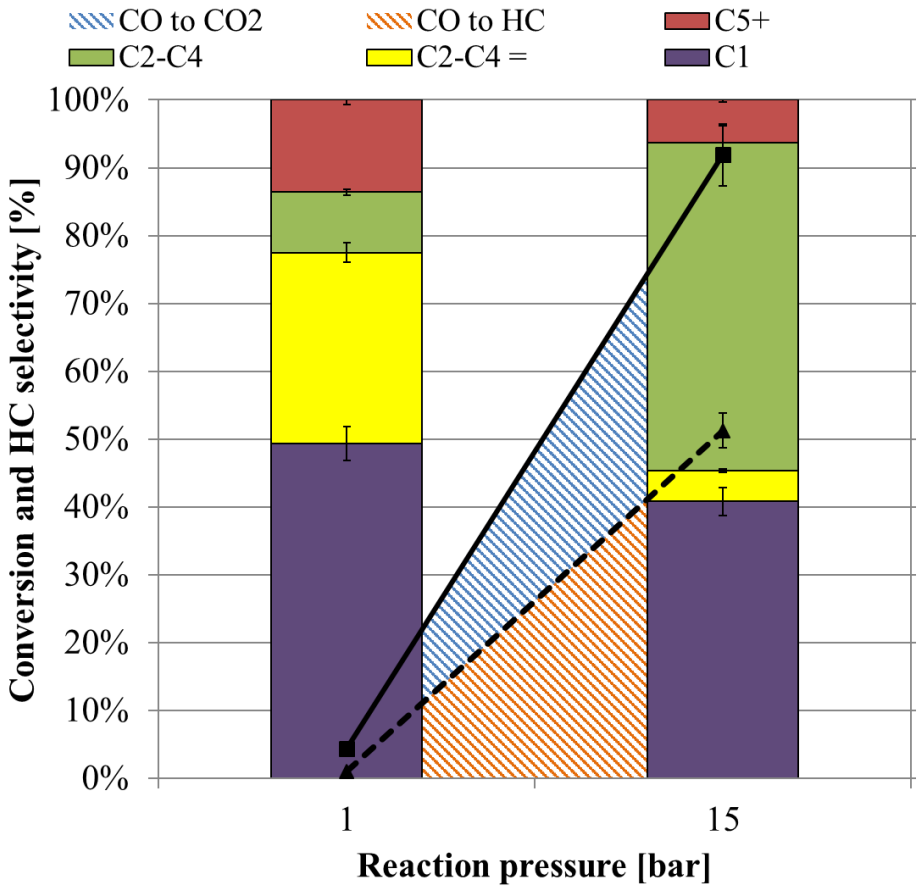

Figure 6.21. FT and WGS activity of Fe@NCNT at varying pressures, 370 °C and a 2:1 H_2:CO feed gas ratio (total flowrate = 8 sccm) after 4 hours on stream. Quantification error is estimated to be ± 5%.

6.3.2. Controlling particle size during CVD synthesis

Nanoparticles have been shown to display high activity for WGS and FT catalysis.[65, 333-335] While a clear understanding of size effects is yet to be established, it is generally accepted that catalyst activity is significantly influenced by particle size.[155, 336] Catalyst activity itself is often measured using (i) activity, or the rate of reactant conversion per gram of active metal or catalyst loading, and (ii) turn over frequency (TOF), or the intrinsic activity of the catalyst active sites. The size of catalyst particles has been shown to affect both of these parameters in Co-based FT catalysts, where activity appears to peak using particles of ca. 7 nm, and TOF decreases at smaller sizes.[154] The decrease in activity observed in particles below 7 nm is initially surprising, as smaller particles are expected to afford a higher reactive surface-area-to-volume ratio. The product distribution was also observed to shift towards methane at smaller particle sizes, which was attributed to increased H_2 coverage on the smaller particles and irreversible CO binding at the particle corner sites. Similar effects have also been observed for iron particles, where activity towards methane products increases with smaller iron carbide particles.[155]

While the single-step CVD synthesis method for Fe@CNT- and Fe@NCNT-type catalysts is beneficial in terms of simple catalyst manufacturing and deep integration of the catalyst components, controlling individual aspects of catalyst composition and morphology *in situ* during synthesis represents a significant challenge. Because the catalytic iron particles in these materials are generally considered to be residual waste metals in the synthesis of pristine commercial CNT products, controlling the size of these particles during CVD synthesis remains an unexplored area of research. To the best of our knowledge, there are no publications available concerning *in situ* control of residual iron particles during the CVD synthesis of highly aligned CNT forests. However, a large number of publications is available investigating the control of the resulting tube morphologies, including properties such as tube length and diameter. Most notably, tube diameter appears to increase with temperature,[206] likely due to particle sintering,[177] an increased rate of ferrocene decomposition,[185] and also varies when using substituted ferrocene complexes as the iron source in the CVD precursor solution.[214] The diameters of CNT produced via CVD are closely related to the size of the iron particles catalysing their growth.[177] As such, studies investigating the control of CNT diameter in CVD synthesis provide a reasonable starting point for investigations targeted at controlling the size of the residual iron particles in these materials as well.

Several aspects of the CVD synthesis protocol were altered in attempts to control particle size in Fe@CNT and Fe@NCNT. These alterations were applied in Fe@CNT synthesis rather than Fe@NCNT synthesis to eliminate complications that might arise from the inclusion of nitrogen in addition to the altered variables. Specifically, in one sample, 10% of the toluene in the precursor solution was replaced with methanol in hopes of stabilising the particles against sintering and inhibiting the rate of ferrocene decomposition through hydroxyl group coordination. This sample is referred to as Fe@CNT-MeOH10. In another sample, a low temperature of 650 °C was used to decrease the rate of ferrocene decomposition, and the space velocity of reactants was increased by a factor of ca. 3.2 by decreasing the diameter of the quartz CVD tube from 25 mm to 14 mm in hopes of decreasing the time available for individual particle growth. This sample is referred to as Fe@CNT-LT,HF. In a final sample, ferrocene was replaced with 1,1-dimethylferrocene in the precursor solution. This has been shown to decrease the diameter of the resulting CNT, though a mechanism explaining this effect has not been proposed.[214] This sample is referred to as FcMe@CNT. The particle size distributions of these samples have been plotted in Figure 6.22.

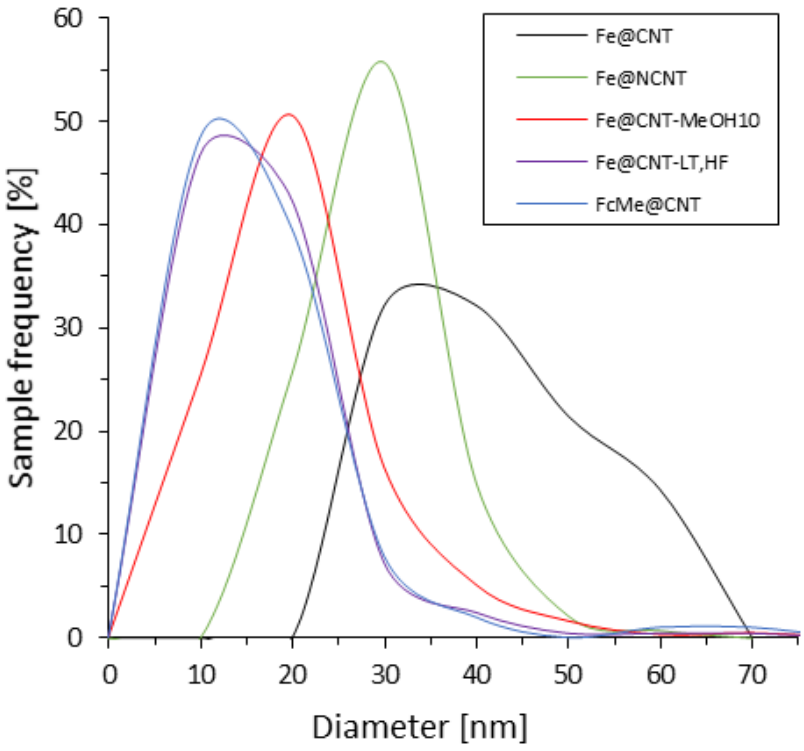

Figure 6.22. Particle size distributions for modified Fe@CNT and Fe@NCNT after activation in air at 570 °C for 40 minutes or 400 °C for 1 hour. Particle sizes were measured via TEM.

All samples displayed bimodal size distributions, which is most clearly exhibited by standard Fe@CNT. This bimodal distribution is likely a result of the two different categories of particles that form during Fe@CNT synthesis. Specifically, (i) particles located at the base or tip of the CNT, which catalyse the initial tube growth process, and (ii) particles that form along the CNT wall structure as a result of excess ferrocene in the precursor solution. Type (i) particles are generally larger (ca. >30 nm) and appear less frequently in the sample, as each of these particles catalyses the growth of a single carbon nanotube. Type (ii) particles are typically smaller (ca. <50 nm) and appear much more frequently in the sample, as the number of these particles that decorates each nanotube ranges from tens to hundreds. It should be noted that type (i) particles are less likely to play a significant role during RWGS/FT catalysis than type (ii) particles. This is due to their relatively larger surface area per particle, the fact that they constitute a significantly smaller portion of total particles in the sample, and the fact that they are typically capped or entirely encapsulated by the CNT structure.

Fe@NCNT display a similar, if slightly smaller particle size than Fe@CNT (25 ±8 nm versus 34 ±11 nm, respectively), which might be explained by particle stabilisation and/or inhibited ferrocene decomposition through nitrile coordination. However, particle size is significantly more influenced by the other attempted control methods. Fe@CNT-MeOH10 display a particle size of (16 ±9 nm), suggesting a stronger stabilisation effect from methanol addition compared to acetonitrile in Fe@NCNT production. FcMe@CNT and Fe@CNT-LT,HF experienced the greatest reduction in particle size and displayed similar small particle sizes of 12 ±10 nm and 12 ±8 nm, respectively. It seems likely that both of these methods would decrease the rate of ferrocene decomposition, though additional studies are required to establish the cause of this trend with greater certainty. When comparing the Raman spectra of the Fe@CNT-based samples, the characteristic D, G and G' peaks are clearly present in all samples, as seen in Figure 6.23. However, particle size modulation appears to increase the I_D/I_G ratio significantly from ca. 0.2 in Fe@CNT to ca. 0.5 in modified samples. This suggests that attempts to affect the rate of iron particle growth also reduce the crystallinity of the resulting CNT support structure. I_D/I_G error is estimated to be ± 0.01.

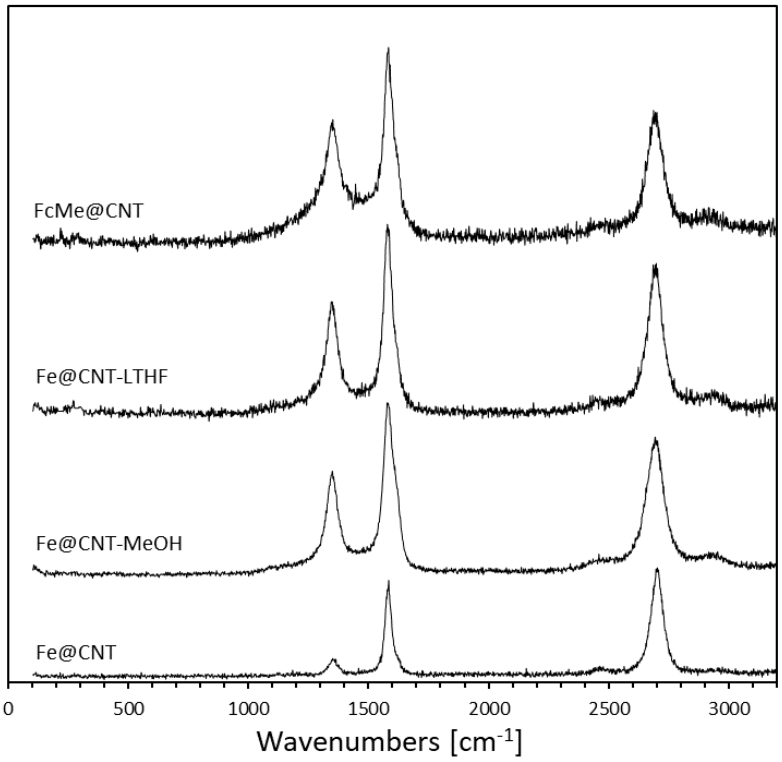

Figure 6.23. Raman spectra of activated Fe@CNT samples with modified particle sizes during synthesis.

When applied in CO_2 hydrogenation, a clear influence of particle size is visible across the samples, as seen in Figure 6.24. CO_2 conversion increased from a low of ca. 40% over Fe@CNT to a maximum of ca. 60% over FcMe@CNT. Selectivity towards methane also increased gradually with smaller particle sizes, as has been previously reported.[155] Interestingly, RWGS/FT reactivity over modulated Fe@CNT samples shifted to resemble Fe@NCNT. Particle size likely influences the reactivity of Fe@NCNT as well, though it is worth noting that the particle sizes of Fe@NCNT and Fe@CNT remain similar, suggesting the nitrogen doping plays a significant role in influencing the differences between their reactivities. However, further studies are required to probe the interactions between catalyst particle size and the influence of *in situ* dopant addition (e.g. nitrogen incorporation) during synthesis.

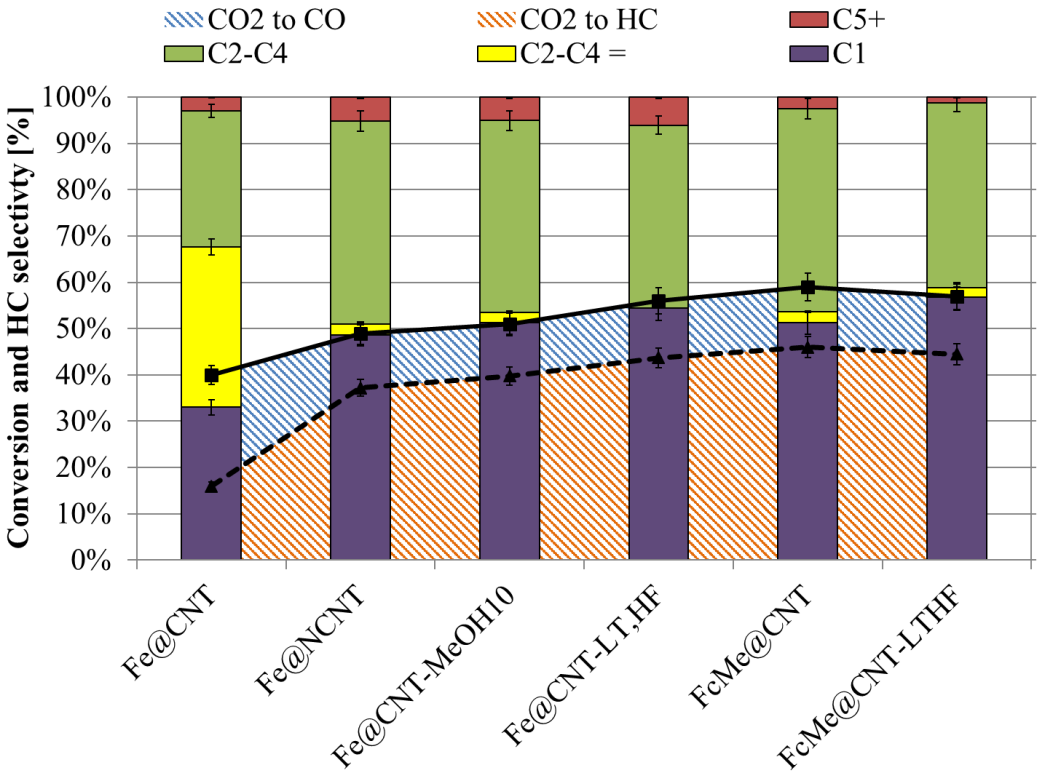

Figure 6.24. Effect of *in situ* particle size control attempts upon the CO_2 hydrogenation performance of modified Fe@CNT and Fe@NCNT. Quantification error is estimated to be ± 5%.

6.3.3. C6 polyol oxidation and oxalic acid production

While this thesis primarily concerns the performance of Fe@NCNT when applied in CO_2 hydrogenation, it is likely that these iron nanocatalysts could be used in a wide variety of chemical processes.[337] As such, a collaboration was established between the University of Bath and leading renewable feedstock researchers at the University of Bari to identify alternative sustainable applications for Fe@CNT and Fe@NCNT. The substitution of nonrenewable fossil resources such as crude oil, coal, and natural gas with renewable carbon sources such as biomass, including lignocellulose and vegetal oils, as a sustainable feedstock has been extensively investigated for the manufacture of biofuels, commodity chemicals, and high value products.[338] Lignocellulosic biomass has attracted considerable attention owing to its potential as a source of numerous platform chemicals such as C6-polyols, 5-hydroxymethylfurfural (5-HMF), levulinic acid (LA) or formic acid (FA), as seen in Figure 6.25.

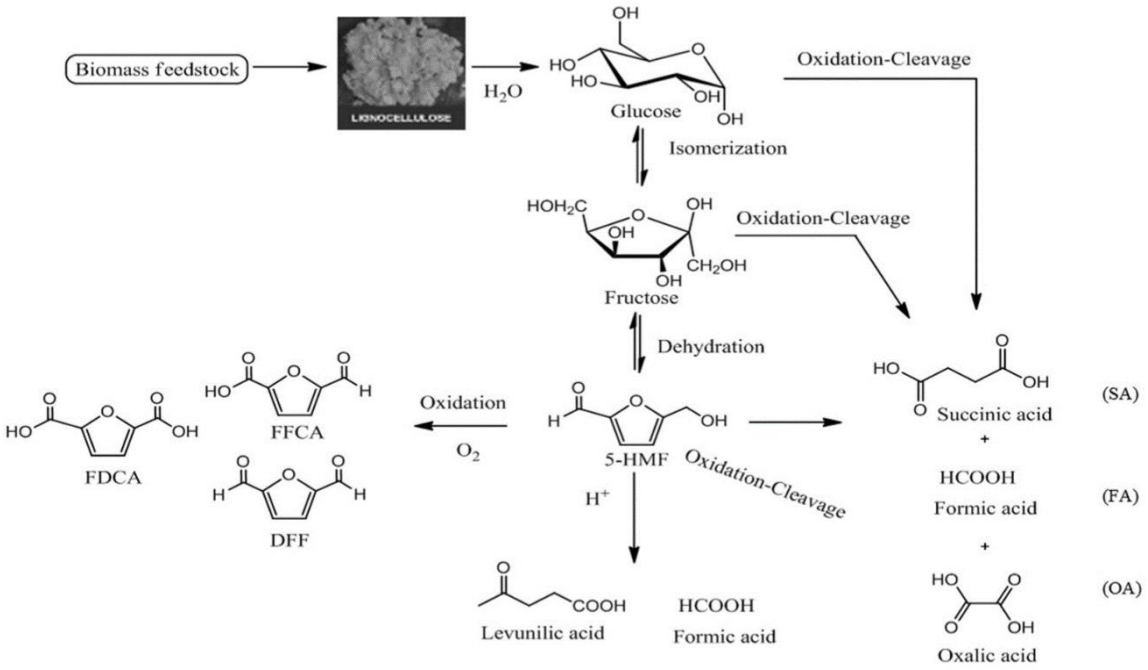

Figure 6.25. Representative schematic for the conversion of cellulosic biomass into green chemicals. Reproduced from reference 115.

5-HMF synthesized by dehydration of fructose or directly from glucose is considered to be one of the most important intermediates due to the wide variety of fossil-fuel-derived products that can be replaced through transformation of its aldehyde- and hydroxyl-bearing furan structure.[115] Alternatively, the oxidative cleavage of glucose or fructose has been considered as a potential route to the sustainable synthesis of mono- and di-carboxylic acids such as lactic, succinic (SA), or oxalic acid (OA). Of these, OA is particularly appealing due to its wide array of industrial applications.[115] The oxidation of C6 polyols with nitric acid is currently the most widely used industrial process for the production of OA. A strong acid solution of HNO_3 and H_2SO_4 with V_2O_5 as the catalyst are used to achieve conversion of 99% and yields of 2.9-54% accompanied by a large volume of waste.[115] Researchers at the University of Bari have previously developed environmentally friendly techniques for the conversion of 5-HMF into 2,5-diformylfuran (DFF), 2-formyl-5-furancrboxylic acid (FFCA), and 2,5-furandicarboxylic acid (FDCA) using water as a solvent and oxygen or air as an oxidant.[338 339] Earth-abundant mixed oxide metal catalysts have been used for selective oxidation of the ring functionalities without interacting with the furan ring.[115] As such, Fe@CNT-type materials were identified as potentially appealing catalysts for the aerobic oxidation of C6 polyols to enhance the viability of cellulose-derived chemicals production.

Interestingly, the tested Fe@CNT-derived catalysts displayed high activity towards ring opening of these C6 polyols, resulting in the production of OA with SA as a co-product.[115] When applied in the oxidative cleavage of 5-HMF, a high conversion of 99% and OA yield of 48% was achieved over Fe@CNT at relatively mild conditions, as seen in Table 6.3.

Table 6.3. Oxidative cleavage of 5-HMF with (A) Fe@CNT, (B) Fe@NCNT, and (C) V-Fe@CNT as catalysts. [5-HMF] = 0.16 M, 0.025 g catalyst. η_x indicates the selectivity towards product x. Reproduced from reference 115.

Catalyst	Stir rate [RPM]	Time [hours]	Temp. [K]	Conv. [%]	η_{DFF} [%]	η_{FFCA} [%]	η_{FDCA} [%]	η_{FA} [%]	η_{OA} [%]	η_{SA} [%]	η_{Fruc} [%]
A	1000	3	383	23.7	4.4	89.6	0	5.6	0	0	0
A	1000	3	403	99	0.4	18.8	22.2	8.5	22.0	8.6	29.0
A	500	3	403	99	4.6	2.4	8.0	15.3	30.6	16.3	21.3
A	250	3	403	99	3.2	4.8	0	18.5	37.8	17.6	17.7
A	250	1.5	413	99	0	0	0	19.4	48.4	7.8	9.2
B	250	1.5	413	47.8	11.7	0	0	16.5	39.8	10.0	21.8
B	250	3	413	90.2	4.9	0	0	27.0	39.9	16.2	4.1
C	250	1.5	413	62.1	3.3	61.8	0	10.8	19.9	1.4	0
C	250	3	413	99	0	65.1	0	25.1	6.3	3.5	0
C	250	6	413	99	0	<1	0	85.3	14.0	0	0

Decreasing the rate of mixing served to increase OA selectivity and reduced damage to the catalyst, allowing it to be collected and recycled several times. Interestingly, fructose formation was observed over Fe@CNT and Fe@NCNT, which has not been previously recorded over mixed oxide catalysts. The inclusion of nitrogen in Fe@NCNT decreased conversion and increased DFF and fructose production, which was attributed to differences in the number of acidic and basic sites in the CNT support structure (as seen in Table 6.2). Furthermore, OA production decreased over V-Fe@CNT, which was unexpected considering the importance of V_2O_5 as a catalyst in typical OA production.

The observed hydration of 5-HMF to fructose and production of SA were noteworthy results of these initial studies. As such, subsequent studies investigated the effects of using fructose and/or SA as substrates for oxidation to determine whether SA could be converted into OA, and whether there is a stepwise cleavage of the initial C6 skeleton to C4 (SA) + C2 (OA) and further to C1 (FA) compounds. When applied in the aerobic oxidation of fructose rather

than 5-HMF, Fe@CNT and V-Fe@CNT resulted in nearly quantitative conversion, as seen in Table 6.4. Fe@CNT resulted in the production of FA, OA and SA in a ratio of ca. 1:2:1, while V-Fe@CNT resulted in the formation of just FA and OA in a ratio of 3:1 after 12 hours. When SA was used as the substrate, OA was formed selectively but conversions remained low at ca. 2.5% even after 12 hours. If FA was added to the SA substrate (1:5 w/w), conversion increased to ca. 12.5% and selective OA formation was preserved at 12 hours. This suggests that FA assisted with the cleavage of SA into OA. However, at reaction times longer than 12 hours, OA degraded into FA.

Table 6.4. Aerobic oxidative cleavage of fructose or SA with (A) Fe@CNT, and (C) V-Fe@CNT. R = residual starting reagents. η_x indicates the selectivity towards product x. Reproduced from reference 115.

Catalyst	Time [hours]	Temp. [K]	Substrate	P_{O2} [bar]	Conv. [%]	η_{FA} [%]	η_{OA} [%]	η_{SA} [%]
A	1	413	Fructose	10	1.2	21.8	--	79.3
A	6	413	Fructose	10	30.5	27.3	46.5	26.3
A	12	413	Fructose	10	99	31.0	46.8	21.0
C	12	413	Fructose	10	98	78.6	22.1	0
A	6	413	SA	10	2.4	0	98	R
A	12	413	SA	10	2.5	0	98	R
A	12	413	SA+FA	10	12.5	R	99	R

Fe@CNT, Fe@NCNT and V-Fe@CNT were eventually also applied in aerobic oxidation of glucose, as seen in Table 6.5, as fructose is generally produced using a base-catalysed glucose isomerisation. A higher temperature was notably required for the oxidation of glucose than fructose. Interestingly, fructose formation was only observed over Fe@NCNT. This is an unexpected result considering the base-catalysed nature of this transformation and the higher number of acidic sites observed in Fe@NCNT compared to Fe@CNT. This observed difference in reactivity can only be explained by the presence of nitrogen in the Fe@NCNT support structure, suggesting that nitrogen incorporation does serve to introduce some basicity to the catalyst support despite potential evidence to the contrary in CO_2 hydrogenation tests and acid/basic site quantification in Table 6.2. No isomerisation whatsoever was observed over Fe@CNT even after 24 hours, though V-Fe@CNT displayed generally higher activity than Fe@NCNT, with higher selectivity towards OA through either direct conversion of glucose into OA, or rapid conversion of fructose into OA resulting in

no observed fructose selectivity. V-Fe@CNT also displayed some activity towards the production of FFCA, which was not observed over Fe@NCNT.

Table 6.5. Aerobic oxidative cleavage of glucose with (A) Fe@CNT, (B) Fe@NCNT, and (C) V-Fe@CNT as catalysts. [glucose] = 0.2 M. η_x indicates the selectivity towards product x. Reproduced from reference 115.

Catalyst	Time [hours]	Temp. [K]	P_{O2} [bar]	Conv. [%]	η_{FFCA} [%]	η_{FA} [%]	η_{OA} [%]	η_{SA} [%]	η_{Fruc} [%]
A	24	403	20	0	--	--	--	--	--
B	6	403	20	10.3	0	32.9	19.4	24.2	8.4
B	12	403	20	22.0	0	41.7	27.0	28.3	0
B	6	423	20	41.8	0	16.4	37.1	17.3	29.2
C	12	403	20	36.8	12.9	50.1	16.6	17.7	0
C	12	423	20	96.6	11.7	31.8	47.9	8.0	0

Conversion and OA yields over the various tested substrates in these experiments were similar to the best performance available from standard industrial technologies. However, the conditions employed were much milder and safer with no airborne emissions and limited waste. As such, these results represent the first report of sustainable OA synthesis from C6 polyols with potential yields of up to 60% under mild conditions.[115]

The author would like to provide explicit thanks and credit to Dr Maria Ventura, Professor Angela Dibenedetto, and Professor Michele Aresta of the University of Bari for their collaboration in this work. Materials synthesis and characterisation (with the exception of acid and base site characterisation) were conducted by the author at the University of Bath. The catalytic testing presented in Tables 6.3-6.5, as well as the acid and base site characterisation presented in Table 6.2 of this thesis, were conducted by collaborators at the University of Bari.

Chapter 7 – Ru-Fe@NCNT

Following the promoter screening studies outlined in section 6.1.3, ruthenium was identified as a noteworthy promoter for its significant increase in conversion and high methane selectivity while further decreasing selectivity towards CO. While liquid fuels and light olefins are considered to be the most valuable and desirable products of CO_2 hydrogenation, CO_2 methanation has been identified as a potentially useful power-to-gas technology for biogas upgrading and renewable energy storage in existing natural gas infrastructure.[35, 103, 340-342] Commercial methanation catalysts typically consist of ruthenium or nickel as the active species, and are generally used for CO and CO_2 methanation to produce synthetic natural gas or avoid catalyst poisoning in ammonia production.[33, 343] These catalysts operate via the Sabatier reaction, which affords the reversible, selective conversion of CO_2 and CO into methane. Ruthenium is the most active catalyst for this transformation but is often avoided due to high costs. As such, nickel-based catalysts are the most common choice for industrial application due to their desirable balance of activity, selectivity and cost.[341, 344] Iron-based catalysts are more active and cheaper than nickel for the conversion of CO_2 and CO, but are typically avoided in methanation applications due to their tendency towards undesired side reactions such as WGS and the production of additional hydrocarbons via FT at low temperatures,[344] while experiencing considerable sintering at high temperatures where methanation becomes more favoured.

Nitrogen doping in Fe@NCNT increases CO_2 conversion and tendency towards methane production when compared with Fe@CNT. As such, experiments were devised to further enhance these methanation properties and produce an iron-based, FT-driven methanation catalyst capable of selective methanation at low temperatures and pressures. This chapter outlines the results of investigations into the CO_2 methanation performance of ruthenium-doped Fe@NCNT (Ru-Fe@NCNT and Ru,Fe@NCNT). The synthesis and characterisation of various ruthenium-doped catalysts is outlined in section 7.1. The reactivity, stability, and mechanism of methanation over these materials is subsequently outlined in section 7.2.

The work discussed in this chapter has been used to produce the following publication:

D. L. Williamson, M. D. Jones and D. Mattia, *Energ. Technol.*, 2019, **7**, 294-306.

7.1. **Ru-Fe@NCNT and Ru,Fe@NCNT**

A variety of ruthenium-doped Fe@NCNT catalysts were produced to explore the methanation capabilities of Fe@NCNT-based materials. Additional Ru-Fe@NCNT samples synthesised via wet impregnation – similar to the catalysts explored in the initial promoter screening discussing in section 6.1.3 – were tested to investigate the effect of ruthenium loading and reaction conditions upon Ru-Fe@NCNT methanation performance. Furthermore, the effect of alternative methods of ruthenium doping were explored by adding ruthenocene, an air-stable ruthenium metallocene complex similar to ferrocene, into the CVD precursor solution. This resulted in the integration of ruthenium into the catalyst directly during CVD synthesis rather than via wet impregnation post-doping. Catalysts containing CVD-doped ruthenium in this manner are referred to as Ru,Fe@NCNT rather than Ru-Fe@NCNT. Ru,Fe@NCNT were produced at two levels of ruthenium loading; in a first sample, 5 mol % of the ferrocene in the CVD precursor solution was replaced with ruthenocene (this sample is referred to as Ru,Fe@NCNT-0.05/0.95). In a second sample, an additional 20 mol % ruthenocene was added to the precursor solution (this sample is referred to as Ru,Fe@NCNT-0.2/1.0).

This section outlines the detailed characterisation of Ru-Fe@NCNT and Ru,Fe@NCNT via SEM, TEM, EDS, Raman, XPS and pXRD. The analysis provided here is intended to serve as a basis for subsequent explanations of the similarities and differences between the observed reactivities of Ru-Fe@NCNT and Ru,Fe@NCNT outlined in section 7.2.

7.1.1. Structural characterisation

FESEM micrographs of post-doped Ru-Fe@NCNT showed the underlying Fe@NCNT bundles in good condition subsequent to the incipient wetness doping process (Figure 7.1 i). The bundles maintained their highly-aligned, tight-packed growth pattern, suggesting that the doping process does not notably disperse the tubes or alter their orientation on the microscale. TEM micrographs of post-doped Ru-Fe@NCNT clearly depicted similar tubes with diameters of 20-100 nm, iron particles with diameters of 20-50 nm embedded in the tube walls, and bamboo-like lateral texturing along the tube wall (Figure 7.1 ii). This is consistent with previous analysis of the Fe@NCNT catalyst (as discussed in Chapter 5), and suggests that the wet impregnation doping process does not notably alter or damage the underlying Fe@NCNT on the nanoscale.

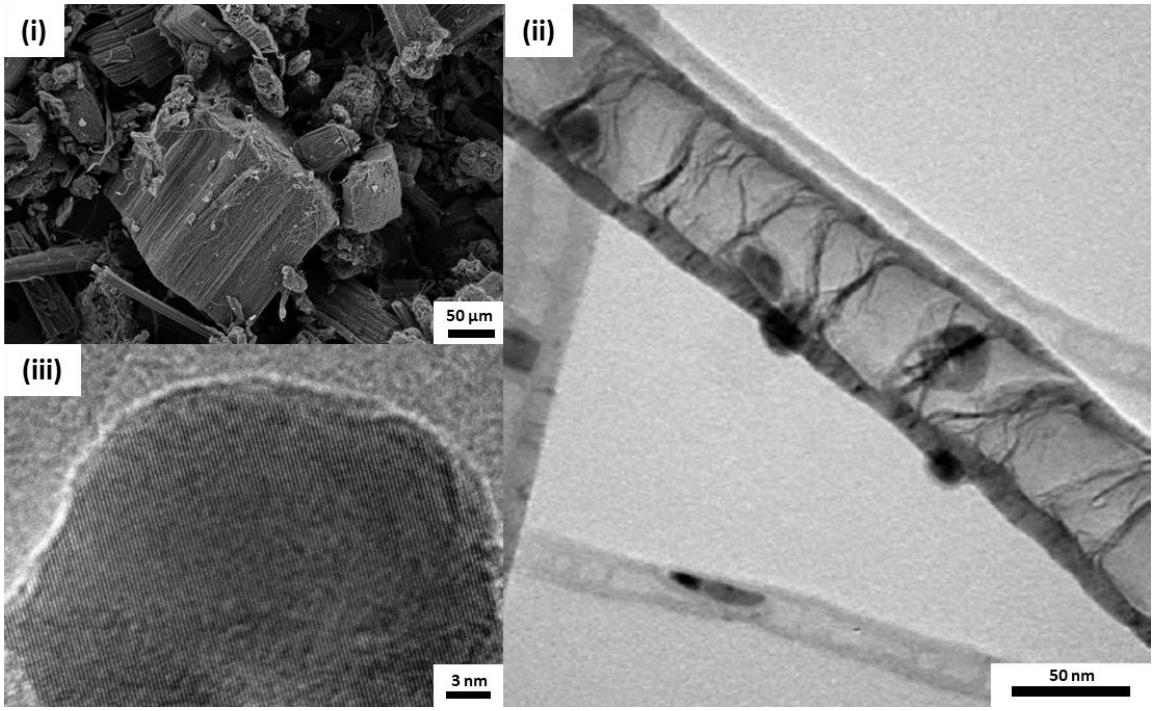

Figure 7.1. (i) FESEM micrograph of Ru-Fe@NCNT directly after incipient wetness doping. (ii) TEM micrograph of Ru-Fe@NCNT after activation at 400 °C in air for 1 hour. (iii) TEM micrograph depicting the crystal lattice of a single supported iron oxide particle after activation at 400 °C in air for 1 hour.

It is difficult to determine from TEM alone whether the particles observed along the NCNT structure consist of iron, ruthenium or both. As such, EDS was used to locate these species in the sample with greater precision, as seen in Figure 7.2. EDS confirmed the presence of nitrogen along the tube support structure, as well as iron in localized particles on both the interior and exterior of the NCNT tube support. Ruthenium appears to be lightly dispersed along the Fe@NCNT in much smaller clusters than the CVD-doped iron particles. In some instances, ruthenium particles of ca. 2-5 nm appeared to agglomerate onto the surface of larger iron particles, though no closer integration of the iron and ruthenium was observed, and there does not appear to be any preference for agglomeration over the iron particles versus the NCNT tubes.

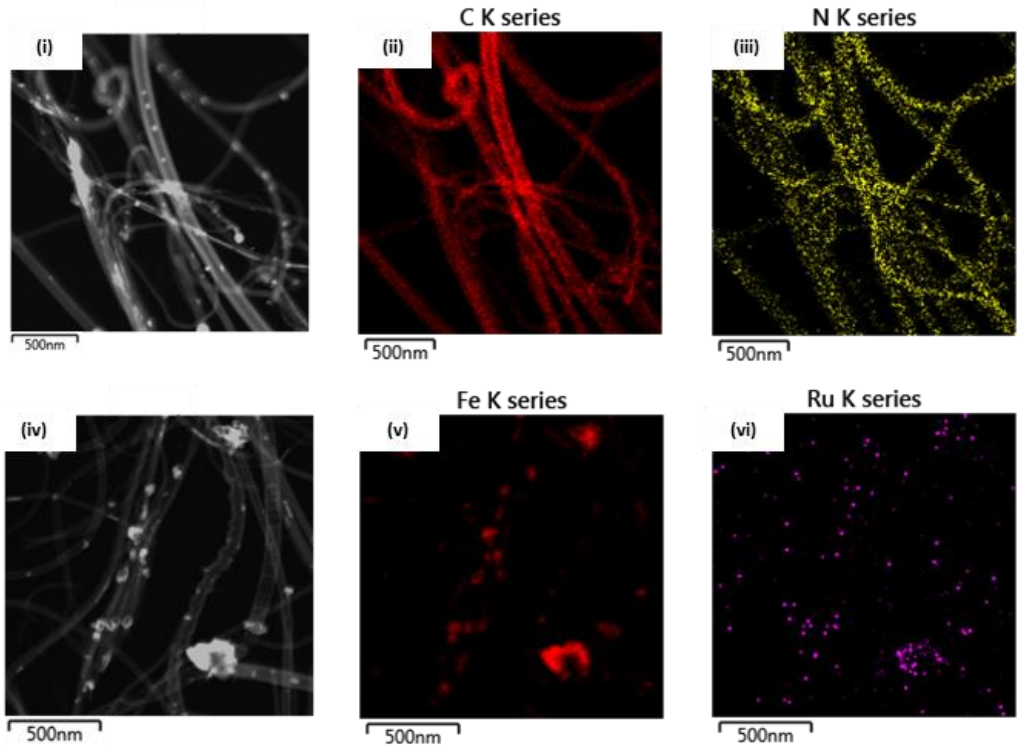

Figure 7.2. EDS maps of Ru-Fe@NCNT after activation at 400 °C in air for 1 hour. (iii) Nitrogen is visibly dispersed throughout the support structure in Ru-Fe@NCNT. (vi) Ruthenium appears dispersed along the catalyst.

SEM and FESEM micrographs of the CVD-doped Ru,Fe@NCNT show the clear formation of tube bundles similar to those formed in standard Fe@NCNT CVD synthesis, as seen in Figure 7.3. Ru,Fe@NCNT-0.05/0.95 displayed highly aligned bundles that were indistinguishable from undoped Fe@NCNT (not shown), suggesting a limited influence from ruthenium doping due to the low loading. Conversely, Ru,Fe@NCNT-0.2/1.0 displayed tube bundles growing in a semi-spherical, orange-peel-like orientation that is

attributed to the greater ruthenocene loading employed during synthesis (Figure 7.3 ii, iv) This is a significant deviation from the tightly packed, linearly aligned bundles observed in typical Fe@CNT and Fe@NCNT, indicating that the addition of ruthenocene interferes with the CNT growth mechanism during synthesis. TEM micrographs of individual Ru,Fe@NCNT-0.2/1.0 tubes clearly display the presence of tubes with similar dimensions to the Ru-Fe@NCNT (Figure 7.3 v-vi). Iron particles remain embedded in the tube walls and wall texturing indicative of nitrogen doping remained visible. While the inclusion of ruthenocene in the CVD precursor solution appears to cause some interference, the similar morphology between these samples suggests that the typical ferrocene-driven growth process still dominates during synthesis.

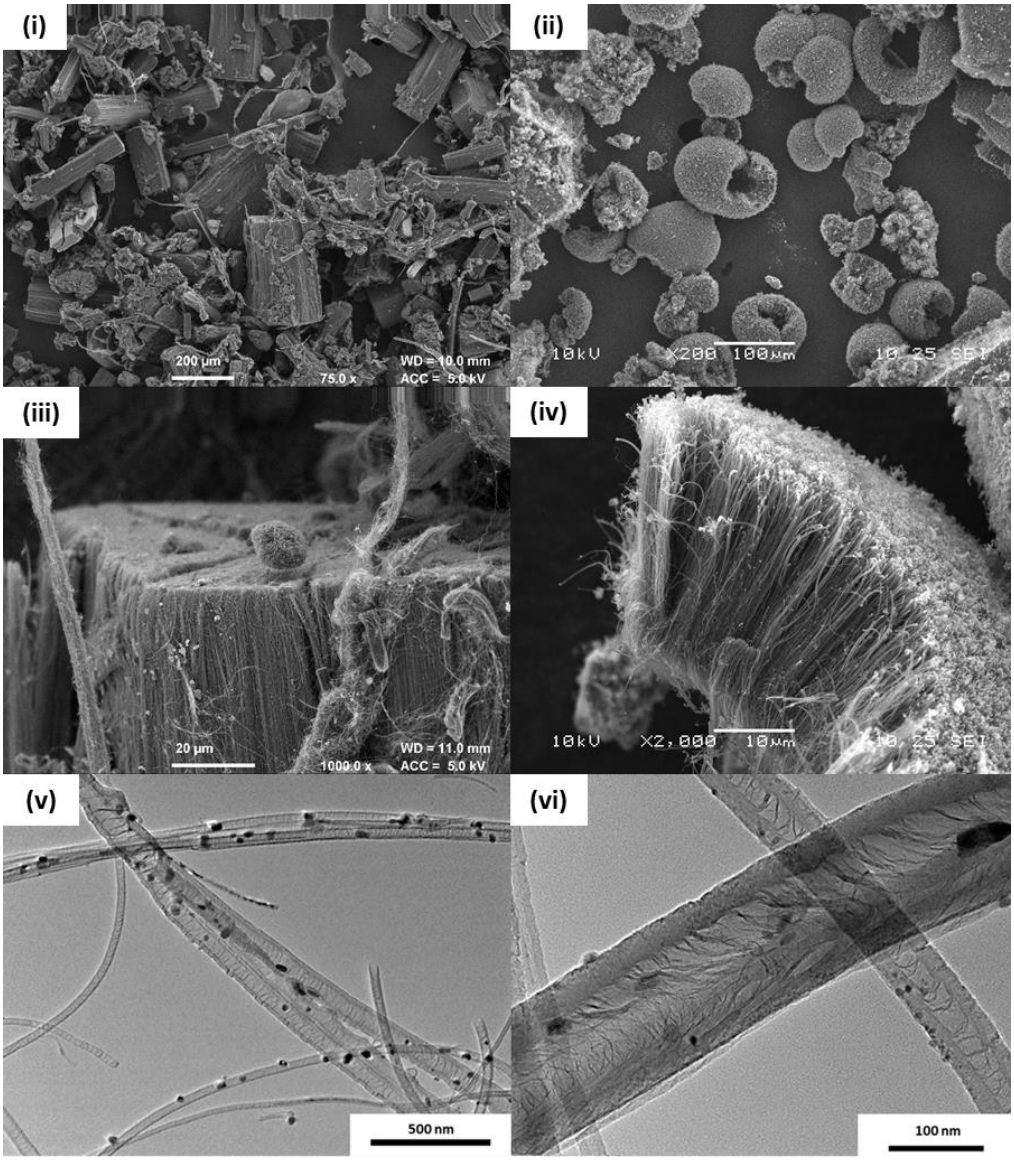

Figure 7.3. SEM, FESEM and TEM micrographs of Ru-Fe@NCNT (i-iii) and Ru,Fe@NCNT-0.2/1.0 (iv-vi). SEM micrographs display catalyst bundles as-synthesised, before activation. TEM micrographs display catalyst tubes after activation in air at 400 °C in air for 1 hour.

EDS maps of CVD-doped Ru,Fe@NCNT again confirm the presence of localised iron particles supported on the tube walls as well as larger iron “slugs” filling the inner tube bore (Figure 7.4 iv-v), as observed in Fe@NCNT and Ru-Fe@NCNT. However, ruthenium appears to be more closely integrated into the iron particles as a result of the CVD doping process. While pure iron oxide particles are clearly visible and abundant in the sample, ruthenium is not observed unless it is part of an existing iron particle (Figure 7.4 vi). This is a significant contrast with Ru-Fe@NCNT, where the doped ruthenium appears uniformly dispersed along the whole catalyst (Figure 7.4 iii), and suggests a greater degree of physical contact and potential electronic interaction between the iron and ruthenium species in Ru,Fe@NCNT compared to Ru-Fe@NCNT.

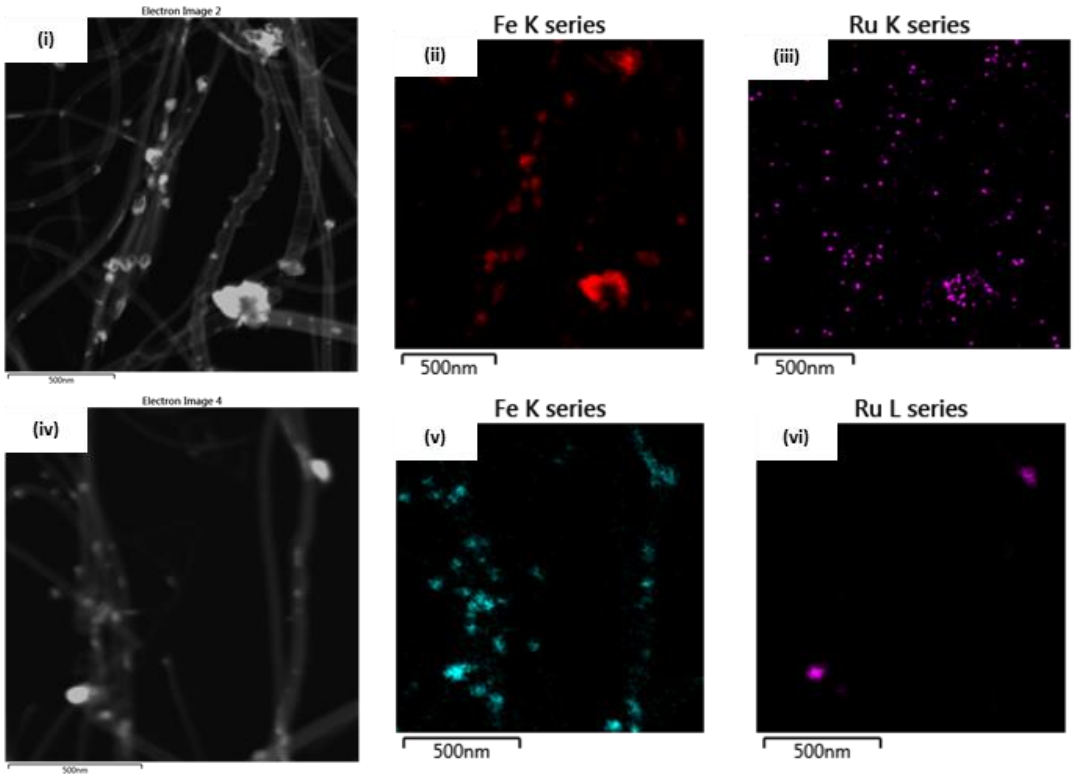

Figure 7.4. EDS maps of (i-iii) Ru-Fe@NCNT and (iv-vi) Ru,Fe@NCNT-0.2/1.0. In Ru-Fe@NCNT, ruthenium appears scattered along the catalyst. Conversely, in Ru,Fe@NCNT ruthenium appears exclusively localized within iron particles, though not all iron particles appear to contain ruthenium.

7.1.2. Chemical characterisation

The Raman spectra of Ru-Fe@NCNT and Ru,Fe@NCNT were compared with Fe@CNT and Fe@NCNT for reference, as seen in Figure 7.5. The typical D and G peaks were observed in both ruthenium-doped samples at 1354 cm^{-1} and 1597 cm^{-1}, respectively. The G' peak at ca. 2666 cm^{-1} is suppressed due to nitrogen inclusion, which disrupts long range order in the sample through the generation of lattice defects. Further discussion concerning the influence of nitrogen doping and lattice defects upon the Raman spectra of CNT materials can be found in section 5.1.2. I_D/I_G values of 0.90, 0.94 and 1.02 were obtained for Fe@NCNT, Ru-Fe@NCNT, and Ru,Fe@NCNT-0.2/1.0, respectively. This confirms progressively increasing disorder in these materials due to nitrogen and ruthenium addition.[270] The slight increase between Fe@NCNT and Ru-Fe@NCNT may be a consequence of minor damage occurring on the NCNT tube structure through prolonged stirring and heating to remove the solvent during and after wet impregnation. However, the largely intact Ru-Fe@NCNT bundles and tubes observed in SEM and TEM suggest that this effect is minor and may be within the margin of error in the Raman spectra. The I_D/I_G increase observed for Ru,Fe@NCNT-0.2/1.0 is more significant and suggests additional structural disorder in the NCNT lattice as a result of ruthenium doping in CVD. This is in good agreement with the deviation in bundle morphology observed via SEM, and further suggests that ruthenocene addition serves to inhibit the typical ordered, ferrocene-driven CNT growth process.

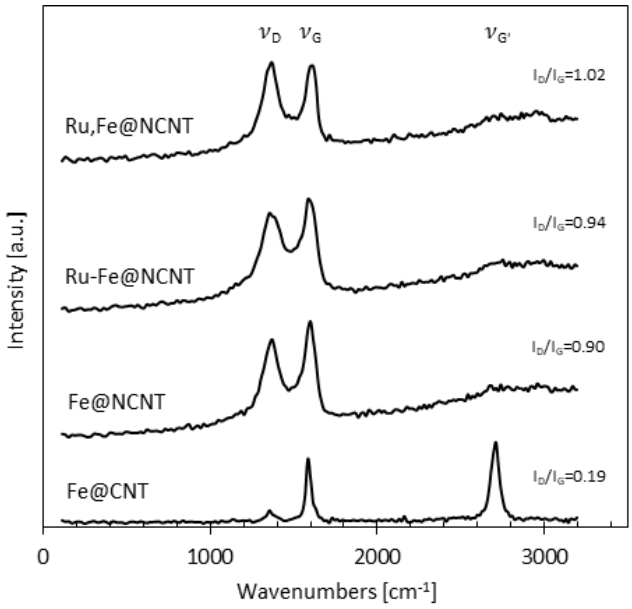

Figure 7.5. Raman spectra of Fe@CNT, Fe@NCNT, Ru-Fe@NCNT, and Ru,Fe@NCNT-0.2/1.0 activated at 400 °C in air for 1 hour. I_D/I_G error is estimated to be ± 0.01.

XPS analysis was used to determine the effect of activation and catalytic application on the elemental composition of the catalysts, as seen in Table 7.1. The trends observed for Fe@NCNT are similar to those discussed in section 5.1.2. XPS of post-doped Ru-Fe@NCNT indicates the presence of iron, nitrogen and ruthenium after the activation step. The ruthenium mass loading was calculated to be 1.6 wt. % from the at. % concentration measured via XPS. This is in reasonable agreement with the 1.0 wt. % mass loading targeted during catalyst synthesis, as individual element concentrations have been noted to vary as much as ±1.1 at. % between sample sites in prior samples (evidenced by Table 5.4). Surface iron loading was similarly determined to be 3.5 wt. %. The observed decrease in iron content between Fe@NCNT and Ru-Fe@NCNT is likely a relative decrease as a consequence of marginally greater oxygen content and the addition of ruthenium to the Ru-Fe@NCNT. After reaction, the iron, nitrogen and ruthenium concentrations also decrease. This is consistent with the decrease in nitrogen and iron observed in standard Fe@NCNT, and may be similarly attributed to the removal of nitrogen during the reduction or reaction steps, and carbon deposition during the reaction resulting in a lower observed concentration of other elements in the sample. These repeated trends in Ru-Fe@NCNT and Fe@NCNT suggest that the incipient wetness ruthenium doping process has little effect on the chemical composition of the underlying Fe@NCNT beyond the desired ruthenium addition.

Table 7.1. Surface compositions of Fe@NCNT, Ru-Fe@NCNT and Ru,Fe@NCNT as-synthesised, after activation, and after methanation testing, as determined by XPS analysis.

Sample		Composition [At. %]				
		C	N	O	Fe	Ru
Fresh	Fe@NCNT	94.3	2.7	2.8	0.3	0
	Ru,Fe@NCNT-0.05/0.95	93.8	2.6	3.4	0.3	0
	Ru,Fe@NCNT-0.20/1.0	95.2	2.5	2.0	0.2	0.1
Activated	Fe@NCNTs	88.9	2.3	7.4	1.5	0
	Ru-Fe@NCNT	87.7	2.2	9.1	0.8	0.2
	Ru,Fe@NCNT-0.05/0.95	89.3	2.2	7.7	0.7	0.1
	Ru,Fe@NCNT-0.20/1.0	88.8	1.4	8.6	1.0	0.2
Post-reaction	Fe@NCNT	91.0	1.2	4.1	0.8	0
	Ru-Fe@NCNT	88.4	1.6	9.7	0.3	0.1
	Ru,Fe@NCNT-0.05/0.95	92.4	2.2	5.1	0.2	0.1
	Ru,Fe@NCNT-0.20/1.0	90.7	2.7	5.8	0.8	0.1

CVD-doped Ru,Fe@NCNT follow several of the same trends observed in Fe@NCNT and post-doped Ru-Fe@NCNT (Table 7.1). The elemental concentrations of iron, nitrogen and ruthenium are similar in the fresh and activated samples. Similarly, the nitrogen content

decreases upon activation, while the iron, oxygen and ruthenium concentrations increase. After reaction, the oxygen, iron and ruthenium content are observed to decrease, similarly to Fe@NCNT and Ru-Fe@NCNT. However, it is noteworthy that the nitrogen content increases rather than decreases, as was observed in all other samples. This could be due to more efficient incorporation of the nitrogen during synthesis as a result of the CVD-doped ruthenium, or it may be due to the different reactivity of this material, as the CVD-doped Ru,Fe@NCNT are later noted to have lower conversion and greater selectivity towards long-chain hydrocarbons than the post-doped Ru-Fe@NCNT. However, this trend should be observed with some caution, as the atom % concentrations of these XPS samples varied by ca. ±0.3 at. % in nitrogen between different scan sites of the same sample. This is likely a result of variance in the activation process (e.g. nonuniform oxygen access in the calcination vessel), as this is significantly larger than the experimental error of XPS measurement. As such, the most significant conclusion that can be drawn from this elemental analysis is that the materials are comparably similar in nitrogen, iron and ruthenium content despite the different methods used to achieve ruthenium doping.

High resolution analysis of the N 1s regions of these materials indicates similar trends in nitrogen composition across all samples (Figure 7.6 i-iii) and is notably identical to the trends for Fe@NCNT discussed previously in section 5.1.2. This suggests that ruthenium doping does not result in significant modulation of the nitrogen species in the NCNT lattice, regardless of doping technique. Fe 2p regions for Fe@NCNT and Ru-Fe@NCNT are also identical to those observed for Fe@NCNT in section 5.1.2 (Figure 7.6 iv-vi). This confirms that the wet impregnation of ruthenium does not significantly influence the character of the iron particles in Ru-Fe@NCNT, and further suggests that there are limited electronic interactions between the iron and ruthenium species in the catalyst.

However, a notable difference in iron species is observed between Fe@NCNT and Ru,Fe@NCNT-0.2/1.0. Similar iron nitrides are observed in all three catalysts immediately after synthesis, as indicated by peaks at 707.2, 708.0, and 710.5 eV, which are attributed to Fe_8N and $Fe_{16}N_2$ (Figure 7.6 iv).[311] Upon activation, these peaks shift to 707.5, 709.9, and 711.3 eV, which are attributed to Fe(0), Fe(II) and Fe(III), respectively (Figure 7.6 v).[312, 313] These peaks suggest a change in the iron species from nitrides to a mix of Fe_2O_3 and Fe_3O_4 as the iron particles are exposed from underneath the graphitic layer of carbon and nitrogen, and transformed into iron oxides. This corresponds with the increase in iron and oxygen concentrations observed after activation (Table 7.1). In Fe@NCNT and Ru-Fe@NCNT,

Fe(III) is the dominant species suggesting a significant concentration of Fe_2O_3 that is confirmed by the presence of a slight satellite peak at ca. 718.8 eV. The small Fe(0) shoulder is attributed to iron that was partially exposed by the activation process but remains unoxidized.[70] In Ru,Fe@NCNT, however, Fe(II) appears to be the dominant species after activation (Figure 7.6 vii.). This suggests that the inclusion of ruthenium during the CVD synthesis process serves to stabilise the iron particles against oxidation. To the authors' knowledge this is the first known example of co-doping bimetallic nanoparticles directly onto carbon nanotube supports via CVD. As such, the precise relationship between the two metals in this doping configuration remains unclear. However, this further suggests that the degree of electronic interactions between iron and ruthenium is notably different depending on ruthenium doping technique. It is difficult to confirm whether these particles exist as a clearly defined alloy at this time. However, their XPS composition is in good agreement with recently published isolated Fe-Ru oxide nanoparticles with diameters of 5-80 nm.[345] Following CO_2 hydrogenation testing the iron species appear largely unchanged across all samples, aside from a slight increase in Fe(0) content in Ru,Fe@NCNT, which further supports the increased reducibility of this material (Figure 7.6 viii).

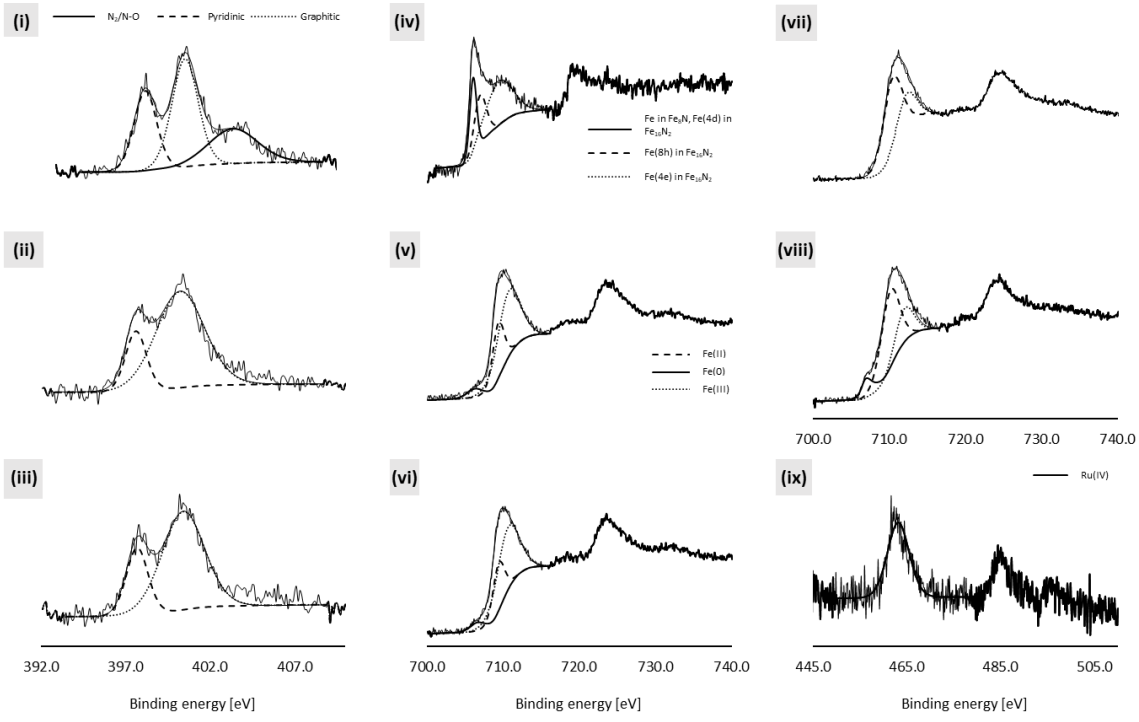

Figure 7.6. XPS spectra of Fe@NCNT N 1s region (i) freshly synthesized, (ii) activated at 400 °C in air for 1 hour, and (iii) after a typical CO_2 reduction reaction. Fe@NCNT Fe 2p region (iv) freshly synthesized, (v) activated at 400 °C in air for 1 hour, and (vi) after a typical CO_2 reduction reaction. Ru,Fe@NCNT Fe 2p region (vii) activated at 400 °C in air for 1 hour, and (viii) after a typical CO_2 reduction reaction. (ix) Ru-Fe@NCNT Ru 3p region activated at 400 °C in air for 1 hour.

Ru 3p regions of the catalysts suggest the possible presence of metallic ruthenium, ruthenium carbide and ruthenium oxide, with some deviation from standard peak positions. Due to the large amount of carbon in these samples and strong overlap between the Ru 3d and C 1s regions of the XPS spectra, the Ru 3p 3/2 region was used instead to determine the composition of the doped ruthenium (Figure 7.6 ix). A single peak is observed in all samples. In post-doped Ru-Fe@NCNT, the peak is observed at 463.1 eV after activation, shifting to 462.7 eV after reaction. This trend is reflected in activated and post-reaction Ru,Fe@NCNT as well, with the observed peak shifting from 463.0 eV to 461.5 eV in Ru,Fe@NCNT-0.05/0.95, and from 463.1 eV to 462.1 eV in Ru,Fe@NCNT-0.2/1.0. Ru(0) has a characteristic peak at ca. 461.2 eV, while RuO_2 has characteristic peaks at 462.6 eV and 464.0 eV.[313, 346, 347] No ruthenium species has been identified with a characteristic peak at 463.1 eV, so this peak shift has been tentatively assigned as either a shift from RuO_2 after activation to Ru(0) after reaction, or merely a shift in the RuO_2 peak with no change in oxidation state.[347] In fresh Ru,Fe@NCNT the peak is observed at 459.2 eV in the Ru,Fe@NCNT-0.05/0.95 sample, and at 461.8 eV in the Ru,Fe@NCNT-0.2/1.0 sample. These peaks are both attributed to either Ru(0) or Ru carbide,[347] as the CVD-doped ruthenium is likely incorporated directly into the NCNT support structure, similar to the Fe nanoparticles. In the absence of characteristic peak positions, these assignments are justified by the oxygen-free CVD synthesis environment, in which the formation of Ru oxides in the fresh samples is significantly less likely than the formation of Ru(0) or Ru carbides as the particles are formed and similarly covered with a graphitic carbon layer.

pXRD was used to further confirm catalyst composition and phase, specifically with respect to identifying the formation of composites or alloys of the iron and ruthenium, as seen in Figure 7.7. This might influence catalytic performance due to electronic interactions between the two metals. The pXRD trends of the Fe@CNT and Fe@NCNT remain identical to those discussed in section 5.1.2. Ruthenium was visible in both Ru-Fe@NCNT and Ru,Fe@NCNT-0.2/1.0 in the form of metallic ruthenium with 2θ peaks at 38.9°, 43.0°, and 44.6°, though the latter peaks are largely obscured by the presence of iron carbides in the sample. RuO_2 was additionally detected, with peaks at 2θ values of 28.0°, 35.1°, and 41.0°.[348-350] While the reflections for all ruthenium species are of a relatively low intensity, as is expected due to the small amount of ruthenium used, the ruthenium species observed in Ru-Fe@NCNT and Ru,Fe@NCNT are distinctly different. Ru-Fe@NCNT shows the clear presence of RuO_2 in small shoulder peaks at 28.0° and 35.1° with no clear contribution

from metallic ruthenium, while Ru,Fe@NCNT shows a clear contribution from metallic ruthenium at 38.9° with no clear contribution from RuO_2.[348-350] Ru,Fe@NCNT display a less intense contribution from the iron oxide species and a stronger contribution from the iron carbides between the two ruthenium-doped materials, while the opposite trend is observed in Ru-Fe@NCNT. This seems to support the trend of enhanced reducibility of Ru,Fe@NCNT as observed via XPS, and may suggest enhanced FT activity for Ru,Fe@NCNT due to more facile formation of the Hägg carbide active phase. However, some caution must be applied in attributing significance to the intensity of these peaks, as their intensities rely significantly upon particle size and crystallinity in addition to the relative concentration of each species in the sample.

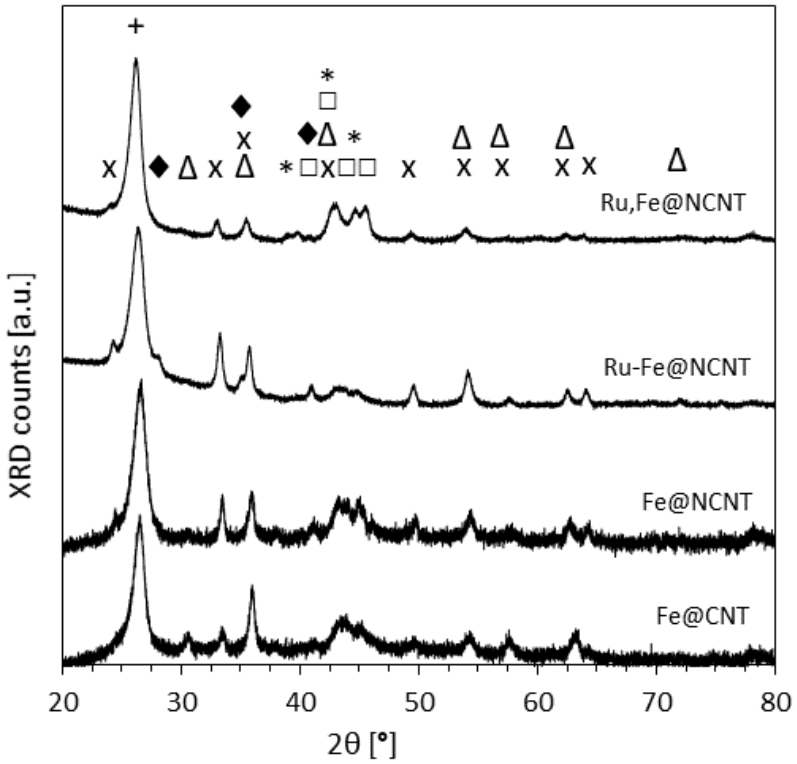

Figure 7.7. XRD spectra of Fe@CNT, Fe@NCNT, Ru-Fe@NCNT and Ru,Fe@NCNT-0.2/1.0 after activation at 400 °C (or 570 °C for Fe@CNT) in air for 1 hour. The spectra indicate the presence of the CNT support (+), Fe_2O_3 (x), Fe_3O_4 (▲), iron carbides (■), metallic Ru (*), and RuO_2 (♦).

7.2. **Ru-Fe@NCNT methanation performance**

Ru-Fe@NCNT and Ru,Fe@NCNT were applied as catalysts in CO_2 hydrogenation to establish the effects of ruthenium loading, reaction conditions and the ruthenium doping techniques upon reactivity. Ruthenium is a well-known CO and CO_2 methanation catalyst that is normally considered to proceed via the reversible Sabatier reaction.[157, 341, 344, 351] As such, it was of particular interest to determine whether the methanation performance of Ru-Fe@NCNT was a consequence of integration between the catalytic iron and ruthenium species, or rather synergistic coupling of the RWGS, FT and Sabatier reactions over distinct iron and ruthenium particles. This section highlights the results of these experiments and provides insights into the presence of mass transfer limitations when using the selected reaction conditions and catalyst loading in a powder packed bed reactor configuration.

The effect of catalyst composition is first discussed in the context of the contribution from each component of the catalyst and the influence of ruthenium loading in Ru-Fe@NCNT. The reactivities of Ru-Fe@NCNT and Ru,Fe@NCNT are then compared and discussed with respect to differences in their characterisation observed in section 7.1. After addressing these differences in the reactivity, the methanation performance of Ru-Fe@NCNT is further explored by probing the influence of reaction conditions such as pressure, gas ratio and WHSV. The influence of WHSV in particular is additionally discussed in the context of mass transfer limitations in the catalyst packed bed. Finally, the stability of Ru-Fe@NCNT is explored over a period of several days and the performance of these catalysts is compared to the equilibrium position of the RWGS reaction at the tested conditions.

Table 7.2 provides an overview of similar or typical methanation catalysts discussed in recent literature, and serves as a benchmark for comparison with Ru-Fe@NCNT. Modern methanation catalysts typically rely on ruthenium or nickel for their catalysis, operating primarily via Sabatier chemistry and requiring a significant amount of the active metal at a 4:1 H_2:CO_2 gas ratio to achieve desirable performance. Conversely, Ru-Fe@NCNT appear to remain primarily iron-driven, requiring ca. 80% less ruthenium than similar catalysts in literature. It should be noted that Ru-Fe@NCNT are operated at higher pressures than the reported literature catalysts, as this is where their methanation capabilities become most noteworthy. Furthermore, the quoted literature catalysts are expected to display comparable conversion and selectivity at similar high pressures, though these experimental data were not reported. As such, it is primarily significant that Ru-Fe@NCNT are capable of producing

comparable results to similar literature catalysts using much less ruthenium an atypical feed gas composition of 3:1 H_2:CO_2. It is additionally noteworthy that Ru-Fe@NCNT achieve desirable methanation performance at 15 bar, while typical industrial methanation processes are cited to operate at higher pressures (ca. 10-30 bar).[35, 352, 353]

Table 7.2. Ru-Fe@NCNT methanation performance compared with literature and commercial catalysts. [a] commercial catalyst [b] this work.

Catalyst	T [°C]	P [bar]	Feed gas, WHSV [hr^{-1}]	X_{CO2} [%]	CH_4 select. [%]	Ru loading [wt. %]
5 wt. % $Co_{0.95}Ru_{0.05}$ nanorods	380	1	4:1 (H_2:CO_2), 12.8	34	98[354]	5
3 wt. % Ru/Al_2O_3[a]	400	1	5:1:10.7 (H_2:CO_2:N_2), NR	84	93[355, 356]	3
5 wt. % $Ce_{0.95}Ru_{0.05}O_2$	450	--	4:1:2.5 (H_2:CO_2:Ar), 12.5	55	99[357]	5
5 wt. % Ru/Mn/Ce-65/Al_2O_3	200	1	4:1:4:1 (H_2:CO_2:N_2:O_2), 0.1	25	91[358]	5
Pd-Mg/SiO_2	450	1	4:1:1 (H_2:CO_2:Ar), 2.6	59	95[34]	--
23 wt. % Ni/CaO/Al_2O_3[a]	400	1	4:1:3.3 (H_2:CO_2:N_2), 12.3	81	80[359]	--
1.0 wt. % Ru-Fe@NCNT[b]	370	15	2.97:1:0.03 (H_2:CO_2:Ar), 0.6	71	91	1

7.2.1. Role of catalyst components

Before exploring the reactivity of Ru-Fe@NCNT in greater detail, the effect of each catalyst component was first isolated, as seen in Figure 7.8. This was achieved by excluding each catalyst component during synthesis, and provided insights into contribution of each component to the reactivity of the final material. It should be noted that CVD-doped Ru,Fe@NCNT play a subsequent supporting role in investigating the relationship between iron and ruthenium in the Ru-Fe@NCNT catalyst, but was not otherwise a primary subject of these investigations into the methanation capabilities of Ru-Fe@NCNT. Fe@CNT (without nitrogen or ruthenium) were used as a baseline reference material during testing and resulted in 48% CO_2 conversion, 16% methane selectivity, 52% CO selectivity and a range of C_{2+} hydrocarbons with an olefin-paraffin ratio of 1.0. Upon incorporating nitrogen into the catalyst support in Fe@NCNT, conversion and methane selectivity both increased to ca. 60% and 48%, respectively. At the same time, CO selectivity decreased to ca. 8%. Based upon the investigations outlined in Chapter 6, these trends in conversion and selectivity appear to be the result of stronger attraction between CO_2, CO, and the catalyst support due to the presence of local C—N dipoles and increased Lewis basicity in the NCNT support that arises from nitrogen doping.[79, 360]

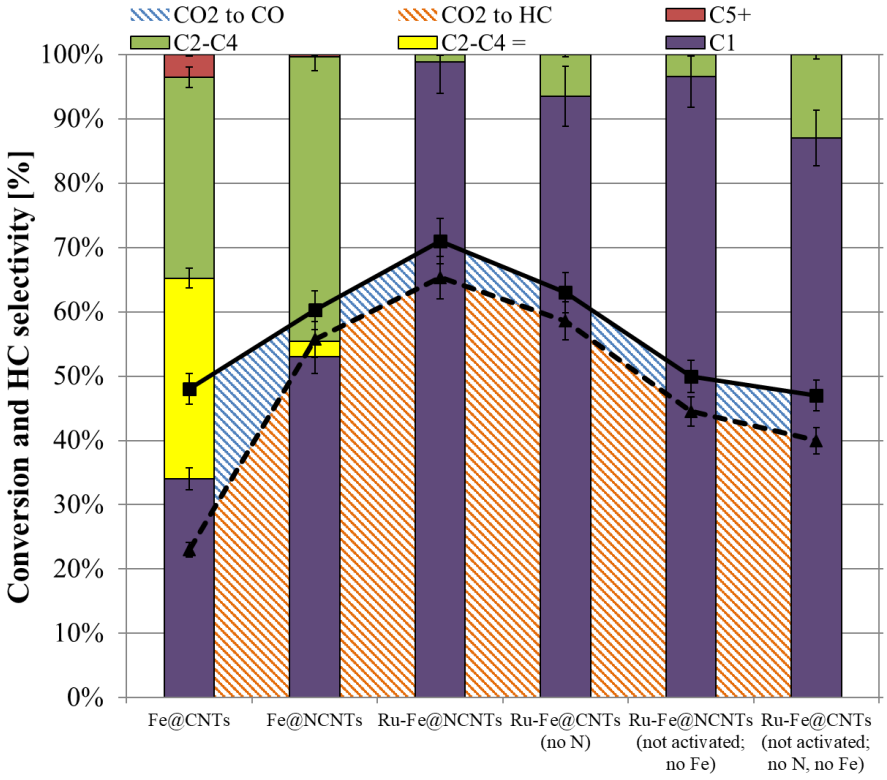

Figure 7.8. Catalytic performance of Fe@CNT, Fe@NCNT, and Ru-Fe@NCNT at 370 °C, 15 bar, 3:1 H_2:CO_2 feed gas ratio, total flowrate of 8 sccm and 0.4 g catalyst.

Doping ruthenium onto the surface of Fe@NCNT to produce Ru-Fe@NCNT further increases conversion and methane selectivity up to 71% and 91%, respectively, while simultaneously decreasing CO selectivity to a minimum of ca. 10%. Excluding nitrogen from the catalyst support after ruthenium doping results in reduced CO_2 conversion by ca. 8%, a slight decrease in methane selectivity and a slight increase in CO selectivity. Excluding iron resulted in a loss of 21% CO_2 conversion, a slightly lesser decrease in methane selectivity and a slightly greater increase in CO selectivity. This confirms the trend established by the initial Fe@CNT, Fe@NCNT, and Ru-Fe@NCNT tests, suggesting that iron, nitrogen and ruthenium all contribute positively to CO_2 conversion, while nitrogen and ruthenium are primarily responsible for shifting the product distribution towards methanation and away from the production of CO and longer hydrocarbons. Excluding both nitrogen and iron from the catalyst results in the lowest conversion and methane selectivity of any ruthenium-doped samples. The observed reactivity of this sample is attributed primarily to the ruthenium catalyst. However, iron appears to play a minor role despite attempting to exclude it by not performing the thermal activation step. This is evidenced by the production of a small amount to $C_{2\text{-}4}$ hydrocarbons, which cannot be explained by Ru-catalysed Sabatier chemistry. Testing uncaclined Fe@NCNT in section 5.3.2 resulted in negligible conversion, confirming that the dedicated activation step is required to achieve significant reactivity from the iron nanocatalysts. This suggests that the ruthenium wet impregnation process serves to expose a small amount of iron in the unactivated catalyst. This might be reasonably explained by the presence of hot spots during catalyst drying.

Ruthenium loading in Ru-Fe@NCNT was subsequently varied between 0-2.0 wt. % ruthenium metal, as seen in Figure 7.9. 1.0 wt. % ruthenium was found to result in the most ideal balance between ruthenium loading and methanation performance. 0.5 wt. % ruthenium resulted in 60% CO_2 conversion and 71% overall methane selectivity, with an increase in CO selectivity and decrease in C_{2+} selectivity versus Fe@NCNT without ruthenium, as expected. 2.0 wt. % ruthenium loading resulted in 75% CO_2 conversion and 93% methane selectivity – a minor increase relative to 1.0 wt. % loading. Considering the employed 3:1 H_2:CO_2 feed gas ratio, a fully methane-selective catalyst would be limited to a maximum of 75% CO_2 conversion. This suggests that the catalyst approaches full hydrogen conversion and maximal CO_2 conversion at 1.0 wt. %, leading to significantly diminished returns on ruthenium loading beyond this point. As such, 1.0 wt. % ruthenium loading was used to synthesize all subsequent Ru-Fe@NCNT samples during these investigations.

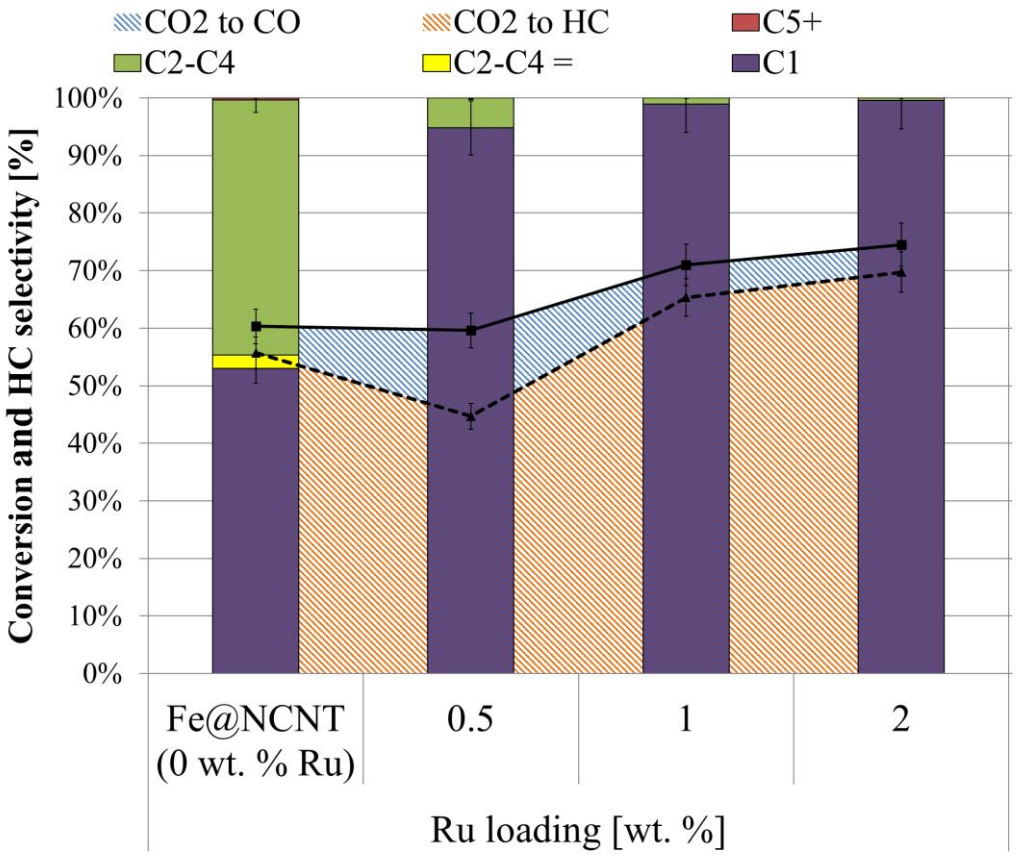

Figure 7.9. Effect of ruthenium loading in Ru-Fe@NCNT at 370 °C, 15 bar, 3:1 H_2:CO_2 feed gas ratio, total flowrate of 8 sccm and 0.4 g catalyst. Quantification error is estimated to be ± 5%.

The reactivities of post-doped Ru-Fe@NCNT and CVD-doped Ru,Fe@NCNT were subsequently compared, as seen in Figure 7.10. These experiments were intended to clarify whether the methanation capabilities of Ru-Fe@NCNT arise as a result of electronic

interactions between the catalytic iron and ruthenium species versus synergistic coupling of the RWGS/FT/Sabatier reactions over distinct iron and ruthenium particles. Characterisation of the chemical composition of Ru-Fe@NCNT and Ru,Fe@NCNT in section 7.1 suggests the formation of Fe-Ru composite particles in Ru,Fe@NCNT with notably different electronic structure than the separate Fe and Ru particles observed in Ru-Fe@NCNT.[345] As such, observed differences in the reactivity of Ru,Fe@NCNT and Ru-Fe@NCNT are likely a consequence of this difference in ruthenium incorporation. Indeed, CVD-doped Ru,Fe@NCNT displayed significantly lower conversion and methane selectivity relative to Ru-Fe@NCNT. C_{2+} selectivity increased drastically, including a surprising increase in C_{5+} selectivity, with conversion and C_{5+} selectivity increasing in accordance with ruthenocene loading.

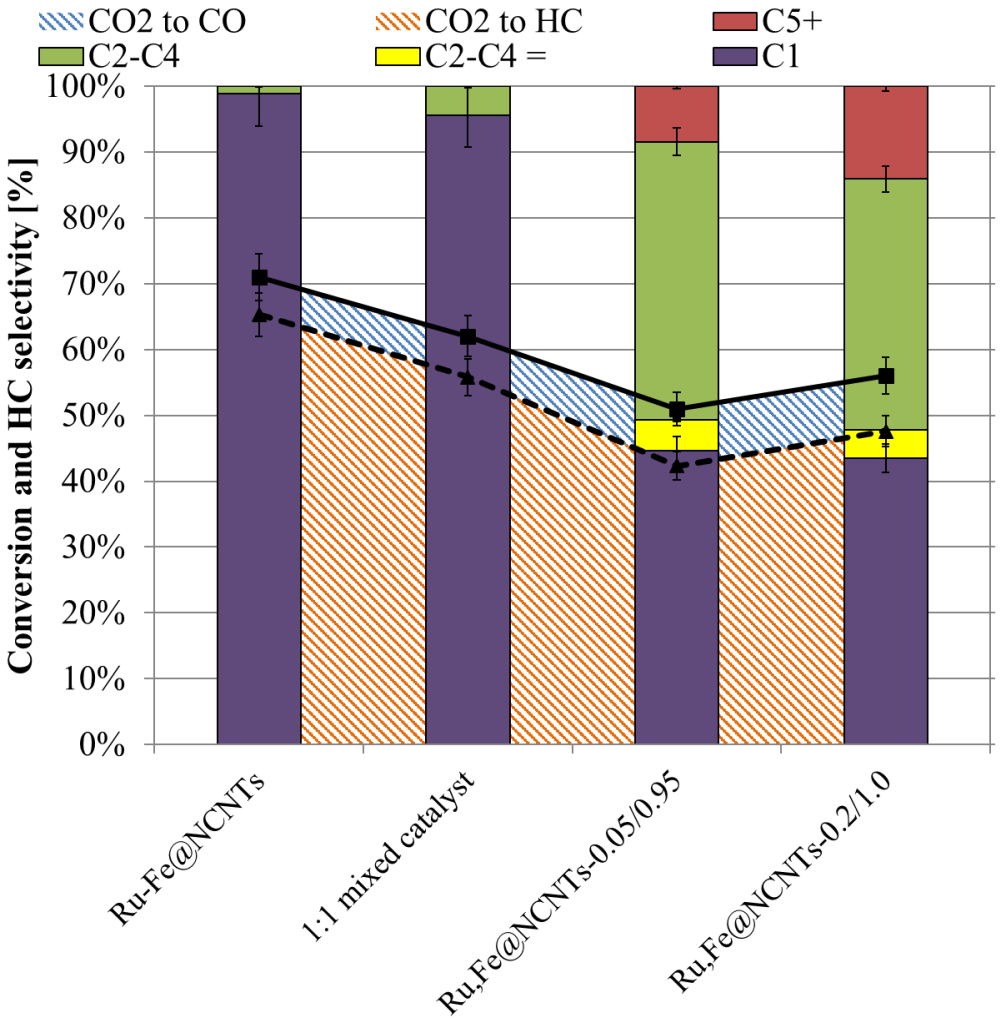

Figure 7.10. Effect of ruthenium doping via CVD versus wet impregnation, and comparison with 1:1 mixed Ru-Fe@NCNT (unactivated) and Fe@NCNT (activated) at 370 °C, 15 bar, 8 sccm total flowrate and 0.4 g catalyst. Quantification error is estimated to be ± 5%.

It was initially expected that integrating ruthenium into the catalyst during CVD synthesis would result in greater contact between the ruthenium, the iron, and the NCNT support, thereby amplifying the methanation performance observed over Ru-Fe@NCNT. However, the formation of Fu-Ru composites instead favours FT chain lengthening rather than Sabatier-driven methanation. The enhanced methanation observed over Ru-Fe@NCNT therefore appears to be a consequence of beneficial coupling of the RWGS, FT and Sabatier reactions to increase conversion and methane selectivity. Much in the same way that the coupling the RWGS and FT processes serves to increase CO_2 conversion over the isolated RWGS reaction by shifting the reaction equilibrium towards products, ruthenium addition in Ru-Fe@NCNT likely serves a similar function by further shifting the RWGS equilibrium through the consumption of CO in Sabatier methanation. A 1:1 mixture of unactivated Ru-Fe@NCNT and activated Fe@NCNT was tested to determine whether close proximity of the iron and ruthenium in Ru-Fe@NCNT serves to enhance methanation activity. This 1:1 mixture displayed in similar activity to Ru-Fe@NCNT, with slightly reduced CO_2 conversion and methane selectivity. This suggests that close proximity of the iron and ruthenium particles in Ru-Fe@NCNT may serve to marginally enhance methanation activity.

7.2.2. Effect of reaction conditions, mass transfer and catalyst stability

The reactivity of Ru-Fe@NCNT was investigated in greater detail by varying reaction conditions during the methanation process. A reaction temperature of 370 °C was used across these experiments to maintain a similar thermodynamic balance between the RWGS and FT processes for clear comparison with previous Fe@NCNT experiments. Furthermore, the 3:1 H_2:CO_2 feed gas ratio was maintained, as is typically cited as the ideal feed gas ratio for CO_2 conversion via RWGS/FT. The effect of reaction pressure was initially probed using pressures of 1-25 bar, as seen in Figure 7.11.

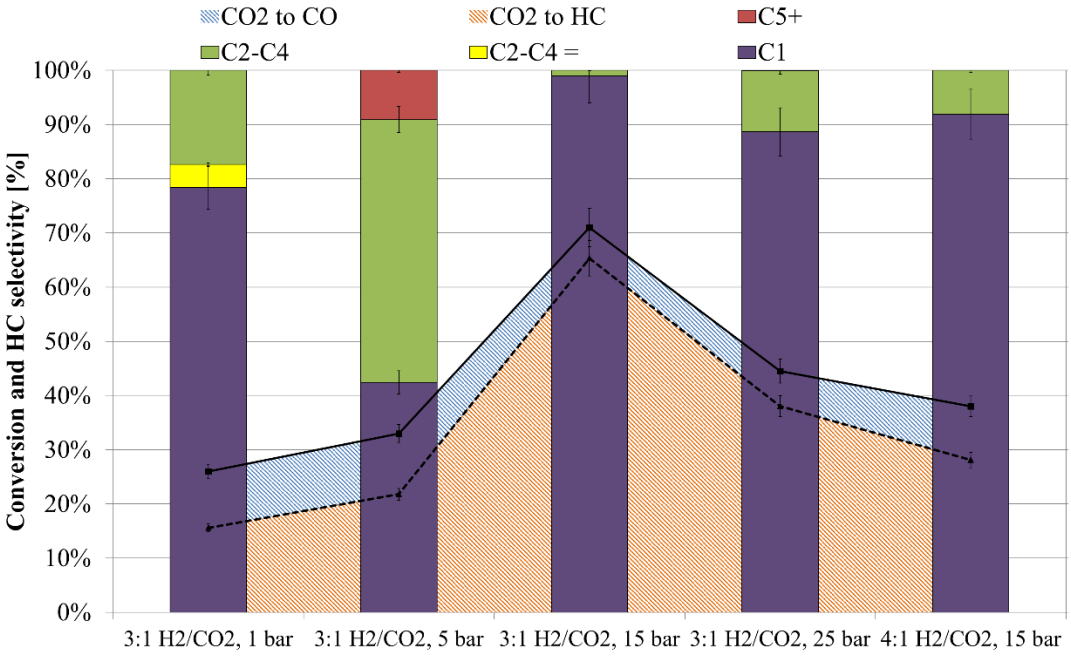

Figure 7.11. Effect of pressure and H_2/CO_2 gas ratio on the catalytic performance of 1 wt. % Ru-Fe@NCNT at 370 °C, 8 sccm total flowrate, and 0.4 g catalyst. Quantification error is estimated to be ± 5%.

At 1 bar, conversion and methane selectivity were relatively low at ca. 26% and 45%, respectively. At 5 bar, conversion increased marginally to ca. 33% and selectivity shifted significantly towards C_{2+} hydrocarbons. This is noteworthy, as the production of C_{2+} hydrocarbons suggests that the catalyst is still capable of significant FT activity and is not entirely government by Sabatier chemistry after ruthenium doping. 15 bar was determined to be the optimal pressure for conversion and methane selectivity, resulting in 71% CO_2 conversion and 91% methane selectivity with only 4% C_{2-4} selectivity and 10% CO selectivity, as previously described. At 25 bar, conversion and methane selectivity both decreased, with selectivity shifting to favour FT again as C_{2+} hydrocarbons reappeared. This is unexpected, and it is unclear why increasing pressure to 25 bar results in decreased activity. FT α values increase with increasing pressure.[146] This is in good agreement with the increased C_2 hydrocarbons produced at 25 bar. When this is considered in conjunction with the inverse relationship between CO_2 conversion and α values highlighted in Figure 6.7, this decreased activity at 25 bar may be a consequence of conflicting methanation and FT chain lengthening mechanisms.

A gas ratio of 3:1 H_2:CO_2 was used for these pressure dependence experiments, as this is well established as an ideal gas ratio for combined RWGS/FT catalysis versus a typical ratio of 4:1 employed in Sabatier-driven methanation catalysts.[67, 78, 226, 361, 362] However, it should be noted that this 3:1 ratio is typically applied to increase the α value of the hydrocarbon

products during CO_2 hydrogenation by starving the reaction of hydrogen. As such, increasing this ratio close to 4:1 is generally expected to result in increased methane production.[67] Interestingly, when the feed gas ratio was increased to 4:1 over Ru-Fe@NCNT at the optimal pressure of 15 bar, CO_2 conversion decreased significantly to ca. 38%, while C_{2+} and CO selectivity both increased marginally. This unexpected result further suggests that the reactivity of Ru-Fe@NCNT is primarily governed by the methane-selective FT process observed over undoped Fe@NCNT, which is marginally enhanced towards methane selectivity through the addition of a small amount of ruthenium rather than entirely governed by ruthenium-driven methanation.

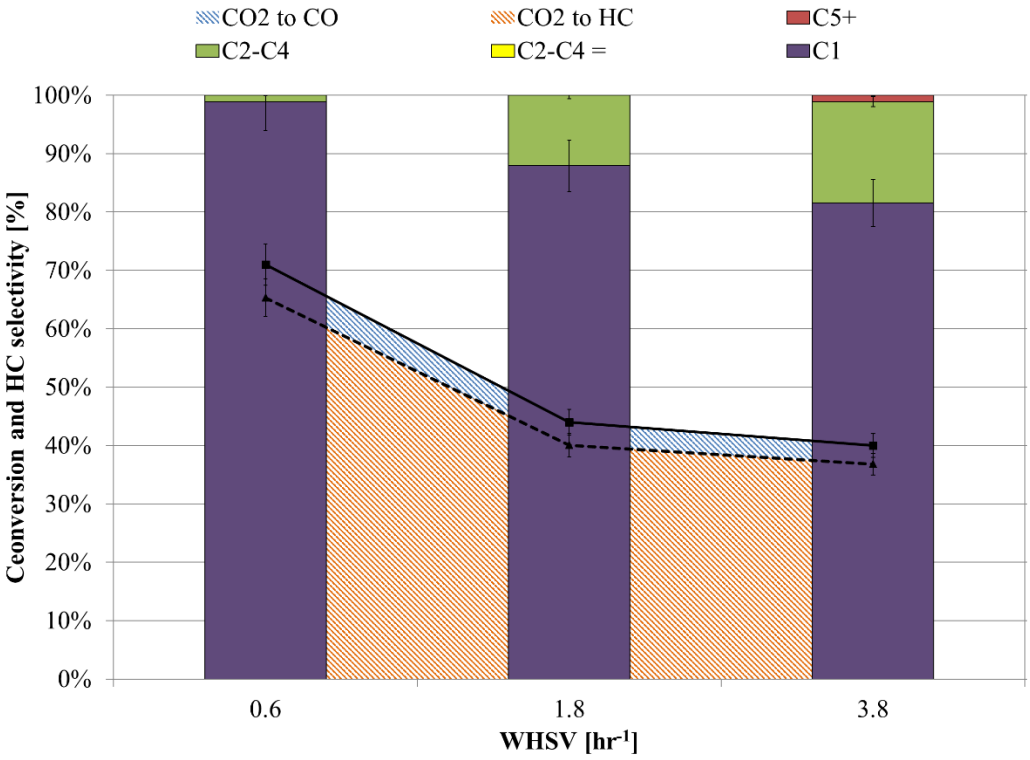

Figure 7.12. Effect of WHSV on conversion and product distribution over Ru-Fe@NCNT at 370 °C, 15 bar, 3:1 H_2:CO_2 feed gas ratio and 0.4 g catalyst. Quantification error is estimated to be ± 5%.

The effect of weight hourly space velocity (WHSV) was subsequently investigated over Ru-Fe@NCNT to gain insights into the kinetics of the Ru-Fe@NCNT methanation process and the influence of residence time upon reactivity, as seen in Figure 7.12. WHSV is defined as the weight of feed flowing per unit weight of catalyst per hour. The feed gas flowrate was varied between 8-50 sccm over 0.4 g catalyst (3.1 cm^3), corresponding to a varied weight hourly space velocity (WHSV) between 0.6-3.8 hr^{-1}. Increasing WHSV in this manner resulted in a decrease in CO_2 conversion from ca. 70% to ca. 43% between 0.6 and 1.8 hr^{-1}, respectively, before finally stabilising at ca. 40% at 3.8 hr^{-1}. Furthermore, C_{2+} hydrocarbon

selectivity increased with increasing WHSV selectivity. This is in good agreement with previous observations of increased α values corresponding to decreased conversion during the initial promoter screening study outlined in section 6.1.3. In the promoter screening, increased α values were also associated with increased CO selectivity, which is not observed in the present WHSV analysis. This is attributed to the presence of rapid Sabatier-driven methanation of excess CO by the ruthenium dopant.

Increasing WHSV also increased the observed rate of CO_2 conversion, as seen in Table 7.3. However, this acceleration of the rate was lessened at larger values of WHSV. This suggests that CO_2 conversion is enhanced by longer residence times, as expected. However, the observed relationship between product selectivity and WHSV was initially surprising. When considering the FT process as a polymerisation of CO intermediates following the initial conversion of CO_2 via RWGS, longer chain hydrocarbon products would be expected to be favoured at longer residence times. Instead, the formation of C_{2+} hydrocarbons over Ru-Fe@NCNT appears increasingly favoured at higher WHSV (i.e. shorter residence times), with methane production being unexpectedly favoured at longer residence times. This suggests that additional factors are influencing the outcome of the observed methanation over Ru-Fe@NCNT. Diffusion limitations are a likely culprit, as the tested values of WHSV are notably low. Specifically, Fickian diffusion limitations whereby H_2 diffuses into the Ru-Fe@NCNT catalyst bundles more quickly than CO_2, resulting in an increased effective H_2:CO_2 ratio at the catalyst surface. This is particularly evidenced at the low WHSV value of 0.6 hr^{-1}, where the relative rate of CO_2 diffusion versus H_2 diffusion is at its lowest. As the flowrate increases, the increased velocity of the feed gas through the catalyst bed improves CO_2 diffusion and brings the effective H_2:CO_2 ratio closer to 3:1, as favoured by FT, hence the observed increase in C_{2+} hydrocarbon production.

Table 7.3. Observed rate of reaction at tested WHSV values for Ru-Fe@NCNT at 370 °C, 15 bar 3:1 H_2:CO_2 feed gas ratio and 0.4 g catalyst. Quantification error is estimated to be ± 5%.

WHSV [hr^{-1}]	$R_{XCO2,obs}$ [µmol g_{cat}^{-1} s^{-1}]	$dR_{XCO2,obs}/dWHSV$
0.6	2.5	4.1
1.8	4.5	2.5
3.8	8.5	2.2

Similar effects were observed when the value of WHSV remained fixed while increasing the flowrate by increasing catalyst loading accordingly, thereby isolating the influence of gas velocity from the influence of residence time entirely (Figure 7.13). As the flowrate increased, conversion decreased and similar C_{2+} hydrocarbon production was observed. This further supports the significance of Fickian diffusion in affecting the methanation performance of Ru-Fe@NCNT. It should be noted that the chosen flowrates were used to remain consistent with previous research on Fe@CNT-type catalysts, which achieved optimal conversion and hydrocarbon selectivity at a flowrate of 8 sccm.[70, 72] These studies were essential in establishing the reactivity of Fe@CNT-type catalysts, though the present findings on the effect of WHSV upon Ru-Fe@NCNT suggest that overcoming mass transfer limitations would be a valuable target in future work to achieve industrially relevant WHSV values, which can be several orders of magnitude greater than those examined here.[363]

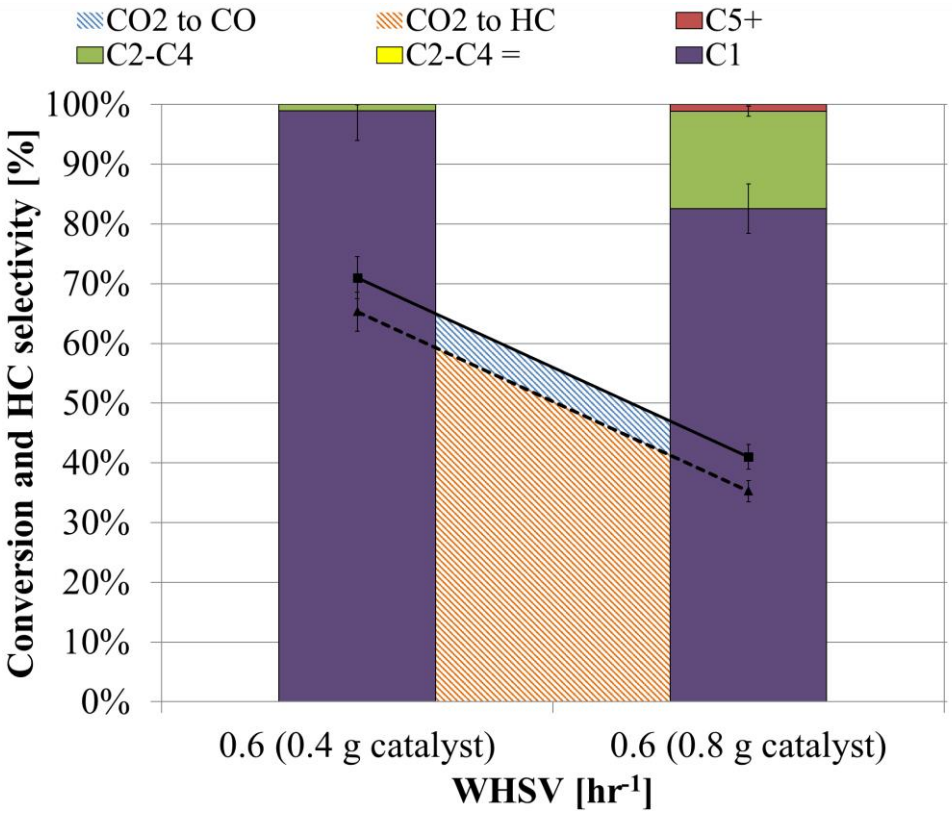

Figure 7.13. Isolated effect of gas velocity over Ru-Fe@NCNT at 370 °C, 15 bar, 3:1 H_2:CO_2 feed gas ratio and 0.4 g catalyst. Quantification error is estimated to be ± 5%.

Given the apparent influence of mass transfer limitations present in the reaction system, calculations were conducted to determine whether the Ru-Fe@NCNT process was deviating significantly from equilibrium. This additionally provided an indication of how isolated process conditions influenced the observed equilibrium versus ideal equilibrium. To achieve this, the equilibrium conversion of the RWGS reaction at 370 °C and varying degrees of CO removal was calculated and compared with experimental data (Figure 7.14). As expected, Ru-Fe@NCNT doped with 1.0 wt. % ruthenium, operating at 15 bar and 8 sccm affords the most desirable balance of mild conditions, reduction in ruthenium loading, high conversion and high methane selectivity while operating close to equilibrium. Additional ruthenium loading does not serve to significantly enhance catalyst performance. Increasing the flowrate beyond 8 sccm results in a notable deviation away from equilibrium, likely due to an increased influence of pressure drop across the catalyst bed. Both increasing and decreasing pressure caused a shift away from equilibrium conversion, confirming the optimal influence of pressure at 15 bar. Alterations in catalyst composition provided a marginal influence on CO_2 conversion and CO removal but did not otherwise result in a notable shift away from equilibrium. Removing both iron and nitrogen from the catalyst was an exception, which shifted performance significantly away from equilibrium, as expected.

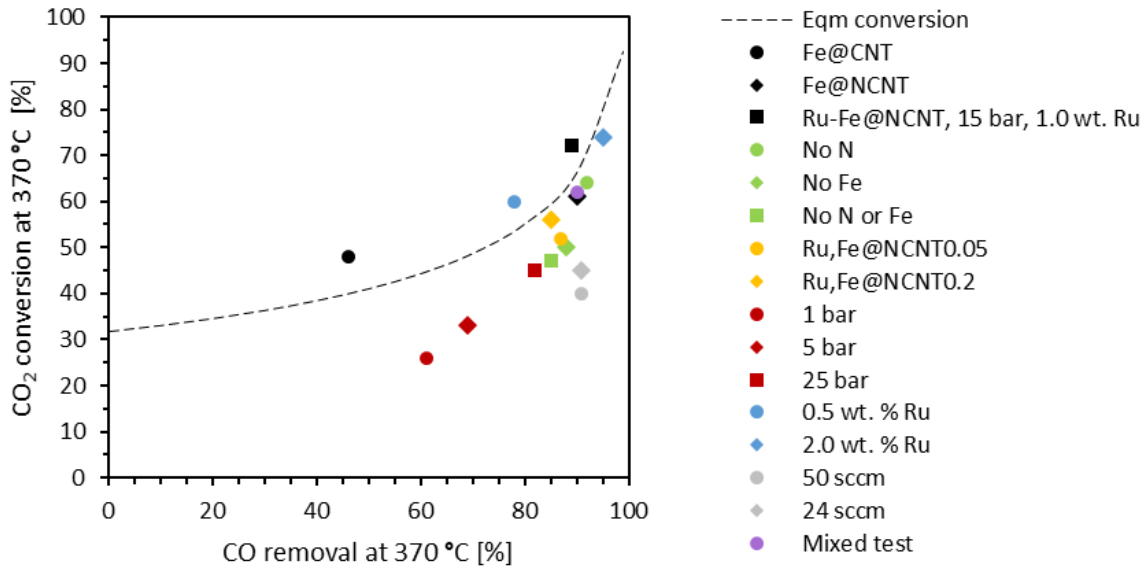

Figure 7.14. CO_2 conversion of all tests conducted for this work plotted versus CO removal from the subsequent FT process, compared with calculated equilibrium CO_2 conversion of the RWGS reaction at 370 °C and 3:1 H_2:CO_2 feed gas ratio from 0-99% CO removal.

These calculation were achieved by initially calculating the equilibrium constant of the isolated RWGS reaction at 370 °C. The reagent concentration terms in the RWGS equilibrium constant equation were then substituted so that the equation was set in terms of CO_2 conversion and subsequent CO removal via FT, as seen in Equation 7.1. By assuming that the equilibrium constant to be constant, regardless of CO removal, equilibrium CO_2 conversion at varying degrees of CO removal could be calculate solving for χ_{CO2} over a range of values for $\chi_{CO,FT}$.

$$\frac{(1-\chi_{CO,FT})\chi_{CO2}{}^2}{(1-\chi_{CO2})(3-\chi_{CO2})} = K_{RWGS,T}$$

Equation 7.1. The equilibrium constant of the RWGS reaction at a given temperature ($K_{RWGS,T}$) is related to CO_2 conversion (χ_{CO2}) and CO removal via FT ($\chi_{CO,FT}$).

Finally, the stability of Ru-Fe@NCNT was tested over 25 hours on stream (80 hours at temperature), as seen in Figure 7.15. The catalyst was tested for 3 days and left under argon at night for safety. After 6 hours on stream, CO_2 conversion decreased to ca. 50% while maintaining ca. 90% methane selectivity. After 8 hours on stream, methane selectivity to decreased to ca. 70%, with CO_2 conversion and methane selectivity stabilising at ca. 40% and 70% respectively after 12 hours. When viewed in the context of the increased carbon content observed in the XPS after reaction, this decrease in activity can likely be attributed in part to carbon deposition during catalysis. Nanoparticle sintering is another common cause of catalyst deactivation that is likely to contribute to the deactivation of Ru-Fe@NCNT.[364] The iron particles remain relatively stable against both particle migration and Ostwald ripening through their integration into the NCNT support. The post-doped ruthenium particles, however, remain susceptible to this phenomenon, which may explain the decrease in methane selectivity, as ruthenium-driven methanation deactivates more rapidly than iron-driven FT, thus resulting in a greater contribution of FT to reaction products over time.

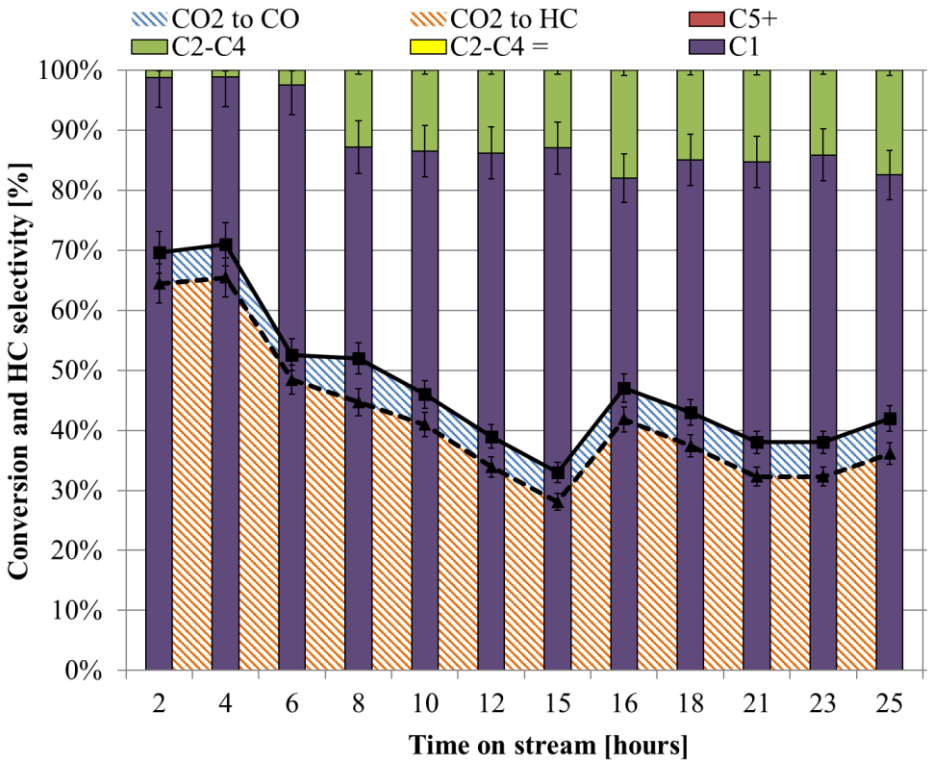

Figure 7.15. Catalyst stability performance over 80 hours at temperature (25 hours on stream) at 370 °C, 15 bar, 3:1 H_2:CO_2 feed gas ratio and 0.4 g catalyst. Quantification error is estimated to be ± 5%.

As a result of the investigations outlined in section 7.2.2, a basic model of the methanation process over Ru-Fe@NCNT was established. Based upon the optimal performance and methane selectivity observed at 15 bar and a 3:1 H_2:CO_2 feed gas ratio, it appears that the reactivity of Ru-Fe@NCNT remains dominated by the same methane-selective, iron-driven FT chemistry that observed in undoped Fe@NCNT. This reactivity appears to be enhanced by the presence of a small amount of ruthenium, presumably through Sabatier-driven CO_2 and CO methanation, though the influence from ruthenium is not significant enough to mask the FT activity of the Fe@NCNT. Furthermore, based upon the enhanced methane selectivity observed over Ru-Fe@NCNT and the increased C_{5+} selectivity observed over Ru,Fe@NCNT, Ru-Fe@NCNT appear to favour methanation via effective coupling of the RWGS, FT, and Sabatier reactions over distinct iron and ruthenium particles rather than significant electronic interaction between the iron and ruthenium. As such, it is proposed that the catalyst remains primarily driven by the combined RWGS/FT process observed over Fe@NCNT. The RWGS reaction produces CO from CO_2, which can then be consumed via iron-driven FT or ruthenium-driven Sabatier chemistry. As such, the addition of a small amount of ruthenium in this manner is capable of shifting the equilibrium of the RWGS reaction further towards products while increasing methane selectivity in the final hydrocarbon products.

Chapter 8 – Conclusions & future work

This thesis summarises the most recent advances in the development of Fe@CNT-type catalysts for combined RWGS/FT CO_2 conversion. The influence of *in situ* CVD nitrogen doping in the CNT support structure to produce Fe@NCNT has been the primary focus of these investigations. Data concerning CO_2 hydrogenation over Fe@NCNT has been supported by further experiments demonstrating the synthesis, activation, and promotion of Fe@NCNT with a variety of promoter metals. Ancillary studies concerning particle size control during CVD synthesis, and the viability of Fe@CNT-type materials as catalysts for the sustainable production of oxalic acid have also been outlined.

Chapters 1 summarises the evidence and consequences of the significant threat posed by human-induced climate change. The value and pathways of CCS and CCU toward the mitigation of greenhouse gas emissions have also been presented there. Indeed, the rate and magnitude of modern worldwide greenhouse gas emissions is unprecedented when compared with historical data, representing a global-scale challenge that can only be addressed by global-scale solutions in society, academia, industry and government. Furthermore, these solutions must be put in place as soon as possible to achieve a 45% decrease in emissions relative to 2010 levels by 2030, and zero net emissions by 2050 to limit warming below 1.5 °C by the end of this century. Ultimately, the key to adequately reducing emissions lies in adopting a new energy infrastructure that does not rely upon the emission of additional CO_2 and similar greenhouse gases into the atmosphere (while also innovating in the construction, refining and agriculture industries). Renewable energy sources such as wind and solar are gaining maturity and commercial adoption, but remain hindered by their intermittent supply patterns and necessary complimentary storage technologies. Reducing atmospheric CO_2 concentrations via CCS is attractive in principle, but also costly. Mitigating this cost by converting the captured CO_2 into value-added chemicals is therefore also appealing, though the negligible mitigation potential represented by the market demand for CO_2-based commodity chemicals limits this as a “silver bullet” solution to reducing atmospheric CO_2 concentrations. However, the production of chemical fuels from CO_2 increases the potential scale of this solution significantly when viewed as a vector for carbon-neutral renewable energy storage (assuming the production of hydrogen from renewable sources such as electrolysis rather than SMR). As such, a combination of CCS and CCU for cost mitigation seems most viable, allowing for emissions reductions by

underground CO_2 sequestration and enhanced efficiency of existing renewable energy technologies.

Chapter 2 summarises the state of literature concerning the Fe@CNT catalyst, which allows for the reduction of CO_2 to hydrocarbons via combined RWGS/FT chemistry over CNT-supported iron nanoparticles. Fe@CNT provide high activity in CO_2 hydrogenation, primarily due to the particle stabilisation and improved hydrogen spill-over afforded by the bridged iron particle-support morphology that arises from incorporating the catalytic iron particles directly into the CNT support during CVD synthesis. Furthermore, this single step synthesis technique makes catalyst manufacturing relatively straightforward when compared with alternative precipitated or impregnated techniques. As such, Fe@CNT have been identified as a valuable platform for further development. Nitrogen doping in CNT-supported iron particles synthesised via post-doping has been observed to increase catalyst activity and α values when applied in pure FT catalysis. This has been previously attributed primarily to improved catalyst reducibility and orbital overlap between the catalytic iron particles and the increased basicity of the N-doped CNT support. However, these studies are limited in number and have either been isolated to pure FT catalysis (without the RWGS component), or have investigated the effect of post-doped iron and nitrogen species in FT and RWGS/FT. As such, *in situ* nitrogen doping of Fe@CNT to produce Fe@NCNT was identified as a valuable subject of further investigation. Chapter 2 therefore provides a background summary of current WGS and FT catalysis, combined RWGS/FT chemistry, MWCNT synthesis and properties, and the current state of knowledge concerning nitrogen doping in CNT materials. From this summary it can be concluded that N-doping in CNT-supported iron particles likely serves to increase catalyst activity in the FT process. However, the origin of this effect remains unclear, and is subject to a wide variety parameters in catalyst synthesis that are difficult to control. Examples of such parameters include particle morphology, CNT morphology, nitrogen content and species, iron content and species, and the physical integration of these catalyst components, among other factors. This is complicated further by the fact that these parameters often influence each other, especially during CVD synthesis, making it difficult to isolate and influence one parameter without inducing additional unintended alterations in the catalyst. However, it seems likely that nitrogen content, nitrogen species, and particle size are additional factors that can influence catalyst activity.

Chapters 5-7 detail the results of investigations into the production, reactivity and modification of the Fe@NCNT catalyst. The key conclusions of these chapters have been outlined below.

8.1. **Experimental conclusions: Chapter 5**

Chapter 5 outlines the production and activation of the Fe@NCNT catalyst. It was demonstrated that Fe@NCNT could be easily produced via the same single step CVD synthesis technique used to produce Fe@CNT by replacing toluene with acetonitrile as the solvent in the CVD precursor solution. Fe@NCNT displayed similar dimensions and morphologies when compared with Fe@CNT, with the exception of bamboo-like compartmentalisation of the wall structure along the inner tube bore due to defects in the sp^2 carbon lattice as a result of nitrogen incorporation. The average particle size of Fe@NCNT was also slightly smaller than Fe@CNT (25 nm versus 34 nm, respectively). However, these values were within one standard deviation of each other, making it difficult to attribute differences in reactivity between them to particle size exclusively. XPS analysis revealed Fe@NCNT to consist of ca. 2-3 at. % nitrogen in a 2:1 ratio of graphitic to pyridinic nitrogen after activation. This configuration of nitrogen incorporation was noteworthy, as graphitic nitrogen provides a shallow electron donor state, thereby enhancing the basicity of the NCNT material. The iron species in the catalyst consisted primarily of iron nitrides immediately after synthesis, but shifted to a mixture of iron oxides after activation and maintained a similar composition after a typical CO_2 hydrogenation reaction. This trend was further reflected in pXRD analysis, which additionally indicated a significant presence of Fe(0) in reduced Fe@NCNT, as expected. In general, the composition and morphology of Fe@NCNT was significantly similar to Fe@CNT after activation and reduction, with the exception of added nitrogen content (and accompanying defects). As such, differences in reactivity between Fe@CNT and Fe@NCNT could be attributed to the presence of nitrogen in the CNT support with greater certainty.

While the synthesis of Fe@NCNT was initially successful, yields remained significantly low (ca. 400-500 mg). This required several days to produce a sufficient quantity of catalyst to compare easily with previously published Fe@CNT data. As such, production scale-up was pursued to improve workflow efficiency and gain further insights into the processes governing Fe@NCNT growth during CVD. Initial efforts targeted increased yields by increasing the surface are available for Fe@CNT growth through the addition of quartz beads

into the CVD furnace. Fe@CNT were chosen as the initial target product to avoid any additional complications arising from modifying the Fe@CNT production technique with both nitrogen doping and increased surface area. Increased yields of 118-148% were achieved via this quartz bead loading technique. While Fe@CNT produced in this manner displayed a similar morphology when compared with typical Fe@CNT via SEM and TEM, Raman spectra indicated a reduced degree of crystallinity in Fe@CNT retrieved from the quartz tube wall when the quartz beads were present. This suggests that the presence of the additional quartz beads inhibited the ordered Fe@CNT growth process along the quartz tube wall, perhaps by affecting the flow of reagents along the quartz tube surface. Furthermore, retrieval of Fe@CNT deposited upon the quartz beads significantly complicated the catalyst synthesis process, requiring several rounds of sonication in methanol and producing large volumes of solvent waste. As such, it was deemed beneficial to pursue alternative scale-up techniques. More successful upscaling was achieved by increasing the precursor injection volume and furnace hold time while keeping the rate of injection constant. Increased yields of 350-400% were achieved when increasing the injection volume from 10 mL to 40 mL, and the furnace hold time from 1 hour to 4 hours. Fe@NCNT produced in this manner displayed similar I_D/I_G values in their Raman spectra, suggesting similar crystallinity of the sample regardless of injection volume. As such, the majority of Fe@NCNT analysed and tested in this thesis were produced using this upscaled synthesis process.

Finally, suitable activation conditions for Fe@NCNT were determined using a combination of TGA, TEM, XPS, and catalytic testing. Fe@CNT have been previously shown to possess a graphitic carbon layer that obscures their catalytic iron particles immediately after synthesis, thereby preventing them from taking part in catalysis. This layer is removed via calcination in air at 570 °C for 40 min for Fe@CNT. However, the defects induced by nitrogen doping in Fe@NCNT significantly reduce the thermal and chemical stability of the CNT support, resulting in more rapid decomposition. As such, new activation conditions had to be established for Fe@NCNT that resulted in oxidation of the graphitic layer without significantly damaging the underling NCNT support structure. TGA in air revealed the onset of decomposition in to be ca. 375 °C in Fe@NCNT versus ca. 400 °C in Fe@CNT, though no decomposition peak was observed for the graphitic layer itself. As such, a range of activation temperatures from 340-420 °C was probed via TEM, XPS and catalytic testing to establish a suitable activation process. Iron content increased in fresh Fe@NCNT was low at ca. 0.2 at. %, but increased steadily with activation temperature until ca. 1 at. % at 400 °C.

This was taken as evidence of progressive removal of the graphitic layer, and was reflected in significantly increased activity after activation. Ultimately, 400 °C for 1 hour was determined to be an ideal activation process, as this exposed a similar amount of iron when compared with activated Fe@CNT while remaining structurally intact. Conversely, when the activation temperature was increased to 420 °C, significant decomposition of the NCNT support structure was observed via TEM.

8.2. **Experimental conclusions: Chapter 6**

Chapter 6 outlines the reactivity of Fe@NCNT in CO_2 hydrogenation. An initial comparison of Fe@NCNT with Fe@CNT is followed by a screening and design of experiments of potentially beneficial promoter metals. The mechanistic influence of nitrogen doping on the RWGS/FT process is subsequently discussed. The chapter concludes with a summary of ancillary experiments concerning the value of *in-situ* particle size control during CVD synthesis, the reactivity of Fe@NCNT in pure FT catalysis, and the applicability of Fe@CNT and Fe@NCNT in sustainable oxalic acid production. The initial comparison of Fe@CNT and Fe@NCNT in RWGS/FT catalysis revealed that Fe@CNT and Fe@NCNT provide similar catalytic activity at 1 bar, though a significant difference is observed when pressure increases to 15 bar. In general, Fe@NCNT provide increased CO_2 conversion and methane selectivity while decreasing CO selectivity. This suggests that the FT process is more favourable than the RWGS process over Fe@NCNT – a trend that is reversed in Fe@CNT. Interestingly, while initial CO conversion in the FT process occurs more favourably over Fe@NCNT, subsequent chain lengthening in the FT appears to be inhibited by the inclusion of nitrogen in the catalyst support, with consistently lower α values observed over Fe@NCNT than Fe@CNT despite the higher conversion. This was an unexpected result, as increasing the basicity of the catalyst support through nitrogen inclusion would be expected to increase both conversion and α values in the final product distribution rather than the observed trade-off.

This trade-off between high α values and high conversion was maintained in metal promoter screening studies, where the addition of promoters to increase α values resulted in decreased CO_2 and CO conversion. Sodium and ruthenium were identified as the most appealing promoters for further investigation, as the addition of sodium resulted in significantly increased olefin production, while the addition of ruthenium resulted in significantly increased conversion and methane selectivity, while further decreasing CO selectivity. A

design of experiments matrix was conducted to probe the influence of sodium loading, temperature and pressure upon reactivity. This confirmed that sodium addition generally inhibited CO_2 and CO conversion in favour of increasing α values and olefin production, thereby providing poor yields of desirable olefin and higher hydrocarbon products. Furthermore, the model established by the design of experiments provided poor predictability of experimental data, suggesting that additional factors were influencing experimental outcomes without being registered as notable variables in the design of experiments model. As such, additional experiments and characterisation were conducted in efforts to gain a greater understanding of the unexpected inverse relationship between conversion and α values.

Local C—N dipoles in N-doped graphitic materials have been shown to attract and activate O_2 molecules for reduction in the ORR. As such, the influence of these C—N dipoles on the adsorption properties of the reactants of the RWGS/FT process was investigated further. H_2 TPR, CO TPD and CO_2 TPD indicated that Fe@NCNT are more easily reduced than Fe@CNT, while inducing stronger adsorption of both CO and CO_2. This was further supported by molecular simulations of the adsorption of the 3:1 H_2:CO_2 feed gas over Fe@CNT and Fe@NCNT at typical reaction temperature and pressure, where the presence of nitrogen resulted in stronger interactions between CO_2 and the catalyst surface. As such, it was proposed that these C—N dipoles in the Fe@NCNT surface are capable of increasing attraction of dipole-containing reactant molecules such as CO_2 and especially CO to the catalyst surface, thereby also disfavouring the adsorption of less polar hydrocarbon product species. This serves to explain the increased CO_2 conversion, increased methane selectivity, and decreased CO selectivity in N-doped samples. Furthermore, this may additionally serve to explain the poor predictability of the design of experiments model, as the addition of dopants could conceivably limit the influence of local C—N dipoles on the RWGS/FT process by favourably adsorbing to (and thereby obscuring) the nitrogen sites in the catalyst surface during wet impregnation. This appears to be supported by the shift back towards typical Fe@CNT reactivity that is observed upon doping sodium onto Fe@NCNT, and the apparent presence of N-coordinated sodium species upon analysing the Na-Fe@NCNT samples via XPS.

Chapter 6 concludes with a series of ancillary experiments outlining the potential for *in situ* particle size control during CVD synthesis, the reactivity of Fe@NCNT in pure FT catalysis, and potential of Fe@CNT and Fe@NCNT as catalysts for sustainable oxalic acid production.

In situ particle size control was attempted by influencing the rate of ferrocene decomposition during CVD in the hope of generating smaller particles embedded along the catalyst wall. This was achieved by increasing the volumetric flow rate of reactants in the quartz CVD, decreasing the temperature of reaction, substituting ferrocene with substituted ferrocene derivatives in the precursor solution, and adding potential stabilising agents such as methanol to the precursor solution. Conversion and methane selectivity increased in accordance with decreasing particle sizes in the resulting samples, which is in good agreement with previous studies on particle size effects of post-doped iron particles supported on carbon nanotubes for pure FT catalysis. Pure FT testing of Fe@NCNT revealed them to be approximately equally active for the WGS reaction and the FT process. This makes them undesirable as a pure FT catalyst, but a promising platform for combined RWGS/FT chemistry. Finally, Fe@CNT and Fe@NCNT were applied in the catalytic oxidative cleavage of C6 polyols for the production oxalic acid. Conversion and oxalic acid yields over the various tested substrates were comparable with the best performance from industry standard techniques, while operating at much milder conditions. While these results are noteworthy in themselves, a particularly significant result from these experiments was the observed production of fructose from glucose over Fe@NCNT, which did not occur at all over Fe@CNT. The conversion of glucose into fructose is a base-catalysed isomerisation; hence, the observed fructose production over Fe@NCNT is a strong indication of increased basicity introduced into Fe@NCNT as a consequence of nitrogen doping. This further supports the theory that local C—N dipoles in the catalyst surface play a significant role in influencing the RWGS/FT process, as increased basicity on its own would certainly be expected to increase long-chain hydrocarbon production rather than the increased methane selectivity observed over Fe@NCNT.

8.3. **Experimental conclusions: Chapter 7**

Chapter 7 concludes the thesis by summarising efforts to develop a highly selective, primarily iron-driven CO_2 methanation catalyst. This is achieved by further exploring the composition and reactivity of the Ru-Fe@NCNT catalyst that was initially identified during the promoter screening experiments outlined in Chapter 6. A key point of investigation in Chapter 7 was whether the enhanced methanation performance observed over Ru-Fe@NCNT arose as a consequence of synergistic reactions over distinct iron and ruthenium particles versus combined iron-ruthenium composite particles. As such, an alternative method of ruthenium doping was also investigated, whereby ruthenium was incorporated

into the Fe@NCNT catalyst during CVD synthesis via the addition of ruthenocene into the CVD precursor solution. This was attempted to encourage greater integration of ruthenium into the catalyst, potentially resulting in more frequent formation of iron-ruthenium composite particles. These CVD-doped materials are referred to as Ru,Fe@NCNT rather than Ru-Fe@NCNT, which are doped with ruthenium via wet impregnation.

Characterisation of Ru-Fe@NCNT and Ru,Fe@NCNT revealed several distinctions between these materials as a result of the different techniques applied to achieve ruthenium doping. While TEM revealed similar tubes with embedded iron particles and bamboo texturing along the tube walls in both materials. In SEM, however, the growth morphologies of the Ru-Fe@NCNT and Ru,Fe@NCNT bundles were notably different. Ru-Fe@NCNT maintained the highly-aligned bundle orientation observed in undoped Fe@NCNT, as expected, while Ru,Fe@NCNT were observed to grow in rounded clusters. This was a first indication that the ruthenium and iron species were more deeply integrated in Ru,Fe@NCNT, as the addition of ruthenium appeared to interfere with the iron-driven Fe@NCNT growth mechanism. EDS maps of the materials revealed that Ru-Fe@NCNT possessed a light dispersion of ruthenium particles along the surface of the underlying Fe@NCNT, while ruthenium only existed in Ru,Fe@NCNT when integrated into an iron-ruthenium composite particle. Furthermore, XPS and pXRD revealed the iron species in Ru,Fe@NCNT to be more stable against oxidation as a result of ruthenium addition, with a potentially greater presence of FT-active iron carbides.

Applying these materials in CO_2 hydrogenation revealed significant differences in reactivity as a result of their ruthenium incorporation method. Ru-Fe@NCNT displayed superior methanation performance, with enhanced conversion and methane selectivity while produced less CO than unpromoted Fe@NCNT. Conversely, Ru,Fe@NCNT displayed marginally decreased CO_2 conversion while producing significantly more C_{5+} hydrocarbons than unpromoted Fe@NCNT. As such, the methanation capabilities of Ru-Fe@NCNT were attributed primarily to synergistic reactivity between distinct iron and ruthenium particles rather than the formation of iron-ruthenium composites. More specifically, it is suggested that the reactivity of Ru-Fe@NCNT relies primarily upon the same methane-selective RWGS/FT process catalysed by the underlying Fe@NCNT, which is enhanced by the addition of a small amount of Sabatier-active ruthenium. This contributes to greater CO_2 and CO methanation both as a result of the additional catalytic metal that is present, but also because the equilibrium of the RWGS step is pulled further towards products as the

ruthenium aids in CO consumption. An optimal ruthenium loading of 1.0 wt. % was identified, and it was found that the catalyst unexpectedly favoured methanation using a feed gas composition of 3:1 H_2:CO_2 rather than the more stoichiometrically justifiable ratio of 4:1. However, varying the WHSV of the feed gas through the catalyst bed suggests that Fickian diffusion limitations of the reactants through the catalyst may be the source of this observation. Furthermore, it Ru-Fe@NCNT were noted to achieve high CO_2 conversion and methane selectivity values of 71% and 91%, respectively, at moderate reaction conditions of 370 °C and 15 bar. This is comparable with similar catalysts cited in recent literature, while requiring ca. 80% less of the costly ruthenium active metal. Unfortunately, probing the long-term stability of the catalyst resulted in a constant decrease in conversion and methane selectivity over the first 12 hours on stream, stabilising at ca. 40% CO_2 conversion and 70% methane selectivity. It is difficult to confirm the mechanism of this deactivation with absolute certainty due to uncertainty in particle size measurements. However, it is likely that sintering and carbon deposition are primarily to blame, as sintering is a commonly observed in supported nanoparticle catalysts at elevated temperatures, and increased carbon content is consistently observed in XPS of these catalysts after catalysis.

8.4. **Future work**

The results presented in this thesis serve as basis for understanding the influence of nitrogen doping in the CNT support of Fe@CNT-type catalysts for CO_2 hydrogenation. Fe@NCNT have been successfully synthesised, thoroughly characterised, and their reactivity has been significantly explored and compared with previously published nitrogen-free Fe@CNT. Nitrogen doping results in increased conversion and methane production in these experiments, which may have valuable applications in renewable energy storage. However, significant work can still be conducted to better control and understand the influence of various components of the Fe@NCNT catalyst (e.g. nitrogen species and particle size), obtain a more desirable product distribution (e.g. by maintaining high conversion and low CO selectivity while increasing the α value of the FT product distribution), and apply Fe@NCNT under more industrially relevant conditions.

It has been shown that the iron particle size and nitrogen content can be controlled in CVD synthesis, and explorations into the influences of these parameters upon CO_2 hydrogenation have already begun by confirming that smaller particles appear to further increase conversion and methane production. These studies could be logically continued by studying the effect

of total nitrogen content upon CO_2 hydrogenation catalysis, with an eventual goal of controlling the concentration and influence of specific nitrogen species (e.g. graphitic, pyrrolic, pyridinic) in the catalyst support. Furthermore, this increased conversion and methane production could build upon the presented investigations into the Ru-Fe@NCNT methanation catalyst in hopes of achieving similar performance with a nickel promoter instead of ruthenium. An eventual goal might entail eliminating the requirement of a promoter altogether to improve the economic viability of Fe@NCNT as an entirely iron-driven methanation catalyst benefiting exclusively from reduced particle size and nitrogen doping. Alternatively, superior control of the Fe@NCNT catalyst composition might eventually allow for a maintained increase in CO_2 conversion by harnessing the influence of the local C—N dipoles observed in theses studies while simultaneously producing higher hydrocarbon FT products. However, it should be noted that all studies contained in this thesis suggest that an inherent trade-off between CO_2 conversion and FT α values exists when performance RWGS/FT catalysis over Fe@NCNT. As an aside, the observed difference in reactivity between Ru-Fe@NCNT and Ru,Fe@NCNT suggests that similar incorporation of other metals into Fe@CNT-type materials could result in a wide range of novel, CNT-integrated materials with unexpected properties.

Finally, significant work can still be conducted to bring Fe@NCNT up to a more industrially-relevant status. The conditions applied in this thesis have allowed for convenient comparison with initial studies on nitrogen-free Fe@CNT. However, a logical continuation of this work would involve supporting Fe@NCNT onto a more practical macro structure such as a cordierite monolith or pellet. This would reduce the effect of pressure drop across the catalyst bed and allow for the development of more meaningful models of reactant diffusion and reaction kinetics at significantly higher flow rates. In this respect, catalyst deactivation and stability are two areas that also require further study to ensure that Fe@NCNT are capable of maintaining their initially high conversion for industrially relevant periods of several thousand hours on stream. Once Fe@NCNT have been optimised in this manner, a comparison of their performance with that of other prominent CO_2 hydrogenation catalysts under standardised conditions would provide valuable insights into the most suitable catalysts for industrial CO_2 conversion.

References

1. R. Lindsey, Climate and Earth's Energy Budget, https://earthobservatory.nasa.gov/Features/EnergyBalance, (accessed 09-11-2019).
2. *Climate Change 2014: Synthesis Report. Contribution of Working Groups I, II and III to the Fifth Assessment Report of the Intergovernmental Panel on Climate Change*, IPCC, Geneva, 2014, p. 46.
3. J. Fourier, *Annales de Chemie et de Physique*, 1824, **27**, 136-167.
4. E. Foote, *American Journal of Science and Arts (1820-1879)*, 1856, **22**, 382.
5. J. Tyndall, *Proceedings of the Royal Institution*, 1859, **3**, 155-158.
6. S. Arrhenius, *The London, Edinburgh, and Dublin Philosophical Magazine and Journal of Science*, 1896, **41**, 237-276.
7. *Global Warming of 1.5 °C: An IPCC Special Report on the impacts of global warming of 1.5 °C above pre-industrial levels and the related global greenhouse gas emission pathways, in the context of strengthening the global response to the threat of climate change, sustainable development, and efforts to eradicate poverty*, IPCC, 2018, p. 82.
8. J. Zalasiewicz, C. N. Waters, M. Williams, A. D. Barnosky, A. Cearreta, P. Crutzen, E. Ellis, M. A. Ellis, I. J. Fairchild, J. Grinevald, P. K. Haff, I. Hajdas, R. Leinfelder, J. McNeill, E. O. Odada, C. Poirier, D. Richter, W. Steffen, C. Summerhayes, J. P. M. Syvitski, D. Vidas, M. Wagreich, S. L. Wing, A. P. Wolfe, Z. An and N. Oreskes, *Quaternary International*, 2015, **383**, 196-203.
9. D. Lüthi, M. Le Floch, B. Bereiter, T. Blunier, J.-M. Barnola, U. Siegenthaler, D. Raynaud, J. Jouzel, H. Fischer, K. Kawamura and T. F. Stocker, *Nature*, 2008, **453**, 379.
10. S. A. Marcott, J. D. Shakun, P. U. Clark and A. C. Mix, *Science*, 2013, **339**, 1198.
11. *Climate Change 2013 – The Physical Science Basis: Working Group I Contribution to the Fifth Assessment Report of the Intergovernmental Panel on Climate Change*, ed. IPCC, Cambridge University Press, Cambridge, 2014, DOI: 10.1017/CBO9781107415324, pp. 383-464.
12. R. Lindsey, Climate Change: Atmospheric Carbon Dioxide, https://www.climate.gov/news-features/understanding-climate/climate-change-atmospheric-carbon-dioxide, (accessed 09-11-2019).
13. J. A. Church, P. U. Clark, A. Cazenave, J. M. Gregory, S. Jevrejeva, A. Levermann, M. A. Merrifield, G. A. Milne, R. S. Nerem and P. D. Nunn, *Science*, 2013, **342**, 1445-1445.
14. M. Bui, C. S. Adjiman, A. Bardow, E. J. Anthony, A. Boston, S. Brown, P. S. Fennell, S. Fuss, A. Galindo, L. A. Hackett, J. P. Hallett, H. J. Herzog, G. Jackson, J. Kemper, S. Krevor, G. C. Maitland, M. Matuszewski, I. S. Metcalfe, C. Petit, G. Puxty, J. Reimer, D. M. Reiner, E. S. Rubin, S. A. Scott, N. Shah, B. Smit, J. P. M. Trusler, P. Webley, J. Wilcox and N. Mac Dowell, *Energy Environ. Sci.*, 2018, DOI: 10.1039/C7EE02342A, 1062-1172.
15. D. Y. C. Leung, G. Caramanna and M. M. Maroto-Valer, *Renewable and Sustainable Energy Reviews*, 2014, **39**, 426-443.
16. A. S. Bhown and B. C. Freeman, *Environmental Science & Technology*, 2011, **45**, 8624-8632.
17. Y. X. Lv, G. H. Yan, C. Q. Xu, M. Xu and L. Sun, *Adv. Mat. Res.*, 2013, **602-604**, 1140-1144.
18. K. S. Lackner, *Science*, 2003, **300**, 1677.
19. S. M. Benson and D. R. Cole, *Elements*, 2008, **4**, 325-331.
20. Deep Saline Sedimentary Formations, https://hub.globalccsinstitute.com/publications/building-cost-curves-co2-storage-north-america/31-deep-saline-sedimentary-formations#fn_14, (accessed 15-09-2018).
21. W. L. Heidug, Juho; McCoy, Sean; Benoit, Philippe, *Storing CO2 through Enhanced Oil Recovery*, International Energy Agency, Paris, France, 2015.

22. J. H. Meessen, *Ullmann's Encyclopedia of Industrial Chemistry*, 2010, DOI: doi:10.1002/14356007.a27_333.pub2.
23. M. Aresta and A. Dibenedetto, *Dalton Trans.*, 2007, DOI: 10.1039/B700658F, 2975-2992.
24. E. A. Quadrelli, G. Centi, J.-L. Duplan and S. Perathoner, *ChemSusChem*, 2011, **4**, 1194-1215.
25. M. R. Kember, A. Buchard and C. K. Williams, *Chem. Commun.*, 2011, **47**, 141-163.
26. A. Otto, T. Grube, S. Schiebahn and D. Stolten, *Energy Environ. Sci.*, 2015, **8**, 3283-3297.
27. C. Federsel, R. Jackstell and M. Beller, *Angewandte Chemie International Edition*, 2010, **49**, 6254-6257.
28. L. Plasseraud, *ChemSusChem*, 2010, **3**, 631-632.
29. BP, Natural gas production, https://www.bp.com/en/global/corporate/energy-economics/statistical-review-of-world-energy/natural-gas/natural-gas-production.html, (accessed 20-09-2018).
30. *Biogas Handbook: Science, Production and Applications*, eds. A. Wellinger, J. Murphy and D. Baxter, Woodhead Publ Ltd, Cambridge, 2013, DOI: 10.1533/9780857097415, pp. 1-476.
31. Global Warming Potential Values, https://www.ghgprotocol.org/sites/default/files/ghgp/Global-Warming-Potential-Values%20%28Feb%2016%202016%29_1.pdf, (accessed 09-11-2019).
32. P. Sabatier and J. Senderens, *CR Acad Sci*, 1902, **134**, 689-691.
33. S. Rönsch, J. Schneider, S. Matthischke, M. Schlüter, M. Götz, J. Lefebvre, P. Prabhakaran and S. Bajohr, *Fuel*, 2016, **166**, 276-296.
34. J.-N. Park and E. W. McFarland, *J. Catal.*, 2009, **266**, 92-97.
35. T. Schaaf, J. Grünig, M. R. Schuster, T. Rothenfluh and A. Orth, *Energy Sustain. Soc.*, 2014, **4**, 2.
36. K. P. Brooks, J. Hu, H. Zhu and R. J. Kee, *Chemical Engineering Science*, 2007, **62**, 1161-1170.
37. N. Perkas, G. Amirian, Z. Zhong, J. Teo, Y. Gofer and A. Gedanken, *Catal. Lett.*, 2009, **130**, 455-462.
38. J. Wambach, A. Baiker and A. Wokaun, *Phys. Chem. Chem. Phys.*, 1999, **1**, 5071-5080.
39. S. K. Wilkinson, L. G. A. van de Water, B. Miller, M. J. H. Simmons, E. H. Stitt and M. J. Watson, *J. Catal.*, 2016, **337**, 208-220.
40. H. Arakawa, M. Aresta, J. N. Armor, M. A. Barteau, E. J. Beckman, A. T. Bell, J. E. Bercaw, C. Creutz, E. Dinjus, D. A. Dixon, K. Domen, D. L. DuBois, J. Eckert, E. Fujita, D. H. Gibson, W. A. Goddard, D. W. Goodman, J. Keller, G. J. Kubas, H. H. Kung, J. E. Lyons, L. E. Manzer, T. J. Marks, K. Morokuma, K. M. Nicholas, R. Periana, L. Que, J. Rostrup-Nielson, W. M. H. Sachtler, L. D. Schmidt, A. Sen, G. A. Somorjai, P. C. Stair, B. R. Stults and W. Tumas, *Chemical Reviews*, 2001, **101**, 953-996.
41. M. Blagoev and S. N. Bizzari, SRI Consulting, 2010, ch. Marketing Research Report: FORMIC ACID.
42. F. Joó, *ChemSusChem*, 2008, **1**, 805-808.
43. X. Yu and P. G. Pickup, *Journal of Power Sources*, 2008, **182**, 124-132.
44. G. A. El-Nagar, M. A. Hassan, I. Lauermann and C. Roth, *Scientific Reports*, 2017, **7**, 17818.
45. M. Grasemann and G. Laurenczy, *Energy Environ. Sci.*, 2012, **5**, 8171-8181.
46. W. Leitner, *Angewandte Chemie International Edition in English*, 1995, **34**, 2207-2221.
47. T. Schaub and R. A. Paciello, *Angewandte Chemie International Edition*, 2011, **50**, 7278-7282.
48. C. Federsel, A. Boddien, R. Jackstell, R. Jennerjahn, P. J. Dyson, R. Scopelliti, G. Laurenczy and M. Beller, *Angewandte Chemie International Edition*, 2010, **49**, 9777-9780.
49. Q. Liu, X. Yang, L. Li, S. Miao, Y. Li, Y. Li, X. Wang, Y. Huang and T. Zhang, *Nat. Commun.*, 2017, **8**, 1407.

50. M. W. Farlow and H. Adkins, *J. Am. Chem. Soc.*, 1935, **57**, 2222-2223.
51. C. Y. Hao, S. P. Wang, M. S. Li, L. Q. Kang and X. B. Ma, *Catal. Today*, 2011, **160**, 184-190.
52. R. Tanaka, M. Yamashita and K. Nozaki, *J. Am. Chem. Soc.*, 2009, **131**, 14168-14169.
53. G. Reuss, W. Disteldorf, A. O. Gamer and A. Hilt, *Ullmann's Encyclopedia of Industrial Chemistry*, Wiley-VCH Verlag GmbH & Co. KGaA, 2000, DOI: doi:10.1002/14356007.a11_619.
54. C. Böhme, *Researchers want to produce formaldehyde from CO2*, BASF SE, 2016, pp. 15-16.
55. L. E. Heim, H. Konnerth and M. H. G. Prechtl, *Green Chemistry*, 2017, **19**, 2347-2355.
56. D.-K. Lee, D.-S. Kim and S.-W. Kim, *Appl. Organomet. Chem.*, 2001, **15**, 148-150.
57. K. Nakata, T. Ozaki, C. Terashima, A. Fujishima and Y. Einaga, *Angewandte Chemie International Edition*, 2014, **53**, 871-874.
58. A. M. Bahmanpour, A. Hoadley and A. Tanksale, *Green Chemistry*, 2015, **17**, 3500-3507.
59. L. Barelli, G. Bidini, F. Gallorini and S. Servili, *Energy*, 2008, **33**, 554-570.
60. J. Kopyscinski, T. J. Schildhauer and S. M. A. Biollaz, *Fuel*, 2010, **89**, 1763-1783.
61. J. A. Rodriguez, P. Liu, J. Hrbek, J. Evans and M. Pérez, *Angewandte Chemie International Edition*, 2007, **46**, 1329-1332.
62. T. L. LeValley, A. R. Richard and M. Fan, *International Journal of Hydrogen Energy*, 2014, **39**, 16983-17000.
63. R. J. B. Smith, M. Loganathan and S. Shantha Murthy, *IJCRE*, 2010, **8**, R4.
64. D. S. Newsome, *Catalysis Reviews*, 1980, **21**, 275-318.
65. C. Ratnasamy and J. P. Wagner, *Catalysis Reviews*, 2009, **51**, 325-440.
66. M. D. Porosoff, B. Yan and J. G. Chen, *Energy Environ. Sci.*, 2016, **9**, 62-73.
67. R. W. Dorner, D. R. Hardy, F. W. Williams, B. H. Davis and H. D. Willauer, *Energy Fuels*, 2009, **23**, 4190-4195.
68. R. E. Owen, D. Mattia, P. Plucinski and M. D. Jones, *ChemPhysChem*, 2017, **18**, 3211-3218.
69. L. Torrente-Murciano, D. Mattia, M. D. Jones and P. K. Plucinski, *J. CO2 Util.*, 2014, **6**, 34-39.
70. J. P. O'Byrne, R. E. Owen, D. R. Minett, S. I. Pascu, P. K. Plucinski, M. D. Jones and D. Mattia, *Catal. Sci. Technol.*, 2013, **3**, 1202-1207.
71. D. R. Minett, Doctor of Philosophy (PhD), University of Bath, 2013.
72. D. Mattia, M. D. Jones, J. P. O'Byrne, O. G. Griffiths, R. E. Owen, E. Sackville, M. McManus and P. Plucinski, *ChemSusChem*, 2015, **8**, 4064-4072.
73. R. W. Dorner, D. R. Hardy, F. W. Williams and H. D. Willauer, *Catal. Commun.*, 2011, **15**, 88-92.
74. P. S. S. Prasad, J. W. Bae, K. W. Jun and K. W. Lee, *Catal. Surv. Asia*, 2008, **12**, 170-183.
75. S.-C. Lee, J.-H. Jang, B.-Y. Lee, J.-S. Kim, M. Kang, S.-B. Lee, M.-J. Choi and S.-J. Choung, *J. Mol. Catal. A: Chem.*, 2004, **210**, 131-141.
76. Y. Huang, X. Meng, Z. Dang, S. Weng and C. Zhang, *J. Chem. Soc., Chem. Commun.*, 1995, DOI: 10.1039/C39950001025, 1025-1026.
77. B. Hu, S. Frueh, H. F. Garces, L. Zhang, M. Aindow, C. Brooks, E. Kreidler and S. L. Suib, *Applied Catalysis B: Environmental*, 2013, **132-133**, 54-61.
78. L. M. Chew, P. Kangvansura, H. Ruland, H. J. Schulte, C. Somsen, W. Xia, G. Eggeler, A. Worayingyong and M. Muhler, *Appl. Catal., A*, 2014, **482**, 163-170.
79. J. Lu, L. Yang, B. Xu, Q. Wu, D. Zhang, S. Yuan, Y. Zhai, X. Wang, Y. Fan and Z. Hu, *ACS Catal.*, 2014, **4**, 613-621.
80. H. M. T. Galvis, J. H. Bitter, T. Davidian, M. Ruitenbeek, A. I. Dugulan and K. P. de Jong, *J. Am. Chem. Soc.*, 2012, **134**, 16207-16215.
81. R. W. Dorner, D. R. Hardy, F. W. Williams and H. D. Willauer, *Energy Environ. Sci.*, 2010, **3**, 884-890.

82. N. von der Assen, L. J. Müller, A. Steingrube, P. Voll and A. Bardow, *Environmental Science & Technology*, 2016, **50**, 1093-1101.
83. R. T. J. Porter, M. Fairweather, M. Pourkashanian and R. M. Woolley, *International Journal of Greenhouse Gas Control*, 2015, **36**, 161-174.
84. A. Brunsvold, J. P. Jakobsen, J. Husebye and A. Kalinin, *Energy Procedia*, 2011, **4**, 3024-3031.
85. Hydrogen Production: Natural Gas Reforming, https://www.energy.gov/eere/fuelcells/hydrogen-production-natural-gas-reforming, (accessed 09-11-2019).
86. M. Carmo, D. L. Fritz, J. Mergel and D. Stolten, *International Journal of Hydrogen Energy*, 2013, **38**, 4901-4934.
87. J. D. Holladay, J. Hu, D. L. King and Y. Wang, *Catal. Today*, 2009, **139**, 244-260.
88. I. Dincer and C. Acar, *International Journal of Hydrogen Energy*, 2017, **42**, 14843-14864.
89. J. Turner, G. Sverdrup, M. K. Mann, P.-C. Maness, B. Kroposki, M. Ghirardi, R. J. Evans and D. Blake, *International Journal of Energy Research*, 2008, **32**, 379-407.
90. M. A. Laguna-Bercero, *Journal of Power Sources*, 2012, **203**, 4-16.
91. H. Ahmad, S. K. Kamarudin, L. J. Minggu and M. Kassim, *Renewable and Sustainable Energy Reviews*, 2015, **43**, 599-610.
92. Y. Kalinci, A. Hepbasli and I. Dincer, *International Journal of Hydrogen Energy*, 2009, **34**, 8799-8817.
93. A. Tanksale, J. N. Beltramini and G. M. Lu, *Renewable and Sustainable Energy Reviews*, 2010, **14**, 166-182.
94. T. Brown, Urea production is not carbon sequestration, https://ammoniaindustry.com/urea-production-is-not-carbon-sequestration/, (accessed 23-09-2018).
95. *Global Energy & CO2 Status Report: The Latest Trends in Energy and Emissions in 2018*, IEA, 2019, p. 3.
96. K. Armstrong and P. Styring, *Frontiers in Energy Research*, 2015, **3**.
97. *World Energy Outlook 2012*, International Energy Agency, Paris, France, 2012, p. 241.
98. C. Hepburn, E. Adlen, J. Beddington, E. A. Carter, S. Fuss, N. Mac Dowell, J. C. Minx, P. Smith and C. K. Williams, *Nature*, 2019, **575**, 87-97.
99. O. Ellabban, H. Abu-Rub and F. Blaabjerg, *Renewable and Sustainable Energy Reviews*, 2014, **39**, 748-764.
100. *Renewables 2018: Analysis and Forecasts to 2023*, IEA Publications, 2018.
101. K. Heussen, S. Koch, A. Ulbig and G. Andersson, *IEEE Systems Journal*, 2012, **6**, 140-151.
102. J. Amouroux, P. Siffert, J. Pierre Massué, S. Cavadias, B. Trujillo, K. Hashimoto, P. Rutberg, S. Dresvin and X. Wang, *Progress in Natural Science: Materials International*, 2014, **24**, 295-304.
103. S. H. Jensen, C. Graves, M. Mogensen, C. Wendel, R. Braun, G. Hughes, Z. Gao and S. A. Barnett, *Energy Environ. Sci.*, 2015, **8**, 2471-2479.
104. M. Aneke and M. Wang, *Applied Energy*, 2016, **179**, 350-377.
105. Hydrogenious, RETHINKING THE WAY WE STORE ENERGY, http://www.hydrogenious.net/en/energy-storage/, (accessed 10-09-2019).
106. H. Ibrahim, A. Ilinca and J. Perron, *Renewable and Sustainable Energy Reviews*, 2008, **12**, 1221-1250.
107. X. Luo, J. Wang, M. Dooner and J. Clarke, *Applied Energy*, 2015, **137**, 511-536.
108. P. J. Hall, I. A. G. Wilson and A. Rennie, *Carbon Dioxide Utilisation*, eds. P. Styring, E. A. Quadrelli and K. Armstrong, Elsevier, Amsterdam, 2015, DOI: 10.1016/B978-0-444-62746-9.00003-7, pp. 33-44.
109. L. Chen, F. Chen and C. Xia, *Energy Environ. Sci.*, 2014, **7**, 4018-4022.
110. G. Laurenczy, *CHIMIA International Journal for Chemistry*, 2011, **65**, 663-666.

111. K. Müller, K. Brooks and T. Autrey, *Energy Fuels*, 2017, **31**, 12603-12611.
112. G. A. Olah, *Angewandte Chemie International Edition*, 2013, **52**, 104-107.
113. *Climate Change Act 2008*, Her Majesty's Government of the United Kingdom of Great Britain and Northern Ireland, London, 2008, pp. 1-102.
114. *Paris Agreement*, United Nations, New York City, 2015, pp. 16.
115. M. Ventura, D. Williamson, F. Lobefaro, M. D. Jones, D. Mattia, F. Nocito, M. Aresta and A. Dibenedetto, *ChemSusChem*, 2018, **11**, 1073-1081.
116. D. R. Minett, J. P. O'Byrne, S. I. Pascu, P. K. Plucinski, R. E. Owen, M. D. Jones and D. Mattia, *Catal. Sci. Technol.*, 2014, **4**, 3351-3358.
117. J. Lin, A. Wang, B. Qiao, X. Liu, X. Yang, X. Wang, J. Liang, J. Li, J. Liu and T. Zhang, *J. Am. Chem. Soc.*, 2013, **135**, 15314-15317.
118. P. Kaiser, R. B. Unde, C. Kern and A. Jess, *Chemie Ingenieur Technik*, 2013, **85**, 489-499.
119. R. Jain and R. Maric, *Applied Catalysis A: General*, 2014, **475**, 461-468.
120. C. A. Callaghan, Worcester Polytechnic Institute Worcester, MA, 2006.
121. N. E. Amadeo and M. A. Laborde, *International Journal of Hydrogen Energy*, 1995, **20**, 949-956.
122. E. S. Lox and G. F. Froment, *Industrial & engineering chemistry research*, 1993, **32**, 71-82.
123. T. Riedel, H. Schulz, G. Schaub, K.-W. Jun, J.-S. Hwang and K.-W. Lee, *Top. Catal.*, 2003, **26**, 41-54.
124. S. Saeidi, S. Najari, F. Fazlollahi, M. K. Nikoo, F. Sefidkon, J. J. Klemeš and L. L. Baxter, *Renewable and Sustainable Energy Reviews*, 2017, **80**, 1292-1311.
125. H. Wang, X. Nie, Y. Chen, X. Guo and C. Song, *J. CO2 Util.*, 2018, **26**, 160-170.
126. S. G. Jadhav, P. D. Vaidya, B. M. Bhanage and J. B. Joshi, *The Canadian Journal of Chemical Engineering*, 2016, **94**, 101-106.
127. A. Goguet, F. C. Meunier, D. Tibiletti, J. P. Breen and R. Burch, *The Journal of Physical Chemistry B*, 2004, **108**, 20240-20246.
128. E. Vesselli, L. De Rogatis, X. Ding, A. Baraldi, L. Savio, L. Vattuone, M. Rocca, P. Fornasiero, M. Peressi, A. Baldereschi, R. Rosei and G. Comelli, *J. Am. Chem. Soc.*, 2008, **130**, 11417-11422.
129. Y. A. Daza and J. N. Kuhn, *RSC Adv.*, 2016, **6**, 49675-49691.
130. C. Liu, L. Munjanja, T. R. Cundari and A. K. Wilson, *The Journal of Physical Chemistry A*, 2010, **114**, 6207-6216.
131. C. Liu, T. R. Cundari and A. K. Wilson, *Inorganic Chemistry*, 2011, **50**, 8782-8789.
132. X. Rozanska and R. Vuilleumier, *Inorganic Chemistry*, 2008, **47**, 8635-8640.
133. H. Schulz, *Applied Catalysis A: General*, 1999, **186**, 3-12.
134. A. de Klerk, *Kirk-Othmer Encyclopedia of Chemical Technology*, 2013, DOI: 10.1002/0471238961.fiscdekl.a01, ch. Fischer–Tropsch Process, pp. 1-36.
135. B. H. Davis, *Catal. Today*, 2009, **141**, 25-33.
136. V. V. Ordomsky, B. Legras, K. Cheng, S. Paul and A. Y. Khodakov, *Catal. Sci. Technol.*, 2015, **5**, 1433-1437.
137. P. F. Schubert, C. A. Bayens, L. Weick and M. O. Haid, *Stud. Surf. Sci. Catal.*, eds. E. Iglesia, J. J. Spivey and T. H. Fleisch, Elsevier, 2001, vol. 136, pp. 459-464.
138. V. V. Ordomsky, B. Legras, K. Cheng, S. Paul and A. Y. Khodakov, *Catal. Sci. Technol.*, 2015, **5**, 1433-1437.
139. T. H. Pham, Y. Qi, J. Yang, X. Duan, G. Qian, X. Zhou, D. Chen and W. Yuan, *ACS Catal.*, 2015, **5**, 2203-2208.
140. N. Lohitharn and J. G. Goodwin, *J. Catal.*, 2008, **257**, 142-151.
141. M. Claeys and E. Van Steen, *Stud. Surf. Sci. Catal.*, Elsevier, 2004, vol. 152, pp. 601-680.
142. J. Kummer, T. DeWitt and P. Emmett, *J. Am. Chem. Soc.*, 1948, **70**, 3632-3643.
143. R. C. Brady III and R. Pettit, *J. Am. Chem. Soc.*, 1980, **102**, 6181-6182.
144. W. A. A. van Barneveld and V. Ponec, *J. Catal.*, 1984, **88**, 382-387.

145. R. Van Santen, I. Ciobîcă, E. Van Steen and M. Ghouri, *Adv. Catal.*, Elsevier, 2011, vol. 54, pp. 127-187.
146. H. G. Stenger and C. F. Askonas, *Industrial & Engineering Chemistry Fundamentals*, 1986, **25**, 410-413.
147. M. Albrecht, U. Rodemerck, M. Schneider, M. Bröring, D. Baabe and E. V. Kondratenko, *Applied Catalysis B: Environmental*, 2017, **204**, 119-126.
148. R. E. Owen, J. P. O'Byrne, D. Mattia, P. Plucinski, S. I. Pascu and M. D. Jones, *Chem. Commun.*, 2013, **49**, 11683-11685.
149. Y.-K. Park, K.-C. Park and S.-K. Ihm, *Catal. Today*, 1998, **44**, 165-173.
150. H. Ahouari, A. Soualah, A. Le Valant, L. Pinard and Y. Pouilloux, *C. R. Chim.*, 2015, **18**, 1264-1269.
151. R. Dziembaj, W. Makowski and H. Papp, *J. Mol. Catal.*, 1992, **75**, 81-99.
152. W. Wang, S. Wang, X. Ma and J. Gong, *Chem. Soc. Rev.*, 2011, **40**, 3703-3727.
153. F. Marques Mota and D. H. Kim, *Chem. Soc. Rev.*, 2019, **48**, 205-259.
154. G. L. Bezemer, J. H. Bitter, H. P. C. E. Kuipers, H. Oosterbeek, J. E. Holewijn, X. Xu, F. Kapteijn, A. J. van Dillen and K. P. de Jong, *J. Am. Chem. Soc.*, 2006, **128**, 3956-3964.
155. H. M. Torres Galvis, J. H. Bitter, T. Davidian, M. Ruitenbeek, A. I. Dugulan and K. P. de Jong, *J. Am. Chem. Soc.*, 2012, **134**, 16207-16215.
156. A. Tavasoli, M. Trepanier, R. M. M. Abbaslou, A. K. Dalai and N. Abatzoglou, *Fuel Process. Technol.*, 2009, **90**, 1486-1494.
157. M. A. Vannice, *J. Catal.*, 1975, **37**, 462-473.
158. E. van Steen and F. F. Prinsloo, *Catal. Today*, 2002, **71**, 327-334.
159. M. C. Bahome, L. L. Jewell, D. Hildebrandt, D. Glasser and N. J. Coville, *Appl. Catal., A*, 2005, **287**, 60-67.
160. R. M. M. Abbaslou, J. Soltan and A. K. Dalai, *Appl. Catal., A*, 2010, **379**, 129-134.
161. W. Chen, Z. L. Fan, X. L. Pan and X. H. Bao, *J. Am. Chem. Soc.*, 2008, **130**, 9414-9419.
162. H. J. Schulte, B. Graf, W. Xia and M. Muhler, *ChemCatChem*, 2012, **4**, 350-355.
163. D. J. Duvenhage and N. J. Coville, *Applied Catalysis A: General*, 2006, **298**, 211-216.
164. E. de Smit and B. M. Weckhuysen, *Chem. Soc. Rev.*, 2008, **37**, 2758-2781.
165. W. Chen, T. F. Kimpel, Y. Song, F.-K. Chiang, B. Zijlstra, R. Pestman, P. Wang and E. J. M. Hensen, *ACS Catal.*, 2018, **8**, 1580-1590.
166. T. Riedel, G. Schaub, K.-W. Jun and K.-W. Lee, *Industrial & Engineering Chemistry Research*, 2001, **40**, 1355-1363.
167. F. Jiang, M. Zhang, B. Liu, Y. Xu and X. Liu, *Catal. Sci. Technol.*, 2017, **7**, 1245-1265.
168. E. T. Thostenson, Z. Ren and T.-W. Chou, *Composites Science and Technology*, 2001, **61**, 1899-1912.
169. D. Vairavapandian, P. Vichchulada and M. D. Lay, *Anal. Chim. Acta*, 2008, **626**, 119-129.
170. H. Dai, *Acc. Chem. Res*, 2002, **35**, 1035-1044.
171. P. Serp, M. Corrias and P. Kalck, *Appl. Catal., A*, 2003, **253**, 337-358.
172. S. Iijima, *Nature*, 1991, **354**, 56.
173. R. Vidu, M. Rahman, M. Mahmoudi, M. Enachescu, T. D. Poteca and I. Opris, *Frontiers in Systems Neuroscience*, 2014, **8**.
174. J. Catherine, P. Matthieu and J. Vincent, *Nanotechnology*, 2012, **23**, 142001.
175. J. Prasek, J. Drbohlavova, J. Chomoucka, J. Hubalek, O. Jasek, V. Adam and R. Kizek, *J. Mater. Chem.*, 2011, **21**, 15872-15884.
176. M. S. Arnold, A. A. Green, J. F. Hulvat, S. I. Stupp and M. C. Hersam, *Nature Nanotechnology*, 2006, **1**, 60-65.
177. V. Jourdain and C. Bichara, *Carbon*, 2013, **58**, 2-39.
178. D. S. Bethune, C. H. Kiang, M. S. de Vries, G. Gorman, R. Savoy, J. Vazquez and R. Beyers, *Nature*, 1993, **363**, 605.

179. A. G. Rinzler, J. Liu, H. Dai, P. Nikolaev, C. B. Huffman, F. J. Rodríguez-Macías, P. J. Boul, A. H. Lu, D. Heymann, D. T. Colbert, R. S. Lee, J. E. Fischer, A. M. Rao, P. C. Eklund and R. E. Smalley, *Applied Physics A*, 1998, **67**, 29-37.
180. P. G. Collins and P. Avouris, *Scientific American*, 2000, **6**, 8.
181. S. M. Kim and L. Gangloff, *Physica E: Low-dimensional Systems and Nanostructures*, 2009, **41**, 1763-1766.
182. A. Hussain, Y. Liao, Q. Zhang, E.-X. Ding, P. Laiho, S. Ahmad, N. Wei, Y. Tian, H. Jiang and E. I. Kauppinen, *Nanoscale*, 2018, **10**, 9752-9759.
183. A. Magrez, J. W. Seo, R. Smajda, M. Mionić and L. Forró, *Materials*, 2010, **3**, 4871-4891.
184. M. I. Ionescu, H. Liu, Y. Zhong, Y. Zhang, R. Li, X. Sun, J.-B. Kpetsu, C. Côté, P. Jedrzejowsk and A. Sarkissian, *ECS Transactions*, 2009, **25**, 737-748.
185. K. Kuwana and K. Saito, *Proceedings of the Combustion Institute*, 2007, **31**, 1857-1864.
186. J.-P. Tessonnier and D. S. Su, *ChemSusChem*, 2011, **4**, 824-847.
187. P. G. Collins, *Oxford Handbook of Nanoscience and Technology: Materials*, Oxford University Press, Oxford, 2009, vol. 2, ch. 2, pp. 31-93.
188. M. Mayne, N. Grobert, M. Terrones, R. Kamalakaran, M. Rühle, H. W. Kroto and D. R. M. Walton, *Chem. Phys. Lett.*, 2001, **338**, 101-107.
189. R. Baker, M. Barber, P. Harris, F. Feates and R. Waite, *J. Catal.*, 1972, **26**, 51-62.
190. R. Baker, P. Harris, R. Thomas and R. Waite, *J. Catal.*, 1973, **30**, 86-95.
191. R. Baker, J. Alonzo, J. Dumesic and D. Yates, *J. Catal.*, 1982, **77**, 74-84.
192. R. Wagner and W. Ellis, *Appl. Phys. Lett.*, 1964, **4**, 89-90.
193. J. Dijon, P. D. Szkutnik, A. Fournier, T. Goislard de Monsabert, H. Okuno, E. Quesnel, V. Muffato, E. De Vito, N. Bendiab, A. Bogner and N. Bernier, *Carbon*, 2010, **48**, 3953-3963.
194. K.-E. Kim, K.-J. Kim, W. S. Jung, S. Y. Bae, J. Park, J. Choi and J. Choo, *Chem. Phys. Lett.*, 2005, **401**, 459-464.
195. S. L. Pirard, S. Douven, C. Bossuot, G. Heyen and J.-P. Pirard, *Carbon*, 2007, **45**, 1167-1175.
196. G. Tibbetts, M. Devour and E. Rodda, *Carbon*, 1987, **25**, 367-375.
197. I. Alstrup, *J. Catal.*, 1988, **109**, 241-251.
198. A. Kock, P. De Bokx, E. Boellaard, W. Klop and J. W. Geus, *J. Catal.*, 1985, **96**, 468-480.
199. O. A. Louchev, T. Laude, Y. Sato and H. Kanda, *The Journal of chemical physics*, 2003, **118**, 7622-7634.
200. J. Rostrup-Nielsen and D. L. Trimm, *J. Catal.*, 1977, **48**, 155-165.
201. A. Sacco Jr, P. Thacker, T. N. Chang and A. T. Chiang, *J. Catal.*, 1984, **85**, 224-236.
202. R. Xiang, Z. Yang, Q. Zhang, G. Luo, W. Qian, F. Wei, M. Kadowaki, E. Einarsson and S. Maruyama, *The Journal of Physical Chemistry C*, 2008, **112**, 4892-4896.
203. C. L. Cheung, A. Kurtz, H. Park and C. M. Lieber, *The Journal of Physical Chemistry B*, 2002, **106**, 2429-2433.
204. F. Schäffel, M. Rümmeli, C. Kramberger, U. Queitsch, E. Mohn, R. Kaltofen, T. Pichler, B. Büchner, B. Rellinghaus and L. Schultz, *physica status solidi (a)*, 2008, **205**, 1382-1385.
205. Y. Chen and J. Zhang, *Carbon*, 2011, **49**, 3316-3324.
206. R. Yadav, P. Dobal, T. Shripathi, R. Katiyar and O. Srivastava, *Nanoscale Res. Lett.*, 2008, **4**, 197.
207. C. Lu and J. Liu, *The Journal of Physical Chemistry B*, 2006, **110**, 20254-20257.
208. K. Tanioku, T. Maruyama and S. Naritsuka, *Diamond Relat. Mater.*, 2008, **17**, 589-593.
209. D. B. Geohegan, A. A. Puretzky, J. J. Jackson, C. M. Rouleau, G. Eres and K. L. More, *ACS nano*, 2011, **5**, 8311-8321.
210. T. Saito, S. Ohshima, T. Okazaki, S. Ohmori, M. Yumura and S. Iijima, *J. Nanosci. Nanotechnol.*, 2008, **8**, 6153-6157.
211. B. Wang, L. Wei, L. Yao, L.-J. Li, Y. Yang and Y. Chen, *The Journal of Physical Chemistry C*, 2007, **111**, 14612-14616.
212. M. Picher, E. Anglaret, R. Arenal and V. Jourdain, *Acs Nano*, 2011, **5**, 2118-2125.

213. Y. Tian, M. Y. Timmermans, S. Kivistö, A. G. Nasibulin, Z. Zhu, H. Jiang, O. G. Okhotnikov and E. I. Kauppinen, *Nano Research*, 2011, **4**, 807.
214. M. S. Mohlala, X.-Y. Liu and N. J. Coville, *J. Organomet. Chem.*, 2006, **691**, 4768-4772.
215. R. Sharma, P. Rez, M. Brown, G. Du and M. Treacy, *Nanotechnology*, 2007, **18**, 125602.
216. H. Zhang, G. Cao, Z. Wang, Y. Yang, Z. Shi and Z. Gu, *The Journal of Physical Chemistry C*, 2008, **112**, 12706-12709.
217. G. G. Tibbetts, *J. Cryst. Growth*, 1984, **66**, 632-638.
218. H. Yoshida, T. Shimizu, T. Uchiyama, H. Kohno, Y. Homma and S. Takeda, *Nano Lett.*, 2009, **9**, 3810-3815.
219. J. M. Simmons, B. M. Nichols, M. S. Marcus, O. M. Castellini, R. J. Hamers and M. A. Eriksson, *Small*, 2006, **2**, 902-909.
220. Q. Fu and T. Wagner, *Surf. Sci. Rep.*, 2007, **62**, 431-498.
221. C. Mattevi, C. T. Wirth, S. Hofmann, R. Blume, M. Cantoro, C. Ducati, C. Cepek, A. Knop-Gericke, S. Milne and C. Castellarin-Cudia, *The Journal of Physical Chemistry C*, 2008, **112**, 12207-12213.
222. K. P. De Jong and J. W. Geus, *Catalysis Reviews*, 2000, **42**, 481-510.
223. M. F. L. De Volder, S. H. Tawfick, R. H. Baughman and A. J. Hart, *Science*, 2013, **339**, 535.
224. M. Menon, A. N. Andriotis and G. E. Froudakis, *Chem. Phys. Lett.*, 2000, **320**, 425-434.
225. K. Balasubramanian and M. Burghard, *Small*, 2005, **1**, 180-192.
226. P. Kangvansura, L. M. Chew, C. Kongmark, P. Santawaja, H. Ruland, W. Xia, H. Schulz, A. Worayingyong and M. Muhler, *Engineering*, 2017, **3**, 385-392.
227. W. J. Lee, U. N. Maiti, J. M. Lee, J. Lim, T. H. Han and S. O. Kim, *Chem. Commun.*, 2014, **50**, 6818-6830.
228. E. Castillejos, P.-J. Debouttière, L. Roiban, A. Solhy, V. Martinez, Y. Kihn, O. Ersen, K. Philippot, B. Chaudret and P. Serp, *Angew. Chem.*, 2009, **121**, 2567-2571.
229. X. Pan and X. Bao, *Acc. Chem. Res*, 2011, **44**, 553-562.
230. M. Kumar and Y. Ando, *J. Nanosci. Nanotechnol.*, 2010, **10**, 3739-3758.
231. J. Pauluhn, *Regulatory Toxicology and Pharmacology*, 2010, **57**, 78-89.
232. G. R. Hutchison, F. M. Christensen, S. Peters, S. Hankin, K. Aschberger and V. Stone, *Nanotoxicology*, 2010, **4**, 207-246.
233. P. Wick, M. J. D. Clift, M. Rösslein and B. Rothen-Rutishauser, *ChemSusChem*, 2011, **4**, 905-911.
234. J. P. Ryman-Rasmussen, E. W. Tewksbury, O. R. Moss, M. F. Cesta, B. A. Wong and J. C. Bonner, *Am. J. Respir. Cell Mol. Biol.*, 2009, **40**, 349-358.
235. J. P. Ryman-Rasmussen, M. F. Cesta, A. R. Brody, J. K. Shipley-Phillips, J. I. Everitt, E. W. Tewksbury, O. R. Moss, B. A. Wong, D. E. Dodd and M. E. Andersen, *Nature nanotechnology*, 2009, **4**, 747.
236. C. A. Poland, R. Duffin, I. Kinloch, A. Maynard, W. A. Wallace, A. Seaton, V. Stone, S. Brown, W. MacNee and K. Donaldson, *Nature nanotechnology*, 2008, **3**, 423.
237. S. Luanpitpong, L. Wang and Y. Rojanasakul, *Nanomedicine (London, England)*, 2014, **9**, 895-912.
238. I. Fenoglio, F. Cesano, E. Gazzano, G. Gulino, D. Scarano, A. Attanasio, G. Mazzucco, D. Ghigo and B. Fubini, *J. Toxicol. Environ. Health, Part A*, 2013, **76**, 1056-1071.
239. S. Y. Madani, A. Mandel and A. M. Seifalian, *Nano reviews*, 2013, **4**, 10.3402/nano.v3404i3400.21521.
240. M. Allegri, D. K. Perivoliotis, M. G. Bianchi, M. Chiu, A. Pagliaro, M. A. Koklioti, A.-F. A. Trompeta, E. Bergamaschi, O. Bussolati and C. A. Charitidis, *Toxicology Reports*, 2016, **3**, 230-243.
241. J. C. Carrero-Sánchez, A. L. Elías, R. Mancilla, G. Arrellín, H. Terrones, J. P. Laclette and M. Terrones, *Nano Lett.*, 2006, **6**, 1609-1616.

242. V. Castranova, B. Asgharian and P. Sayre, *Journal of Toxicology and Environmental Health, Part B*, 2015, **18**, 121-212.
243. S. Fukushima, T. Kasai, Y. Umeda, M. Ohnishi, T. Sasaki and M. Matsumoto, *Journal of Occupational Health*, 2018, **60**, 10-30.
244. H. J. Johnston, V. Stone, R. J. Aitken, S. M. Hankin, S. A. K. Peters, C. L. Tran and F. M. Christensen, *Critical Reviews in Toxicology*, 2010, **40**, 759-790.
245. H.S.E., *Using nanomaterials at work*, 2013.
246. N.I.O.H.S., *Occupational Exposure to Carbon Nanotubes and Nanofibers*, 2013.
247. 3M, *Technical Data Bulletin #171: Nanotechnology and Respirator Use* 2015, **2019**.
248. R. Czerw, M. Terrones, J. C. Charlier, X. Blase, B. Foley, R. Kamalakaran, N. Grobert, H. Terrones, D. Tekleab, P. M. Ajayan, W. Blau, M. Rühle and D. L. Carroll, *Nano Lett.*, 2001, **1**, 457-460.
249. G. Keru, P. G. Ndungu and V. O. Nyamori, *Mater. Chem. Phys.*, 2015, **153**, 323-332.
250. F. H. Monteiro, D. G. Larrude, M. E. H. Maia da Costa, L. A. Terrazos, R. B. Capaz and F. L. Freire, *The Journal of Physical Chemistry C*, 2012, **116**, 3281-3285.
251. K. C. Mondal, N. J. Coville, M. J. Witcomb, G. Tejral and J. Havel, *Chem. Phys. Lett.*, 2007, **437**, 87-91.
252. L. Yang, S. Jiang, Y. Zhao, L. Zhu, S. Chen, X. Wang, Q. Wu, J. Ma, Y. Ma and Z. Hu, *Angewandte Chemie International Edition*, 2011, **50**, 7132-7135.
253. J. W. Jang, C. E. Lee, S. C. Lyu, T. J. Lee and C. J. Lee, *Appl. Phys. Lett.*, 2004, **84**, 2877-2879.
254. R. M. Yadav, A. Srivastava and O. N. Srivastava, *J. Nanosci. Nanotechnol.*, 2004, **4**, 719-721.
255. S. Webster, J. Maultzsch, C. Thomsen, J. Liu, R. Czerw, M. Terrones, F. Adar, C. John, A. Whitley and D. L. Carroll, *Mater. Res. Soc. Symp. Proc.*, 2003, **772**, M7.8.
256. A. M. El-Sawy, I. M. Mosa, D. Su, C. J. Guild, S. Khalid, R. Joesten, J. F. Rusling and S. L. Suib, *Advanced Energy Materials*, 2016, **6**, 1501966.
257. Y. S. Lee, T. H. Cho, B. K. Lee, J. S. Rho, K. H. An and Y. H. Lee, *J. Fluorine Chem.*, 2003, **120**, 99-104.
258. E. Cruz-Silva, D. A. Cullen, L. Gu, J. M. Romo-Herrera, E. Muñoz-Sandoval, F. López-Urías, B. G. Sumpter, V. Meunier, J.-C. Charlier and D. J. Smith, *ACS nano*, 2008, **2**, 441-448.
259. L. Dai, D. W. Chang, J.-B. Baek and W. Lu, *Small*, 2012, **8**, 1130-1166.
260. R. Arrigo, M. Hävecker, R. Schlögl and D. S. Su, *Chem. Commun.*, 2008, DOI: 10.1039/B812769G, 4891-4893.
261. J. Zhang, Z. Xia and L. Dai, *Science Advances*, 2015, **1**, e1500564.
262. E. N. Nxumalo and N. J. Coville, *Materials*, 2010, **3**, 2141-2171.
263. X.-F. Li, K.-Y. Lian, L. Liu, Y. Wu, Q. Qiu, J. Jiang, M. Deng and Y. Luo, *Scientific Reports*, 2016, **6**, 23495.
264. S. van Dommele, A. Romero-Izquirdo, R. Brydson, K. P. de Jong and J. H. Bitter, *Carbon*, 2008, **46**, 138-148.
265. C. Ewels and M. Glerup, *J. Nanosci. Nanotechnol.*, 2005, **5**, 1345-1363.
266. S. Maldonado, S. Morin and K. J. Stevenson, *Carbon*, 2006, **44**, 1429-1437.
267. H. Liu, Y. Zhang, R. Li, X. Sun and H. Abou-Rachid, *Journal of Nanoparticle Research*, 2012, **14**, 1016.
268. A. Dettlaff, M. Sawczak, E. Klugmann-Radziemska, D. Czylkowski, R. Miotk and M. Wilamowska-Zawłocka, *RSC Adv.*, 2017, **7**, 31940-31949.
269. Y. T. Lee, N. S. Kim, S. Y. Bae, J. Park, S.-C. Yu, H. Ryu and H. J. Lee, *The Journal of Physical Chemistry B*, 2003, **107**, 12958-12963.
270. T. Sharifi, F. Nitze, H. R. Barzegar, C.-W. Tai, M. Mazurkiewicz, A. Malolepszy, L. Stobinski and T. Wågberg, *Carbon*, 2012, **50**, 3535-3541.
271. P. Ayala, R. Arenal, M. Rümmeli, A. Rubio and T. Pichler, *Carbon*, 2010, **48**, 575-586.
272. L. Sun, C. Wang, Y. Zhou, X. Zhang, B. Cai and J. Qiu, *Appl. Surf. Sci.*, 2013, **277**, 88-93.

273. C. Cao, F. Huang, C. Cao, J. Li and H. Zhu, *Chemistry of Materials*, 2004, **16**, 5213-5215.
274. Y. Zhang, H. Gu, K. Suenaga and S. Iijima, *Chem. Phys. Lett.*, 1997, **279**, 264-269.
275. H. Xiong, M. A. Motchelaho, M. Moyo, L. L. Jewell and N. J. Coville, *Appl. Catal., A*, 2014, **482**, 377-386.
276. J. Wu, R. M. Yadav, M. Liu, P. P. Sharma, C. S. Tiwary, L. Ma, X. Zou, X.-D. Zhou, B. I. Yakobson, J. Lou and P. M. Ajayan, *ACS Nano*, 2015, **9**, 5364-5371.
277. R. M. Yadav, T. Shripathi, A. Srivastava and O. N. Srivastava, *J. Nanosci. Nanotechnol.*, 2005, **5**, 820-824.
278. B. G. Sumpter, V. Meunier, J. M. Romo-Herrera, E. Cruz-Silva, D. A. Cullen, H. Terrones, D. J. Smith and M. Terrones, *ACS Nano*, 2007, **1**, 369-375.
279. C. H. Lin, H. L. Chang, C. M. Hsu, A. Y. Lo and C. T. Kuo, *Diamond Relat. Mater.*, 2003, **12**, 1851-1857.
280. S. W. Pattinson, R. E. Diaz, N. A. Stelmashenko, A. H. Windle, C. Ducati, E. A. Stach and K. K. K. Koziol, *Chemistry of Materials*, 2013, **25**, 2921-2923.
281. T. E. Bell, G. Zhan, K. Wu, H. C. Zeng and L. Torrente-Murciano, *Top. Catal.*, 2017, **60**, 1251-1259.
282. W. Xia, C. Jin, S. Kundu and M. Muhler, *Carbon*, 2009, **47**, 919-922.
283. K. L. Choy, *Progress in Materials Science*, 2003, **48**, 57-170.
284. V. P. Lehto and J. Riikonen, *Porous Silicon for Biomedical Applications*, ed. H. A. Santos, Woodhead Publishing, 2014, DOI: 10.1533/9780857097156.3.337, pp. 337-355.
285. P. Munnik, P. E. de Jongh and K. P. de Jong, *Chemical Reviews*, 2015, **115**, 6687-6718.
286. L. o. Riley, BET Multilayer Adsorption, https://commons.wikimedia.org/wiki/File:BET_Multilayer_Adsorption.svg, (accessed 09-11-2019).
287. P. W. Atkins and J. De Paula, *Atkins' Physical chemistry*, 2014.
288. Moxfyre, Molecular energy levels and Raman effect, https://commons.wikimedia.org/wiki/File:Raman_energy_levels.svg, (accessed 09-11-2019).
289. S. Costa, E. Borowiak-Palen, M. Kruszynska, A. Bachmatiuk and R. J. Kalenczuk, *Mater. Sci.*, 2008, **26**, 433-441.
290. T. Belin and F. Epron, *Mater. Sci. Eng. B-Solid State Mater. Adv. Technol.*, 2005, **119**, 105-118.
291. J. H. Lehman, M. Terrones, E. Mansfield, K. E. Hurst and V. Meunier, *Carbon*, 2011, **49**, 2581-2602.
292. T. C. Hirschmann, M. S. Dresselhaus, H. Muramatsu, M. Seifert, U. Wurstbauer, E. Parzinger, K. Nielsch, Y. A. Kim and P. T. Araujo, *Phys. Rev. B*, 2015, **91**, 075402.
293. An Introduction to Electron Microscopy, https://www.fei.com/introduction-to-electron-microscopy/sem/, (accessed 09-11-2019).
294. R. F. Egerton, *Ultramicroscopy*, 2014, **145**, 85-93.
295. Claudionico, Schematic of electron-sample interactions in SEM and TEM, https://en.wikipedia.org/wiki/File:Electron_Interaction_with_Matter.svg#/media/File:Electron_Interaction_with_Matter.svg, (accessed 09-11-2019).
296. P. J. Potts, J. Bowles, S. J. Reed and R. Cave, *Microprobe techniques in the earth sciences*, Springer Science & Business Media, 1995, pp. 82-83.
297. Thermal desorption spectroscopy, http://www.rsc.org/publishing/journals/prospect/ontology.asp?id=CMO:0002673&MSID=C2JM30470H, (accessed 12-10-2018).
298. V. Rakić and L. Damjanović, *Calorimetry and Thermal Methods in Catalysis*, ed. A. Auroux, Springer Berlin Heidelberg, Berlin, Heidelberg, 2013, DOI: 10.1007/978-3-642-11954-5_4, pp. 131-174.
299. A. W. Coats and J. P. Redfern, *Analyst*, 1963, **88**, 906-924.

300. D. Briggs, C. D. Wanger, W. M. Riggs, L. E. Davis, J. F. Moulder and G. E. Muilenberg, *Handbook of X-ray Photoelectron Spectroscopy*, Perkin-Elmer Corp., Eden Prairie, MN, USA, 1981, pp. 16.
301. ThermoScientific, What is X-Ray Photoelectron Spectroscopy (XPS)?, https://xpssimplified.com/whatisxps.php, (accessed 09-11-2019).
302. S. Tanuma, C. J. Powell and D. R. Penn, *Surface and Interface Analysis*, 1994, **21**, 165-176.
303. Y. Waseda, E. Matsubara and K. Shinoda, *X-Ray Diffraction Crystallography: Introduction, Examples and Solved Problems*, eds. Y. Waseda, E. Matsubara and K. Shinoda, Springer Berlin Heidelberg, Berlin, Heidelberg, 2011, DOI: 10.1007/978-3-642-16635-8_4, pp. 107-167.
304. S. A. Speakman, Basics of X-Ray Powder Diffraction, http://prism.mit.edu/xray/Basics%20of%20X-Ray%20Powder%20Diffraction.pdf, (accessed 09-11-2019).
305. U. Holzwarth and N. Gibson, *Nature Nanotechnology*, 2011, **6**, 534-534.
306. Inverse Gas Chromatography and Its Applications – Surface Measurement Systems' Automated Solution, https://www.azom.com/article.aspx?ArticleID=11831, (accessed 09-11-2019).
307. Offnfopt, Diagram of a gas chromatograph apparatus, https://en.wikipedia.org/wiki/Gas_chromatography, (accessed 09-11-2019).
308. M. S. Dresselhaus, A. Jorio, A. G. Souza Filho and R. Saito, *Philos. Trans. Royal Soc. A*, 2010, **368**, 5355.
309. R. A. DiLeo, B. J. Landi and R. P. Raffaelle, *J. Appl. Phys.*, 2007, **101**, 5.
310. K. K. Kim, J. S. Park, S. J. Kim, H. Z. Geng, K. H. An, C.-M. Yang, K. Sato, R. Saito and Y. H. Lee, *Phys. Rev. B*, 2007, **76**, 205426.
311. L. Yin-Chih, H. Jhen-Yong, Y. Chia-Nan, T. Shi-Yuan, T. Mean-Jue, S. Hung-Wei, C. Chia-Hao and L. Minn-Tsong, *Jpn. J. Appl. Phys*, 2015, **54**, 033002.
312. T. Yamashita and P. Hayes, *Appl. Surf. Sci.*, 2008, **254**, 2441-2449.
313. M. C. Biesinger, B. P. Payne, A. P. Grosvenor, L. W. M. Lau, A. R. Gerson and R. S. C. Smart, *Appl. Surf. Sci.*, 2011, **257**, 2717-2730.
314. D. Chen, Q. Tang, X. Li, X. Zhou, J. Zang, W.-q. Xue, J.-y. Xiang and C.-q. Guo, *Int. J. Nanomedicine*, 2012, **7**, 4973-4982.
315. A. Azam, A. S. Ahmed, M. Oves, M. S. Khan, S. S. Habib and A. Memic, *Int. J. Nanomedicine*, 2012, **7**, 6003-6009.
316. N. Abatzoglou and B. Legras, *IJEPR*, 2015, **3**, 9-15.
317. Y. Li, Y. Hu, G. Huang and C. Li, *Particuology*, 2013, **11**, 460-467.
318. H. D. Willauer, R. Ananth, M. T. Olsen, D. M. Drab, D. R. Hardy and F. W. Williams, *J. CO2 Util.*, 2013, **3-4**, 56-64.
319. W. M. Hexana and N. J. Coville, *Applied Catalysis A: General*, 2010, **377**, 150-157.
320. P. Kangvansura, L. M. Chew, W. Saengsui, P. Santawaja, Y. Poo-arporn, M. Muhler, H. Schulz and A. Worayingyong, *Catal. Today*, 2016, **275**, 59-65.
321. Z. Chen, D. Higgins, H. Tao, R. S. Hsu and Z. Chen, *The Journal of Physical Chemistry C*, 2009, **113**, 21008-21013.
322. R. Ma, G. Lin, Y. Zhou, Q. Liu, T. Zhang, G. Shan, M. Yang and J. Wang, *npj Computational Materials*, 2019, **5**, 78.
323. F. Blanco, I. Alkorta, M. Solimannejad and J. Elguero, *The Journal of Physical Chemistry A*, 2009, **113**, 3237-3244.
324. P. Politzer, C. W. Kammeyer, J. Bauer and W. L. Hedges, *The Journal of Physical Chemistry*, 1981, **85**, 4057-4060.
325. H.-S. Choi and M. P. Suh, *Angewandte Chemie International Edition*, 2009, **48**, 6865-6869.
326. P. Raveendran, Y. Ikushima and S. L. Wallen, *Acc. Chem. Res*, 2005, **38**, 478-485.

327. V. Krstić, G. L. J. A. Rikken, P. Bernier, S. Roth and M. Glerup, *Europhysics Letters (EPL)*, 2007, **77**, 37001.
328. D. L. Williamson, C. Herdes, L. Torrente-Murciano, M. D. Jones and D. Mattia, *ACS Sustainable Chemistry & Engineering*, 2019, **7**, 7395-7402.
329. B. C. Beard, *Surface Science Spectra*, 1993, **2**, 91-96.
330. S. Wu, W. Wang, M. Li, L. Cao, F. Lyu, M. Yang, Z. Wang, Y. Shi, B. Nan, S. Yu, Z. Sun, Y. Liu and Z. Lu, *Nat. Commun.*, 2016, **7**, 13318.
331. K. Takanabe, A. M. Khan, Y. Tang, L. Nguyen, A. Ziani, B. W. Jacobs, A. M. Elbaz, S. M. Sarathy and F. Tao, *Angewandte Chemie International Edition*, 2017, **56**, 10403-10407.
332. D. B. Bukur, B. Todic and N. Elbashir, *Catal. Today*, 2016, **275**, 66-75.
333. M. Zhu and I. E. Wachs, *ACS Catal.*, 2016, **6**, 722-732.
334. M. Zhu and I. E. Wachs, *Catal. Today*, 2018, **311**, 2-7.
335. R. Xu, P. S. Vengsarkar, D. Roe and C. B. Roberts, *Energy Fuels*, 2017, **31**, 4343-4352.
336. J.-X. Liu, P. Wang, W. Xu and E. J. M. Hensen, *Engineering*, 2017, **3**, 467-476.
337. D. Lopez-Tejedor, R. Benavente and J. M. Palomo, *Catal. Sci. Technol.*, 2018, **8**, 1754-1776.
338. M. Ventura, A. Dibenedetto and M. Aresta, *Inorg. Chim. Acta*, 2018, **470**, 11-21.
339. M. Ventura, M. Aresta and A. Dibenedetto, *ChemSusChem*, 2016, **9**, 1096-1100.
340. K. Ghaib and F. Z. Ben-Fares, *Renew. Sust. Energ. Rev.*, 2018, **81**, 433-446.
341. J. Kirchner, J. K. Anolleck, H. Lösch and S. Kureti, *Applied Catalysis B: Environmental*, 2018, **223**, 47-59.
342. J. Gao, Q. Liu, F. Gu, B. Liu, Z. Zhong and F. Su, *RSC Adv.*, 2015, **5**, 22759-22776.
343. T. A. Le, M. S. Kim, S. H. Lee, T. W. Kim and E. D. Park, *Catal. Today*, 2017, **293-294**, 89-96.
344. I. Kuznecova and J. Gusca, *Energy Procedia*, 2017, **128**, 255-260.
345. S.-J. Lee, H. Lee, K.-J. Jeon, H. Park, Y.-K. Park and S.-C. Jung, *Nanoscale Res. Lett.*, 2016, **11**, 344.
346. D. J. Morgan, *Surface and Interface Analysis*, 2015, **47**, 1072-1079.
347. R. Bavand, A. Yelon and E. Sacher, *Appl. Surf. Sci.*, 2015, **355**, 279-289.
348. J. Z. Bloh, R. Dillert and D. W. Bahnemann, *Phys. Chem. Chem. Phys.*, 2014, **16**, 5833-5845.
349. L. S. Panchakarla and A. Govindaraj, *Bull. Mater. Sci.*, 2007, **30**, 23-29.
350. J. Liu, P. Bai and X. S. Zhao, *Phys. Chem. Chem. Phys.*, 2011, **13**, 3758-3763.
351. P. J. Lunde and F. L. Kester, *J. Catal.*, 1973, **30**, 423-429.
352. Z. He, X. Wang, S. Gao and T. Xiao, *Applied Petrochemical Research*, 2015, **5**, 413-417.
353. K. Ghaib, *Das Power-to-Methane-Konzept*, Springer, 2017, pp. 29-32.
354. Y. Zhu, S. Zhang, Y. Ye, X. Zhang, L. Wang, W. Zhu, F. Cheng and F. Tao, *ACS Catal.*, 2012, **2**, 2403-2408.
355. G. Garbarino, D. Bellotti, P. Riani, L. Magistri and G. Busca, *International Journal of Hydrogen Energy*, 2015, **40**, 9171-9182.
356. P. Frontera, A. Macario, M. Ferraro and P. Antonucci, *Catalysts*, 2017, **7**, 59.
357. S. Sharma, Z. Hu, P. Zhang, E. W. McFarland and H. Metiu, *J. Catal.*, 2011, **278**, 297-309.
358. S. Toemen, W. A. W. A. Bakar and R. Ali, *Journal of the Taiwan Institute of Chemical Engineers*, 2014, **45**, 2370-2378.
359. B. Mutz, H. W. P. Carvalho, S. Mangold, W. Kleist and J.-D. Grunwaldt, *J. Catal.*, 2015, **327**, 48-53.
360. H. Kiuchi, R. Shibuya, T. Kondo, J. Nakamura, H. Niwa, J. Miyawaki, M. Kawai, M. Oshima and Y. Harada, *Nanoscale Res. Lett.*, 2016, **11**, 127.
361. Y. A. Daza and J. N. Kuhn, *RSC Adv.*, 2016, **6**, 49675-49691.
362. J. Wei, Q. Ge, R. Yao, Z. Wen, C. Fang, L. Guo, H. Xu and J. Sun, *Nat. Commun.*, 2017, **8**, 15174.
363. D. Grove, *Platinum Metals Review*, 2002, **46**, 144-144.
364. T. W. Hansen, A. T. DeLaRiva, S. R. Challa and A. K. Datye, *Acc. Chem. Res*, 2013, **46**, 1720-1730.

365. H. Berro, N. Fillot and P. Vergne, *Tribology International*, 2010, **43**, 1811-1822.
366. M. Kaukonen, A. Gulans, P. Havu and E. Kauppinen, *J. Comput. Chem.*, 2012, **33**, 652-658.
367. D. Cristancho, I. Y. Akkutlu, L. J. Criscenti and Y. Wang, presented in part at the SPE Europec featured at 78th EAGE Conference and Exhibition, Vienna, Austria, 2016/5/30/, 2016.
368. J. M. Simon, O. E. Haas and S. Kjelstrup, *The Journal of Physical Chemistry C*, 2010, **114**, 10212-10220.
369. J. G. Harris and K. H. Yung, *The Journal of Physical Chemistry*, 1995, **99**, 12021-12024.
370. S. Pałucha, Z. Gburski and J. Biesiada, *J. Mol. Struct.*, 2004, **704**, 269-273.
371. H. Berendsen, J. Grigera and T. Straatsma, *J. Phys. Chem.*, 1987, **91**, 6269-6271.

Appendix 1: Copyright & Permissions statements

	Element	Ref.	Permissions statement
1	Figure 1.1 (i)	1	NASA content - images, audio, video, and computer files used in the rendition of 3-dimensional models, such as texture maps and polygon data in any format - generally are not copyrighted. You may use this material for educational or informational purposes, including photo collections, textbooks, public exhibits, computer graphical simulations and Internet Web pages. This general permission extends to personal Web pages. News outlets, schools, and text-book authors may use NASA content without needing explicit permission. NASA content used in a factual manner that does not imply endorsement may be used without needing explicit permission. NASA should be acknowledged as the source of the material. NASA occasionally uses copyrighted material by permission on its website. Those images will be marked copyright with the name of the copyright holder. NASA's use does not convey any rights to others to use the same material. Those wishing to use copyrighted material must contact the copyright holder directly.
2	Figure 1.1 (ii)	2	Reproduction of limited number of figures or short excerpts of IPCC material is authorized free of charge and without formal written permission provided that the original source is properly acknowledged, with mention of the complete name of the report, the publisher and the numbering of the page(s) or the figure(s). Permission can only be granted to use the material exactly as it is in the report. Please be aware that figures cannot be altered in any way, including the full legend. For media use it is sufficient to cite the source while using the original graphic or figure. In line with established Internet usage, any external website may provide a hyperlink to the IPCC website or to any of its pages without requesting permission. Reproduced from IPCC, 2014: *Climate Change 2014: Synthesis Report*. *Contribution of Working Groups I, II and III to the Fifth Assessment Report of the Intergovernmental Panel on Climate Change* [Core Writing Team, R.K. Pachauri and L.A. Meyer (eds.)]. IPCC, Geneva, Switzerland, 151 pp. Figure located on page 46, Figure 1.6.
3	Figure 1.2	7	Reproduction of limited number of figures or short excerpts of IPCC material is authorized free of charge and without formal written permission provided that the original source is properly acknowledged, with mention of the complete name of the report, the publisher and the numbering of the page(s) or the figure(s). Permission can only be granted to use the material exactly as it is in the report. Please be aware that figures cannot be altered in any way, including the full legend. For media use it is sufficient to cite the source while using the original graphic or figure. In line with established Internet usage, any external website may provide a hyperlink to the IPCC website or to any of its pages without requesting permission.

			Allen, M.R., O.P. Dube, W. Solecki, F. Aragón-Durand, W. Cramer, S. Humphreys, M. Kainuma, J. Kala, N. Mahowald, Y. Mulugetta, R. Perez, M. Wairiu, and K. Zickfeld, 2018: Framing and Context. In: *Global Warming of 1.5°C. An IPCC Special Report on the impacts of global warming of 1.5°C above pre-industrial levels and related global greenhouse gas emission pathways, in the context of strengthening the global response to the threat of climate change, sustainable development, and efforts to eradicate poverty* [Masson-Delmotte, V., P. Zhai, H.-O. Pörtner, D. Roberts, J. Skea, P.R. Shukla, A. Pirani, W. Moufouma-Okia, C. Péan, R. Pidcock, S. Connors, J.B.R. Matthews, Y. Chen, X. Zhou, M.I. Gomis, E. Lonnoy, T. Maycock, M. Tignor, and T. Waterfield (eds.)]. In Press. Figure located on page 82, FAQ 1.2, Figure 1.
4	Figure 1.3	12	Anything credited to NOAA Climate.gov can be freely re-used with proper attribution.
5	Figure 1.4	7	Reproduction of limited number of figures or short excerpts of IPCC material is authorized free of charge and without formal written permission provided that the original source is properly acknowledged, with mention of the complete name of the report, the publisher and the numbering of the page(s) or the figure(s). Permission can only be granted to use the material exactly as it is in the report. Please be aware that figures cannot be altered in any way, including the full legend. For media use it is sufficient to cite the source while using the original graphic or figure. In line with established Internet usage, any external website may provide a hyperlink to the IPCC website or to any of its pages without requesting permission. O. Hoegh-Guldberg, D. Jacob, M. Taylor, M. Bindi, S. Brown, I. Camilloni, A. Diedhiou, R. Djalante, K. Ebi, F. Engelbrecht, J. Guiot, Y. Hijioka, S. Mehrotra, A. Payne, S. I. Seneviratne, A. Thomas, R. Warren, G. Zhou, 2018, Impacts of 1.5ºC global warming on natural and human systems. In: *Global warming of 1.5°C. An IPCC Special Report on the impacts of global warming of 1.5°C above pre-industrial levels and related global greenhouse gas emission pathways, in the context of strengthening the global response to the threat of climate change, sustainable development, and efforts to eradicate poverty* [V. Masson-Delmotte, P. Zhai, H. O. Pörtner, D. Roberts, J. Skea, P.R. Shukla,A. Pirani, W. Moufouma-Okia, C.Péan, R. Pidcock, S. Connors, J. B. R. Matthews, Y. Chen, X. Zhou, M. I. Gomis, E. Lonnoy, T. Maycock, M. Tignor, T. Waterfield(eds.)]. In Press. Figure located on page 283, FAQ 3.1, Figure 1.
6	Figure 1.5	2	Reproduction of limited number of figures or short excerpts of IPCC material is authorized free of charge and without formal written permission provided that the original source is properly acknowledged, with mention of the complete name of the report, the publisher and the numbering of the page(s) or the figure(s). Permission can only be granted to use the material exactly as it is in the report. Please be aware that figures cannot be altered in any way, including the full legend. For media use it is sufficient to cite the source while using the original graphic or figure. In line with established Internet usage, any

			external website may provide a hyperlink to the IPCC website or to any of its pages without requesting permission. Reproduced from IPCC, 2014: *Climate Change 2014: Synthesis Report*. *Contribution of Working Groups I, II and III to the Fifth Assessment Report of the Intergovernmental Panel on Climate Change* [Core Writing Team, R.K. Pachauri and L.A. Meyer (eds.)]. IPCC, Geneva, Switzerland, 151 pp. Figure located on page 88, Box 3.2, Figure 1.
7	Figure 1.6	14	This article is licensed under a Creative Commons Attribution 3.0 Unported Licence. Material from this article can be used in other publications provided that the correct acknowledgement is given with the reproduced material. **Carbon capture and storage (CCS): the way forward** M. Bui, C. S. Adjiman, A. Bardow, E. J. Anthony, A. Boston, S. Brown, P. S. Fennell, S. Fuss, A. Galindo, L. A. Hackett, J. P. Hallett, H. J. Herzog, G. Jackson, J. Kemper, S. Krevor, G. C. Maitland, M. Matuszewski, I. S. Metcalfe, C. Petit, G. Puxty, J. Reimer, D. M. Reiner, E. S. Rubin, S. A. Scott, N. Shah, B. Smit, J. P. M. Trusler, P. Webley, J. Wilcox and N. Mac Dowell, *Energy Environ. Sci.*, 2018, **11**, 1062, **DOI:** 10.1039/C7EE02342A – Published by the Royal Society of Chemistry
8	Figure 1.7	18	From K. S. Lackner, *Science*, 2003, **300**, 1677. Reprinted with permission from AAAS.
9	Figure 1.8	28	Adapted with permission from Ref. 28: Carbon Dioxide as Chemical Feedstock. Edited by Michele Aresta. Published by John Wiley & Sons, Inc. © 2010 WILEY-VCH Verlag GmbH & Co. KGaA, Weinheim All rights reserved (including those of translation into other languages). No part of this book may be reproduced in any form – by photoprinting, microfilm, or any other means – nor transmitted or translated into a machine language without written permission from the publishers. Registered names, trademarks, etc. used in this book, even when not specifically marked as such, are not to be considered unprotected by law.
10	Table 1.1	82	Reprinted (adapted) with permission from N. von der Assen, L. J. Müller, A. Steingrube, P. Voll and A. Bardow, *Environmental Science & Technology*, 2016, **50**, 1093-1101. Copyright 2016 American Chemical Society.
11	Figure 1.9	26	This article is licensed under a Creative Commons Attribution 3.0 Unported Licence. Material from this article can be used in other publications provided that the correct acknowledgement is given with the reproduced material. **Closing the loop: captured CO_2 as a feedstock in the chemical industry.** A. Otto, T. Grube, S. Schiebahn and D. Stolten, *Energy Environ. Sci.*, 2015, **8**, 3283, **DOI:** 10.1039/C5EE02591E – Published by the Royal Society of Chemistry.
12	Figure 1.10	100	Source: IEA (2018), Renewables 2018: Analysis and Forecasts to 2023, All rights reserved.

13	Figure 1.12	35	This article is distributed under the terms of the Creative Commons Attribution 4.0 International License (https://creativecommons.org/licenses/by/4.0), which permits use, duplication, adaptation, distribution, and reproduction in any medium or format, as long as you give appropriate credit to the original author(s) and the source, provide a link to the Creative Commons license, and indicate if changes were made. Reproduced (without changes) from: T. Schaaf, J. Grünig, M. R. Schuster, T. Rothenfluh and A. Orth, *Energy Sustain. Soc.*, 2014, **4**, 2. **DOI:** 10.1186/s13705-014-0029-1.
14	Figure 1.13	35	This article is distributed under the terms of the Creative Commons Attribution 4.0 International License (https://creativecommons.org/licenses/by/4.0), which permits use, duplication, adaptation, distribution, and reproduction in any medium or format, as long as you give appropriate credit to the original author(s) and the source, provide a link to the Creative Commons license, and indicate if changes were made. Reproduced (without changes) from: T. Schaaf, J. Grünig, M. R. Schuster, T. Rothenfluh and A. Orth, *Energy Sustain. Soc.*, 2014, **4**, 2. **DOI:** 10.1186/s13705-014-0029-1.
15	Figure 2.1	127	Reprinted (adapted) with permission from A. Goguet, F. C. Meunier, D. Tibiletti, J. P. Breen and R. Burch, *The Journal of Physical Chemistry B*, 2004, **108**, 20240-20246. Copyright 2004 American Chemical Society.
16	Figure 2.2	68	Adapted with permission from Ref. 68: Kinetics of CO2 Hydrogenation to Hydrocarbons over Iron–Silica Catalysts. Authored by RE Owen, D Mattia, P Plucinski, MD Jones. Published by John Wiley & Sons, Inc. © 2017 Wiley-VCHVerlag GmbH&Co. KGaA,Weinheim
17	Figure 2.3	81	Adapted from Ref. 81 with permission from the Royal Society of Chemistry.
18	Figure 2.4	134	Adapted with permission from Ref. 134: Fischer–Tropsch Process. Authored by Arno de Klerk. Published by John Wiley & Sons, Inc. Copyright © 2013 by John Wiley & Sons, Inc. All rights reserved.
19	Table 2.1	124	Reprinted from Renewable and Sustainable Energy Reviews, 80, Saeidi, Samrand; Najari, Sara; Fazlollahi, Farhad; Nikoo, Maryam Khoshtinat; Sefidkon, Fatemeh; Klemeš, Jiří Jaromír; Baxter, Larry L., Mechanisms and kinetics of CO2 hydrogenation to value-added products: A detailed review on current status and future trends, 1292-1311, Copyright 2017, with permission from Elsevier.
20	Figure 2.5	81	Adapted from Ref. 81 with permission from the Royal Society of Chemistry.
21	Figure 2.6	146	Reprinted (adapted) with permission from H. G. Stenger and C. F. Askonas, *Industrial & Engineering Chemistry Fundamentals*, 1986, **25**, 410-413. Copyright 1986 American Chemical Society.
22	Figure 2.7	154	Reprinted (adapted) with permission from G. L. Bezemer, J. H. Bitter, H. P. C. E. Kuipers, H. Oosterbeek, J. E. Holewijn, X. Xu, F. Kapteijn, A. J. van Dillen and K. P. de Jong, *J. Am. Chem. Soc.*, 2006, **128**, 3956-3964. Copyright 2006 American Chemical Society.

23	Figure 2.8	118	Reproduced with permission from Ref. 118: Production of Liquid Hydrocarbons with CO2 as Carbon Source based on Reverse Water-Gas Shift and Fischer-Tropsch Synthesis. Authored by Andreas Jess, Christoph Kern, Rajabhau Bajirao Unde, et al. Published by John Wiley & Sons, Inc. Copyright © 2013 WILEY-VCH Verlag GmbH & Co. KGaA, Weinheim
24	Figure 2.9	153	Reproduced from Ref. 153 with permission from The Royal Society of Chemistry.
25	Figure 2.10	173	Copyright © 2014 Vidu, Rahman, Mahmoudi, Enachescu, Poteca and Opris. This is an open-access article distributed under the terms of the Creative Commons Attribution License (CC BY). The use, distribution or reproduction in other forums is permitted, provided the original author(s) or licensor are credited and that the original publication in this journal is cited, in accordance with accepted academic practice. No use, distribution or reproduction is permitted which does not comply with these terms.
26	Figure 2.11	176	Reprinted by permission from Springer Nature: Springer Nature. Nature Nanotechnology. Sorting carbon nanotubes by electronic structure using density differentiation, Michael S. Arnold et al., 2006.
27	Figure 2.12	175	Reproduced from Ref. 175 with permission from The Royal Society of Chemistry.
28	Figure 2.13	174	Authors: Catherine Journet, Matthieu Picher and Vincent Jourdain. Title: Carbon nanotube synthesis: from large-scale production to atom-by-atom growth. Journal: Nanotechnology. Volume 23. Issue number 14. Page range 142001. 2012. https://doi.org/10.1088/0957-4484/23/14/142001 © IOP Publishing. Reproduced with permission. All rights reserved
29	Figure 2.14	186	Reproduced with permission from Ref. 186: Recent Progress on the Growth Mechanism of Carbon Nanotubes: A Review. Authored by Jean-Philippe Tessonnier, Dang Sheng Su, et al. Published by John Wiley & Sons, Inc. Copyright © 2011 WILEY-VCH Verlag GmbH & Co. KGaA, Weinheim
30	Figure 2.14	177	Reprinted from Carbon, 58, Vincent Jourdain and Christophe Bichara, Current understanding of the growth of carbon nanotubes in catalytic chemical vapour deposition, 2-39, Copyright 2013, with permission from Elsevier.
31	Figure 2.15	188	Reprinted from Chemical Physics Letters, 338, M. Mayne,N. Grobert,M. Terrones,R. Kamalakaran,M. Rühle,H.W. Kroto,D.R.M. Walton, Pyrolytic production of aligned carbon nanotubes from homogeneously dispersed benzene-based aerosols, 101-107, Copyright 2001, with permission from Elsevier.
32	Figure 2.16	186	Reproduced with permission from Ref. 185: Recent Progress on the Growth Mechanism of Carbon Nanotubes: A Review. Authored by Jean-Philippe Tessonnier, Dang Sheng Su, et al. Published by John Wiley & Sons, Inc. Copyright © 2011 WILEY-VCH Verlag GmbH & Co. KGaA, Weinheim

33	Figure 2.17	177	Reprinted from Carbon, 58, Vincent Jourdain and Christophe Bichara, Current understanding of the growth of carbon nanotubes in catalytic chemical vapour deposition, 2-39, Copyright 2013, with permission from Elsevier.
34	Figure 2.18	218	Reprinted (adapted) with permission from H. Yoshida, T. Shimizu, T. Uchiyama, H. Kohno, Y. Homma and S. Takeda, *Nano Lett.*, 2009, **9**, 3810-3815. Copyright 2009 American Chemical Society.
35	Figure 2.19	177	Reprinted from Carbon, 58, Vincent Jourdain and Christophe Bichara, Current understanding of the growth of carbon nanotubes in catalytic chemical vapour deposition, 2-39, Copyright 2013, with permission from Elsevier.
36	Figure 2.20	207	Reprinted (adapted) with permission from C. Lu and J. Liu, *The Journal of Physical Chemistry B*, 2006, **110**, 20254-20257. Copyright 2006 American Chemical Society.
37	Table 2.2	171	Reprinted from Applied Catalysis A: General, 253, Philippe Serp, Massimiliano Corrias and Philippe Kalck, Carbon nanotubes and nanofibers in catalysis, 337-358, Copyright 2003, with permission from Elsevier.
38	Figure 2.21	233	Reproduced with permission from Ref. 232: A Brief Summary of Carbon Nanotubes Science and Technology: A Health and Safety Perspective. Authored by Peter Wick, Martin J. D. Clift, Matthias Rösslein, et al. Published by John Wiley & Sons, Inc. Copyright © 2011 WILEY-VCH Verlag GmbH & Co. KGaA, Weinheim
39	Figure 2.22	236	Reprinted by permission from Springer Nature: Springer Nature. Nature Nanotechnology. Carbon nanotubes introduced into the abdominal cavity of mice show asbestos-like pathogenicity in a pilot study, Craig A. Poland, Rodger Duffin, Ian Kinloch, Andrew Maynard, William A. H. Wallace et al., 2008.
40	Figure 2.22	237	Republished with permission of FUTURE MEDICINE LTD, from The effects of carbon nanotubes on lung and dermal cellular behaviors, Luanpitpong, Sudjit; Wang, Liying; Rojanasakul, Yon, volume 9, edition number 6, 2014; permission conveyed through Copyright Clearance Center, Inc.
41	Figure 2.23	259	Reproduced with permission from Ref. 258: Carbon Nanomaterials for Advanced Energy Conversion and Storage. Authored by Wen Lu, Jong-Beom Baek, Dong Wook Chang, et al. Published by John Wiley & Sons, Inc. Copyright © 2012 WILEY-VCH Verlag GmbH & Co. KGaA, Weinheim
42	Figure 2.24	266	Reprinted from Carbon, 44, Stephen Maldonado, Stephen Morin, Keith J. Stevenson, Structure, composition, and chemical reactivity of carbon nanotubes by selective nitrogen doping, 1429-1437, Copyright 2003, with permission from Elsevier.
43	Figure 2.25	253	Reprinted from J. W. Jang, C. E. Lee, S. C. Lyu, T. J. Lee and C. J. Lee, *Appl. Phys. Lett.*, 2004, **84**, 2877-2879., with the permission of AIP Publishing.
44	Figure 2.27	70	Reproduced from Ref. 70 with permission from The Royal Society of Chemistry.
45	Figure 2.28	116	Reproduced from Ref. 115 with permission from The Royal Society of Chemistry.

46	Figure 2.29, Figure 2.30	72	Reproduced with permission from Ref. 72: Towards Carbon-Neutral CO2 Conversion to Hydrocarbons. Authored by Pawel Plucinski, Marcelle McManus, Emma Sackville, et al. Published by John Wiley & Sons, Inc. © 2015 WILEY-VCH Verlag GmbH & Co. KGaA, Weinheim
47	Figure 4.2	286	Originally produced by author *Life of Riley* via the Wikimedia Commons (see: https://commons.wikimedia.org/wiki/File:BET_Multilayer_Adsorption.svg). Published under the Attribution-Share Alike 3.0 Unported license (see: https://creativecommons.org/licenses/by-sa/3.0/deed.en).
48	Figure 4.3	288	Originally produced by author *Moxfyre*, based on work of User:*Pavlina2.0* via the Wikimedia Commons (see: https://commons.wikimedia.org/wiki/File:Raman_energy_levels.svg). Published under the Attribution-Share Alike 3.0 Unported license (see: https://creativecommons.org/licenses/by-sa/3.0/deed.en).
49	Figure 4.4	290	Reprinted from Materials Science and Engineering: B, 119, T. Belin; F. Epron, Characterization methods of carbon nanotubes: a review, 105-118, Copyright 2005, with permission from Elsevier.
50	Figure 4.5	295	Originally produced by author *Claudionico~commonswiki* via the Wikimedia Commons (see: https://en.wikipedia.org/wiki/File:Electron_Interaction_with_Matter.svg#/media/File:Electron_Interaction_with_Matter.svg). Published under the Attribution-ShareAlike 4.0 International license (see: https://creativecommons.org/licenses/by-sa/3.0/deed.en).
51	Figure 4.6	296	Republished with permission of CHAPMAN & HALL, from Microprobe Techniques in the Earth Sciences, P.J. Potts, J.F.W. Bowles, S.J.B. Reed and M.R. Cave, volume 6, edition number 1, Copyright 1995; permission conveyed through Copyright Clearance Center, Inc.
52	Figure 4.7	298	Reprinted by permission from Springer Nature: Springer Nature. Calorimetry and Thermal Methods in Catalysis. Chapter 4: Temperature-Programmed Desorption (TPD) Methods, Vesna Rakić and Ljiljana Damjanović, 2013.
53	Figure 4.11	307	This work has been released into the public domain by its author, *Offnfopt* at English Wikipedia. This applies worldwide.
54	Figure 5.8	71	Reproduced with permission from Ref. 71
55	Figure 6.5	71	Reproduced with permission from Ref. 71

Appendix 2: Molecular Dynamics simulation parameters

Simulations were conducted using GROMACS ver. 5.0.7. Full simulation methodology is freely available in the Supplementary Information of D. L. Williamson, C. Herdes, L. Torrente-Murciano, M. D. Jones and D. Mattia, *ACS Sustain Chem Eng*, 2019, **7**, 7395-7402.

The author would like to provide explicit thanks and credit to Dr Carmelo Herdes of the University of Bath Department of Chemical Engineering for his work in configuring and performing these simulations. While establishing the concept and parameters of these simulations was a joint effort, the simulations presented in this thesis were set up and executed entirely by Dr Herdes. The accompanying experimental and characterisation work in Section 6.2.1 was conducted entirely by the author, with the exception of the BET analysis in Table 6.2, which was conducted by Professors Michele Aresta and Angela Dibenedetto at the University of Bari, Italy.

Molecular models

All species were modelled with available full atomistic force fields, specifically, iron(III) oxide nanoparticles (Fe_2O_3) were simulated via a Lennard-Jones (LJ) potential with constant columbic charges,[365] carbon nanotubes (CNT) by LJ parameters derived for small diameter CNTs from van der Waals density functional calculations,[366] nitrogen doping atoms followed a model for surface heterogeneities on kerogen for gas storage[367] a diatomic hydrogen model used for adsorption (and desorption) molecular dynamics studies on graphite,[368] a simple three-site model of carbon dioxide (CO_2) molecules previously validated for its pure vapour-liquid equilibrium and critical properties predictions,[369] a two site model of carbon oxide, used to simulate its relaxation process at fullerene environment, was selected,[370] and water molecules were represented by the well-known SPC/E model from Berendsen.[371] Models were used without further modifications from the originals, for predictive aim. Cross-interactions followed the common Lorentz-Berthelot combining rules with the exception of the CO_2 model were optimised parameters exists for $\boldsymbol{\sigma}_{C\text{-}O}$=0.2892 nm and $\boldsymbol{\varepsilon}_{C\text{-}O}/k_B$=47.588 K.[368] The implemented molecular parameters are summarized in Table A1.

Table A1. Lennard-Jones potential and coulombic parameters summary for studied species.

	Atom (Molecule)	σ [nm]	ε/k_B [K]	q [e]	Reference
Catalyst	**Fe** (Fe_2O_3)	0.220000	42.749	0.7710	[365]
	O (Fe_2O_3)	0.296000	85.497	-0.5140	
	C (CNT)	0.351400	35.914	-	[366]
	N (NCNT)	0.390000	48.320	-	[367]
Reactants	**H** (H_2)*	0.263984	27.655	-	[368]
	C (CO_2)**	0.275700	28.129	0.6512	[369]
	O (CO_2)	0.303300	80.507	-0.3256	
Products	**C** (CO)***	0.355000	37.152	0.0223	[370]
	O (CO)	0.295000	61.579	-0.0223	
	H (H_2O)§	-	-	0.4238	[371]
	O (H_2O)	0.355330	78.202	-0.8476	

* H-H interatomic distance 0.07414 nm.

** C-O interatomic distance 0.1149 nm.

*** C-O interatomic distance 0.1128 nm.

§ H-O interatomic distance 0.1 nm; H-O-H angle 109.47 deg.

Simulation details

MD simulations were performed under the NVT, NPT and NPzzAT ensembles, at common wet laboratory conditions, with pressure and temperature maintained via the Parrinello-Rahman barostat and Nose-Hoover thermostat respectively, meanwhile, the number of molecules in each studied system was kept constant and followed the needed experimental composition. MD simulations were carried out using GROMACS v5.1. Periodic boundary conditions were applied to the simulation cells. A simple cut-off radius of 1.2 nm was applied. Long-range interactions were calculated by standard PME method. The LINCS algorithm was employed to constrain the molecular bonds. The time resolution of the equations of motions was set to 2 fs. The different systems were monitored until the relevant properties (e.g. density, total energy, etc.) attained equilibrium, afterwards, production runs were extended at least 2 ns for the reported averages.

Appendix 3: A guide to interpreting CO_2 conversion and selectivity figures

The combined RWGS/FT CO_2 conversion experiments conducted in this thesis produce a complex data set, from which the conversion and selectivity of the RWGS and FT reactions must be extracted, processed and displayed for easy comparison. As such, this thesis relies on a previously published data presentation format to ensure consistency across experiments and publications (see: D. Mattia, M. D. Jones, J. P. O'Byrne, O. G. Griffiths, R. E. Owen, E. Sackville, M. McManus and P. Plucinski, *ChemSusChem*, 2015, **8**, 4064-4072.). A slight modification has been made to figures presented in this thesis when compared with their original publication in order to allow for data plotting against a single fixed axis that remains constant between figures.

Figure A1 displays a representative CO_2 conversion figure, as can be found throughout this thesis. A definition of product selectivity and instructions for interpretation of these figures are outlined below.

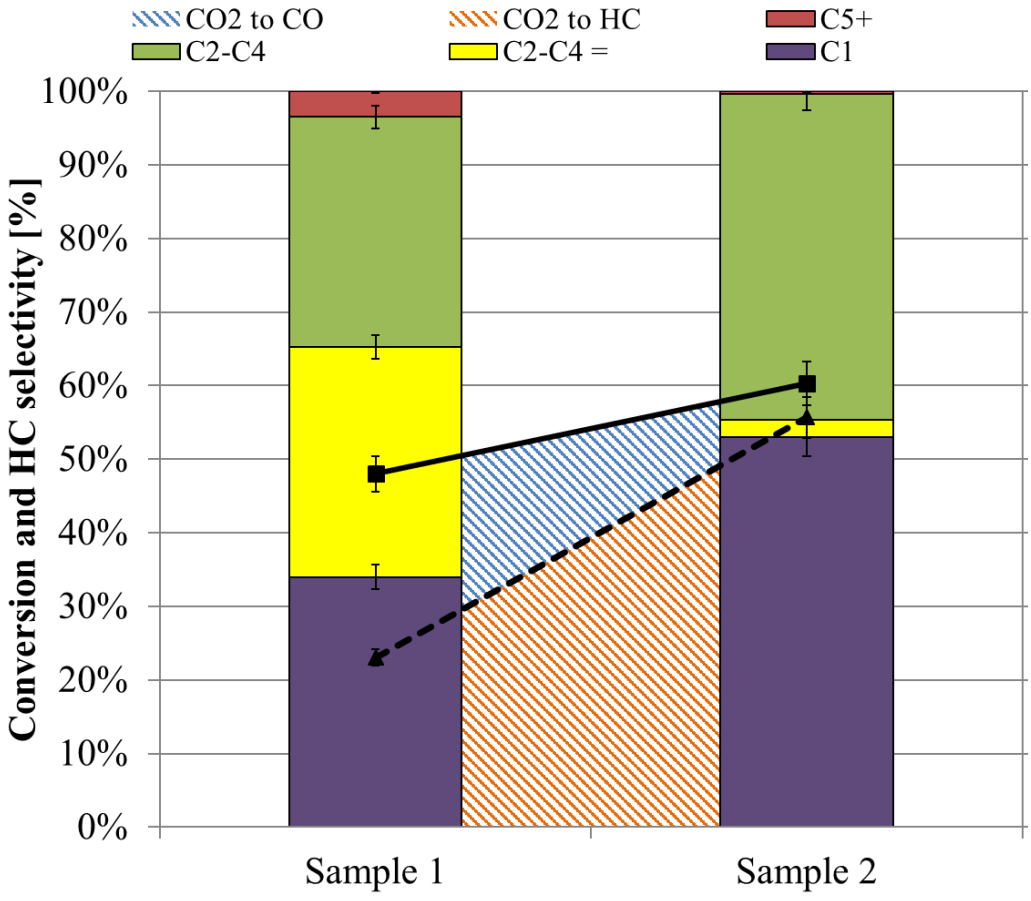

Figure A1. An example plot of CO_2 conversion and selectivity data, as presented throughout this thesis.

Each entry along the x-axis represents a unique CO_2 conversion sample or experiment. The y-axis displays the percentage CO_2 conversion into CO and hydrocarbons, and product selectivities for each entry on the x-axis. The blue and red shaded areas beneath the solid and dashed lines represent the percentage CO_2 conversion into CO and CO_2 conversion into hydrocarbon products, respectively. The multi-coloured vertical bars overlaid on top of the conversion data represents the product distribution of the Fischer-Tropsch reaction.

To aid interpretation, Table A2 provides the data contained in Figure A1 in a tabulated form:

Table A2. Tabulated data contained in Figure A1.

Parameter	Sample 1 [%]	Sample 2 [%]
Total CO_2 conversion	48	60
CO_2 conversion to hydrocarbons	24	56
FT C1 selectivity	34	52
FT C2-C4 selectivity	31	3
FT C2-C4= selectivity	31	44
FT C5+ selectivity	4	1

C1 refers to FT selectivity towards methane. C2-C4 refers to total FT selectivity towards ethane, propane and butane paraffin products. C2-C4= refers to total FT selectivity towards ethene, propene and butene olefin products. C5+ refers to total selectivity towards combined olefin and paraffin products with a carbon number of 5 or greater. The selectivity towards C5+ species in this thesis is not generally significant enough to justify differentiating these species further.

Presenting data in this manner allows for quick visual comparison of key outcomes for each experiment such as CO_2 conversion, total conversion of CO_2 into hydrocarbons, and the product distribution of the FT step with a y-axis that remains fixed even when comparing between different figures in the thesis. Some interpretation from the reader is required to obtain more detailed information such as CO selectivity of the overall process, which can be easily calculated from the figures using the following equation:

$$\gamma_{CO} = \frac{\mathrm{X}_{CO2,total} - \mathrm{X}_{CO2,hydrocarbon}}{\mathrm{X}_{CO2,total}} \times 100$$

Equation A1. CO selectivity is calculated from total CO_2 conversion and CO_2 conversion to hydrocarbons. γ_{CO} is CO selectivity $\mathrm{X}_{CO2,total}$ is total CO_2 conversion, and $\mathrm{X}_{CO2,hydrocarbon}$ is conversion of CO_2 into hydrocarbons.

In this manner, CO selectivity is calculated to be 50% and 93% for Sample 1 and Sample 2, respectively.

The selectivity of an specific hydrocarbon species can be calculated by multiplying its selectivity in the FT process with the total conversion of CO_2 into hydrocarbons, as seen below:

$$\gamma_{HC*,RWGS/FT} = \frac{\gamma_{HC*,FT} \times X_{CO2,hydrocarbon}}{100}$$

Equation A2. The selectivity of a specific hydrocarbon species is calculated from its selectivity in the FT process and CO_2 conversion to hydrocarbons. $\gamma_{HC*,RWGS/FT}$ is the selectivity of the desired hydrocarbon species. $X_{CO2,hydrocarbon}$ is conversion of CO_2 into hydrocarbons.

In this manner, overall methane selectivity is calculated to be 8% and 29% for Sample 1 and Sample 2, respectively. In all instances where these specific values are critical to discussion of the data, these calculations have been performed for the reader and discussed in the thesis text.

In this thesis, the selectivity of a product is defined as:

$$\gamma_x = \frac{N_x}{N_{all\ products}} \times 100$$

Equation A3. The selectivity of product x is described by the moles of product x produced divided by the moles of all products produced, multiplied by 100.

It should be noted that in this context, the selectivities of hydrocarbon and CO products analysed in this thesis can be considered either within their isolated reaction (e.g. CO in RWGS and hydrocarbons in FT), or within the overall RWGS/FT process. Which selectivity value is calculated depends entirely upon which products are included in the $N_{all\ products}$ term of Equation A3. The format of the CO_2 conversion figures presented in this thesis allows for easy determination of either selectivity value from the information provided.

Please note that full calculations for each step of the GC-MS data processing conducted in this thesis have been provided in Chapter 4 in case further clarification is required.

Acknowledgements

The author would like to provide his sincerest thanks to the following entities for their critical contribution to this work:

- My supervisors, Professor Davide Mattia and Dr Matthew Jones, for their unwavering attention, support, and the many hours they have dedicated to guiding my personal and academic development throughout the course of this research.
- Dr Tomos Clark for his guidance in initially establishing the CO_2 conversion process over Fe@NCNT.
- Professors Michele Aresta and Angela Dibenedetto of the University of Bari, Italy, for their expertise in CO_2 chemistry, their work on sustainable synthesis of oxalic and succinic acid over Fe@NCNT-based materials, and for providing BET surface area analysis of Fe@CNT and Fe@NCNT.
- Mrs Ursula Potter, Dr Philip Fletcher, and Ms Diana Lednitzky of the Microscopy and Analysis Suite (MAS) at the University of Bath for their assistance and expertise in characterising the described materials via Raman, SEM, FESEM, TEM and EDS.
- The National EPSRC XPS Users' Service (NEXUS) at Newcastle University for their assistance and expertise in characterising the underling Fe@NCNT materials via XPS.
- Dr Laura Torrente of the University of Cambridge for providing TPD analysis of Fe@CNT and Fe@NCNT.
- Dr Carmelo Herdes for his assistance and expertise in simulating the adsorption properties of Fe@CNT and Fe@NCNT.
- Dr David Morgan and the XP Spectrometry Suite at Cardiff University for their assistance and expertise in characterising the ruthenium-doped samples via XPS.
- Dr Pawel Plucinski of the University of Bath for his expertise in reaction kinetics and thermodynamics.
- MEng students: Jordan Moore for his efforts in scaling up the Fe@CNT and Fe@NCNT production processes using added quartz beads in the CVD reactor. Li Sheng Yew for his efforts in producing and characterizing the initial Fe@NCNT catalyst samples. Chris Ball for his efforts in exploring the activity of iron nanoparticles doped onto a g-C_3N_4 support (not detailed in this thesis).
- The UK Engineering and Physical Sciences Research Council (EPSRC) for their generous funding of this research.

Furthermore, I would like to thank my friends and family around the world who have helped me reach this point. In particular I would like to thank Michael Fitzpatrick, Walid Aslan, Amy Middleton, Ruaridh Thomson, the delightful members of Illuminati HQ, and the entirely indecent members of SPAAAAAACCEEEE for providing friendship and entertainment throughout my PhD.

I would also like to thank Maria Kannov for sharing the good and bad times over the past four years, always listening and believing in the best in me, and patiently waiting for me to come home.

Finally, I would like to thank my family: Herbert Capers Williamson, Maria (Maya) Christina Bijvoet Williamson, Sarah Maria Williamson, and Ayisha Hassan for always supporting me and sacrificing so much to give me the experiences and opportunities I have had. I owe everything to you.